Extended MHD Study of Interchange Modes in Spheromaks

By

Eric C. Howell

A Dissertation submitted in partial fulfillment of the
requirements for the degree of

Doctor of Philosophy
(Engineering Physics)

at the
UNIVERSITY OF WISCONSIN – MADISON
2015

Date of final oral examination: 5/20/2015

The disseration is approved by the following members of the final oral committee:

Carl R. Sovinec, Professor, Engineering Physics
Chris C. Hegna, Professor, Engineering Physics
Oliver Schmitz, Assistant Professor, Engineering Physics
Paul W. Terry, Professor, Physics
David T. Anderson, Professor, Electrical and Computer Engineering

Abstract

Extended MHD effects on pressure driven interchange modes are studied in decaying spheromak equilibria. Equilibria at conditions relevant to high temperature SSPX[Hooper et al., Nucl. Fus. 1999] discharges are ideal interchange unstable. Extended MHD introduces drifts which have a stabilizing effect, reducing the linear growth rate, on the high-n modes. However, extended MHD has a mixed effect on the low-n modes. The low-n modes have the greatest impact on confinement. In some cases extended MHD is destabilizing, increasing the growth rate, while in other cases extended MHD is stabilizing.

A cylindrical screw-pinch model that approximates decaying spheromaks, is studied to better understand the lack of stabilization on the low-n modes. The extended MHD effects reduce the growth rate at small Hall parameter (d_i/a), but a second instability exists at finite Hall parameter. The second mode grows at a rate comparable to the MHD interchange mode. The diamagnetic heat flux (q_*) has an important stabilizing effect, delaying the onset of the second mode. In calculations that neglect the diamagnetic heat flux, the second mode is dominant at experimentally relevant Hall parameters, and its growth rate exceeds the MHD growth rate. However, including the diamagnetic heat flux delays the onset of the second mode. Here significant stabilization is observed at experiential conditions for Suydam parameters $D_s \lesssim 1.0$. This is four times the marginal ideal stable condition.

An extended MHD dispersion relation for the gravitational interchange mode[Zhu et al., Phys. Rev. Lett. 2008] is analyzed to understand the nature of the second instability. The inclusion of the two-fluid Ohm's law introduces an ion drift wave. The ion drift wave can interact with the gravitational interchange mode producing a second instability.

Acknowledgements

I would like to thank my advisor, Carl Sovinec, without his support and guidance this thesis would not be possible. I also want to thank my family and friends who provided moral support throughout my graduate studies.

This work is supported by the US department of Energy.

Contents

Chapter 1

Introduction

The spheromak is a magnetic confinement concept that relies primarily on internal plasma currents to generate the confining magnetic field. Spheromaks are compact, unlike many other confinement concepts, and no material surfaces necessarily link the plasma. As a result, spheromaks can be confined in topologically spherical chambers, and the engineering simplicity of these chambers make the spheromak an attractive confinement concept. The fact that spheromaks are confined primarily by internal plasma currents adds complexity. Understanding the nonlinear evolution of the internal currents is critical to the success of spheromak research.

One outstanding issue in spheromak research is to identify the mechanisms that limit the pressure[1]. In several experiments it is not clear if the pressure is limited by ohmic power balance or pressure driven instabilities. Several experiments observe spheromaks that violate ideal stability boundaries by large margins[2]. Most spheromak experiments to-date are ohmically heated, and the absence of auxiliary heating also limits the achievable pressure.

We use the NIMROD code[3] to study the stability of spheromaks relevant to the sustained spheromak experiment (SSPX)[4]. Prior resistive MHD simulations of SSPX using NIMROD reproduce many aspects of the current evolution[5]. However, the simulations systematically underpredict the peak temperatures observed in the experiment[6]. The simulations also appear to be less stable than the experiment. Our initial hypothesis is that the simulations are limited by a pressure driven instability, and that extended MHD drifts not considered previously stabilize pressure driven modes. By stabilizing these modes, the extended MHD effects allow the experiment to reach hotter temperatures. However, we find that while extended MHD can have a significant effect on the stability, this stabilization it not enough to alter the stability properties of the hottest SSPX discharges.

1.1 The Spheromak

Spheromaks are compact magnetic confinement devices. They are comprised of poloidal and toroidal magnetic fields of similar magnitude. The toroidal magnetic field goes to zero at the plasma boundary. Spheromaks are primarily confined by magnetic fields generated from internal plasma currents. However, a nearby conducting wall is necessary to enforce $\vec{B} \cdot \hat{n} \approx 0$ at the boundary. The eddy currents which enforce the boundary condition ensure that spheromak equilibria do not violate the Virial theorem.

A compact device is one where no material surfaces link the plasma. These devices do not require a center-stack. The vessel surrounding the plasma is topologically equivalent to a sphere; however, the magnetic field configuration is still toroidal. In the center-stack of non-compact devices, magnets and other critical components link the plasma. The shielding necessary to protect these magnets from high energy neutrons constrains the size of the device. The simplicity of the spheromak confinement vessel and the absence of a center-stack are two features that make the spheromak an attractive reactor concept.

This project focuses on spheromaks relevant to the sustained spheromak experiment (SSPX). SSPX was a coaxial helicity injected (CHI) spheromak operated at Lawrence Livermore National Laboratory[4]. SSPX studied the physics of long pulse quasi-steady-state high temperature spheromaks. It achieved peak electron temperatures of $T_e \sim 500\,\mathrm{eV}$, the hottest temperatures measured in spheromaks to-date[7]. The experimental data is bounded by $\beta_E \sim 5\%$[8]. Core electron thermal diffusivities of $\chi_e \sim 1\,\mathrm{m}^2/\mathrm{s}$, inferred from equilibrium reconstructions, are comparable with L-mode tokamaks. A more detailed account of SSPX is given in Chapter 2.

The operation of SSPX is divided into two phases: formation and decay. During the formation phase strong currents are driven across two electrodes in the CHI guns. These electrodes are linked by poloidal flux, and $J \times B$ forces push the flux into the flux conserver. As the flux balloons out into the flux conserver, it goes unstable and relaxes into a spheromak-like state. This relaxation process amplifies the flux and current. A major thrust of the spheromak research is to understand and optimize this formation process.

The strong currents during the formation drive fluctuations which amplify the flux. These fluctuations prevent flux surface formation and significantly affect confinement[9]. Flux amplification and good confinement are mutually exclusive in CHI spheromaks. Good confinement is obtained by reducing the current across the electrodes in both the experiment and nonlinear simulations.

Reducing the gun current below a critical threshold eliminates the fluctuation drive, halts flux amplification, but allows flux surfaces to form. High temperatures and good confinement are observed during this controlled decay phase. The experiment is optimized by controlling the safety factor profile to avoid the $q = \frac{1}{2}$ and $q = \frac{2}{3}$ rational surfaces[10]. The safety factor is controlled by driving relatively weak currents across the electrodes. This maintains the currents on the open field surrounding the spheromak, and it maintains the safety factor at the edge of the spheromak. An integral part of the success of the SSPX program is 3D resistive MHD modeling using the NIMROD code[3]. These simulations elucidated much of the physics involved in the spheromak formation and controlled decay phases.

1.2 Our Approach

The 2009 research needs for magnetic fusion energy sciences workshop (ReNeW) identified 3 challenges that need to be addressed for spheromaks: *formation and stability in the fusion-plasma regime, transport and energy confinement, and efficient current drive and flux sustainment*[1]. In particular the ReNeW report highlights the need to understand mechanisms that limit β. Many spheromak experiments have achieved high β, but it is not clear if the pressure in these experiments is limited by ohmic power balance or the onset of pressure driven modes. The report also identifies simulations as an important tool to address this issue.

In this project we use the NIMROD code to investigate pressure limits in spheromaks. Resistive MHD simulations using NIMROD successfully reproduce many aspects of the current evolution and magnetic field evolution in SSPX discharges. However, the resistive MHD simulations routinely underpredict the peak electron temperatures observed in the experiment. The difference is most pronounced in the later high performance discharges, where there is a 40% difference between the experiment and simulation[6]. The simulations are also less stable than the experiment, and the instabilities are limiting the simulated temperatures. We test the hypothesis that extended MHD effects, absent in the resistive MHD simulations, have a significant stabilizing effect. This delays the onset of instabilities, and allows the spheromak to reach hotter temperatures.

We perform linear analysis on a variety of spheromak equilibria relevant to high temperature SSPX discharges. To facilitate this analysis we develop NIMEQ[11]. NIMEQ solves the Grad-Shafranov equation to generate axisymmetric magneto-static equilibria. It uses NIMROD's numerical representation, eliminating interpolation errors that would otherwise occur when importing an externally generated equilibrium. The ability to generate equilibria "in-house" also allows us to study the stability over a wide range of parameters.

The linear analysis shows that equilibria relevant to SSPX are ideal interchange unstable in resistive MHD. The extended MHD stabilization is inhibited by the introduction of a second instability. The onset of this second mode and its linear growth rate are sensitive to which terms are included in the extended MHD model. The diamagnetic heat flux, which is often neglected in analysis, provides an important stabilizing contribution that delays the onset of this mode. When this term is included in the calculations, extended MHD is strongly stabilizing at four times the ideal stability limit. However, this stabilization is not enough to significantly alter the stability properties of the highest performing SSPX discharges.

Nonlinear simulations are also performed self-constantly modeling the collisional thermal transport with the evolution of the current density and magnetic field. We perform full discharge simulations that model the formation and the controlled decay. We initialize other nonlinear simulations using NIMEQ equilibria. This allows us to avoid simulating the computationally expensive formation phase.

1.3 Outline of the Remaining Chapters

Chapter 2 reviews prior work relevant to this thesis. We start by defining the extended MHD model with closure terms based on Braginskii's collisional model[12]. A brief discussion of magneto-static equilibria and Grad-Shafranov theory follows. We then review pressure driven interchange. This is followed by a discussion of physics issues relevant to spheromaks and a review of SSPX experimental results. Finally we introduce aspects of the NIMROD code.

Chapter 3 discusses the development of NIMEQ: a Grad-Shafranov solver for NIMROD. NIMEQ is designed to be a general-purpose equilibrium solver. The formulation is generalized to treat geometries that contain the geometric axis at $R = 0$, and it allows current density on the open field. These are needed to model CHI spheromak equilibria. NIMEQ is benchmarked against analytic solutions of the Grad-Shafranov equation that represent idealization of tokamaks, field reversed configurations, and spheromaks.

Chapter 4 considers the linear stability of interchange modes in extended MHD. We start by studying the stability of decaying spheromak equilibria. These equilibria are ideal interchange unstable, even at low pressure. Extended MHD is found to have a minimal effect on instabilities with small toroidal mode numbers. Experimentally these low-n modes have the greatest effect on confinement. To better understand these results we study the extended MHD effects using a family of linear periodic screw-pinch equilibria that approximate decaying spheromak equilibria. The pressure in these equilibria is prescribed according to the ideal stability parameter. This allows us to study the extended MHD effects on resistive and ideal interchange modes. A second instability exists in the extended MHD model that inhibits the stabilization. The diamagnetic heat flux, absent in the decaying spheromak calculations, has a significant stabilizing effect on this second mode. This chapter also studies the extended MHD effects on the gravitational interchange mode. The two-fluid Ohm's law introduces an ion drift wave that interacts with the gravitational interchange mode producing a second instability.

Chapter 5 summarizes several nonlinear simulations. The first series of simulations model early SSPX discharges comparing different resistive and extended MHD models. These simulations model the full discharge (both formation and decay). However, the extended MHD simulations are noisy near the curved regions of the SSPX flux conserver. Ultimately, this noise leads to an unphysical enhanced rate of poloidal flux decay. To avoid this issue, other simulations use a rectangular mesh to approximate the poloidal cross-section of the SSPX flux conserver. These simulations are also initialized with NIMEQ equilibria to avoid simulating the computationally expensive formation.

Chapter 6 summarizes our results. The linear analysis shows that extended MHD can have a significant stabilizing effect at conditions up to four times the ideal interchange stability limit. The diamagnetic heat flux, a term often neglected in extended MHD models, has an important stabilizing effect that is needed to obtain this result. However, the extended MHD effects are not strong enough to significantly alter the stability properties in conditions of the highest performing SSPX discharges.

Chapter 2

Theory and Background

This chapter provides a review of the relevant theory and literature. Section 2.1 discusses the extended MHD model that is used in this study. The Grad-Shafranov equation describing 2 dimensional plasma equilibria is reviewed in Section 2.2. Section 2.3 discusses the plasma interchange mode. An overview of spheromak physics is presented in Section 2.4. Included in this discussion is a review of three coaxially injected spheromaks, highlights of early spheromak simulations, and a detailed discussion of previous work studying interchange modes in spheromak equilibria. Finally, an introduction to the NIMROD code is given in 2.5.

2.1 The Extended MHD Model

The kinetic description is one of the most fundamental descriptions of a plasma. The kinetic model describes each species (electrons and ions) by a distribution function, $f_s\left(\vec{x},\vec{v},t\right)$, in 6 dimensional phase space. The evolution of the distribution function is governed by the Fokker-Planck equation

$$\frac{\partial f_s}{\partial t}+\vec{v}\cdot\nabla f_s+\frac{q_s}{m_s}\left(\vec{E}+\vec{v}\times\vec{B}\right)\cdot\nabla_v f_s=C_s\left(f_s\right), \tag{2.1}$$

where q_s and m_s are the charge and mass of particles of species s, $\vec{E}$ and $\vec{B}$ are the macroscopic electric and magnetic fields, and C_s is the Coulomb collision operator.

The evolution of $\vec{E}$ and $\vec{B}$ are governed by Maxwell's equations

$$\nabla \cdot \vec{E} = \frac{\rho_e}{\epsilon_0} \tag{2.2}$$

$$\nabla \times \vec{E} = -\frac{\partial \vec{B}}{\partial t} \tag{2.3}$$

$$\nabla \cdot \vec{B} = 0 \tag{2.4}$$

$$\nabla \times \vec{B} = \mu_0 \vec{J} + \mu_0 \epsilon_0 \frac{\partial \vec{E}}{\partial t}, \tag{2.5}$$

where ϵ_0 is the permittivity of free space, and μ_0 is the permeability of free space. The charge density ρ_e and current density $\vec{J}$ are related to the plasma distribution function by the equations

$$\rho_e = \sum_s q_s \int d^3v f_s \tag{2.6}$$

$$\vec{J} = \sum_s q_s \int d^3v \vec{v} f_s. \tag{2.7}$$

Equations 2.1-2.7 are a closed set of equations that self-consistently describe the evolution of a plasma. In practice analytic solutions to these equations only exist for special cases. Numerical simulations that evolve the distribution function in both physical and velocity space are computationally demanding and often prohibitively expensive.

Fluid models are often used to describe the dynamics of plasmas due to the difficulties associated with solving the kinetic equation. These models are obtained by taking velocity moments of the kinetic equation. Magnetohydrodynamics is one such model. MHD is widely used to model macroscopic low frequency dynamics of fusion-relevant magnetically confined plasma. Despite its many successes, MHD neglects many physical processes relevant to these plasmas.

Extended MHD is an extension of the MHD model that accounts for some of the neglected physics without reverting to a full kinetic model. In this work we use an extended MHD model that accounts for two-fluid effects and finite Larmor radius (FLR) effects. MHD treats the plasma as a single species neutral conducting fluid, while in reality plasmas are composed of electrons and multiple ion species. The two-fluid model treats the electrons and ions as separate fluids, but it treats the ions as a single species. MHD also assumes that Larmor radii are negligibly small. Our FLR model accounts for the fact that ion Larmor orbits have a finite radius, but it assumes that the radius is small compared to the length scales of interest. A kinetic treatment is needed if the radius is comparable to these length scales.

Two-fluid and FLR corrections can have both stabilizing and destabilizing effects. For example both effects introduce drifts which can stabilize interchange modes[13]. Two-fluid effects increase the rate of magnetic reconnection, and can enhance the growth rate of tearing modes[14]. Similarly, FLR effects destabilize a number of drift waves[15].

The extended MHD model used in this thesis is described by the equations

$$\frac{\partial n}{\partial t} + \vec{V} \cdot \nabla n = -n \nabla \cdot \vec{V} \tag{2.8}$$

$$nm \left(\frac{\partial \vec{V}}{\partial t} + \vec{V} \cdot \nabla \vec{V} \right) = \vec{J} \times \vec{B} - \nabla p - \nabla \cdot \vec{\vec{\pi}}_i \tag{2.9}$$

$$\frac{n}{\gamma_s - 1} \left(\frac{\partial T_s}{\partial t} + \vec{V}_s \cdot \nabla T_s \right) = -p_s \nabla \cdot \vec{V}_s - \nabla \cdot \vec{q}_s - \vec{\vec{\pi}}_s : \nabla \vec{V}_s + Q_s \tag{2.10}$$

$$\nabla \times \vec{B} = \mu_0 \vec{J} \tag{2.11}$$

$$\nabla \cdot \vec{B} = 0 \tag{2.12}$$

$$\frac{\partial \vec{B}}{\partial t} = -\nabla \times \vec{E} \tag{2.13}$$

$$\vec{E} = -\vec{V} \times \vec{B} + \eta \vec{J} + \frac{1}{ne} \left(\vec{J} \times \vec{B} - \nabla p_e \right) + \frac{m_e}{ne^2} \frac{\partial \vec{J}}{\partial t} \tag{2.14}$$

Equations 2.8-2.9 are the continuity and momentum equations for the bulk fluid. Here n is the number density (quasi-neutrality has been assumed), m is the total mass $(m_i + m_e)$, $\vec{V} = \frac{m_i \vec{V}_i + m_e \vec{V}_e}{m_i + m_e} \approx \vec{V}_i + O\left(\frac{m_e}{m_i}\right)$ is the center of mass flow velocity, $p = p_i + p_e$ is the total pressure, and $\vec{\vec{\pi}}_i$ is the ion viscous stress tensor. Equation 2.10 is the temperature evolution equation for each species. Here γ_s is the ratio of specific heats, $\vec{q}_s$ is the heat flux, $\vec{\vec{\pi}}_s : \nabla \vec{V}_s$ is the viscous heating, and Q_s accounts for other heating sources (including Ohmic heating). The electron flow velocity is computed from the current density $\vec{V}_e = \vec{V}_i - \frac{\vec{J}}{ne} \approx \vec{V} - \frac{\vec{J}}{ne}$. Equations 2.11-2.13 are Ampere's law, the magnetic divergence constraint, and Faraday's Law. Equation 2.11 neglects the displacement current $\mu_0 \epsilon_0 \frac{\partial \vec{E}}{\partial t}$, which is appropriate for the low-frequency dynamics that are of interest here. Equation 2.14 is the two-fluid Ohm's law and represents the electron momentum equation, here η is the electrical resistivity. The first two terms on the right side are the standard MHD Ohm's law. The Hall term $\vec{J} \times \vec{B}$, electron pressure ∇p_e, and electron inertia $\frac{m_e}{ne^2} \frac{\partial \vec{J}}{\partial t}$ represent two-fluid corrections to MHD. Equation 2.14 neglects the electron stress tensor $\vec{\vec{\pi}}_e$ and electron advection.

FLR effects enter the extended MHD model through the ion viscous stress tensor $\vec{\vec{\pi}}_i$ and through the electron and ion heat fluxes $\vec{q}_s$. We use a model for $\vec{q}_s$, $\vec{\vec{\pi}}_i$, Q_s, and η that is based on the Braginskii model [12]. Braginskii treats a 2 component plasma in the collisional limit. It is valid when the collision frequency, ν, is faster than the characteristic frequency of the dynamics of interest, $\frac{d}{dt} << \nu$, and the collisional mean free path, λ, is smaller than the length scales of interest, $\lambda \ll \nabla^{-1}$. It also assumes that the thermal speeds are small relative to the flow speeds. We consider the strongly magnetized limit for a hydrogen plasma with an ion charge $Z_{eff} = 1$. In this limit the ion cyclotron frequency, $\Omega = \frac{eB}{m}$, is faster than the collision frequency, $\Omega \gg \nu$. Here the mean free path must be smaller than parallel length scales $\lambda \ll \nabla_{\parallel}^{-1}$, and the ion Larmor radius, ρ_l, must be smaller than perpendicular length scales, $\rho_l << \nabla_{\perp}^{-1}$. The collisional mean free path increases with increasing temperature, and the assumption $\lambda \ll \nabla_{\parallel}^{-1}$ is often violated in high temperature plasmas. In these plasmas, applying the Braginskii model tends to over predict the parallel transport.

Braginskii gives a Spitzer like resistivity where

$$\eta \approx 0.51 \frac{m_e}{ne\tau_e}, \tag{2.15}$$

$\tau_e = \nu_e^{-1}$ is the electron collision time

$$\tau_e = \frac{6\sqrt{2}\pi^{3/2}\epsilon_0^2\sqrt{m_e}T_e^{3/2}}{ne^4 \ln\Lambda}, \tag{2.16}$$

and $\ln\Lambda$ is the Coulomb logarithm. The ion collision time $\tau_i = \nu_i^{-1}$ is

$$\tau_i = \frac{12\pi^{3/2}\epsilon_0^2\sqrt{m_i}T_i^{3/2}}{ne^4 \ln\Lambda}. \tag{2.17}$$

The electron heating term, Q_e, includes Ohmic heating, ηJ^2, and a collisional thermal equilibration between the electrons and ions

$$Q_e = \eta J^2 + \frac{3m_e}{m_i}\frac{n}{\tau_e}\left(T_i - T_e\right). \tag{2.18}$$

The ion heating term, Q_i, is just the thermal equilibration between ions and electrons

$$Q_i = -\frac{3m_e}{m_i}\frac{n}{\tau_e}\left(T_i - T_e\right). \tag{2.19}$$

The ion viscous heating is explicitly included in Equation 2.10.

The heat fluxes are split into parallel, perpendicular, and cross field components

$$\vec{q}_s = -k_{\|s}\nabla_{\|}T_s - k_{\perp s}\nabla_{\perp}T_s - k_{\wedge s}\nabla_{\wedge}T_s, \tag{2.20}$$

where $\nabla_{\|} = \hat{b}\left(\hat{b}\cdot\nabla\right)$, $\nabla_{\perp} = \nabla - \nabla_{\|}$, $\nabla_{\wedge} = \hat{b}\times\nabla$, and $\hat{b} = \vec{B}/\left|B\right|$. The electron thermal conductivities are

$$k_{\|e} = 3.2\frac{n\tau_e T_e}{m_e} \tag{2.21}$$

$$k_{\perp e} = 4.7\frac{nT_e}{m_e\Omega_e^2\tau_e} \tag{2.22}$$

$$k_{\wedge e} = \frac{5nT_e}{2m_e\Omega_e}. \tag{2.23}$$

The ion thermal conductivities are

$$k_{\|i} = 3.2\frac{n\tau_i T_i}{m_i} \tag{2.24}$$

$$k_{\perp i} = 4.7\frac{nT_i}{m_i\Omega_i^2\tau_i} \tag{2.25}$$

$$k_{\wedge i} = -\frac{5nT_i}{2m_i\Omega_i}. \tag{2.26}$$

For both species the parallel conductivity is order $\Omega_s\tau_s$ larger than the cross field conductivity $k_{\wedge s}$, which is order $\Omega_s\tau_s$ larger than the perpendicular conductivity. The electron parallel thermal conductivity is much larger than the ion parallel thermal conductivity when T_e and T_i are similar, but the ion perpendicular thermal conductivity is much larger than the electron perpendicular thermal conductivity. In a collisional plasma where the electron and ion temperatures are similar, the parallel thermal conduction is primarily due to electrons and the perpendicular thermal conduction is primarily due to the ions.

The cross field heat flux $k_{\wedge s}\nabla_{\wedge}T_s$, also called the diamagnetic heat flux, is a first-order FLR correction and does not depend on the collision frequency. The electron and ion diamagnetic heat fluxes cancel when $T_i = T_e$.

The ion stress tensor can also be separated into perpendicular, parallel, and cross field tensors. The components of the stress tensor are

$$\vec{\vec{\pi}}_{\perp i} \approx \vec{\vec{\pi}}_{iso} = \mu_{iso}\vec{\vec{W}} \tag{2.27}$$

$$\vec{\vec{\pi}}_{\| i} = 0.96 n T_i \tau_i \left(\hat{b}\cdot\vec{\vec{W}}\cdot\hat{b}\right)\left(\vec{\vec{I}} - 3\hat{b}\hat{b}\right) \tag{2.28}$$

$$\vec{\vec{\pi}}_{\wedge i} = \vec{\vec{\pi}}_{gyr} = \frac{nT_i}{4\Omega_i}\left[\hat{b}\times\vec{\vec{W}}\cdot\left(\vec{\vec{I}} - 3\hat{b}\hat{b}\right) - \left(\vec{\vec{I}} - 3\hat{b}\hat{b}\right)\cdot\vec{\vec{W}}\times\hat{b}\right] \tag{2.29}$$

where $\vec{\vec{I}}$ is the identity tensor and $\vec{\vec{W}}$ is the rate of strain tensor

$$\vec{\vec{W}} = \nabla\vec{V} + \left(\nabla\vec{V}\right)^{\intercal} - \frac{2}{3}\vec{\vec{I}}\nabla\cdot\vec{V}. \tag{2.30}$$

The perpendicular stress tensor is approximated by an isotropic stress tensor. Physically, the viscosity μ_{iso} should scale as $\mu_{iso} \sim \frac{nT_i}{\Omega_i^2\tau_i}$. Similar to the thermal conductivity, the parallel viscosity is larger than the cross-field viscosity by a factor of $\Omega_i\tau_i$, and the cross field viscosity is larger than the perpendicular viscosity by the same factor.

The cross field component of the stress tensor is commonly called the gyroviscous stress tensor. The gyroviscous stress tensor is the other FLR correction in our model. Similar to the diamagnetic heat flux, the gyroviscous stress is independent of the collision frequency.

MHD and extended MHD are characterized by a number of non-dimensional quantities. In resistive MHD two relevant time scales are the Alfven time, $\tau_A = \frac{L}{V_a}$, and the resistive diffusion time, $\tau_R = \frac{\mu_0}{\eta}L^2$. The Alfven time measures how long it takes Alfven waves, which propagates at the speed $V_a = B/\sqrt{\mu_0\rho}$, to travel across a characteristic distance L. The Lundquist number, $S = \frac{\tau_R}{\tau_A}$, is the ratio of the two time scales. It is a dimensionless measure of a plasma resistivity. The magnetic Prandtl number $Pr = \frac{\nu\mu_0}{\eta}$ is a measure of the rate of viscous diffusion to the rate of resistive diffusion. The ratio of the thermal pressure to the magnetic pressure is $\beta = \frac{2\mu_0 p}{B^2}$. This number also characterizes the ratio of the sound speed $V_s = \sqrt{\gamma p/\rho}$ to the Alfven speed $\beta = \frac{2}{\gamma}\frac{V_s^2}{V_a^2}$.

The ion-skin depth, $d_i = \frac{c}{\omega_{pi}} = \frac{V_A}{\Omega_i}$, characterizes the length scales on which two-fluid effects are important. On length scales that are large compared to the ion-skin depth the electrons move with the ions. Here the single fluid approximation of MHD is valid. On length scales that are small compared to the ion-skin depth, the electron motion can be independent of the ions. We refer to normalized ion-skin depth, $\Lambda = d_i/L$, as the Hall parameter.

The normalized ion Larmor radius $\frac{\rho_i}{L} = \frac{1}{L\Omega_i}\sqrt{\frac{p_i}{\rho}} = \frac{d_i}{L}\sqrt{\frac{\beta_i}{2}}$ characterizes the importance of ion FLR effects. FLR effects are negligible when the Larmor radius is much smaller than all characteristic length scales, $\frac{\rho_i}{L} \ll 1$. The Braginskii model includes FLR effects, but the model breaks down when $\frac{\rho_i}{L}$ becomes too large. For example, a comparison between extended MHD calculations and hybrid kinetic calculations (kinetic ions + fluid electrons) for the ion-temperature gradient mode shows that the extended MHD model is a good approximation for $\frac{\rho_i}{L_{Ti}} < 0.01$ and $k_\perp \rho_i < 0.2$, here L_{Ti} is the equilibrium ion temperature length scale and $k_\perp$ is the perpendicular wave vector on the mode[15].

2.2 Magnetostatic Equilibria

Plasma equilibria play an important role in magnetic confinement. It is commonly assumed that confined plasmas evolve slowly through a series of quasi-steady equilibria that are in force balance (magnetized plasmas not in force balance will evolve rapidly on Alfvenic time scales). In most cases, the evolution of these equilibria is slow compared to the dynamical times scales of instabilities that arise. This leads naturally to a separation of time scales, whereby equilibria are assumed to be stationary throughout the evolution of instabilities.

Magnetostatic equilibria are governed by the magnetic divergence constraint, MHD force balance, and Ampere's law

$$\nabla \cdot \vec{B} = 0 \tag{2.31}$$

$$\vec{J} \times \vec{B} = \nabla p \tag{2.32}$$

$$\nabla \times \vec{B} = \mu_0 \vec{J}. \tag{2.33}$$

For conditions of axisymmetry, the magnetic field is expressed as

$$\vec{B} = \nabla\phi \times \nabla\psi + F\nabla\phi \tag{2.34}$$

in the cylindrical coordinate system (R, Z, ϕ). The magnetic flux function ψ is related to the physical poloidal flux, divided by a factor of 2π. A similar expression for the current is found using Ampere's law

$$\mu_0 \vec{J} = \mu_0 R J_\phi \nabla\phi + \nabla F \times \nabla\phi, \tag{2.35}$$

where the toroidal current satisfies the equation

$$\mu_0 J_\phi = \frac{1}{R}\Delta^* \psi \tag{2.36}$$

and the elliptic Grad-Shafranov operator is defined as

$$\Delta^* \psi \equiv \frac{\partial^2 \psi}{\partial r^2} - \frac{1}{R}\frac{\partial \psi}{\partial r} + \frac{\partial^2 \psi}{\partial z^2}. \tag{2.37}$$

From the MHD force balance, Equation 2.32, it is observed that $\vec{B} \cdot \nabla p = 0$, implying that the pressure is a flux function $p = P(\psi)$. Similarly, $\vec{J} \cdot \nabla p = 0$, and $F(\psi) = RB_\phi$ is also a flux function. Inserting the expressions for $\vec{B}$ and $\vec{J}$ (Equations 2.34 and 2.35) in to Equation 2.32 yields the Grad-Shafranov equation [16][17]

$$\Delta^* \psi = -F(\psi)\frac{dF(\psi)}{d\psi} - \mu_0 R^2 \frac{dP(\psi)}{d\psi}. \tag{2.38}$$

Equation 2.38 is a second-order nonlinear elliptic equation describing axisymmetric plasma in toroidal geometry. The two free functions $P(\psi)$ and $F(\psi)$ are either prescribed or determined from transport effects.

In Cartesian coordinates (x, y, z) with no variation in the z direction the Grad-Shafranov equation reduces to a nonlinear Poisson equation

$$\frac{\partial^2 \psi}{\partial x^2} + \frac{\partial^2 \psi}{\partial y^2} = -F(\psi)\frac{dF(\psi)}{d\psi} - \mu_0 \frac{dP(\psi)}{d\psi}, \tag{2.39}$$

with $\vec{B} = \nabla z \times \nabla \psi + F\nabla z$ and $\mu_0 \vec{J} = \mu_0 J_z \nabla z + \nabla F \times \nabla z$.

The parallel current density, $\lambda = \mu_0 \vec{J} \cdot \vec{B}/B^2$, is important in the theory of spheromaks. Evaluating λ for axisymmetric equilibria using Equations 2.34, 2.35, and 2.38 yields the relation $\lambda = -F' - \mu_0 P'/B^2$, where primes denote derivatives in ψ. In spheromaks and other low-β systems the approximation $\lambda = -F'$ is frequently used. Formally this equality is only exact for force-free equilibria where $P' = 0$, and this approximation introduces errors of order β.

2.2.1 Analytic Solutions of the Grad-Shafranov Equation

Analytic solutions to the Grad-Shafranov equation are known for several specifications of the plasma pressure, $P(\psi)$, and the toroidal field, $F(\psi)$, in simple geometries. In this section we present several such solutions. These solutions often serve as idealized models for different confinement concepts, but they do not accurately represent modern day experiments. Nonetheless, they are also useful tools for confirming the accuracy of equilibrium solvers. In Chapter 3, some of the equilibria presented here are used to verify the accuracy of NIMEQ and to study its convergence properties.

Solov'ev showed that series solutions to the Grad-Shafranov equation are obtainable in toroidal geometry when both $\mu_0 P' = S_1$ and $FF' = S_2$ are constant[18]. Substituting these definitions into the Grad-Shafranov equation yields the equation

$$R\frac{\partial}{\partial R}\left(\frac{1}{R}\frac{\partial\psi}{\partial R}\right)+\frac{\partial^2\psi}{\partial z^2}=-S_1R^2-S_2. \tag{2.40}$$

Equation 2.40 is a linear inhomogeneous equation. It has the general solution $\psi = \psi_0 + \psi_p$ where ψ_0 satisfies the homogeneous equation and $\psi_p = -S_1R^2/8 - S_2Z^2/2$ is the particular solution. Solutions to the homogeneous equation are found using the expansion $\psi = \sum_n f_n\left(R\right)Z^n$. Substitution of this expansion into $\Delta^*\psi = 0$ yields the recursion relation

$$R\frac{\partial}{\partial R}\left(\frac{1}{R}\frac{\partial f_n}{\partial R}\right)=-\left(n+1\right)\left(n+2\right)f_{n+2}. \tag{2.41}$$

The series is truncated by assuming that $f_n = 0$ for $n > n_{max}$[19]. For example setting $n_{max} = 2$ and assuming up-down symmetry yields the solution

$$\psi=-S_1R^2/8-S_2Z^2/2+C_1+C_2R^2+C_3\left(R^4-4R^2Z^2\right)+C_4\left(R^2\ln R-Z^2\right). \tag{2.42}$$

The coefficients S_1, S_2 and C_n are determined by specifying the plasmas shape (major radius, minor radius, elongation, triangularity, etc) and/or several figures of merit (β_{pol}, I_p, etc). A procedure to find the coefficients for an up-down symmetric tokamak is worked out in [19]. This procedure has been generalized, by including higher order terms in the expansion of ψ, to create both up-down symmetric and asymmetric equilibria relevant to tokamaks, spheromak, and FRCs[20].

Analytic solutions to the Grad-Shafranov equation are known for force-free ($P' = 0$) configurations with constant λ in several geometries. In a periodic cylinder of radius a the equilibrium fields are

$$B_r = 0 \tag{2.43}$$

$$B_\theta = B_0 J_1(\lambda r) \tag{2.44}$$

$$B_z = B_0 J_0(\lambda r), \tag{2.45}$$

where J_n is the n^{th} order Bessel function, B_0 is the longitudinal field, B_z, at $r = 0$, and $\vec{B} \cdot \hat{n}$ is enforced along the boundary. These equations are often used to model reversed field pinches (RFP) where the toroidal effects are often negligible. The longitudinal magnetic field, B_z, reverses sign if $\lambda a > \chi_{01}$, where $\chi_{01} \approx 2.4048$ is the first zero of J_0.

The lowest order nontrivial force-free solution in a sphere of radius a is

$$B_r = 2B_0 \cos(\theta)\, j_1(\lambda r) \tag{2.46}$$

$$B_\theta = -B_0 \sin(\theta) \frac{1}{\lambda r} \frac{\partial}{\partial r} \left(r j_1(\lambda r)\right) \tag{2.47}$$

$$B_\phi = B_0 \sin(\theta)\, j_1(\lambda r), \tag{2.48}$$

where spherical coordinates (r, θ, ϕ) are used and $j_1(x) = \sin(x)/x^2 - \cos(x)/x$ is the first spherical Bessel function [21]. The radial magnetic field must go to zero at $r = a$ in order to satisfy the boundary condition $\vec{B} \cdot \hat{n} = 0$. Thus λa must be equal to a zero of j_1, the first of which is approximately 4.4934. In force-free spherical equilibria, unlike periodic cylindrical equilibria, λ is not a free parameter. Instead it is an eigenvalue that characterizes the geometry. We note that the toroidal magnetic field, B_ϕ, is zero at the boundary. This is a characteristic of topologically spherical equilibria since no external currents link the domain.

A third analytic force-free equilibrium is known for a finite cylinder of height h and radius a. Here the equilibrium fields are

$$\psi = \psi_0 \frac{\gamma_{11} R}{\chi_{01}} \frac{J_1(\gamma_{11} R)}{J_1(\chi_{01})} \sin\left(\frac{\pi}{h} Z\right) \tag{2.49}$$

$$B_R = -\psi_0 \frac{\pi}{h} \frac{\gamma_{11}}{\chi_{01}} \frac{J_1(\gamma_{11} R)}{J_1(\chi_{01})} \cos\left(\frac{\pi}{h} Z\right) \tag{2.50}$$

$$B_Z = \psi_0 \frac{\gamma_{11}^2}{\chi_{01}} \frac{J_0(\gamma_{11} R)}{J_1(\chi_{01})} \sin\left(\frac{\pi}{h} Z\right) \tag{2.51}$$

$$B_\phi = -\lambda \psi_0 \frac{\gamma_{11}}{\chi_{01}} \frac{J_1(\gamma_{11} R)}{J_1(\chi_{01})} \sin\left(\frac{\pi}{h} Z\right), \tag{2.52}$$

where ψ_0 is the value of the flux at the magnetic axis. The boundary condition $\vec{B} \cdot \hat{n} = 0$ at $r = a$ requires that $\gamma_{11} = \chi_{11}/a$, where $\chi_{11} \approx 3.8317$ is the first zero of the Bessel function J_1. The parallel current satisfies the relation $\lambda = \sqrt{\gamma_{11}^2 + (\pi^2/h^2)}$ [22]. As with the spherical case, λ is an eigenvalue that characterizes the geometry, and the toroidal magnetic field is zero at the boundary. The force-free spherical and finite cylindrical equilibria are commonly used idealizations of spheromak equilibria.

Complementary to the force-free equilibrium, we now consider the case where F is zero. This case is relevant to field reversed configurations where the toroidal magnetic field is small. Specifying the pressure to be the quadratic $P = P_0 + P_2 \left(\psi^2/\psi_0^2\right)$ yields the linear equation

$$\Delta^* \psi + 2\mu_0 R^2 P_2 \frac{\psi}{\psi_0^2} = 0. \tag{2.53}$$

Equation 2.53 can be solved for a cylinder of height h and radius a with the boundary condition $\vec{B} \cdot \hat{n} = 0$. The resulting equilibrium is

$$\psi = \psi_0 \frac{F_0\left(\eta, \frac{1}{2}\sqrt{d} R^2\right)}{F_0\left(\eta, \frac{1}{2}\sqrt{d} R_0^2\right)} \sin\left(\Lambda Z\right) \tag{2.54}$$

$$B_r = -\frac{\lambda}{R} \psi_0 \frac{F_0\left(\eta, \frac{1}{2}\sqrt{d} R^2\right)}{F_0\left(\eta, \frac{1}{2}\sqrt{d} R_0^2\right)} \cos\left(\Lambda Z\right) \tag{2.55}$$

$$B_z = \sqrt{d} \psi_0 \frac{F_0'\left(\eta, \frac{1}{2}\sqrt{d} R^2\right)}{F_0\left(\eta, \frac{1}{2}\sqrt{d} R_0^2\right)} \sin\left(\Lambda Z\right), \tag{2.56}$$

where F_0 is the 0-th order Coulomb wave function, $d = 2\mu_0 P_2/\psi_0^2$, $\Lambda = \pi/h$, $\eta = \Lambda^2/\left(4\sqrt{d}\right)$, and ψ_0 is the magnetic flux at the magnetic axis[23][24]. The term d is an eigenvalue characterizing the geometry of the system; it is analogous to λ in the idealized spheromak equilibria. The eigenvalue is calculated by finding the roots to the equation $F_0\left(\eta, \sqrt{d}a^2/2\right) = 0$. This ensures that the boundary condition $\hat{B} \cdot \hat{n} = 0$ is satisfied at the $r = a$.

2.3 Plasma Interchange

2.3.1 Ideal and Resistive Interchange

We begin the discussion of plasma interchange by considering the ideal MHD energy principle[25]. The energy principle states that a static equilibrium is ideal MHD unstable if a displacement ξ exists such that perturbed energy δW is negative. With a close-fitting wall, the perturbed energy is

$$\delta W_F = \frac{1}{2}\int d^3r \left[\frac{Q_\perp^2}{\mu_0} + \frac{B_0^2}{\mu_0}\left(\nabla \cdot \xi_\perp + 2\xi_\perp \cdot \kappa\right)^2 + \gamma p_0 \left(\nabla \cdot \xi\right)^2 \right. \\ \left. -2\left(\xi_\perp \cdot \nabla p_0\right)\left(\kappa \cdot \xi_\perp\right) - \frac{\lambda}{\mu_0}\xi_\perp \times B_0 \cdot Q_\perp\right], \quad (2.57)$$

where $Q = \nabla \times (\xi \times B_0)$ is the perturbed magnetic field, $\kappa = \hat{b} \cdot \nabla\hat{b}$ is the magnetic curvature, γ is the ratio of specific heats, λ is the parallel current, the subscript $\perp$ represents the direction perpendicular to the equilibrium magnetic field B_0, and p_0 is the equilibrium pressure. The first three terms in the integral are all non-negative and stabilizing. Physically the first term is associated with the shear Alfven wave and represents the energy required to bend magnetic field lines. The second term represents energy associated with compressing magnetic field lines and is related to the fast magnetoacoustic wave. The third term is the energy required to compress the plasma fluid and relates to sound waves.

The last two terms can be either positive or negative, and thus they can be destabilizing. The fourth term represents a connection between the pressure gradient and the magnetic curvature. This term is destabilizing if the pressure gradient and the curvature are in the same direction. Regions where the pressure gradient and curvature are in the same direction are said to have *bad curvature*. It is this term that drives interchange instabilities. The last term stems from parallel current density and is related to the twist of the magnetic field. The term represents the source of free energy that drives kink and peeling instabilities.

In plasmas relevant to magnetic fusion, the pressure decreases from the magnetic axis to the plasma edge. This results in a negative pressure gradient. The magnetic curvature vector is positive if the magnetic field is convex with respect to the magnetic axis. The curvature is negative if it is concave towards the magnetic axis. Thus the term $(\xi_\perp \cdot \nabla p_0)(\kappa \cdot \xi_\perp)$ will in general be destabilizing if the magnetic field is concave. In many confinement devices the poloidal magnetic field encircles the magnetic axis, it is concave towards the magnetic axis, and thus it has bad curvature. The toroidal field circles the geometric axis ($R = 0$). On the inboard side, the toroidal field is convex with respect to the magnetic axis and has good curvature. On the outboard side it is concave and has bad curvature. In tokamaks, the toroidal field is much stronger than the poloidal field. This leads to regions of net good curvature inboard of the magnetic axis, and regions of net bad curvature outboard of the magnetic axis. Spheromaks are comprised of poloidal and toroidal magnetic fields of similar amplitude, and they have net bad curvature almost everywhere.

Categorically there are two types of pressure driven instabilities: interchange and ballooning modes. Interchange modes are perturbations that are distributed along an entire flux surface. In contrast, ballooning modes are localized to regions of bad curvature. Interchange modes are sensitive to the average curvature since they are distributed along the flux surface. The stability of tokamaks with respect to interchange modes is greatly enhanced by their regions of good curvature. Spheromaks are more susceptible to interchange modes than tokamaks since their regions of favorable curvature are greatly reduced.

Average bad curvature does not necessary imply ideal instability since the first three terms in Equation 2.57 are stabilizing. Typically, the most unstable perturbations vary slowly parallel to the magnetic field in order to minimize field-line bending. The traditional interchange varies rapidly perpendicular to the magnetic field. This leads to the interchange ordering $k_\parallel / k_\perp \ll 1$ and $k_\perp a >> 1$, where $k_{\parallel(\perp)}$ is the parallel (perpendicular) wave vector and a is the minor radius.

Interchange modes are often studied using the local approximation where the instability is localized within a thin volume around a particular flux surface. Suydam considered the case for a linear screw pinch, and showed that instability will result if $D_s > \frac{1}{4}$ where,

$$D_s = -\frac{2\mu_0 p'}{rB_z^2}\frac{q^2}{q'^2}, \tag{2.58}$$

the primes denote derivatives in r, and all values are evaluated at the rational surface r_s[26]. The negative sign in D_s results from the fact that screw pinches have bad curvature. Here the curvature is entirely due to the poloidal field B_θ, which encircles the magnetic axis. The factor of q^2/q'^2 represents the stabilizing contribution from field-line bending. If the equilibrium magnetic field has shear, $q' \neq 0$, then it is impossible to construct a perturbation that is everywhere parallel to the magnetic field.

The Mercier criteria is analogous to the Suydam criteria in toroidal systems[27]. It states that a toroidal system will be ideal interchange unstable if $D_M > 0$, where D_M is

$$D_M = \frac{\mu_0 P' V'}{q'^2} W_M - \frac{1}{4} \tag{2.59}$$

$$\begin{aligned} W_m = {} & \frac{-V''}{4\pi^2}\left\langle \frac{B^2}{(\nabla\psi)^2}\right\rangle + \frac{Fq'}{2\pi}\left\langle \frac{1}{(\nabla\psi)^2}\right\rangle + \frac{\mu_0 P' V'}{4\pi^2}\left\langle \frac{1}{B^2}\right\rangle\left\langle \frac{B^2}{(\nabla\psi)^2}\right\rangle + \\ & \frac{\mu_0 P' V' F^2}{4\pi^2}\left(\left\langle \frac{1}{B^2(\nabla\psi)^2}\right\rangle\left\langle \frac{B^2}{(\nabla\psi)^2}\right\rangle - \left\langle \frac{1}{(\nabla\psi)^2}\right\rangle^2\right), \end{aligned} \tag{2.60}$$

where V is the volume inside a flux surface, $F = RB_\phi$ is the toroidal magnetic field, primes indicate derivatives with respect to the poloidal flux ψ, and brackets indicate flux surface averages. W_M is an effective magnetic well parameter, with positive W_m indicating good average curvature[28]. The stabilization from line bending is represented by the explicit term of a quarter. This is evident when multiplying D_M by the positive quantity q'^2. In the absences of shear, $q' = 0$, there is no stabilization from line bending, and $P'V'W_M > 0$ indicates instability.

In the large aspect ratio low-β limit with circular flux surfaces the Mercier criteria is

$$-\frac{2\mu_0 P'}{rB_0^2}\frac{q^2}{q'^2}\left(1 - q^2\right) > \frac{1}{4}. \tag{2.61}$$

Here the connection between the Mercier and Suydam criteria, Equation 2.58, is apparent. The Mercier criteria contain an additional factor proportional to $1 - q^2$. This factor is a toroidal correction that accounts for the fact the toroidal field has good curvature on the inboard side. In this limit, these toroidal effects completely stabilize Mercier modes for $q > 1$. Toroidicity also has a stabilizing effect for $q < 1$, but does not provide complete stabilization. The stabilizing effect decreases with decreasing

q^2. The large aspect ratio limit does not apply to spheromaks which have aspect ratios of order unity. However, this model provides a simple illustration as to why interchange stability is a concern for spheromaks which have $q < 1$.

Violating the Suydam and Mercier criteria indicates ideal interchange instability; however, near marginal stability these modes have exponentially small growth rates and are strongly localized to regions near the rational surface [29][30][31]. Here non-ideal effects can be significant.

Resistivity allows the magnetic field to diffuse through fluid elements, breaking the frozen flux condition. This weakens the stabilizing effect of magnetic shear. A screw pinch is resistive interchange unstable if $D_s > 0$. The resistive interchange growth rate scales with the resistivity as $\eta^{1/3}$[32]. Equilibria can still be unstable to pressure driven tearing modes even if $D_s \leq 0$; these modes grow at a rate proportional to $\eta^{3/5}$.

A toroidal system is resistive interchange unstable if $D_R > 0$, where

$$D_R = D_M + \left(\frac{1}{2} - H\right)^2 \tag{2.62}$$

$$H = \frac{\mu_0 P' V' F}{2\pi q'} \left(\left\langle \frac{1}{(\nabla\psi)^2} \right\rangle - \left\langle \frac{B^2}{(\nabla\psi)^2} \right\rangle \frac{1}{\langle B^2 \rangle} \right), \tag{2.63}$$

and D_M is the Mercier criteria defined in Equation 2.59[33]. The connection to the Suydam case is obvious if $H = 0$. In this instance the ideal and resistive stability criteria differ by $\frac{1}{4}$, as is the case for the cylindrical screw pinch. Resistive interchange modes in a toroidal equilibrium grow at the rate proportional to $\eta^{1/3}$ if $D_R > 0$. Similarly if $D_R \leq 0$ then the possibility still exists for pressure driven tearing modes; however, their growth rates are more complicated than the $\eta^{3/5}$ rate derived for the screw pinch [33].

2.3.2 The Gravitational Interchange Mode

We begin the discussion of extended MHD stabilization of the interchange mode by considering the gravitational interchange mode. This is a simplified model that is often analyzed using algebraic dispersion relations that result from asserting a local approximation. In Section 2.3.3 we discuss the extended MHD effects on pressure driven interchange modes.

The gravitational interchange mode (g-mode) is a simplified model frequently used to study interchange physics. The magnetic field topology plays a critical role in the analysis of the pressure driven interchange. On one hand the magnetic field has a destabilizing effect due to bad curvature. On the other hand the magnetic field can also be stabilizing due to magnetic shear. The g-mode simplifies the analysis by introducing a fictitious gravity to mimic magnetic curvature[34]. This gravity allows one to increase the drive for instability independent of the magnetic shear. It also allows for the study of interchange dynamics in simplified slab geometries.

The momentum equation with gravity is

$$\rho(\frac{\partial \vec{V}}{\partial t} + \vec{V} \cdot \nabla \vec{V}) = \vec{J} \times \vec{B} - \nabla P - \nabla \cdot \vec{\vec{\Pi}}_i + \rho \vec{g}. \tag{2.64}$$

The gravitational acceleration g roughly corresponds to magnetic curvature of order V_a^2/R_C, where R_C is the radius of curvature.

In discussing the g-mode we consider a slab geometry where the background magnetic field points in the z-direction and gravity points in the positive x-direction. Equilibrium quantities are only allowed to vary in the x direction, but the perturbed quantities are assumed to vary in both the x and y directions. The assumption that perturbed quantities don't vary in z enforces $\vec{k} \cdot \vec{B} = 0$ and eliminates the stabilizing effects due to field line bending. In MHD these perturbations are the most unstable modes. However, in extended MHD there are unstable drift waves that require finite but small $k_{\|}$.

A common approximation used in studying the g-mode is the local approximation. The local approximation assumes that characteristic length scales of the g-mode are small compared to the variation of the equilibrium fields. Where this approximation is valid, variations of the equilibrium quantities can be neglected and the gradients of the equilibrium quantities are characterized by constant length scales. For example, the density length scale is $L_n^{-1} = n_0'/n_0$, where the prime denotes the derivative in x.

In MHD the 0-β incompressible localized g-mode has the dispersion relation

$$\omega^2 + \Gamma_M^2 = 0, \tag{2.65}$$

where $\Gamma_M^2 = -g\rho'/\rho$. The condition for instability is $g\rho'/\rho < 0$. Thus instability arises when the equilibrium density decreases in the direction of gravity. This instability is analogous to hydrodynamic situation where a heavy fluid is supported by a lighter fluid, which gives rise to the Rayleigh-Taylor instability.

Two-fluid and FLR effects introduce drifts which can stabilize the g-mode. A frequently used model dispersion relation that accounts for these effects is

$$\omega^2 + \omega\omega_* + \Gamma_M^2 = 0, \tag{2.66}$$

where the drift frequency $\omega_* = \frac{k_y}{\Omega}\left[(2-\gamma)\frac{p_i\rho'}{\rho} - g\right]$ is a combination of ion diamagnetic and gravitational drifts. Analysis of this dispersion relation shows that complete stability occurs when $\omega_*^2 > 4\Gamma_M^2$. Rosenbluth, Krall, and Rostoker first arrived at this result using a kinetic treatment in the electrostatic limit for isothermal plasma[35]. Their calculation accounts for first-order corrections due to finite ion Larmor radii. Roberts and Taylor reproduced this result using a fluid model that includes gyroviscosity and two-fluid effects[13].

In this model both two-fluid and gyroviscous effects provide similar corrections to the dispersion relation. The ion diamagnetic drift arises due to the ion gyroviscosity and the gravitational drift arises due to the two-fluid Ohm's law. Both drifts increase linearly with k, and they have the strongest effect at high k.

Zhu et. al, generalized the analysis of the localized g-mode to arbitrary β using a single-temperature extended MHD model that includes both gyroviscosity and two-fluid effects[36]. A unique feature of Zhu's derivation is that it makes no explicit assumptions about the ordering of the ion Larmor radius r_i. The resulting dispersion relation reproduces the dynamics of the extended MHD model to all orders in Larmor radius. However, extended MHD is only valid in the small Larmor radius limit. The resulting dispersion relation is

$$\omega\left(\omega^2 + \omega_{*FLR}\omega + \Gamma_{FLR}^2 + \Gamma_{GYR}^2\right) + D_{FLR} = 0, \tag{2.67}$$

where

$$\omega_{*FLR} = \frac{k_y}{\Omega} \frac{\delta\tau\left[\left(1+\gamma\beta\right)\left(1+\beta\right)\frac{p'}{\rho} - \left(2+\gamma\beta\right)g\beta\right] - \lambda\left[g - \frac{\tau p}{\rho}\left(\ln\frac{p}{\rho^{\gamma}}\right)' + \delta^2\frac{k_y^2 r_i^2}{4}\frac{\tau p_i \rho'}{\rho^2}\right]}{\left(1+\gamma\beta\right)\left(1+\delta^2\frac{k_y^2 r_i^2}{4}\frac{\beta}{1+\gamma\beta}\right)} \tag{2.68}$$

$$\Gamma^2_{FLR} = \lambda\delta\frac{k_y^2}{\Omega^2}\frac{\tau p}{\rho}\frac{\left(1+\beta\right)\left(\frac{\tau p'}{\rho} - g\right)\frac{p'}{p} + \left[\left(1+\gamma\beta\tau\right)g - \left(1+\beta\right)\gamma\frac{\tau p'}{\rho}\right]\frac{\rho'}{\rho} + \left(\frac{\rho g}{p} - \frac{\tau p'}{p}\right)g\beta}{\left(1+\gamma\beta\right)\left(1+\delta^2\frac{k_y^2 r_i^2}{4}\frac{\beta}{1+\gamma\beta}\right)} \tag{2.69}$$

$$\Gamma^2_{GYR} = \frac{\Gamma^2_{MHD}}{1+\delta^2\frac{k_y^2 r_i^2}{4}\frac{\beta}{1+\gamma\beta}} \tag{2.70}$$

$$\Gamma^2_{MHD} = \frac{g^2}{V_a^2\left(1+\gamma\beta\right)} - \frac{\rho'}{\rho}g \tag{2.71}$$

$$D_{FLR} = -\frac{k_y\lambda}{\Omega}\frac{\frac{\rho'}{\rho}g\tau\frac{p}{\rho}\left(\ln\frac{p}{\rho^{\gamma}}\right)'}{\left(1+\gamma\beta\right)\left(1+\delta^2\frac{k_y^2 r_i^2}{4}\frac{\beta}{1+\gamma\beta}\right)}. \tag{2.72}$$

The markers δ and λ indicate contributions due to gyroviscous and two-fluid effects, respectively, the ion pressure is assumed to be a scalar multiple of the total pressure $p_i = \tau p$, $\beta = \mu_0 p/B^2$, $V_a^2 = B^2/\mu_0\rho$, $\Omega = eB/m_i$, and the ion gyro-radius is $r_i^2 = \tau p/\left(\rho\Omega^2\right)$.

The term in parenthesis in Equation 2.67 reduces to the classic g-mode dispersion relation, Equation 2.66, for isothermal plasma in the 0-β limit. The constant term, D_{FLR}, introduces an ion drift wave into the system.

There are two simplified models contained within Zhu's extended MHD dispersion relation. The gyroviscous model includes gyroviscosity but neglects terms that arise due to the two-fluid Ohm's law. This model is obtained by setting $\delta = 1$ and $\lambda = 0$. The two-fluid model neglects gyroviscosity but includes the other two-fluid terms. This model is obtained by setting $\delta = 0$ and $\lambda = 1$. (The fully consistent model has both $\delta = 1$ and $\lambda = 1$).

The gyroviscous dispersion relation [36] is

$$\omega\left(\omega^2 + \omega_{*FLR}\omega + \Gamma^2_{GYR}\right) = 0 \tag{2.73}$$

$$\omega_{*FLR} = \frac{k_y}{\Omega}\frac{\delta\tau\left[\left(1+\gamma\beta\right)\left(1+\beta\right)\frac{p'}{\rho} - \left(2+\gamma\beta\right)g\beta\right]}{\left(1+\gamma\beta\right)\left(1+\delta^2\frac{k_y^2 r_i^2}{4}\frac{\beta}{1+\gamma\beta}\right)} \tag{2.74}$$

$$\Gamma^2_{GYR} = \frac{\Gamma^2_{MHD}}{1+\delta^2\frac{k_y^2 r_i^2}{4}\frac{\beta}{1+\gamma\beta}} \tag{2.75}$$

$$\Gamma^2_{MHD} = \frac{g^2}{V_a^2\left(1+\gamma\beta\right)} - \frac{\rho'}{\rho}g. \tag{2.76}$$

In this model the dispersion relation reduces to a quadratic, and the solutions are found using the quadratic formula. Zhu showed that there is cutoff wave number,

$$\frac{k_c^2\tau^2}{\Omega^2} = \frac{4\Gamma^2_{MHD}}{\left[(1+\beta)\frac{p'}{\rho} - \frac{2+\gamma\beta}{2+\gamma\beta}g\beta\right]^2 - \frac{p}{\rho}\frac{\beta}{1+\gamma\beta}\Gamma^2_{MHD}}, \tag{2.77}$$

such that complete stabilization of the g-mode occurs for all wave numbers greater than the cutoff wave number $k_y > k_c$. However, there are instances where no cutoff wave number exists and complete stabilization does not occur. Zhu showed that complete stabilization always occurs in the $\beta \to 0$ limit and for isothermal equilibria with $T' = 0$[36]. In Chapter 4 we show that a real cutoff wave number always exists for equilibria when the equilibrium density and temperature gradients point in the same direction $n'T' \geq 0$.

The two-fluid model dispersion relation is

$$\omega\left(\omega^2 + \omega_{*FLR}\omega + \Gamma^2_{MHD}\right) + D_{FLR} = 0 \tag{2.78}$$

$$\omega_{*FLR} = -\lambda\frac{k_y}{\Omega}\frac{g - \frac{\tau p}{\rho}\left(\ln\frac{p}{\rho^\gamma}\right)'}{(1+\gamma\beta)} \tag{2.79}$$

$$\Gamma^2_{MHD} = \frac{g^2}{V_a^2(1+\gamma\beta)} - \frac{\rho'}{\rho}g \tag{2.80}$$

$$D_{FLR} = -\frac{k_y\lambda}{\Omega}\frac{\frac{\rho'}{\rho}g\tau\frac{p}{\rho}\left(\ln\frac{p}{\rho^\gamma}\right)'}{(1+\gamma\beta)}. \tag{2.81}$$

In this model the dispersion relation maintains its cubic nature, and the term D_{FLR} introduces an ion drift wave. In Chapter 4 we show that the stability of the model depends on the sign of $\left(\ln\frac{p}{\rho^\gamma}\right)'$. There exists a second instability at finite k when this term is positive. This second instability results from the interaction of the g-mode and the ion drift wave. It grows at a rate comparable to the MHD g-mode, and it persists to infinite k.

Multiple instabilities exist in the full extended MHD model that includes two-fluid effects and gyroviscosity. Similar to the two-fluid model, there is an instability that is driven unstable by the interaction between the ion drift wave and the g-mode. However, unlike the second instability in the two-fluid model, this mode is stabilized at finite k. Other instabilities exist at higher k. These instabilities grow faster than the MHD g-mode, but only exist in regimes where the small Larmor radius approximation breaks down and the extended MHD model is not valid. We refer the reader to Chapter 4 for a more detailed analysis of this model.

The analysis of the g-mode dispersion relation under the different models is a cautionary tale. In the Roberts-Taylor model dispersion relation, Equation 2.66, two-fluid effects and gyroviscosity have a similar effect on the g-mode. They both introduce drifts which are stabilizing, and these effects are represented by the ω_* term. This simple picture suggests that reduced models reproduce the qualitative dynamics of the full extended MHD model. However, in actuality the three models contain qualitatively different dynamics. This highlights the importance of using a consistent model.

The analysis of this extended MHD g-mode also reveals the importance of the equilibrium density and temperature profiles. The qualitative stability properties of all three models are dependent on both the density and temperature profiles. This is different than MHD, where the stability properties depend on the total pressure gradient.

Ferraro and Jardin use the g-mode as a numerical benchmark of their extended MHD algorithm that includes both gyroviscosity and a two-fluid Ohm's law[37]. They extended the Roberts-Taylor dispersion relation to arbitrary β and allow for finite perturbations parallel to gravity. One notable aspect of their work is that they explored various approximations of the gyroviscous stress. A common approximation is the gyroviscous cancellation where the gyroviscous stress is approximated as $\nabla \cdot \vec{\vec{\Pi}}_i \approx -\rho \vec{v}_* \cdot \nabla \vec{v}$. The left side of the momentum equation is then approximated as

$$\rho \left(\frac{\partial \vec{v}}{\partial t} + \vec{v} \cdot \nabla \vec{v} \right) + \nabla \cdot \vec{\vec{\Pi}}_i \approx \rho \left[\frac{\partial \vec{v}}{\partial t} + (\vec{v} - \vec{v}_*) \cdot \nabla \vec{v} \right]. \tag{2.82}$$

The term $\vec{v}_*$ is frequently assumed to be the ion diamagnetic drift velocity $\vec{v}_* = \frac{-1}{ne} \frac{\nabla p_i \times \vec{B}}{B^2}$; however, a better approximation is to use the magnetization velocity $\vec{v}_* = \frac{-1}{ne} \nabla \times \left(\frac{p_i \vec{B}}{B^2} \right)$[38]. Ferraro and Jardin calculate the g-mode growth rate using both the full gyroviscous stress tensor and using the gyroviscous cancellation. They show that gyroviscous cancellation is a fair approximation for the g-mode. However, they also show that the gyroviscous cancellation breaks down in cases where compression is important.

Huba performed linear and nonlinear simulations of the g-mode in isothermal plasma using a model that includes gyroviscosity with an MHD Ohm's law[39]. The nonlinear simulations are performed with and without gyroviscosity. Without gyroviscosity the instability develops into a mushroom structure characteristic of Rayleigh-Taylor instabilities. Late in time these structures develop small scale turbulent structures. The introduction of gyroviscosity has three effects. First, it reduces the growth rate of the modes. Second, it causes the modes to drift perpendicular to the gravity. Finally, gyroviscosity has a strong smoothing effect, suppressing many of the small scale fluctuations.

2.3.3 Extended MHD Interchange

Gupta, Callen, and Hegna consider interchange stability in a slab using a sheared magnetic field

$$\vec{B}_0 = B_0 \left[\left(1 + \frac{x}{L_B} \right) \hat{e}_z + \frac{z}{R_c} \hat{e}_x + \frac{x}{L_s} \hat{e}_y \right], \tag{2.83}$$

where L_B characterizes the perpendicular gradient of the magnetic field, L_s is the magnetic shear length scale, and $\kappa = -1/R_c$ is the magnetic field curvature[31]. The pressure is calculated consistently from perpendicular force balance $\beta/r_p = 1/R_c - 1/L_B$, where r_p is the pressure gradient length scale. The authors study the stability of the equilibrium in an extended MHD model that includes gyroviscosity and two-fluid effects in the low-β incompressible limit.

In ideal MHD these equilibria are stable to local interchange if $D_I < \frac{1}{4}$, where $D_I = \frac{\beta L_s^2}{R_c r_p}$ is equivalent to the Suydam stability criteria. Near marginal stability, $D_I \gtrsim \frac{1}{4}$, the MHD growth rate scales approximately $\gamma\tau_a \approx e^{-\pi/\lambda}$, where $\lambda^2 = D_I - \frac{1}{4}$. Modes near the marginal stability point have exponentially small growth rates. Including gyroviscosity in the model introduces drifts that are stabilizing. These drifts have the greatest effect on modes near the marginal stability point where the growth rates are small. The authors show that gyroviscosity completely stabilizes the interchange mode for $D_I \lesssim 0.45$. However, gyroviscosity has a negligible effect on the growth rate for $D_I > 0.5$.

The authors also study the effect on resistive interchange modes. In the absence of the extended MHD effects the resistive interchange mode has the characteristic scaling $\gamma \sim S^{-1/3}$ for $D_I < \frac{1}{4}$. The scaling is reduced to $\gamma \sim S^{-1}$ in both the weakly resistive and highly resistive limits when extended MHD effects are included.

Stringer studied effect the of FLR corrections on ideal interchange modes in screw pinch equilibria in the low-β electrostatic limit[30]. The conclusions are in close agreement with Gupta et al. The growth rate is exponentially small near the marginal stability point in ideal MHD. Including FLR has a strong stabilizing effect for these small growth rates, but has a minimal effect on the growth rate far from marginal stability. FLR effects almost double the marginal stability point, with $D_s \lesssim 0.5$ being stable.

Finn, Manheimer, and Antonsen studied resistive interchange modes in a cylinder using a model that includes the two-fluid Ohm's law but neglects gyroviscosity[40]. They found that two-fluid effects can completely stabilize the resistive interchange mode at moderate ω_{*e}. The stabilization is due to both finite plasma compressibility and coupling to outgoing damped drift waves.

Hastie, Ramos, and Porcelli studied ballooning modes using a model the includes both electron diamagnetic effects and finite ion-Larmor radius effects[41]. A key aspect of their model is that it allows for a finite sound wave frequency. This allows for coupling between ion drift waves and electron drift-acoustic waves. They find an island of instability, at intermediate toroidal mode numbers, where the coupling is strongest. Outside of this island extended MHD is stabling, and the growth rate is greatly reduced. Inside the island the growth rate of ideal ballooning modes is modified by a factor of approximately $\frac{2q}{\sqrt{3}}$. The growth rates of these ideal modes is increased over their MHD growth rates for $q \gtrsim 0.87$. The coupling between the ion drift waves and electron drift-acoustic waves also leads to strongly unstable resistive ballooning modes that have growth rates comparable to those ideal ballooning modes.

Benilov and Power studied ideal interchange in a toroidal magnetic field using a model that includes the two-fluid Ohm's law and electron diamagnetic heat flux[42]. They assume cold ions which is consistent with neglecting the ion gyroviscosity. A local approximation with $k_{\|} = 0$ is used to arrive at a cubic dispersion relation. This dispersion relation permits islands of instability at intermediate k. In some regimes finite β leads to an ultra-violet catastrophe where the growth rate goes to infinity as k goes to infinity.

2.4 Review of Spheromak Physics

This section provides an overview of physics issues relevant to coaxial helicity injected spheromaks (CHI). Sections 2.4.1-2.4.3 review 3 CHI spheromak experiments: CTX, SPHEX and SSPX. Section 2.4.4 presents a review of early spheromak simulations, and Section 2.4.5 reviews previous work studying pressure driven instabilities in spheromaks.

CHI was explored as a possible path to a steady-state fusion reactor by first forming a spheromak and then sustaining it against resistive decay. However, simulations and experimental observations show that strongly driving the current guns, necessary for formation and current drive, produces 3-D fluctuations that prevent flux surface formation and degrade confinement. Reducing the gun drive below a critical threshold stabilizes the 3-D fluctuations, allowing flux surfaces to form, and improving confinement. This result, discussed in more detail in 2.4.3, implies that CHI alone cannot sustain a steady-state reactor.

All CHI spheromaks operate in the same basic way. First a biased magnetic flux is applied linking two coaxial electrodes that form the gun. Then gas is puffed into the gun region, and a voltage is applied across the electrodes. The gas breakdowns into a plasma, and current flows across the electrodes. If sufficient current is driven, then $\vec{J} \times \vec{B}$ forces cause the current sheet to balloon out into a flux conserver. The current sheet eventually goes unstable and relaxes into a spheromak. Maintaining the current drives instabilities that amplify helicity and flux. As stated above, these instabilities prevent flux surface formation while the drive is maintained.

Turning the gun current off removes the source of free energy that drives the instabilities. The instabilities decay faster than the amplified flux, and flux surfaces form. Transport is reduced, confinement is improved, and the spheromak heats up ohmically. Peak electron temperatures are observed during this decay phase. However, performance is limited by resistive decay. As the spheromak decays, the centrally peaked temperature profile causes nonuniform decay of the plasma currents. Currents near the colder edge decay faster than currents in the core due to an increased resistance. This uneven decay leads to a centrally peaked current profile, and the safety factor, q, decreases over time. Eventually q drops below $\frac{1}{2}$, and a resonant $\frac{m}{n} = \frac{1}{2}$ or $\frac{2}{4}$ current driven mode appears that usually terminates the plasma.

SSPX explored an alternative controlled decay where the gun currents are reduced, but not turned off completely. Reducing the gun currents below a threshold stabilizes the instabilities. Fluctuation levels in the plasma are significantly reduced, good flux surfaces form, and the spheromak heats up. The plasma decays as before, but the guns maintain the current on the open field that surrounds the spheromak. This current helps maintain the current on the edge of the spheromak. This limits the peaking of the current profile, keeps q above $\frac{1}{2}$ longer, and delays the onset of the disruptive instabilities. Control of gun currents allowed SSPX to achieve the highest electron temperatures observed in a spheromak to-date. The performance of SSPX was limited by the amount of Volt-seconds available to drive the current.

2.4.1 CTX

The CTX experiment was a CHI spheromak operated at Los Alamos National Laboratory in the 1980's and early 1990's. Throughout the lifetime of the CTX program, spheromaks were formed in a variety of flux conservers of different shapes and sizes. The radii of the flux conservers ranged from 0.28 m to 0.67 m, and the heights ranged from 0.40 m to 0.70 m. Early on, it was found that switching from prolate to oblate flux conservers stabilized tilting modes [43]. Early experiments, that used a copper wire mesh flux conserver, underwent cyclical current relaxation events similar to sawteeth. Initially, the measured edge magnetic fields were consistent with constant-λ spheromak equilibria. These fields slowly depart from the constant-λ state as the spheromak decayed. Eventually the spheromak went unstable, the fields rapidly relaxed towards the constant-λ state, and the process started anew. Usually only one or two cycles could be observed before the capacitors ran out of energy to drive current[43].

The CTX team also studied the evolution of the global magnetic helicity $K = \int \vec{A} \cdot \vec{B} dV$. They found that the evolution of the helicity could be accurately modeled using the equation

$$\frac{\partial K}{\partial t} = -\frac{K}{\tau_k} + 2V_g\phi_g, \tag{2.84}$$

where τ_k is the characteristic decay time of the helicity, V_g is the voltage across the injector guns, and ϕ_g is the flux linking the guns. The term $2V_g\phi_g$ is the rate of helicity injection, and $\frac{K}{\tau_k}$ is the resistive decay rate of helicity. In this model τ_k is the only free parameter. Initially, when the helicity is small, $K \ll V_g\phi_p\tau_k$, the resistive decay term is negligible, and the global helicity evolution is determined by the voltage and the flux across the gun. Here the model agrees with experiments within an error of 12% [44].

Significant improvements in performance were achieved by switching to a solid flux conserver [45]. Previous spheromaks had large error fields resulting from the use of a mesh flux conserver. These large error fields caused a significant amount of poloidal field to intersect the wall. Temperatures and confinement times were limited by increased resistivity in the edge due to ion-neutral collisions. Switching to a solid conducting flux conserver greatly reduced these error fields. The switch increased confinement times from 0.02 ms to 0.2 ms, and the electron temperatures increased from 100 eV to

180 eV[46].

The temperatures in these improved confinement spheromaks were limited by a pressure driven instability, not present in lower-confinement spheromaks [2]. These instabilities resulted in a sudden decrease in core density and electron pressure, but an increase in edge density and electron pressure. Little change is observed in the magnetic signals indicating that the mode is pressure driven, not current driven. In the worst cases, the interchange mode leads to the termination of the spheromak. In less severe cases, the spheromak recovers and the pressure builds up until a second or third instability occurs. In some cases no large events are measured but many small ones occur that lead to complete loss of density [2] [45]. Evaluation of the ideal Mercier criteria show that at the time of instability, the electron pressure exceeds the maximum stable pressure by a factor of 20! The ion temperature/pressure is not included in these calculations, and the actual pressure might exceed the Mercier limited pressure by a factor of 40 [2]. The authors speculate that the huge discrepancy between the measured electron pressures and the predicted Mercier stable pressures may be due to limitations in the models used to reconstruct CTX equilibria.

Ion temperatures in CTX were inferred from impurity ion Doppler measurements. These measurements had limited temporal and spatial resolution and do not directly measure the majority ion species. Late in the experimental program, a 1-D charged particle transport model, combined with the impurity ion temperature measurements, was used to obtain a better estimate of the majority ion temperature [47]. The electron and ion temperatures are comparable with $T_e \approx T_i$ during quiescent phases. However, the ions are hotter than the electrons, $T_i \gg T_e$, during turbulent phases with lots of magnetic activity[47].

2.4.2 SPHEX

SPHEX was a coaxial gun injected spheromak operated at The University on Manchester Institute of Science and Technology (UMIST) [48]. Hydrogen plasmas were created in a $0.25\,\mathrm{m}^3$ copper flux conserver. The flux conserver was specifically designed with no sharp corners to minimize flux losses. SPHEX normally operated 1 ms pulses with 60 kA of gun current and 3.2 mWb of flux across the guns. Typical electron temperatures were around 30 eV and densities were around $4 \times 10^{19}\,\mathrm{m}^{-3}$[49]. A time history of a SPHEX discharge is shown in Figure 1. Periodic fluctuations corresponding to an $n = 1$ kink are visible in the B field diagnostic when the gun current is large. These fluctuations disappear when the gun currents are shorted-out. The goal of the SPHEX experiment was to study how current generated by the guns coupled to and sustain the spheromak.

Early measurements of the potential profile showed that the SPHEX spheromak could be broken into two distinct regions: a high potential circular column extending the length of the flux conserver centered around the geometric axis and a low potential annulus. Additionally a 20 kHz $n = 1$ mode is observed throughout the plasma. Calculations of the Poynting flux show that the $n = 1$ mode transfers 2.5 MW of power from the column to the annulus [50]. This picture is consistent with the idea that current driven by the guns (the plasma column) is sustaining the spheromak against decay (the annulus). Direct measurements of the parallel current during the driven phase produced a hollow parallel current profile in the annulus and a peaked profile during the decay phase [51]. The current profile inside the central column has a complicated spatial structure, but in general λ in the column is greater than λ in the annulus. Measurements of the MHD dynamo electric field suggest that the dynamo plays a role in transferring current from the column to the annulus [52].

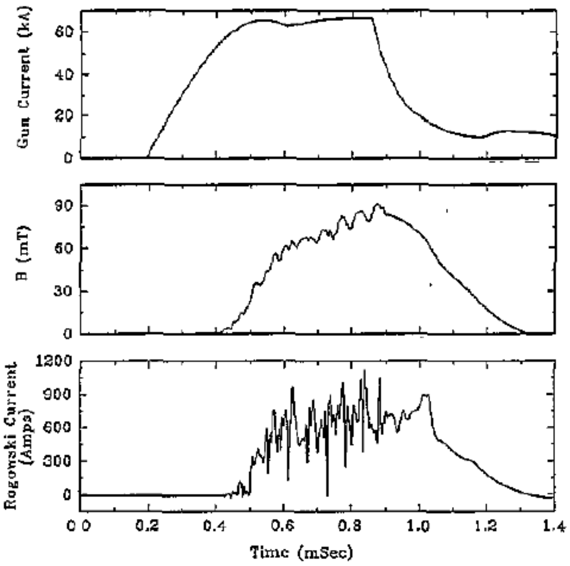

Figure 1: Time history of SPHEX discharge. The guns were shorted around 1 ms. The large fluctuations in B, corresponding to an n=1 kink of the central column, go away when the guns are turned off. [51]

Fluctuations of the potential along the flux conserver are used to reconstruct the $n = 1$ mode, showing that it is a kink distortion of the central column[53]. The $n = 1$ mode would become intermittent with an active phase followed by a quiescent phase during higher performance discharges. This dynamic was modeled using one-dimensional force-free equilibria with a step-wise constant current profile. This model is stable when currents are representative of the parallel currents in the column and the annulus during quiescent phases. However, these model equilibria are kink unstable when the currents are representative of experimental conditions immediately prior to mode activity[54]. Experimental reconstructions of the current profiles show that the current in the annulus is slowly decaying during the quiescent phase, while the current in the column is steadily increasing. When active, the kink mode quickly flattens out the current profile, decreasing the current in the column and increasing it in the annulus[49]. This suggests that the $n = 1$ mode is responsible for driving current in the annulus via a relaxation process. Fluctuation levels of $\sim 100\%$ the background current density are observed on the magnetic axis during the driven phase of the spheromak[55].

2.4.3 SSPX

The Sustained Spheromak experiment (SSPX), operated at Lawrence Livermore National Laboratory (LLNL), is the highest performance spheromak to-date[4]. SSPX used CHI to both form the spheromak and control the resistive decay. SSPX used a cylindrical copper flux conserver with a height of 0.5 m and a diameter of 1 m. The SSPX flux conserver is shown in Figure 2. SSPX spheromaks typically have a major radius of $R \approx 0.31\,\mathrm{m}$, a minor radius of $a \approx 0.23\,\mathrm{m}$, and a lifetime of 2 ms. Typical plasma parameters for early SSPX discharges are $n_e \approx 1 \times 10^{20}\,\mathrm{m}^{-3}$, $I_p \approx 350\,\mathrm{kA}$, $T_e \approx 120\,\mathrm{eV}$, and $B_{wall} \approx 0.25\,\mathrm{T}$ [56]. An upgrade in the power supply and optimized operation allowed SSPX to achieve peak $T_e > 500\,\mathrm{eV}$ and peak toroidal magnetic fields $B_T > 1\,\mathrm{T}$ [7]. The goals of the SSPX program were to better understand the formation of the spheromak to optimize the current drive, and to study the sustainment of the spheromak against resistive decay. Unlike previous CHI injected spheromaks, SSPX has a set of external shaping coils. SSPX also had a second capacitor bank, used to drive current on the open field during the decay. Numerical simulations, using the NIMROD code, have been integral in understanding the physics of SSPX discharges. In the remaining part of this section, when applicable, numerical simulation results will be presented alongside SSPX experimental results.

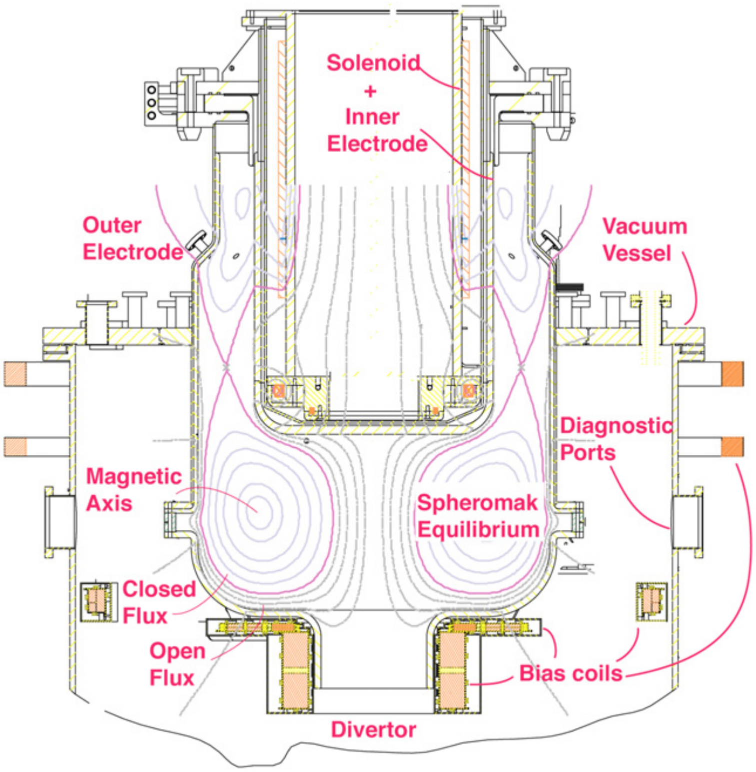

Figure 2: Schematic of SSPX experiment [8].

Figure 3 shows the time histories of two SSPX discharges. The black discharge used a single current pulse to form the spheromak. Following its formation, the spheromak freely decays until an MHD instability arises around 1.2 ms into the discharge. This instability, which is driven by a peaked current profile, terminates the discharge. The second discharge, shown in red, uses a second pulse to increase the life of the spheromak. The second pulse drives current on the edge of the spheromak which delay the onset of instability[5][8]. Control of this pulse is essential to achieving high temperatures. The maximum electron temperatures are measured in quiescent times of low magnetic activity. If the applied current is too large, then it will drive $n = 1$ activity that is consistent with the column kink observed in SPHEX. However, $n = 2$, 3, and 4 mode activity is observed if the applied current is too small[56].

Resistive MHD NIMROD simulations of SSPX discharges show similar behavior, with maximum T_e occurring during quiescent periods with small fluctuations[5]. Magnetic field line traces show an absence

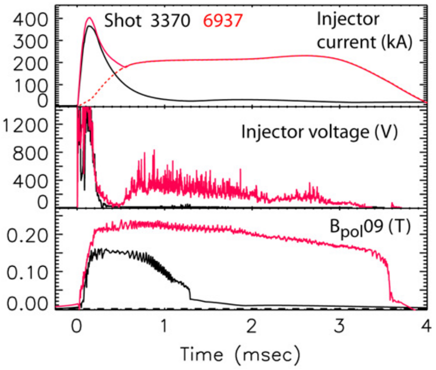

Figure 3: A comparison of SSPX discharges with just the formation pulse (black) and both the formation and second pulse (red). The second pulse drives current along the edge of the spheromak, and delays the onset of a disruptive instability[8].

of closed flux surfaces at the end of the initial formation pulse. Here the simulated temperature is relatively flat. Later in time, field line traces show closed flux surfaces and centrally peaked temperatures. Simulations of early SSPX discharges are limited to a peak temperature of approximately 40 eV when the second pulse is not applied. However, when the second pulse is applied these simulations reach 80 eV. Without the second pulse, q drops below $\frac{1}{2}$ and a $m = 1, n = 2$ mode is resonant in the core. In the simulations with the second pulse, the gun-driven current maintains q above $\frac{1}{2}$ longer, and the $m = 1, n = 2$ mode is delayed until late in the simulation. The peak observed temperature is a point of disagreement between simulation and experiment. The NIMROD simulations calculate a peak electron temperature of approximately 80 eV while the peak electron temperature in the corresponding SSPX discharge is approximately 120 eV.

Experimentally, the peak temperatures are correlated with the gun current, λ_{gun}, applied during the second pulse. The hottest temperatures are observed when $\lambda_{gun}/\lambda_{fc} \approx 0.93$, where $\lambda_{fc} \approx 9.9\,\mathrm{m}^{-1}$ is the eigenvalue of the SSPX flux conserver[8]. This is consistent with the picture that driving small amounts of current on the open field maintains the current on the edge of the spheromak. The guns drive helicity into the core when the gun current exceeds the flux conserver eigenvalue. Therefore driving the guns with $\lambda_{gun}/\lambda_{fc} \gtrsim 1$ will drive fluctuations that degrade confinement. If the gun current is too weak, $\lambda_{gun}/\lambda_{fc} \ll 1$, then currents in the edge decay rapidly. This results in a strongly peaked current profile which drives instabilities. Driving the guns such that $\lambda_{gun}/\lambda_{fc}$ is slightly less than unity maintains the edge currents without driving fluctuations that degrade confinement.

Prior to a capacitor bank upgrade, optimization of the second pulse enabled SSPX to reach electron temperatures around $350\,\mathrm{eV}$. These optimized discharges had parabolic temperature profiles. Electron thermal diffusivities in the core as low as $\chi_e < 10\,\mathrm{m}^2/\mathrm{s}$ are inferred from reconstructed equilibria, where the diffusivity decreases with increasing T_e. Empirically, the peak electron temperature is bounded by $\beta_e \sim 5\%$[8].

SSPX had no external heating sources, and the dominant heating mechanism is Ohmic. It is not clear if the observed β_e limit is a consequence of the heating method, or if there a pressure limit due to some pressure-driven instability. The limiting factor in these optimized discharges was the amount of energy stored in the capacitor banks to form the spheromak and maintain the edge current.

Several direct observations of pressure driven instabilities in SSPX are reported. Early SSPX discharges experienced a drop in the core electron number density without a corresponding drop in current, similar to the instabilities observed in CTX[57]. A more pronounced instability is observed in a modified operating configuration with large vertical background magnetic fields. In this configuration, the q-profile drops below 0.5, and a resonant $n = 2, m = 4$ mode appears. This mode leads to a sudden drop in the core density and an increase in the core temperature. Equilibrium reconstructions are used to determine the Mercier stability parameter. Prior to the crash the stability criterion is exceeded. Following the crash the spheromak recovers and the peak electron pressure evolves with Mercier stable pressure [58].

An upgrade to the SSPX power supply increased the amount of energy available to drive currents across the guns. The upgrade also improved the modularity of the capacitors, and provided more flexibility in the pulsing of the gun currents[59]. This increased flexibility was used to study the effects of different formation schemes on the maximum poloidal field B_p [7]. The standard operation of a large formation pulse followed by a second pulse is compared with a slowly building formation pulse, a double pulse, and an extended formation pulse. The slowly building pulse and the extended formation pulse are most efficient in generating magnetic field, producing the strongest magnetic field for a given gun current. An empirical limit for the maximum magnetic field for these discharges is found to be $B_p/I_{gun} = 0.85\,\mathrm{T/MA}$. The highest magnetic fields in SSPX are produced using the extended formation pulse. Prior to final operation, the height of the SSPX flux conserver was increased by 10 cm, while keeping the radius constant. After the modification the maximum magnetic field for the extended formation discharges were governed by the limit $B_p/I_{gun} = 0.9\,\mathrm{T/MA}$[60].

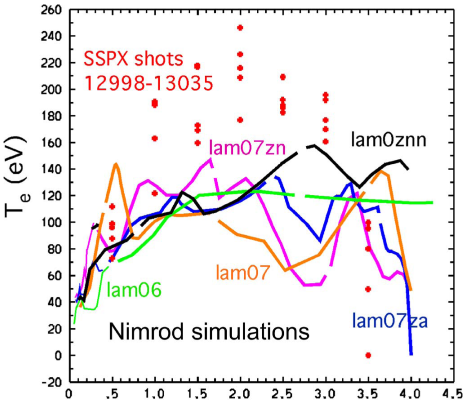

Figure 4: Time histories of electron temperature in high performance SSPX discharges (●) and NIMROD simulations (lines) [6].

A comprehensive series of NIMROD simulations were performed to understand the sensitivity of simulation results to physical and numerical parameters[6]. The work was motivated, in part, by an observable difference between peak electron temperatures measured in high-performance SSPX discharges and the corresponding temperatures observed in previous NIMROD simulations. The simulations, which use anisotropic collisional thermal conduction, tend to under-predict the peak electron temperatures by as much as 40%. A series of simulations were performed varying density, viscosity, and effective ion charge (the ion charge is used to calculate transport coefficients self-consistently). The resulting temperatures are compared with several high-performance discharges in Figure 4. Varying these parameters has a noticeable effect on the evolution of the electron temperature. However, the observed variations are not enough to explain the discrepancy between simulation and experiment. The simulations are susceptible to large scale fluctuations which degrade confinement. An axisymmetric NIMROD simulation was performed to quantify the effect of these fluctuations. The axisymmetric simulation zeros out the fluctuations, effectively stabilizing all MHD activity. This simulation reached temperatures comparable to the experiment. This suggests a possible explanation for the observed discrepancy. Resistive MHD simulations are under-predicting the stability, and the resulting instabilities are limiting the temperatures in the simulation.

An alternative explanation for the temperature discrepancy is proposed by Ji et al. [61]. They consider the effect of kinetic modifications that limit the parallel heat flux at low collisionality. They use an integral closure that is calculated by taking moments of the drift kinetic equation, and it is valid for general collisionality. The authors evolve a high resolution NIMROD simulation of an early SSPX discharge using resistive MHD with a collisional closure. Late in the simulation the authors apply the kinetic closure. The temperature is evolved to equilibration, keeping all the other fields fixed in time. With the kinetic closure the temperature is 6% hotter than the collisional closure. This temperature still falls short of the experimental measurement. The experiments modeled by these simulations were limited to 120 eV, and the difference between the two closures is expected to be more pronounced at hotter temperatures.

2.4.4 Computational Studies

Some of the earliest simulations of spheromaks modeled various formation schemes in 2-D. Lui et al.[62], Jardin and Park[63], and Sato et al.[64] modeled the formation of spheromaks in the Princeton S-1 experiment, which used induction to form the spheromak. Here a flux core creates both poloidal and toroidal magnetic fields. After breakdown occurs, the toroidal current in the flux core is decreased and reversed, inducing a toroidal current in the plasma. The toroidal currents in the plasma are anti-parallel to the toroidal currents in the flux core. These currents repel, causing the plasma to detach and move away from the flux core. The plasma then relaxes into a spheromak. Lui et al. studied the use of an additional set of coils, both inside and outside of the flux conserver, to help pinch the plasma off from the flux core. They also show that if the toroidal current in the flux core is too large, then a doublet plasma with two magnetic axes forms. Jardin and Park's simulations relied entirely on the decrease of toroidal current in the flux core to detach the plasma. They show that not only does this method simplify the design by removing an extra set of coils, it also allows for greater efficiency in transferring toroidal flux from the coil to the plasma. Sato et al. looked at how different ramp rates in the toroidal current affected the final spheromak. They find that a faster ramp rate, which decreases the formation time, leads to the creation of a smaller spheromak. Similar studies for the formation of spheromaks using the theta pinch method were performed by Sgro and Winske[65] and Guzdar et al.[66]. Sato et al.[67] simulated the formation of a spheromak through the merging of two smaller spheromaks. They observe that during the merging process, magnetic energy dissipates faster than the magnetic helicity, and the final toroidal flux is the sum of the toroidal fluxes of the initial spheromaks.

Sato and Hayashi performed the first series of 3-D nonlinear simulations of spheromaks[68][69][70]. In these papers the authors studied the 0-β stability properties of the S-1 spheromak. These spheromaks are unstable to an $n = 1$ $m = 1$ tilt mode, which leads to disruption. A close-fitting conducting wall can be used to stabilize the mode through line tying. The authors also study the nonlinear evolution of $n = 2$ and $n = 3$ kink modes. The $n = 2$ mode is an external kink, and its nonlinear evolution eventually destroys the spheromak. The $n = 3$ mode is initially an external kink, but during its evolution it transitions to an internal kink. It saturates without disrupting. Again a close-fitting conducting wall stabilized these kink modes.

Oda performed the first nonlinear simulations of pressure driven modes in spheromaks[71]. Oda used the same code as Sato and Hayashi, but considered finite pressure. The spheromak is modeled in a cylindrical conducting shell with a conducting rod along the geometric axis. The equilibrium is generated from a Grad-Shafranov solution, and an initial $n = 1$ $m = 1$ perturbation is applied. This perturbation grows slowly in time and eventually a linear $n = 1$ $m = 3$ mode becomes dominate. A number of other linear modes are observed to be unstable ($n = 2$ $m = 2$, $n = 2$ $m = 3$, etc). The $n = 1$ $m = 3$ destroys magnetic surfaces as it saturates. Calculations of the linear growth rates vs β show that there is a critical pressure $\beta \sim 5\%$ below which the modes are stable.

Katayama and Katsurai simulated both current and pressure driven instabilities in spheromaks using several different equilibria[72]. They placed an emphasis on studying the relaxation dynamics. The initial equilibria are force-free Grad-Shafranov solutions. Two generic types of equilibria are presented: ones with $q_{axis} > 1$ and ones with $q_{axis} = 0.12$. Both equilibria are kink unstable, and while the nature of the kink modes is different, both equilibria relax towards a Taylor state as the modes grow and saturate.

Sgro, et al.[73] and Horiuchi et al.[74] performed two different simulations of the evolution of a decaying spheromak with temperature profiles peaked on the magnetic axis. Sgro et al. model the decay of an initial Taylor state spheromak using a 1.5D transport code. A hollow resistivity profile is used to model a centrally peaked temperature. They assume that the spheromak decays though a series of quasi-static equilibria. The increased resistivity near the edge causes the currents to decay more rapidly than current in the core, leading to a peaked current profile and decreasing q. Eventually q drops below 0.5, and the spheromak becomes kink unstable. An ideal-MHD code is used to periodically check the stability of the equilibrium. Once an instability is found, a resistive MHD 3-D simulation is performed. The first mode to appear is a $n = 2$, $m = 1$ kink. The kink displaces the magnetic axis as it evolves, and eventually destroys flux surfaces. As the mode saturates, the flux surfaces heal on a slow time scale due to magnetic diffusion, and a new magnetic axis is formed. The resulting equilibria has a flat current profile. As the spheromak continues to decay, the current profile peaks in the center, and the process begins anew. The work of Horiuchi et al. performed a similar set of simulations, but they start with a slightly peaked current profile and use resistive 3D MHD with spatially dependent resistivity for the entire simulation. They use several different resistivity profiles, noting that the evolution of the kinks are similar for all resistivity profiles, but the time-scales over which the evolution occurs changes. This difference in time-scales is due to the rate at which the magnetic flux surfaces heal, which depends on the resistivity. Profiles with lower resistivity on axis take longer for good magnetic surfaces to form.

Sovinec, Finn, and del-Castillo-Negrete performed the first simulations of electrostatic formation and sustainment of spheromaks[9]. They used the 0-β 3-D resistive MHD model within NIMROD. These simulations reproduce many of the key features of the experiments, including flux amplification, the role of the $n = 1$ central column kink during formation and sustainment, and relaxation of the mean field into a spheromak-like state. These simulations are the first to show that fluctuations, associated with the formation, prevent flux-surface formation. They also show that flux surfaces form as the spheromak decays after the guns are turned off.

2.4.5 Pressure Driven Instability in Spheromaks

This section reviews existing studies that examined pressure driven instability in spheromaks. Most of these studies attempt to determine the maximum stable β for a prescribed class of equilibria. Often equilibria are constructed specifying the pressure gradient to be marginally Mercier stable. The pressure that results is then used to calculate the β limit. Other studies use numerical calculations to determine the onset of low-n interchange modes or infinite-n ballooning modes. Some of these studies also calculate the linear growth rates. Most of the existing work focuses on linear ideal stability. A limited number of studies consider resistivity, kinetic effects, or the nonlinear evolution of interchange modes.

Rosenbluth and Bussac consider pressure limits in a constant-λ spheromak bounded by a spherical flux conserver[21]. They consider the low-β case and neglect the pressure in equilibrium calculations. The pressure is prescribed to be marginally Mercier stable by requiring $D_M = 0$ on each flux surface. This is achieved by solving the Mercier equation, Equation 2.59, for P'. The authors neglect terms that are quadratic in P' in their calculations. The resulting pressure on the magnetic axis is calculated to be $\beta_0 = 2 \times 10^{-3}$. This low beta is attributed to the fact that the constant-λ spheromak has very little shear. In a spherical domain, the constant-λ spheromak has a safety factor that varies from $0.7 - 0.8$.

Freire and Clemente consider spheromak equilibria in both spherical and cylindrical flux conservers using an analytic equilibrium with constant F'[75]. The spherical case uses a linear pressure profile, and the cylindrical case uses a quadratic pressure profile. The marginally stable $\langle\beta\rangle$ is calculated by considering the Mercier criteria. The authors find that the spherical equilibrium is limited to $\langle\beta\rangle < 0.003$ which corresponds to $\beta_0 = 0.0046$ on axis. For the cylindrical case, the beta limit increases with the elongation of the cylinder $\frac{L}{2R}$. It has an asymptotic value of $\langle\beta\rangle = 0.083$ ($\beta_0 = 0.217$). The increased stability of the cylinder is due to increased shear, which increases with elongation. The small stable β values are consistent with other work for constant-λ spheromaks.

Mayo et al. study the stability of spheromak equilibria in a cylindrical flux conserver using a linear parallel current profile $\lambda = \bar{\lambda}\left(1 + \alpha\left(2\psi - 1\right)\right)$, where $\bar{\lambda}$ is the average parallel current[76]. Positive α yields a current peaked at the magnetic axis and corresponds to a decaying spheromak. A negative α has a current that peaks near the wall and corresponds to a driven spheromak. Internal current driven kink modes limit the current gradient α. Equilibria are unstable to an $n = 1$ kink for $\alpha < -0.3$, and they are unstable to an $n = 2$ mode for $\alpha > 0.2$. The equilibrium pressure gradient on each flux surface is calculated to give $D_M = 0$, and the pressure is assumed to be small such that $\lambda = -F'$. The volume averaged $\langle\beta\rangle$ is minimum near $\alpha = 0.3$ with a value of 0.004 and increases with decreasing α. At $\alpha = -.35$ the maximum stable β increases to $\langle\beta\rangle = 0.015$, indicating that driven spheromaks are more stable to interchange modes than decaying spheromaks.

This work also explores the effect of adding a current hole by using the modified current profile

$\lambda = \bar{\lambda}\left(1+\alpha\left(2\psi-1\right)\right)\left(1-\exp\left(\psi/\psi_c\right)\right)$. This modification forces $\lambda = 0$ at the wall and down the geometric axis. This forces $q = 0$ at the wall and geometric axis, increasing q', and increasing the maximum stable pressure gradient on flux surfaces near the wall. A significant increase in the stable β is achieved with $\psi_c = 0.1$. For $\alpha = -0.35$ the maximum stable β increases to $\langle\beta\rangle = 0.08$, and for $\alpha = 0.3$ the maximum $\langle\beta\rangle$ increases to 0.02.

Gautier et al. study the stability of oblate spheromaks using the ERATO code[77]. The boundary is prescribed by the equation

$$\frac{r^2}{R}\left[j_1\left(R\right)+\epsilon\frac{4z^2-r^2}{R^2}j_3\left(R\right)\right]=\delta, \tag{2.85}$$

where $R^2 = r^2 + z^2$ and j_i is the i-th spherical Bessel function. The free parameters δ and ϵ control the shape of the outer boundary. Adjusting ϵ adjusts the oblateness of the spheromak, where $\epsilon < 0$ generates an oblate spheromak and $\epsilon > 0$ generates a prolate spheromak. The study focuses on the oblate spheromak with $\epsilon = -0.3$. The boundary for $\delta = 0$ is topologically spherical and passes through the geometric axis ($R = 0$). For $\delta > 0$ the boundary is toroidal, and there is a gap between $R = 0$ and the boundary of the plasma. This creates a current hole similar to that of Mayo et al. Equilibria are calculated using a linear pressure gradient $P' \sim \psi$ and $F^2 = C\psi^2\left(1+\frac{2}{3}\alpha\right)$. Here ψ is normalized such that $\alpha = 0$ corresponds to a centrally peaked toroidal current, and increasing α creates a hollow toroidal current profile akin to a driven spheromak.

Gauter et al. examine stability in three ways. They evaluate the infinite-n ballooning equation on each flux surface. They also calculate the Mercier criteria for each surface. Finally they calculate the linear growth rates for low-n modes. In general they find that the ballooning equation sets the most stringent limit on stability, with larger α (increasingly hollow current profiles) supporting larger pressure gradients and higher stable β. However, if α is too large, then the $q = 1$ surface is resonant, and the $n = 1$ kink mode is destabilized.

The authors also note that near the Mercier stability limit, the linear growth rates are too small to calculate. For example, for the case with $\alpha = 0$, the $n = 2$ mode violates the Mercier stability limit at $\beta_C = 3\%$, but linear calculations show that the growth rate rapidly decreases for $\beta < 8\%$. They also show that below $\beta = 8\%$ the inertial layer becomes extremely small, and non-ideal effects should be significant.

With $\alpha = 1.5$ and no current hole ($\delta = 0$) the authors find a maximum stable $\langle\beta\rangle$ of 12%. The maximum stable β increases with increasing current hole.

Hooper et al. consider Mercier limits in SSPX geometry[4]. They use the current profile

$$\lambda = \lambda_0 \left(1 + \sum_{1}^{3} \psi^n + a_{ns}\psi^{ns}\right) \tag{2.86}$$

in the closed flux region, and take λ to be constant in the open region. They generalize the definition λ to include pressure contributions such that $\lambda = F'$. The pressure is calculated to satisfy $D_M = 0$ on each flux surface. The highest stable β_p occurs for hollow current profiles, with β_p as large as 12% being stable. Unlike previous studies, Hooper et al. account for finite current on the open field. This current keeps $q > 0$ at the edge of the spheromak and reduces the amount of shear.

Jardin uses PEST-II to study ideal stability properties of a cylindrical screw pinch designed to model spheromak equilibria[78]. The stability properties of these equilibria are compared with the stability properties of toroidal spheromak equilibria. The screw pinch equilibria are defined to have the safety factor profile $q = q_0\left(1 - r^2\right)$, where the plasma boundary is at $r = 1$. The pressure profile is $dp/dr = -\alpha r B_z^2/8\left(q'/q\right)^2$, where $\alpha = 1$ gives a pressure that is everywhere marginally Suydam stable ($D_s = 1/4$). The toroidal equilibria are similarly defined with $q = q_0\left(1 - \left(\frac{\psi}{\psi_0}\right)\right)$ and $p' = \alpha p'_m$, where p'_m is the marginally Mercier stable pressure gradient. The last closed flux surface of the toroidal equilibria is prescribed using an equation similar to Equation 2.85. Jardin allows for a vacuum region between the plasma boundary and the wall in both the cylindrical and toroidal configurations.

The force-free, $\alpha = 0$, screw pinch has a threshold in q_0 below which the equilibria are unstable to internal current-driven modes. Without a vacuum region the minimum stable value is $q_0 R = 0.67$, where $2\pi R$ is the length of the cylinder. There is also a maximum stable q_0 at finite α, this limit corresponds to the onset of pressure driven interchange modes. For $\alpha = 0.5$ the maximum stable value is $q_0 R = 2.4$, and $\alpha = 1$ is limited by $q_0 R = 1.1$. In general increasing α decreases the range of stable q_0 by both increasing the minimum stable q_0 and decreasing the maximum stable q_0. Increasing the distance between the plasma boundary and the wall has a similar effect on reducing the range of stable q_0.

Jardin finds that the toroidal spheromak equilibrium has similar stability properties, where the minimum stable q_0 is limited by the onset of current driven instabilities and the maximum stable q_0 is limited by pressure driven modes[78]. The toroidal spheromak is also unstable to an internal $n = 1$ kink when the $q = 1$ surface is resonant. This $n = 1$ kink is always stable in the cylindrical case. The maximum stable β_θ for the toroidal equilibrium depends on both the separation between the plasma and the wall and the size of the current hole. For a tight-fitting wall, with a modest current hole ($\delta = 0.3$) the maximum stable β is $\beta_\theta = 65\%$.

DeLucia et al. study the resistive stability properties of Jardin's cylindrical spheromak equilibria [79]. The study focuses on equilibria that are ideal interchange stable, $\alpha < 1$. Two methods are used to numerically calculate resistive growth rates. Their first method calculates the linear growth rates by using a boundary-layer approach, matching resistive layers to ideal outer regions. The second approach uses a linear finite-difference initial-value code. The boundary-layer approach is ideal for high S or very low α equilibria. Here the resistive layers are very thin, and the growth rates are very small, making the finite difference calculations prohibitively expensive (by 1984 standards). However, at small S and large α the boundary-layer analysis is not valid. Here the finite difference calculations excel, and the two methods complement each other. Agreement is observed between the two methods at intermediate S and α.

In agreement with theory, the resistive interchange growth rate scales as $\gamma \sim S^{-1/3}$ at high S, where S is the Lundquist number. However as S is decreased the growth departs from the asymptotic scaling and peaks at some critical S_c. Decreasing S below this critical S_c reduces the growth rate. The critical value of S_C decreases with increasing pressure. At fixed S the growth rate scales with increasing pressure. At moderate pressure the growth rate scales as $\gamma \sim (\beta_0)^{1/3}$. At small pressures with $\beta_0 < 10^{-3}$ the resistive interchange is partially stabilized by coupling to the external tearing stable region. Here the growth rate has a stronger dependence on the pressure $\gamma \sim \beta_0^2$. The authors also study current driven tearing modes in these equilibria. The growth rates of current driven tearing modes do not have a maximal value, and their growth rates continue to increase with decreasing S. The authors briefly consider the effect of the Hall term on resistive interchange modes. Complete stabilization is observed for large Hall parameters, $\Lambda = (\Omega_{ci}\tau_A)^{-1}$. At $S = 10^5$ and $\alpha = 0.7$ Hall parameters as large as $10 - 20\%$ are needed to stabilize the low-n modes.

DeLucia and Jardin [80] also studied the nonlinear evolution of resistive interchange modes in these cylindrical equilibria. They simulate the nonlinear evolution of single helicity modes. The evolution of these nonlinear modes goes through three distinct phases. Initially exponential growth is observed during the linear growth phase. Then when the nonlinear terms become significant the growth rate slows down and changes to an algebraic rate. The algebraic growth rate is further decreased in a late nonlinear growth phase. The reduction of the growth rate is due to a quasi-linear flattening of the equilibrium pressure profile across the resonant surface. This final nonlinear growth rate occurs on a time scale that is slow compared to the resistive time scale. The nonlinear algebraic growth phase is not observed for modes located near the magnetic axis where the magnetic shear is weak.

Hammet and Tang studied kinetic and resistive effects on interchange modes in these cylindrical spheromak equilibria[81]. They use ballooning equations derived from gyrokinetics to calculate linear growth rates. A Krook operator is included to model collisions, and drift waves are ordered out of the system by assuming small $E_{\|}$. In the collisionless limit, they find that kinetic effects can stabilize $n = 1$ modes when $D_s < 0.375$. Higher-n modes are more easily stabilized since the drift frequency scales with n. In the collisional case, they recover the traditional resistive interchange scaling $\gamma \sim S^{-1/3}$ in the limit when the diamagnetic drift frequency is small $\omega_* << \gamma$. In the opposite limit $\omega_* >> \gamma$ the growth rate is greatly reduced and scales as $\gamma \sim S^{-1}$.

Shumlak and Jarboe investigate the stability properties of a concave “bowtie” flux conserver[82]. The “knot” of the bowtie is located at the geometric axis, and the two “lobes” are poloidal cross sections separated by 180 degrees. The authors consider the same linear current profile of Mayo et al.[76], and focus on hollow current profiles. Linear calculations of $n = 1$ and $n = 2$ current driven $0 - \beta$ modes are used to determine the marginally stable current gradient. The marginally Mercier stable pressure profile is then calculated for equilibria with this current gradient. The equilibria and pressure calculations are performed iteratively for consistency. Following this procedure the authors show that the maximum stable $\langle\beta\rangle$ increases as the height of the flux conserver at the geometric axis is decreased. The maximum stable $\langle\beta\rangle$ increases from $1-2\%$ for a cylindrical flux conserver to 20% for tightly pinched bowtie. Pinching the flux conserver has a stabilizing effect on the $n = 1$ kink mode. This increases the maximum stable current gradient. Pinching the flux conserver also decreases q_{wall} which increases the magnetic shear. The combination of these two effects is responsible for the increased β limit of the bowtie flux conserver.

In summary, a number of studies have looked at pressure limits in spheromaks due to ideal stability. Most of these studies use the ideal Mercier stability limit to determine the maximum stable β. Others have looked at ballooning limits or directly calculated linear growth rates. The constant-λ spheromak has poor stability with a maximum β of only a few percent. This is due to the fact that constant-λ spheromaks have very little shear. Stability can be improved by allowing λ to vary and by shaping the last closed flux surface. Both methods improve stability by increasing the shear. It is found that hollow current profiles, where λ has a minimum at the magnetic axis, have the highest stable β. Current driven instabilities limit the hollowness of the current profile. This is turn limits the maximum stable β. Most studies that look at shaping attempt to minimize q at the wall. An effective way of doing so is to introduce a current-less region between the spheromak and the geometric axis. This forces $q = 0$ at the boundary. The highest stable β are achieved when q varies from 0 at the wall to just below 1 on axis.

The highest temperatures in SSPX were obtained in spheromaks with limited magnetic shear and currents on the open field. In addition these temperatures were observed in decaying equilibria with peaked current profiles. This result is not well described by the above optimization procedure and warrants further investigation.

2.5 The NIMROD Code

The NIMROD code (Non-Ideal Magnetohydrodynamics with Rotation - Open Discussion)[3] is used in this work to model decaying spheromaks. The code maintains a certain degree of flexibility designed to study a variety of issues related to magnetic confinement. In this section we present an introduction to the code and discuss aspects of the code directly related to this work.

NIMROD evolves the extended MHD fluid equations and the pre-Maxwell's equations (neglecting the displacement current) in 3-D for fusion-relevant plasma parameters. The poloidal plane is represented using 2-D spectral elements. The 3rd direction is assumed to be periodic and is represented using finite Fourier series. This spatial representation is designed to efficiently model the complex poloidal cross-sections of modern day experiments, and it takes advantage of the toroidal symmetry present in many experiments. The convergence properties of the spectral elements aid in resolving extreme anisotropies that arise in magnetically confined plasmas and help enforce the magnetic divergence constraint. A leapfrog scheme advances the fields in time, and a semi-implicit operator is used in the velocity advance permitting large time steps. NIMROD uses two coordinate systems based on the problem of interest: (X, Y, Z) for linear periodic systems and (R, Z, ϕ) for toroidal systems.

2.5.1 NIMROD's Fluid Model

The single and 2-fluid models that NIMROD solves are described by the system of equations

$$\frac{\partial n}{\partial t} + \vec{V} \cdot \nabla n + n \nabla \cdot \vec{V} = \nabla \cdot (D \nabla n) + \nabla \cdot \left(D_h \nabla \nabla^2 n \right) \tag{2.87}$$

$$\rho \left(\frac{\partial \vec{V}}{\partial t} + \vec{V} \cdot \nabla \vec{V} \right) = \vec{J} \times \vec{B} - \nabla P - \nabla \cdot \Pi_i \tag{2.88}$$

$$\frac{n}{\gamma - 1} \left(\frac{\partial T_s}{\partial t} + \vec{V}_s \cdot \nabla T_s \right) = -P_s \nabla \cdot \vec{V}_s - \nabla \cdot \vec{q}_s + Q_s \tag{2.89}$$

$$\frac{\partial \vec{B}}{\partial t} = -\nabla \times \vec{E} + \kappa_{divb} \nabla \nabla \cdot \vec{B} \tag{2.90}$$

$$E = -\vec{V} \times \vec{B} + \eta \vec{J} + \frac{1}{ne} \left(\vec{J} \times \vec{B} - \nabla P_e \right) + \frac{m_e}{ne^2} \frac{\partial \vec{J}}{\partial t} \tag{2.91}$$

$$\mu_0 \vec{J} = \nabla \times \vec{B}. \tag{2.92}$$

These equations comprise the extended MHD model discussed in Section 2.1. Artificial number density diffusivity and hyper-diffusivity are added to continuity equations (Equation 2.87) to smooth small scale density fluctuations. The magnetic divergence constraint, $\nabla \cdot \vec{B} = 0$, is not solved directly, instead artificial magnetic diffusivity is introduced in Faraday's law, as shown in Equation 2.90, to diffusive out magnetic divergence errors.

The first two terms on the right side of Equation 2.91 are the MHD contribution to Ohm's law. They are the only terms that appear in single-fluid calculations. The next two terms are the Hall term and electron pressure. They are included in all two-fluid calculations. These two terms introduce the dispersive Whistler and kinetic Alfven waves, whose dispersion relations are of the form $\omega^2 \sim k^4$ [34]. That last term is a partial representation of the electron inertia, and it is included in most two-fluid calculations. However, electron advection is neglected. Electron inertia introduces resonances at the electron cyclotron frequency, which limits the frequency range of the Whistler and kinetic Alfven waves.

NIMROD decomposes the physical fields into steady-state components and time varying perturbed components. The steady-state components do not vary in the periodic direction and are assumed to be in force balance. For example, in toroidal geometry NIMROD represents the pressure as $p\left(R, Z, \phi, t\right) = p_{eq}\left(R, Z\right) + \tilde{p}\left(R, Z, \phi, t\right)$. This decomposition allows both time-dependent linear and nonlinear calculations. Linear calculations neglect terms that are the product of two or more perturbed quantities. The decomposition also improves numerical accuracy, especially when the perturbed quantities are smaller than the steady-state components.

2.5.2 NIMROD's Time Advance

NIMROD uses a semi-implicit time advance to evolve the perturbed fields using Equations 2.87-2.92. The temporal derivatives are approximated using a finite difference leap-frog scheme. The density, temperature, and magnetic field are defined on integer time steps, while the velocity is defined on half-integer time steps. The velocity is advanced first, followed by the density, temperature, and then the magnetic field.

A self-adjoint semi-implicit operator is applied to the velocity advance to eliminate time-step restrictions due to high frequency waves. The time steps of explicit schemes are typically limited by the condition $k_{max} C \Delta t < \alpha$, where k_{max} is the magnitude of the largest wave vector included in the system, C is a characteristic wave speed, Δt is the time step, and α is a numerical factor of order unity. These explicit time-step restrictions are prohibitive in many magnetic confinement applications, where the evolution of the system occurs over many Alfven times. The introduction of the semi-implicit operator introduces an effective numerical inertia, eliminating time-step restrictions due to waves. The accuracy at large Δt is limited by how well the operator reproduces the physical system.

NIMROD uses a semi-implicit operator based on the ideal-MHD force operator, $L\left(\frac{\partial \vec{V}}{\partial t}\right)$[3]. Most systems of interest have large Lundquist numbers, $S \gg 1$, and the ideal-MHD force operator is a reasonable choice. The momentum equation with the semi-implicit operator is

$$\rho\left(\frac{\partial \vec{V}}{\partial t} + \vec{V}\cdot\nabla\vec{V}\right) - C_1 \Delta t^2 L\left(\frac{\partial \vec{V}}{\partial t}\right) - C_2 p_{nl} \Delta t^2 \nabla^2 \frac{\partial \vec{V}}{\partial t} = \vec{J}\times\vec{B} - \nabla p - \nabla\cdot\vec{\vec{\Pi}}_i, \tag{2.93}$$

where the coefficients C_1 and C_2 are tunable numerical parameters which determine the relative magnitude of the semi-implicit operator, and p_{nl} scales with the toroidal variation of the total pressure. The ideal MHD force operator is

$$L\left(\vec{W}\right) = \mu_0^{-1}\left[\nabla \times \nabla \times \left(\vec{W} \times \vec{B}_0\right)\right] \times \vec{B}_0 + \vec{J}_0 \times \nabla \times \left(\vec{W} \times \vec{B}_0\right) + \nabla\left(\vec{W} \cdot \nabla p_0 + \gamma p_0 \nabla \cdot \vec{W}\right), \quad (2.94)$$

where B_0, J_0, and p_0 are the symmetric components of the respective fields. They include both the steady-state and time-varying $n = 0$ components. The third term in Equation 2.93, $C_2 p_{nl} \Delta t^2 \nabla^2 \frac{\partial \vec{V}}{\partial t}$, is a second semi-implicit operator. It helps provide stability when large asymmetric pressures develop.

The semi-implicit operator eliminates time-step restrictions due to waves. However, a weaker restriction exists due to the advective terms, $\vec{V} \cdot \nabla$. NIMROD uses two different time advance algorithms: a predictor-corrector time advance whose time step is restricted by the advection term, and an implicit advection time advance.

The predictor-corrector algorithm advances each field in two steps[3]. The first step calculates the change in a field using data from the old time step. This is used to calculate a prediction for the field at the new step. This prediction is then used in a second advance to calculate a corrected value of the field at the new time. We illustrate this approach using the continuity equation. First the value of the density at the N-th time step is used to calculate a prediction for the density at the $N + 1$ time step

$$\Delta n_{pre} = -\Delta t\left[\vec{V}^{N+1/2} \cdot \nabla n^N + n^N \nabla \cdot \vec{V}^{N+1/2}\right] \quad (2.95)$$

$$n^* = n^N + f_n \Delta n_{pre}, \quad (2.96)$$

where n^* is the predicted density, f_n is a centering parameter, and the velocity at the $N + 1/2$ time step is known because the velocity advance precedes the density advance. The predicted density is then used to calculate a new corrected density

$$\Delta n_{cor} = -\Delta t\left[\vec{V}^{N+1/2} \cdot \nabla n^* + n^* \nabla \cdot \vec{V}^{N+1/2}\right] \quad (2.97)$$

$$n^{N+1} = n^N + \Delta n_{cor}. \quad (2.98)$$

A similar procedure is used to advance the other fields.

The implicit advection algorithm is used in calculations that use the two-fluid Ohm's law[83]. (Calculations that use the MHD Ohm's law can use either algorithm). The implicit advection algorithm advances each field in one step. The advective terms and two-fluid terms are time-centered in each step.

This is illustrated using the continuity equation

$$\Delta n + \frac{\Delta t}{2} \nabla \cdot \left(\vec{V}^{N+1/2} \Delta n \right) = -\Delta t \nabla \cdot \left(\vec{V}^{N+1/2} n^N \right) \tag{2.99}$$

The implicit advection algorithm with centered advection and two-fluid terms allows for stability with flow at arbitrary large Δt. Additionally NIMROD's time advance introduces no numerical dissipation.

2.5.3 NIMROD's Spatial Representation

NIMROD uses 2D spectral elements to represent the poloidal plane and finite Fourier series to represent the third periodic dimension. The spectral elements enable the representation of shaped poloidal cross-sections. Their convergence properties aid in resolving extreme anisotropies and facilitate representation of the magnetic divergence constraint. The finite Fourier representation takes advantage of the symmetry in many fusion experiments.

NIMROD represents the scalar fields using the expansion

$$s\left(R, Z, \phi\right) = \sum_i s_{i0} \alpha_i + \sum_{i,n} \left(s_{in} e^{in\phi} + s_{in}^* e^{-in\phi} \right) \alpha_i, \tag{2.100}$$

and the vector fields use the expansion

$$\vec{F}\left(R, Z, \phi\right) = \sum_{iv} \hat{e}_v F_{iv0} \alpha_i + \sum_{i,v,n} \hat{e}_v \left(F_{ivn} e^{in\phi} + F_{ivn}^* e^{-in\phi} \right) \alpha_i, \tag{2.101}$$

where the "star" denotes the complex conjugate and $\hat{e}_v$ are unit vectors. The index i corresponds to the spectral element basis function, the index v corresponds the direction of the vector component, and the index n is the toroidal mode number.

The spectral element basis functions, $\alpha\left(R, Z\right)$, are expressed in terms of the logical coordinates within each element: $\alpha_i\left(R, Z\right) = \alpha_i\left(\xi\left(R, Z\right), \eta\left(R, Z\right)\right)$. Logically rectangular elements are used with $0 \leq \xi \leq 1$ and $0 \leq \eta \leq 1$. The basis functions $\alpha_i\left(\xi, \eta\right)$ are 2D Lagrange type polynomials of order P. A series of node locations $\left(\xi_n, \eta_m\right)$ are defined in each element, where $P+1$ nodes are needed in each direction. These node locations are used to define the Lagrange basis, which has the property that $l_{nm} = 1$ at the node located at $\left(\xi_n, \eta_m\right)$ and $l_{nm} = 0$ at all other node locations. The 1D Lagrange polynomials are defined by the product

$$l_i\left(x\right) = \Pi_{0 \leq m \leq P, m \neq i} \frac{x - x_m}{x_i - x_m} \tag{2.102}$$

and the 2D Lagrange basis functions are products of two 1D Lagrange polynomials

$$\alpha_i = l_n(\xi)\, l_m(\eta), \tag{2.103}$$

where each l_n, l_m pair corresponds to a different basis function α_i.

The choice of node locations influences the convergence properties of the spectral elements. NIMROD allows users to chose between uniformly spaced nodes and Gauss-Lobatto-Lagrange (GLL) nodes. The GLL node spacing is needed to achieve spectral convergence. Spectral convergence is the property that the error decreases geometrically with increasing P for a sufficiently smooth solution[84].

2.5.4 NIMROD Organization

In addition to the NIMROD code, there are a number of pre- and post-processors within the NIMROD framework that perform specialized tasks. This section provides a discussion of many of these programs and lays out the general work flow involved in running NIMROD.

The NIMROD executable is the primary code within the NIMROD framework. It evolves the fluid equations in time using the semi-implicit time advance. It requires an initial "dump" file that contains the spectral element mesh and the values of the physical fields at the initial time. NIMROD reads an input file, nimrod.in, that contains a number of physical and numerical input parameters. The code periodically writes dump files that contain the 3-D representation of the physical fields at specific time steps. NIMROD also writes binary files that contain the time evolution of various quantities including the volume integrated magnetic and kinetic energies, linear growth rates, and the physical fields calculated at discrete "probe" locations. NIMROD has the ability to run both linear calculations and fully nonlinear calculations. The linear calculations will converge on the dominant mode for each Fourier component.

FLUXGRID is a preprocessor that imports equilibrium data from various external equilibrium solvers (such as TOQ and EFIT). This data is used to create a flux-aligned mesh and create an initial steady-state equilibrium. FLUXGRID can also calculate the ideal and resistive Mercier stability parameters for these flux-aligned meshes. The output from FLUXGRID still has to be processed by NIMSET before it can be used by NIMROD.

NIMSET is the main preprocessor within NIMROD. It generates the mesh, places the equilibrium fields, and sets the initial perturbation. NIMSET contains functionality to generate rectangular and polar meshes, and it is easily modified to construct shaped meshes. It can generate a variety of equilibria from analytic models. NIMSET is also used to process the output from FLUXGRID for use with the main NIMROD executable.

NIMEQ is a fixed-boundary Grad-Shafranov solver that is used to generate 2-D magnetostatic equilibria. NIMEQ can generate equilibria in both linear periodic and toroidal geometries on arbitrary poloidal meshes. NIMEQ is designed to be run after NIMSET. It uses the mesh generated by NIMSET, and it uses the equilibrium magnetic fields specified in NIMSET to calculate the poloidal flux along the boundary. The development of NIMEQ is a part of this thesis work, and it is discussed in detail in Chapter 3.

NIMPLOT is the main post-processor. It is an interactive program that is used to create graphic files from NIMROD's output files. NIMFL is a post-processor that performs field line traces by integrating along the magnetic field. We primarily use it to create Poincare plots of the magnetic field.

Chapter 3

NIMEQ: A Grad-Shafranov Solver for NIMROD

This chapter discusses the development of NIMEQ: a two dimensional MHD equilibrium solver developed within the NIMROD framework[85]. NIMEQ uses spectral elements to model the poloidal plane. Special consideration is given to ensure regularity at the geometric axis, to permit the generation of spheromak equilibria. However, the algorithm is completely general, and NIMEQ can be used to create Grad-Shafranov equilibrium for a variety of configurations in both linearly periodic and toroidally symmetric geometries.

3.1 Development of NIMEQ

NIMEQ generates 2D magneto-static equilibria by solving the Grad-Shafranov equation, Equation 2.38, in the weak form. As previously mentioned, NIMEQ generates equilibria in both linearly periodic and toroidally symmetric geometries, although the following formulation assumes toroidal geometry, (R, Z, ϕ). The formulation for linear geometries is similar, and it is obtained by settings factors of R appearing explicitly to unity.

Substituting the scalar field $\Lambda = \psi/R^2$ into Equation 2.38 transforms the Grad-Shafranov operator into a divergence of a vector, $\Delta^*\psi = \nabla \cdot R^2 \nabla \Lambda$. This is convenient for topologically cylindrical domains, because all surface terms that arise are at physical boundaries and not along $R = 0$. The field Λ is then spilt into a known component Λ_0 and an unknown component Λ_h. Λ_0 satisfies the specified boundary condition for Λ, and Λ_h satisfies the boundary condition $\Lambda_h = 0$. The unknown field is expanded onto a series of spectral element basis functions $\Lambda_h = \sum_i \Lambda_i \alpha_i$. Substituting this expression for Λ into

Equation 2.38, multiplying the equation by the test function α_j, and integrating over the domain yields the following weak form of the Grad-Shafranov equation:

$$\sum_i \Lambda_i \int dV R^2 \nabla\alpha_i \cdot \nabla\alpha_j = \int dV \left(FF' + \mu_0 R^2 P'\right) \alpha_j - \int dV R^2 \nabla\Lambda_0 \cdot \nabla\alpha_j. \tag{3.1}$$

The above expression holds for all test functions α_j. For compactness equation 3.1 is written as $M\Lambda = Q$. The matrix M in positive definite and symmetric. In general, the right-hand-side vector Q is nonlinear, due to the functions $P(\psi)$ and $F(\psi)$. This nonlinear system is solved using modified Picard iterations,

$$M\Lambda^n = (1-\theta)\, M\Lambda^{n-1} + \theta Q^{n-1}, \tag{3.2}$$

where the relaxation parameter $\theta \in (0,1]$ is introduced to aid convergence. The matrix in equation 3.2 is inverted using standard numerical techniques. Convergence is achieved when the ratio of the norms of the residual error $\|\Delta^*\psi + FF' + \mu_0 R^2 P'\|_2$ and the Grad-Shafranov operator $\|\Delta^*\psi\|_2$ is less than a user specified tolerance.

A normalized loop flux $\hat{\psi} = (\psi - \psi_a) / (\psi_l - \psi_a)$ is defined to help constrain the physical region over which different $P(\psi)$ and $F(\psi)$ profiles are applied. The loop flux is defined to be 0 at the magnetic axis, ψ_a, and 1 at the last closed flux surface, ψ_l. The last closed flux surface is assumed to be the extreme value of the flux on the boundary. The loop flux also serves as a marker to distinguish between regions of open and closed flux. This enables the tailoring of $P(\psi)$ and $F(\psi)$ to account for different physical effects that occur in the two regions.

In topologically cylindrical domains, regularity requires the flux function to vary as $\psi(R,Z) = \psi_0 + \psi_2(Z) R^2 + O\left(R^4\right)$ in the limit of $R \to 0$. The corresponding behavior for Λ is $\Lambda = \psi_0/R^2 + \psi_2(Z) + O\left(R^2\right)$. A gauge freedom exists in that the magnetic field and the current density only depend on the derivatives of ψ. The choice $\psi_0 = 0$ implies that Λ satisfies standard regularity conditions for an axisymmetric scalar field and, hence, is well behaved near the geometric axis in our computations.

The final step is to calculate the equilibrium fields from the converged solution for Λ. NIMROD computations require the equilibrium quantities $\vec{B}_p$, $\vec{J}_p$, RB_ϕ, $R^{-1}J_\phi$, and P at each node of the spectral-element expansion. The pressure and RB_ϕ values are calculated directly from the prescribed $P(\psi)$ and $F(\psi)$ profiles using the computed $\Lambda(R,Z)$ field. The poloidal magnetic field is expressed in terms of Λ,

$$\vec{B}_p = R^{-1}\hat{e}_\phi \times \left(2R\hat{e}_r\Lambda + R^2\nabla\Lambda\right), \tag{3.3}$$

and projected onto the spectral element bases by solving the weak from of Equation 3.3. The poloidal current is calculated directly from the poloidal magnetic field using the relation $\mu_0\vec{J}_p = -F'\vec{B}_p$. The toroidal current density is calculated by solving the weak form of $\mu_0 R^{-1}J_\phi = R^{-2}\Delta^*\psi = \mu_0 P' + R^{-2}FF'$.

3.2 NIMEQ Benchmarking and Convergence Studies

This section presents the verification and convergence properties of our spectral element computations. In three of the test cases, the Grad-Shafranov equation is linear in ψ, and analytical solutions are known. These equilibria represent idealizations of a tokamak[86], a spheromak[87], and a field-reversed configuration (FRC)[88]. The Grad-Shafranov equation is nonlinear in ψ in a fourth case, and analytical solutions are not known.

Convergence studies using both h-refinement and p-refinement are performed for the first three equilibria by comparing numerically generated equilibria with their known solutions. H-refinement increases the number of elements in a computation but keeps the polynomial degree of the elements constant. P-refinement maintains the number of elements but increases the polynomial degree of each element. Another measure of convergence is determined by defining a spectral error based on the truncation of the spectral representation. This is done by projecting the solution onto 2D Legendre polynomials within each element. The spectral error is defined as $E_s \equiv \sqrt{\sum_e c_e^2/n^2}$, where c_e is the coefficient of the highest order Legendre polynomial in each element and n is the number of elements. The spectral error gives an estimate of the truncation error (E_T), which results from keeping a finite number of terms in an expansion. As a rule of thumb, the truncation error for a geometrically converging series is $E_T \sim O(E_s)$, and for an algebraically converging expansion, the error is $E_T \sim O(\mathrm{p}E_s)$, where p is the degree of the highest-order term in the expansion[84]. The convergence properties of the spectral error is compared with the numerical error for the first three equilibria. The spectral error alone is used to investigate the convergence properties of the nonlinear equilibrium.

3.2.1 Equilibria

The first test case, representative of a tokamak, is the Solov'ev solution to Equation 2.38. Solutions are obtained by asserting that both $\mu_0 P' = -S_1$ and $FF' = S_2$ are constant[18]. The resulting equilibrium equation is linear, and series solutions are straightforward to calculate[19, 20]. Here, we use a simple nontrivial case, where the analytic solution is:

$$\psi = -\frac{S_1}{8}R^2 - \frac{S_2}{2}Z^2 + S_3 + S_4 R^2 + S_5\left(R^4 - 4R^2Z^2\right). \tag{3.4}$$

Convergence studies are performed in a domain of rectangular poloidal cross section with $-1.5 < Z < 1.5$ and $1.5 < R < 4.5$. The equilibrium is parameterized using $S_1 = 0.176$, $S_2 = 0.5$, $S_3 = -0.496$, $S_4 = 0.198$ and $S_5 = 0.011$. The poloidal flux along the boundary is prescribed using Equation 3.4. When analyzing the convergence properties of this equilibrium, it is worth noting that while ψ is a 4-th order polynomial, our dependent variable Λ has terms that are proportional to R^{-2}. Consequently, ψ can be represented exactly by a single 4-th order element but Λ cannot. Thus, the numerical accuracy in Λ and ψ continue to increase as our mesh is refined when using 4-th order or higher elements.

The second test case is a field-reversed configuration (FRC). FRCs are characterized by small or zero toroidal field, so $F = 0$ is prescribed in the Grad-Shafranov computations. A quadratic pressure profile $P = P_0 + P_2\left(\psi^2/\psi_0^2\right)$ is specified, and the resulting equation for ψ is linear:

$$\Delta^*\psi + 2\mu_0 R^2 P_2 \frac{\psi}{\psi_0^2} = 0. \tag{3.5}$$

Equation 3.5 can be solved for a cylinder of height h and radius a with the boundary condition $\psi = 0$. The resulting equilibrium is:

$$\psi = \psi_0 \frac{F_0\left(\eta, \frac{1}{2}\sqrt{d}r^2\right)}{F_0\left(\eta, \frac{1}{2}\sqrt{d}r_0^2\right)} \sin\left(\lambda z\right) \tag{3.6}$$

$$B_r = -\frac{\lambda}{r}\psi_0 \frac{F_0\left(\eta, \frac{1}{2}\sqrt{d}r^2\right)}{F_0\left(\eta, \frac{1}{2}\sqrt{d}r_0^2\right)} \cos\left(\lambda z\right) \tag{3.7}$$

$$B_z = \sqrt{d}\psi_0 \frac{F_0'\left(\eta, \frac{1}{2}\sqrt{d}r^2\right)}{F_0\left(\eta, \frac{1}{2}\sqrt{d}r_0^2\right)} \sin\left(\lambda z\right), \tag{3.8}$$

where F_0 is the 0-th order Coulomb wave function, $d = 2\mu_0 P_2/\psi_0^2$, $\lambda = \pi/h$, and $\eta = \lambda^2/\left(4\sqrt{d}\right)$[23, 24]. The flux at the magnetic axis ψ_0 is determined self-consistently such that the radial boundary condition $F_0\left(\eta, \sqrt{d}a^2/2\right) = 0$ is satisfied.

We calculate the zeros of the Coulomb wave function $F_0\left(\eta, \rho\right)$ numerically to ten significant digits using Newton's method. We set the equilibrium parameters to make $\eta = 0.3315$ so that B_r has its first zero at $\rho \equiv \sqrt{d}a^2/2 = 4$. This corresponds to a FRC with elongation $E \equiv a/2h = 0.52$. The domain is a cylinder of height $h = 1.0$ and radius $a = 1.04$. The pressure is set to $\mu_0 P_2 = 0.277$, corresponding to a flux on axis of $\psi = \pm 0.1$. The solution that a numerical algorithm converges on is determined by the initial guess used to seed the nonlinear iterations. In this study NIMEQ converges on the negative root.

The third test case is the idealized spheromak. Under the assumption of constant pressure, the magnetic field is parallel to the current and Ampere's law becomes $\nabla \times \vec{B} = \lambda \vec{B}$. The parallel current, $\lambda = \mu_0 \vec{J} \cdot \vec{B}/B^2$, is related to the flux function $F\left(\psi\right)$ by $\lambda = -F'\left(\psi\right)$. In a cylinder of height h and radius a, and considering constant λ, the lowest order nontrivial solution is:

$$\psi = \psi_0 \frac{\gamma_{11} r}{\chi_{01}} \frac{J_1(\gamma_{11} r)}{J_1(\chi_{01})} \sin\left(\frac{\pi}{h} z\right) \tag{3.9}$$

$$B_r = -\psi_0 \frac{\pi}{h} \frac{\gamma_{11}}{\chi_{01}} \frac{J_1(\gamma_{11} r)}{J_1(\chi_{01})} \cos\left(\frac{\pi}{h} z\right) \tag{3.10}$$

$$B_z = \psi_0 \frac{\gamma_{11}^2}{\chi_{01}} \frac{J_0(\gamma_{11} r)}{J_1(\chi_{01})} \sin\left(\frac{\pi}{h} z\right) \tag{3.11}$$

$$B_\phi = -\lambda \psi_0 \frac{\gamma_{11}}{\chi_{01}} \frac{J_1(\gamma_{11} r)}{J_1(\chi_{01})} \sin\left(\frac{\pi}{h} z\right). \tag{3.12}$$

The parallel current satisfies $\lambda^2 = \gamma_{11}^2 + \left(\pi^2/h^2\right)$ where $\gamma_{11} = \chi_{11}/a$ and χ_{i1} is the first zero of the Bessel function J_i[22].

A cylindrical spheromak is modeled with height $h = 0.5$ and radius $a = 0.5$, and $\psi = 0$ at the boundary. A uniform pressure profile is specified by setting $P' = 0$, and a linear poloidal current function is specified $F = \left(\hat{\psi} - 1\right)$. We note that prescribing P and F in terms of the normalized flux $\hat{\psi}$ sets the magnitude of the right side of Equation 2.38, independent of $|\psi_l - \psi_a|$. Thus, cases such as our FRC and spheromak equilibria, where the right side of Equation 2.38 is a linear monomial in ψ, have a unique solution, apart from a sign. As noted for the FRC case, the sign of the flux is determined by the seed field used at the start of the iteration. For our spheromak cases, we choose $\lambda \psi_a = 1$.

The fourth case is more representative of applications where the Grad-Shafranov equation is nonlinear in ψ. We specify a quadratic F profile, $F = \left(1 - \hat{\psi}\right)^2$, and either a cubic pressure profile, $\mu_0 P = \mu_0 P_a \left(1 - 3\hat{\psi}^2 + 2\hat{\psi}^3\right)$, or a uniform pressure profile. Calculations are performed in a cylinder of height $h = 1$ and radius $a = 0.5$ with $\psi = 0$ on the boundary. The calculations presented use $\mu_0 P_a = 1$.

Equilibria	F model	P model
Solov'ev	$FF' = S_2$	$P = -S_1\psi + P_0$
FRC	$F = 0$	$P = P_0 + P_2(1 - \hat{\psi}^2)$
Spheromak	$F = f_1(1 - \hat{\psi})$	$P = P_0$
Nonlinear	$F = (1 - \hat{\psi})^2$	$P = P_a(1 - 3\hat{\psi}^2 + 2\hat{\psi}^3)$, and $P = P_a$

Table 1: A summary of the pressure and toroidal field models used for each of equilibria.

Table 1 summarizes the four different equilibria, and the calculated equilibrium fluxes are shown in Figure 5.

3.2.2 Convergence Studies

Convergence studies are performed for the Solov'ev, FRC, and spheromak equilibria by comparing the numerical and analytic solutions. The numerical error of a quantity ξ is defined to be $E_n \equiv \sqrt{\sum \left(\xi_n - \xi_a\right)^2 / \sum \xi_a^2}$, where ξ_n is the numerical solution and ξ_a is the analytic solution. The summation is performed over all of the spectral-element nodes. Convergence studies using h-refinement are performed by increasing the number of elements at a fixed polynomial degree. Here the error for a sufficiently smooth solution of a second order differential equation is bounded by the asymptotic rate of convergence $\mathrm{h}^{(\mathrm{p}+1)}$, where h is a characteristic element length and p is the polynomial degree. The error in derivatives of the solution is bounded by the rate h^{P}[89].

Our studies are performed using meshes with equal numbers of elements in the radial and vertical directions. H-refinement studies are repeated using elements with polynomial degrees ranging from 2 to 10. The error in ψ is plotted versus the number of elements in the radial direction on a log-log plot for the Solov'ev equilibrium in Figure 6. The error in ψ and B_r is also plotted for the FRC and

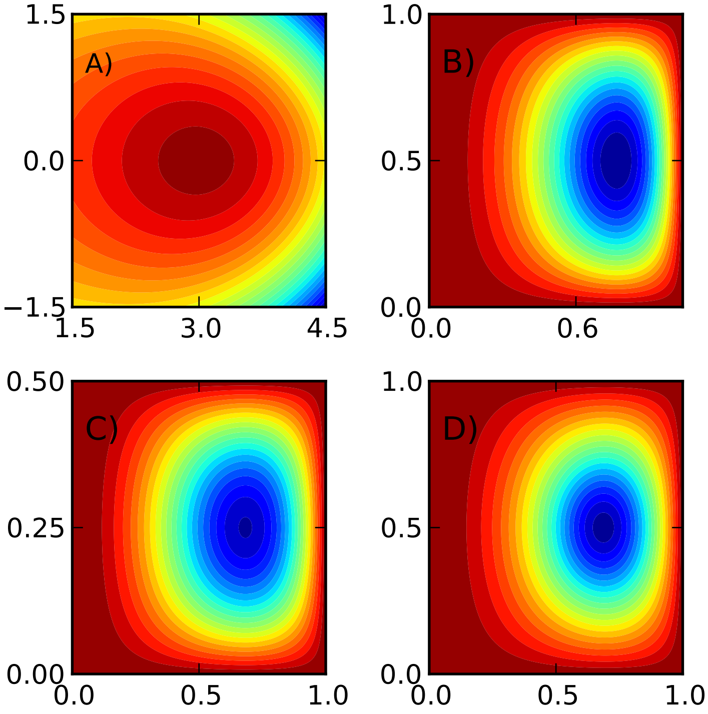

Figure 5: Equilibrium poloidal flux contours for the A) Solov'ev equilibrium, B) FRC equilibrium, C) spheromak equilibrium, and D) nonlinear equilibrium.

spheromak equilibria. In all cases, the error decays linearly to a minimum error (discussed below), indicating algebraic convergence. The asymptotic rate of convergence is indicated by the slopes of these lines. The toroidal field, RB_ϕ, is calculated directly from ψ and converges at a similar rate to ψ. Both B_r and B_z are calculated from $\nabla\psi$, and B_z converges at a rate similar to B_r, but at a reduced rate compared to ψ.

The calculated rates of convergence for ψ are shown in Table 2. For lower-order polynomials the rates of convergence in ψ are between $\mathrm{p}+1$ and $\mathrm{p}+2$. With higher-order polynomials, $\mathrm{p} > 6$, the solutions reach accuracies limited by double-precision error before a clear asymptotic range of convergence is observed. It is not apparent as to why the flux converges faster than the rate of $\mathrm{p}+1$ expected from analysis, nor is it clear if the trend continues to higher polynomial degree. The calculated rates of convergence for B_r are given in Table 3 for the FRC and spheromak equilibria. The obtained rates of

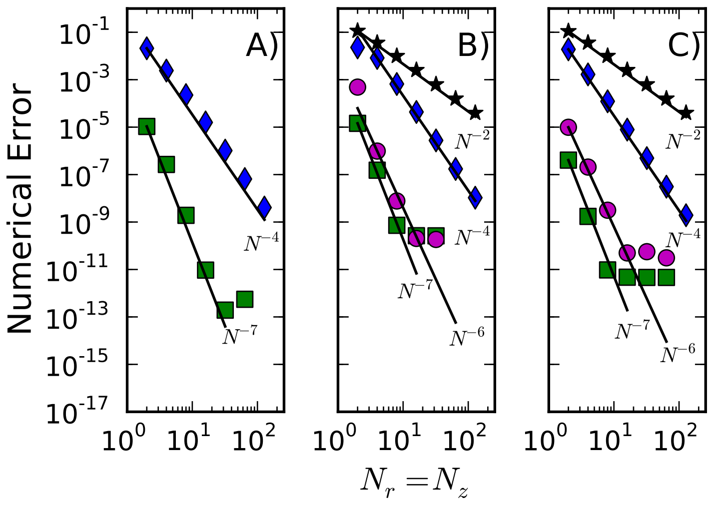

Figure 6: H-refinement convergence studies for the A)Solov'ev equilibrium, B)FRC equilibrium, and C) spheromak equilibrium. The numerical error in ψ is plotted for 2nd order elements (♦) and 6th order elements (■). The numerical error in B_r is also plotted for the FRC and spheromak equilibria for polynomials of degree 2 ($\star$) and polynomials of degree 6 (●). Reference lines are added showing indicated rates of convergence.

convergence are close to the expected rate p.

Errors as small as 10^{-14} are achieved for the Solov'ev equilibrium and 10^{-13} for the spheromak equilibrium. The accuracy of these two cases is limited by double precision error. Our reported errors in the FRC cases are as small as 10^{-10}. This minimum is a reflection of the accuracy in computing the analytic solution. Due to the difficulty in calculating zeros of the Coulomb wave function, the reference solution is only available to ten significant digits.

P-refinement convergence studies are performed by increasing the polynomial degree of the element basis functions while keeping the number of elements in a mesh fixed. The numerical error is calculated as before for the Solov'ev, FRC, and spheromak cases. The numerical errors are plotted versus the polynomial degree on a semi-log scale for 2×2 and 8×8 element meshes in Figure 7. The linear nature of the plots indicates geometric convergence[84]. The spectral error in ψ is calculated for these cases and plotted on a semi-log plot versus the polynomial degree in Figure 8. Similar to the numerical error,

Polynomial degree	Solov'ev	FRC	Spheromak
2	-3.8	-3.5	-3.9
3	-4.9	-4.5	-4.9
4	-5.5	-5.2	-6.0

Table 2: Algebraic rates of convergence of ψ for the Solov'ev, FRC, and Spheromak equilibria.

Polynomial degree	FRC	Spheromak
2	-1.9	-1.9
3	-3.2	-3.2
4	-3.9	-3.9

Table 3: Algebraic rates of convergence of B_r for the FRC, and Spheromak equilibria.

geometric convergence is observed up to double precision error.

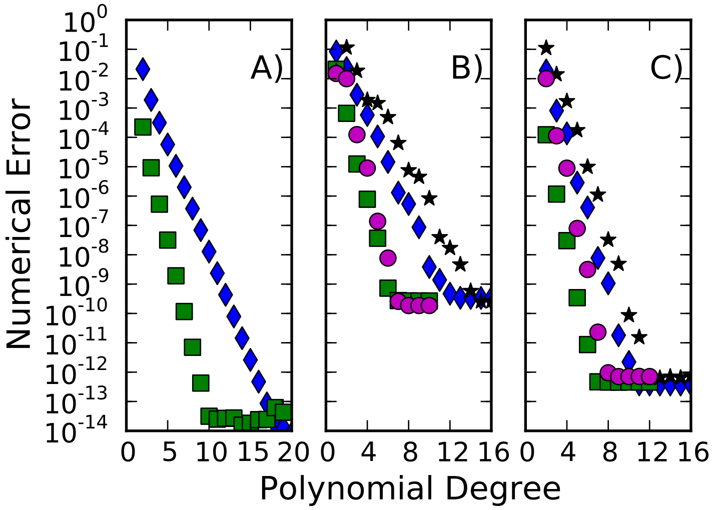

Figure 7: P-refinement convergence studies for the A)Solov'ev equilibrium, B)FRC equilibrium, and C) spheromak equilibrium. The numerical error in ψ is plotted for a 2x2 (◆) and 8x8 (■) element mesh. The numerical error in B_r is also plotted for the FRC and spheromak equilibria for the 2x2 mesh ($\star$) and 8x8 (●) element mesh.

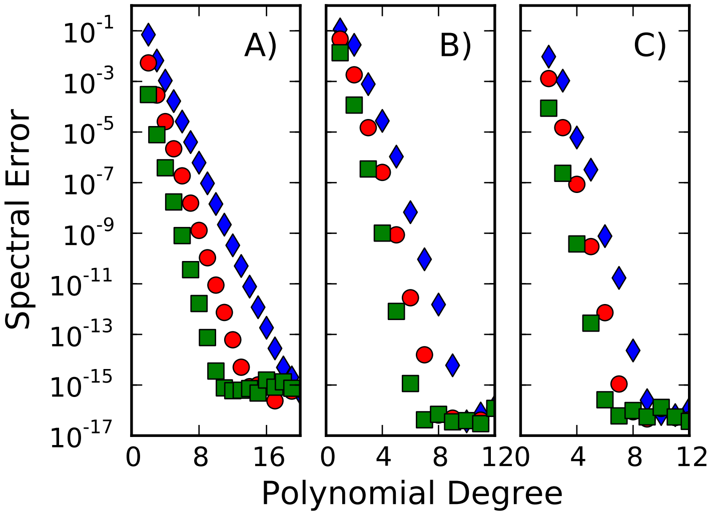

Figure 8: Spectral error in ψ for the A)Solov'ev equilibrium, B)FRC equilibrium, and C) spheromak equilibrium for a 2x2 (♦), 4x4 (●), and 8x8 (■) element mesh.

The spectral error for the nonlinear equilibrium with the cubic pressure profile is plotted as a function of polynomial degree for the 8x8 mesh in Figures 9A-B. Algebraic convergence is observed as the error is linear on the log-log scale but not on the log-linear scale . The error converges as p^{-k} with k approximately equal to 12 or 13. Even with this algebraic convergence, accurate solutions are obtained for the nonlinear equilibrium. For the 8×8 element mesh, the spectral error reaches the double-precession limit of 10^{-16}, at 17-th order polynomials. Calculations using 20-th order polynomials on 2×2 and 4×4 element meshes have spectral errors of 1.99×10^{-13} and 1.45×10^{-15}, respectively.

A second nonlinear equilibrium is studied that uses the same geometry and $F(\psi)$ profile as the first. However, the second equilibrium uses a constant $P(\psi)$ instead of the cubic profile. The second case is nonlinear because FF' is cubic in ψ. The spectral error for this equilibrium is shown in Figure 9C. Geometric convergence is obtained with the constant pressure profile.

Figure 9 also shows the contributions to the spectral error from the two outer corner elements of the 8×8 mesh and that from the other 62 “interior” elements. The total error with the cubic pressure profile is mostly due to the two elements at the outer corners of the cross-section for polynomials of degree 6 through 15. In the constant pressure case, the error from the corner elements accounts for a

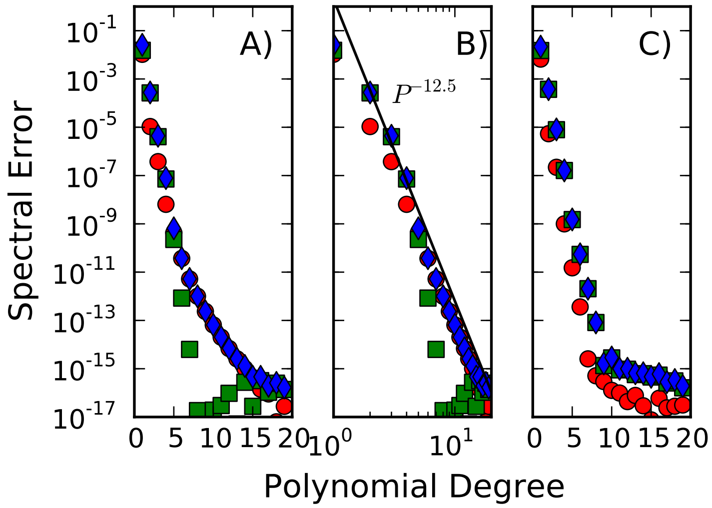

Figure 9: Spectral error in ψ for the nonlinear equilibrium with a cubic pressure profile on a A)log-linear plot, B) a log-log plot, and C) the error with a constant pressure profile on a log-linear plot for an 8x8 mesh (◆). The error in the corner elements (●) accounts for over 95% of the error in the cubic pressure equilibrium at moderate polynomial degree $(6-15)$. The error in the remaining non-corner elements (■) accounts for most of the error in the constant pressure equilibrium. The reference line in (B) shows the rate of convergence that is expected with the weak corner singularity.

small fraction of the total error and converges geometrically.

The observed convergence is consistent with the analysis given in the Section 3.2.3, where the behavior of the Grad-Shafranov equation near either corner is approximated using the nonlinear Poisson equation. The relevant boundary condition has $\psi = 0$ along the physical surfaces, and the right side of the equation contains sources of the form ψ^n. The contribution from each source term is weakly singular in the corner if n is even but nonsingular if n is odd. For even n the singularity is of the form $\rho^{2n+2} \ln \rho$, where ρ is the distance from the corner. It is weak in the sense that ψ is finite at $\rho = 0$ but its $2n+2$ derivative is not. This singularity causes spectral methods to converge algebraically[90]. The even-n analytic rate of convergence is $\mathrm{p}^{-(4n+4.5)}$ for Legendre polynomials[1].

Our two nonlinear equilibria use a quadratic F profile which produces an odd source term, $FF' \sim \psi^3$.

---

[1] The asymptotic rate of convergence calculated in Reference [90] is for Chebyshev polynomials. The algebraic rate of convergence for Legendre polynomials is smaller than that for Chebyshev polynomials by 1/2[84].

This term produces a solution that is nonsingular in the corner. It is the only source term for the constant pressure equilibrium and geometric convergence is expected. The cubic pressure equilibrium has a source of the form $\mu_0 P' \sim \psi - \psi^2$. Here the quadratic term introduces a weak singularity of the from $\rho^6 \ln \rho$, so algebraic convergence at the rate $\mathrm{p}^{-12.5}$ is expected.

Our results with the FRC and Spheromak equilibria are also consistent with this analysis. These equilibria have source terms that are proportional to ψ^1, and thus their solutions are expected to be nonsingular in the corners. The Solov'ev equilibrium is generated by specifying a spatially varying ψ along the boundary to match a smooth analytical solution. The derivation presented in the Section 3.2.3 is for the case with homogeneous Dirichlet conditions along the physical surfaces and does not apply.

3.2.3 Analysis of the Grad-Shafranov Equation Near a Corner

The behavior of the Grad-Shafranov equation near the corners of our domain's cross-section is analyzed to explain the convergence properties of the nonlinear equilibria studied in Section 3.2.2. These equilibria use the profiles $F = \left(1 - \hat{\psi}\right)^2$ and $\mu_0 P = \left[1 - \hat{\beta}\left(3\hat{\psi}^2 + 2\hat{\psi}^3\right)\right]$ where $\hat{\beta}$ is 0 for the constant pressure equilibrium and 1 for the cubic pressure equilibrium. The homogeneous boundary condition $\psi = 0$ is used, and the normalized flux simplifies to $\hat{\psi} = 1 - \psi/\psi_a$. Inserting these profiles into Equation 2.38 yields $\Delta^*\psi = -6\hat{\beta}R^2\left(\psi/\psi_a^2 - \psi^2/\psi_a^3\right) - 2\psi^3/\psi_a^4$.

We use the approximation $\Delta^*\psi \approx \nabla^2\psi$ in Cartesian components and treat explicit factors of R as constants. This is justified by expanding the Grad-Shafranov operator around a corner location (R_0, Z_0) and by letting $R = R_0 + r$ and $Z = Z_0 + z$. In the limit that $r \ll R_0$, the Grad-Shafranov operator behaves like a Cartesian Laplacian:

$$\Delta^* = \frac{\partial^2}{\partial r^2} - \frac{1}{R_0 + r}\frac{\partial}{\partial r} + \frac{\partial^2}{\partial z^2} \approx \frac{\partial^2}{\partial r^2} + \frac{\partial^2}{\partial z^2}. \tag{3.13}$$

To study the behavior near the corners, we use the model equation

$$\nabla^2\phi = c_1\phi + c_2\phi^2 + c_3\phi^3 \tag{3.14}$$

in a polar domain with $0 \leq \theta \leq \pi/2$ and ρ is the distance from the corner. The constants c_1, c_2, and c_3 are of order unity. Homogeneous Dirichlet boundary conditions $\phi = 0$ are applied at $\theta = 0$ and

$\theta = \pi/2$. The solution at some distance a from the corner is expected to match the global solution of the full Grad-Shafranov equation. This effectively sets the boundary condition along $\rho = a$ in our model problem.

Near the corner we expect ϕ to be small. To verify this we consider the equation $\nabla^2\phi_1 = 0$. This equation is separable with the solution $\phi_1 = \sum_i \nu_i \rho^{2i} \sin 2i\theta$. Most solutions of interest only have one maxima in θ, thus the term $\rho^2 \sin 2\theta$ is dominant. Near the corner where $\rho \ll a$, ϕ_1 is small and scales as ρ^2.

With ϵ being a small parameter of order ρ^2 near the corner, we expand $\phi = \epsilon\phi_1 + \epsilon^2\phi_2 + \epsilon^3\phi_3 + \dots$, using factors of ϵ to indicate the size of each term. We recognize that ∇^2 is order ϵ^{-1} and expand Equation 3.14 into a hierarchy of linear equations of varying orders in ϵ. The lowest order equation is $\nabla^2\phi_1 = 0$. This equation satisfies the inhomogeneous boundary condition at $\rho = a$, and all higher order equations are subject to the homogeneous boundary condition $\phi = 0$ at $\rho = a$. The next few higher order equations are

$$\nabla^2\phi_2 = c_1\phi_1 \tag{3.15}$$

$$\nabla^2\phi_3 = c_1\phi_2 + c_2\phi_1^2 \tag{3.16}$$

$$\nabla^2\phi_4 = c_1\phi_3 + 2c_2\phi_1\phi_2 + c_3\phi_1^3. \tag{3.17}$$

Equations 3.15-3.17 can be solved via integration of a common Green's Function $H(\rho, \theta; \rho', \theta')$; here ρ' and θ' are source-field coordinates that span the same domain as ρ and θ. The Green's function satisfies the equations:

$$\nabla^2 H(\rho, \theta; \rho', \theta') = \frac{1}{\rho}\delta(\rho - \rho')\,\delta(\theta - \theta'), \tag{3.18}$$

subject to the Dirichlet boundary condition $H = 0$ at $\rho = a$, $\theta = 0$, and $\theta = \pi/2$. The Green's function that satisfies Equation 3.18 is:

$$H(\rho, \theta; \rho'\theta') = \frac{-1}{\pi}\sum_{i=1}^{\infty}\frac{1}{i}\rho_<^{2i}\left(\frac{1}{\rho_>^{2i}} - \frac{\rho_>^{2i}}{a^{4i}}\right)\sin 2i\theta \sin 2i\theta', \tag{3.19}$$

where $\rho_< = \min(\rho, \rho')$ and $\rho_> = \max(\rho, \rho')$. The solution to the equation $\nabla^2\phi = f(\rho, \theta)$ is found by integrating the Green's function:

$$\phi(\rho, \theta) = \int_0^{\pi/2} d\theta' \int_0^a d\rho' \rho' f(\rho', \theta')\, H(\rho, \theta, \rho'\theta'). \tag{3.20}$$

We define F_S to be the space of functions of the form $\sum_i A_i \rho^{2\alpha_i} \sin 2\beta_i\theta$ with integer $\alpha_i \geq \beta_i \geq 0$ for each i. Similarly, F_C is the space of functions of the form $\sum_i B_i \rho^{2\alpha_i} \cos 2\beta_i\theta$ with integer $\alpha_i \geq \beta_i \geq 0$. Note that if $s, t \in F_S$ then $s \times t = r$ with $r \in F_C$, and if $p \in F_C$ then $s \times p = q$ with $q \in F_S$. Due to this cyclic nature, the product of n series in F_S results in a series in F_C if n is even, and the product is in F_S if n is odd. We note that $\phi_1 \in F_S$ thus $\phi_1^2 \in F_C$, $\phi_1^3 \in F_S$, etc.

Our perturbative approach, Equations 3.15-3.17, to solving Equation 3.14 is linear at each step, so we use superposition and integrate term by term. Integrating the two general functions $f_s = \rho^{2\alpha} \sin 2\beta\theta$ and $f_c = \rho^{2\alpha} \cos 2\beta\theta$, where α and β are integers greater than or equal to 0, provides all the necessary information.

Inserting f_s into Equation 3.20 yields:

$$\phi_s = \begin{cases} \frac{-1}{4\beta}\rho^{2\beta}\left(\ln a - \ln \rho\right) \sin 2\beta\theta & \text{if } \alpha = \beta - 1 \\ \frac{-1}{4(\alpha+1)^2 - 4\beta^2}\left(\rho^{2\beta} a^{2\alpha - 2\beta + 2} - \rho^{2\alpha+2}\right) \sin 2\beta\theta & \text{if } \alpha \neq \beta - 1. \end{cases} \tag{3.21}$$

Note that ϕ_s and all its derivatives with respect to ρ are nonsingular at $\rho = 0$ if $\alpha \geq \beta$. Also if $\alpha \geq \beta$, then $\phi_s \in F_S$. Inserting f_c into Equation 3.20 yields:

$$\phi_c = \sum_s \frac{-1}{\pi} \frac{\sin 2s\theta}{s^2 - \beta^2} g\left(\rho, a; \alpha, s\right) \tag{3.22}$$

where the summation is over positive odd s if β is even and even s if β is odd and

$$g\left(\rho, a; \alpha, s\right) = \begin{cases} \rho^{2s}\left(\ln a - \ln \rho\right) & \text{if } \alpha = s - 1 \\ \frac{s}{(\alpha+1)^2 - s^2}\left(\rho^{2s} a^{2\alpha - 2s + 2} - \rho^{2\alpha+2}\right) & \text{if } \alpha \neq s - 1. \end{cases} \tag{3.23}$$

If α and β are both even or both odd, then ϕ_c contains the term $\rho^{2\alpha+2} \ln \rho \sin\left(2\alpha + 2\right)\theta$, and its $2\alpha + 2$ radial derivative is singular at $\rho = 0$.

With $\phi_1 = \nu_1 \rho^2 \sin 2\theta$ from the dominant part of the lowest order solution, we have $\phi_1 \in F_S$. Applying Equation 3.21 shows that $\phi_2 \in F_S$. At third order, there are two sources terms, ϕ_2 and ϕ_1^2. The contribution to ϕ_3 from ϕ_2 is evaluated using Equation 3.21 and is in F_S since $\phi_2 \in F_S$. The ϕ_1^2 contribution to the source lies in F_C and includes $\nu_1^2 \rho^4 \cos 4\theta$. Evaluating this term using Equation 3.22 yields the weakly singular contribution $\rho^6 \ln \rho \sin 6\theta$. Thus if c_2 is nonzero, as is the case for the cubic pressure profile, the solution is weakly singular in the corner.

To consider the constant pressure profile, we let $c_1 = c_2 = 0$. Here Equations 3.15 and 3.16 are trivially solved and $\phi_2 = \phi_3 = 0$. The source in Equation 3.17 is $\phi_1^3 \in F_S$. Equation 3.17 is solved using Equation 3.21 giving $\phi_4 \in F_S$. The next nontrivial equation in the perturbative expansion is $\nabla^2\phi_7 = 3\phi_1^2\phi_4$. Both ϕ_1 and ϕ_4 are in F_S and the product $\phi_1^2\phi_4$ is in F_S. The term ϕ_7 is found from evaluating Equation 26 giving $\phi_7 \in F_S$. This pattern applies to all higher order equations for ϕ_i. The source in each equation for ϕ_i is composed of terms that are a product of $\phi_j\phi_k\phi_l$ with $j+k+l = i-1$. If ϕ_j, ϕ_k, and ϕ_l are in F_S, then the product $\phi_j\phi_k\phi_l$ is also in F_S. Equation 3.21 produces the result that $\phi_i \in F_S$. From the homogeneous equation $\phi_1 \in F_S$, and it follows from induction that all $\phi_i \in F_S$ and the solution to $\nabla^2\phi = c_3\phi^3$ is in F_S and nonsingular.

Perturbative expansions similar to Equations 3.15-3.17 can be used to provide the general result for any source that is a monomial ϕ^n of the dependent variable. If n is even then $\phi_1^n \in F_C$. The solution follows from Equation 3.22, and it is weakly singular in the corner. The dominate singularity is $\rho^{2n+2}\ln\rho\sin(2n+2)\,\theta$. This agrees with the well known weak singularity, $\rho^2\ln\rho\sin 2\theta$, for Poisson's equation with a constant source[84].

If n is odd, similar to the uniform pressure case, all source terms in the equation for $\nabla^2\phi_i$ are a sum of terms of the form $\phi_j\phi_k\phi_l\ldots$ where there are n factors in each term, and $j+k+l+\cdots = i-1$. If each of the odd-n factors are in F_S, then the product is in F_S. It follows from Equation 3.21 that $\phi_i \in F_S$. The starting point is $\phi_1 \in F_S$, and it follows from induction that all $\phi_i \in F_S$ if n is odd, hence the solution $\phi \in F_S$ and nonsingular at the corner.

These results are unchanged when using the full expansion for the boundary condition at $\rho = a$, such that ϕ_1 has other terms in F_S besides $\nu_1\rho^2\sin 2\theta$. However, the dominant singularity for even n is higher order in ρ if $\nu_1 = 0$.

3.3 Evaluation of Mercier Stability within NIMEQ

This section describes the development of a utility that calculates the ideal, D_M, and resistive, D_R, Mercier stability criteria. The utility calculates the criteria for arbitrary meshes. FLUXGRID, one of NIMROD's preprocessors, can evaluate the Mercier criteria for flux-aligned meshes. This capability is used to benchmark the utility.

The calculation of the Mercier criteria assumes axisymmetry. This assumption greatly simplifies the field line integration that is used to evaluate flux-surface averaged quantities. The utility can evaluate the stability criteria for both axisymmetric equilibria used to seed NIMROD calculations and the evolved fields that result from nonlinear simulations. The utility gives the correct result, within numerical accuracy, when used to asses the stability of axisymmetric static equilibria. However, the utility gives only an estimate of the stability criteria when used to analyze evolved fields, since the 3-D components are neglected.

It is important to consider the representation of the Mercier criteria used in calculating the stability criteria. There are multiple representations of the Mercier criteria that are mathematically equivalent. However, some of these representations are more amenable to numerical analysis than others. NIMROD's spatial representation uses C^0 elements to represent the poloidal plane. The physical fields represented by these elements are continuous across element boundaries, but their derivatives are not. These discontinuities can cause problems with the field line integrator, which uses an adaptive step size. When integrating along the field line, the integrator compares the change in the integrand before and after a finite integration step. The integrator reduces the step size and repeats the previous step if the change in the integrand is greater than a preset tolerance. This refinement can fail if the integrand is discontinuous. Here the integrator will repeatedly reduce the step size, trying to find a spatial scale on which the discontinuity is sufficiently smooth. No such scale exists. To avoid this difficulty we choose a representation of the Mercier criteria in which all flux surfaced averaged quantities have a continuous representation in NIMROD.

The representation of the Mercier criteria given in [28] has this property:

$$D_M = \frac{P'V'}{q'^2} W_m - \frac{1}{4} \tag{3.24}$$

$$D_R = D_M + \left(\frac{1}{2} - H\right)^2 \tag{3.25}$$

$$\begin{aligned} W_m = {} & \frac{-V''}{4\pi^2} \left\langle \frac{B^2}{(RB_p)^2} \right\rangle + \frac{Fq'}{2\pi} \left\langle \frac{1}{(RB_p)^2} \right\rangle + \frac{\mu_0 P'V'}{4\pi^2} \left\langle \frac{1}{B^2} \right\rangle \left\langle \frac{B^2}{(RB_p)^2} \right\rangle + \\ & \frac{\mu_0 P'V'F^2}{4\pi^2} \left(\left\langle \frac{1}{B^2 (RB_p)^2} \right\rangle \left\langle \frac{B^2}{(RB_p)^2} \right\rangle - \left\langle \frac{1}{(RB_p)^2} \right\rangle^2 \right) \end{aligned} \tag{3.26}$$

$$H = \frac{\mu_0 P'V'F}{2\pi q'} \left(\left\langle \frac{1}{(RB_p)^2} \right\rangle - \left\langle \frac{B^2}{(RB_p)^2} \right\rangle \frac{1}{\langle B^2 \rangle} \right) \tag{3.27}$$

$$V' = \frac{2\pi q}{F \langle 1/R^2 \rangle} \tag{3.28}$$

$$q = \frac{1}{2\pi} \oint \frac{B_\phi}{RB_p} dl_p \tag{3.29}$$

$$\langle Q \rangle = \frac{\oint Q/B_p dl_p}{\oint 1/B_p dl_p}, \tag{3.30}$$

where V is the volume inside a flux surface, primes indicate derivatives with respect to ψ, and dl_p is an infinitesimal arc length parallel to the poloidal magnetic field. The field line integration is only performed in the poloidal plane since axisymmetry is assumed.

The first step in calculating the Mercier criteria is to calculate the poloidal flux function, ψ, from the toroidal current density using $\Delta^*\psi = \mu_0 R J_\phi$. This equation is solved in the weak form using a method similar to the method outlined in Section 3.1 for solving the Grad-Shafranov equation:

$$\sum_i \Lambda_i \int dV R^2 \nabla\alpha_i \cdot \nabla\alpha_j = -\int dV \mu_0 R J_\phi \alpha_j - \int dV R^2 \nabla\Lambda_0 \cdot \nabla\alpha_j, \tag{3.31}$$

where all quantities are defined in Section 3.1. After solving this equation for Λ, the flux is calculated using $\psi = R^2\Lambda$.

The next step after calculating the poloidal flux function ψ is to evaluate the flux-surface averaged quantities. Field line integrations are performed in the poloidal plane in order to evaluate these quantities. The assumption of axisymmetry allows us to ignore the toroidal direction. Here the integration following the poloidal magnetic field along a closed flux surface will return to the starting point after one complete revolution around the magnetic axis.

There are 8 different quantities that have to be calculated using field line integration: 6 flux surface averaged quantities, the flux surface normalization $\oint dl_p/B_p$, and the safety factor q. The different integrals are evaluated simultaneously using the implicit Adams method within the LSODE software package[91]. Field line integrations are performed on a multitude of flux surfaces starting near the magnetic axis and moving radially outwards. The field line integrations are repeated on one flux surface after another until a field line leaves the computational domain. This marks the beginning of the open flux region, and the previous flux surface is taken to be the last closed flux surface.

The last step, before assembling the Mercier criteria, is to calculate V'', q', P', and F'. These ψ derivatives are calculated using a central finite difference operator:

$$P'^{i} = \frac{P^{i+1} - P^{i-1}}{\psi^{i+1} - \psi^{i-1}}, \tag{3.32}$$

where i is the index of the flux surface. The functions $F\left(\psi\right)$ and $P\left(\psi\right)$ are evaluated for each flux surface at the first point used to seed the field line integration.

The finite difference calculation of the derivatives introduces some error in the final calculation of the Mercier criteria. This is particularly noticeable near the magnetic axis when q' is small. Here small errors in q' are greatly magnified due to the fact that D_M scales as $1/q'^2$. Cubic splines were investigated as a alternative method to calculating the derivatives; however, they were problematic.

After calculating all the necessary quantities, the utility calculates the stability criteria using Equations 3.24-3.30.

The Mercier utility is tested using a Solov'ev equilibrium with constant $\mu_0 P' = -0.177\,\mathrm{T}^2/\mathrm{Wb}$ and uniform $F = RB_\phi = 3\,\mathrm{Tm}$ $(FF' = 0)$. The ideal and resistive stability criteria are calculated on a flux aligned mesh using FLUXGRID. The same equilibria is generated on a rectangular non-aligned mesh using NIMEQ, and then the stability criteria are evaluated using the new utility.

Table 4 shows a comparison of the stability criteria calculated using FLUXGRID and the new utility. The values of D_M and D_R are shown for several values of $\rho = \sqrt{\hat{\psi}}$, where $\hat{\psi} = 0$ at the magnetic axis, and $\hat{\psi} = 1$ at the last closed flux surface. The two calculations agree to within 1% across the entire domain. The stability criteria calculated using the new utility are always slightly greater than the stability criteria calculated using FLUXGRID. The difference between these two results is likely due small

$\rho = \sqrt{\psi}$	D_M FLUXGRID	D_M utility	D_R FLUXGRID	D_R utility
0.2	-6.700	-6.651	-6.675	-6.627
0.4	-2.194	-2.184	-2.175	-2.166
0.6	-1.321	-1.316	-1.313	-1.308
0.8	-0.9715	-0.9681	-0.9701	-0.9667
0.9	-0.8564	-0.8530	-0.8563	-0.8530

Table 4: Comparison of the Mercier stability criteria calculated using the old utility in FLUXGRID which only works for flux-aligned meshes, and the new utility which works for arbitrary meshes.

inaccuracies in identifying the magnetic axis and the separatrix. The normalization used to calculate ρ is dependent on the flux on axis and at the separatrix. Small errors in the value of flux at these two locations will lead to slightly different definitions of the radial coordinate ρ. Slight differences in the definition of ρ will shift the curves of $D_M(\rho)$.

In this particular equilibrium the parameter H, defined in Equation 3.27, ranges from approximately 0.65 near the magnetic axis to approximately 0.5 near the separatrix. The resistive stability criteria is related to the ideal stability criteria by $D_R = D_M + (1/2 - H)^2$. Throughout the entirety of the domain, H is farily close to 1/2 and the ideal and resistive stability criteria don't differ by a substantial amount.

In conclusion, we have developed a new utility that calculates the ideal and resistive Mercier stability criteria for arbitrary meshes. The utility assumes axisymmetry, but it can be used to assess the stability of both initial equilibria and evolved nonlinear states. Capability previously existed within NIMROD to calculate the stability for flux-aligned meshes. This capability is also limited in that it can only evaluate the stability of an initial equilibrium, since the nonlinear evolution of a perturbation will lead to a non-aligned state. A comparison between the two utilities show that they agree to within 1%.

3.4 NIMEQ Conclusion

A new Grad-Shafranov solver has been implemented using 2-D spectral elements. To our knowledge this is the first code to use spectral elements to solve the Grad-Shafranov equation. Unlike many equilibrium codes designed specifically for tokamaks, NIMEQ accounts for regularity at the geometric axis. This affords us additional generality allowing for the modeling of compact devices in addition to tokamaks and other toroidal configurations. Our spheromak and FRC equilibria contain the geometric axis in their domain and provide tests of regularity. Highly accurate solutions of ψ and $\vec{B}$ with numerical errors on the order 10^{-13} or smaller are obtained. A spectral error based on the truncation error of the spectral element expansion is defined. This error reproduces the same qualitative behavior observed in the numerical error in our first three tests, but it does not require knowledge of the exact solution.

The equilibria considered in this chapter are relatively simple and allow direct comparison between numerically calculated equilibria and analytic solutions of the Grad-Shafranov equation. However, NIMEQ is routinely used to generate spheromak equilibria with currents on the open flux outside of the separatrix. It has also been used to generate tokamak equilibria with steep pressure gradients for the study of edge localized modes [92], and it has been used to investigate spherical torus equilibria driven by coaxial helicity injection [93].

We close by highlighting the power of the spectral element representation over traditional finite elements. Consider the FRC equilibrium, where a 128×128 element mesh with 2nd order polynomial elements produces a numerical error in ψ of 1.06×10^{-8}. This mesh has approximately $100,000$ degrees of freedom. The numerical error in ψ for a 2×2 mesh with 10-th order elements is 3.83×10^{-9}. This mesh has approximately 500 degrees of freedom. Although the matrix for the high-order computation is less sparse than with the low-order approach, the smaller system size reduces the CPU time to solution by a factor of 400 on a serial laptop.

Chapter 4

Linear Stability Analysis

This chapter considers the linear stability of SSPX relevant equilibria. We first show calculations for two different families of decaying spheromak equilibria. These equilibria are ideal interchange unstable at conditions relevant to the freely decaying and controlled decay phases of SSPX discharges. Calculations show that the extended MHD effects captured by the two-fluid Ohm's law and ion gyroviscosity significantly reduce the growth rate of high-n modes. However, the stabilization of the low-n modes is weak, and in some cases extended MHD effects increase the growth rate.

The linear stability of interchange modes in a periodic screw pinch is studied to better understand this lack of stabilization of the low-n modes. This set of equilibria approximates decaying spheromaks and has previously been used to study spheromak stability[78][79]. Extended MHD effects stabilize the interchange mode at small Hall parameter ($\Lambda = d_i/a = 1/\tau_a\Omega_i$), but a second instability exists at moderate Hall parameter. This second instability grows at a rate comparable to the MHD interchange mode. This mode is dominant at experimentally relevant Hall parameters when $T_i = T_e$ is assumed. However, the onset of this second mode is delayed to higher Hall parameter when T_i and T_e are evolved independently. Here the extended MHD effects have a significant stabilizing effect at experimentally relevant Hall parameters.

An extended MHD analysis of the gravitational interchange mode is performed in slab geometry to better understand the nature of this secondary instability. The analysis uses the dispersion relation derived by Zhu et al. [36]. The two-fluid Ohm's law introduces an ion drift wave that interacts with the gravitational interchange to produce a new instability at moderate Hall parameters. This model also exhibits additional instabilities that only exist at large Hall parameters, where the extended MHD model isn't valid. The growth rate of these unphysical instabilities greatly exceeds that of the MHD g-mode. They are a concern for codes that use the extended MHD model.

4.1 First Series of Decaying Spheromak Equilibria

Decaying spheromak equilibria are created with centrally peaked pressure and parallel current density profiles in a cylindrical flux conserver with a height of 0.5 m and a radius of 0.5 m. Equilibria are constructed using quadratic $P(\psi)$ and $F(\psi)$ profiles in the closed flux region. $F(\psi)$ is linear in the open flux region to allow for currents on the open field, but $P(\psi)$ is constant in this region. A deuterium plasma is used, and unless stated otherwise calculations are performed without ion flow and with B_ϕ =0.49 T, $S = 10^5$, $Pm = 0.01$, τ_A =4.78 × 10^{-7} s, $T_i = T_e$, and uniform n =5 × 10^{19} m^{-3}. Figure 10 shows the safety factor, q, and parallel current density, λ, as functions of the normalized flux function, ψ, at $\beta = 10.1\%$. The magnetic axis is located at $\psi = 0$, and the last closed flux surface is located near $\psi \approx 0.6$. The safety factor has a local maximum on the magnetic axis equal to $q = 0.582$, it decreases to its minimum $q = 0.544$ near $\psi \approx 0.45$, and then it diverges at the separatrix. Outside of the separatrix, $\psi > 0.6$, the field lines are open and q isn't well defined. These profiles are characteristic of high temperature SSPX equilibria where the q-profile lies between 1/2 and 2/3, avoiding low-order resonances, and λ is centrally peaked.

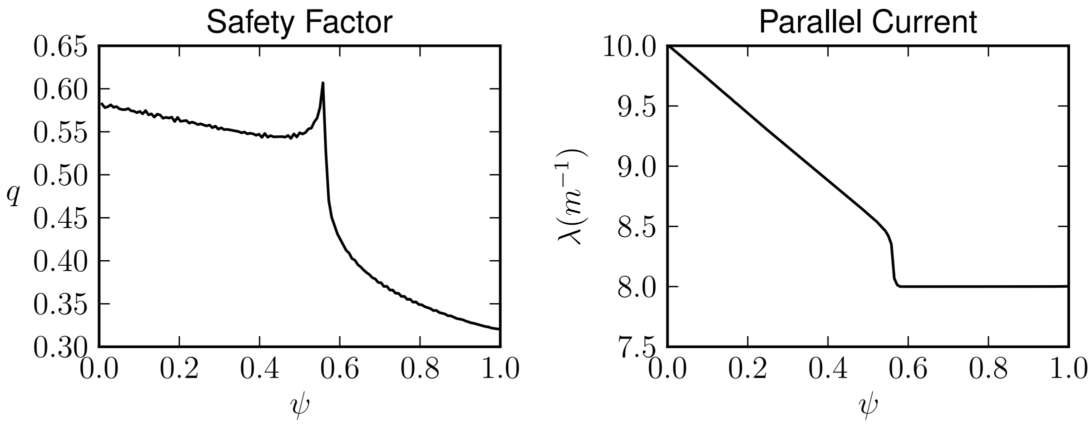

Figure 10: Safety factor q and parallel current density λ profiles for the decaying spheromak equilibrium with $\beta = 10.1\%$.

These spheromak equilibria are found to be unstable to ideal interchange modes. The linear growth rate of the first few low-n modes are shown in Figure 11 as a function of the equilibrium β. All the modes are stable in the absence of any pressure gradients. Introducing a pressure gradient destabilizes resonant modes, and their growth rates scales nearly linearly with pressure. This linear scaling is indicative of pressure-driven instabilities. Numerical convergence is verified by increasing the spatial and temporal resolution. The numerically calculated growth rates are accurate to within 2%.

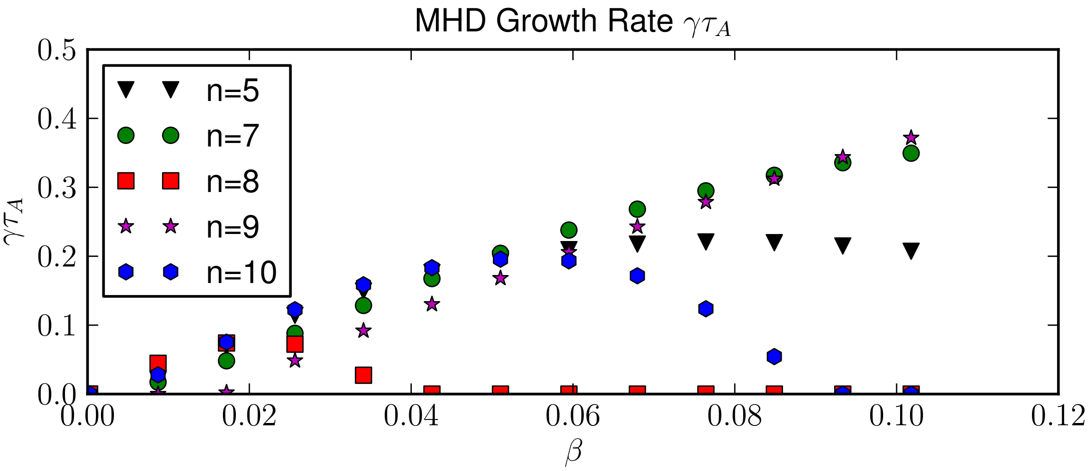

Figure 11: Resistive MHD growth rates scale with β.

The departure from purely linear scaling is due to changes in the safety factor profile that results from increasing the pressure. Increasing the pressure decreases q across the entire domain. At $\beta \lesssim 5\%$ q is greater than 3/5 at the magnetic axis. Here both the $n = 5$ $m = 3$ and the $n = 10$ $m = 6$ modes are resonant. These modes are unstable and have similar growth rates. Increasing β decreases q, and eventually the safety factor at the magnetic axis drops below 3/5. When this happens the $n = 5$ and $n = 10$ modes become non-resonant. Beyond this point, the growth rate of the $n = 5$ mode is nearly constant independent of β, while the growth rate of the $n = 10$ decreases with increasing β.

Similarly, at small β the minimum value of safety factor, q_{min}, is greater than 5/9, and the non-resonant $n = 9$ $m = 5$ mode is stable. Increasing β above 2% causes q_{min} to drop below 5/9, the $n = 9$ mode goes unstable as it becomes resonant, and its growth rate increases linearly with β.

The growth rates of several modes over a range of Lundquist numbers are shown in Figure 12 for $\beta = 10.1\%$. These growth rates are not sensitive to the resistivity at experimentally relevant S. This indicates ideal behavior. An approximate change of 7% is observed for the $n = 5$ mode as S is varied

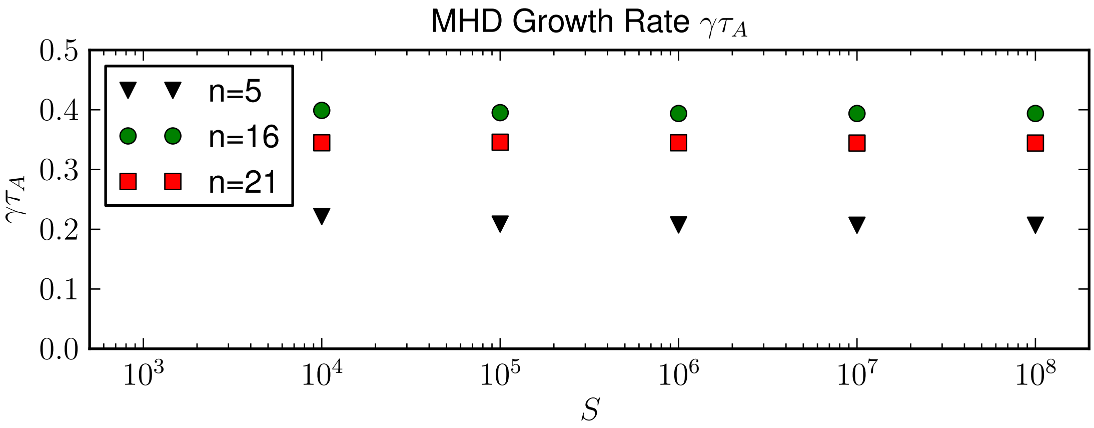

Figure 12: Resistive MHD growth rates are insensitive to the resistivity indicating ideal behavior.

from 10^4 to 10^8. Most of this change occurs at small S where the growth rate increases with S. The higher-n modes are less sensitive to S; the $n = 16$ growth rate varies by 1% over the same range in S, and the variation in the $n = 21$ growth rate is less than 1%. A similar scan of the viscosity and thermal conductivity shows little variation of the growth rates if the dissipation coefficients are sufficiently small. However, increasing both the thermal conductivity and the viscosity beyond a critical threshold has a stabilizing effect.

Figure 13 shows the spectrum of unstable modes for $\beta = 10.1\%$. Only the most unstable mode for each toroidal mode number is shown. We identify different "bands" of modes, indicated by the different colors, to add clarity. Within each band the radial distance of the mode resonant surface to the magnetic axis increases with the toroidal mode number. In a particular band, modes with smaller mode numbers are located near the magnetic axis, and modes with larger mode numbers are located near the separatrix. Modes located near the magnetic axis or the separatrix have smaller growth rates than modes located in the middle where the pressure gradients are the steepest. Modes in different bands that are resonant on the same surface have similar growth rates.

The linear calculation is repeated using the extended MHD model that includes both ion gyroviscosity and the two-fluid Ohm's law. The results are shown in Figure 14 (for clarity the different bands are plotted in different graphs). In extended MHD the unstable modes have both a real (drifting) frequency

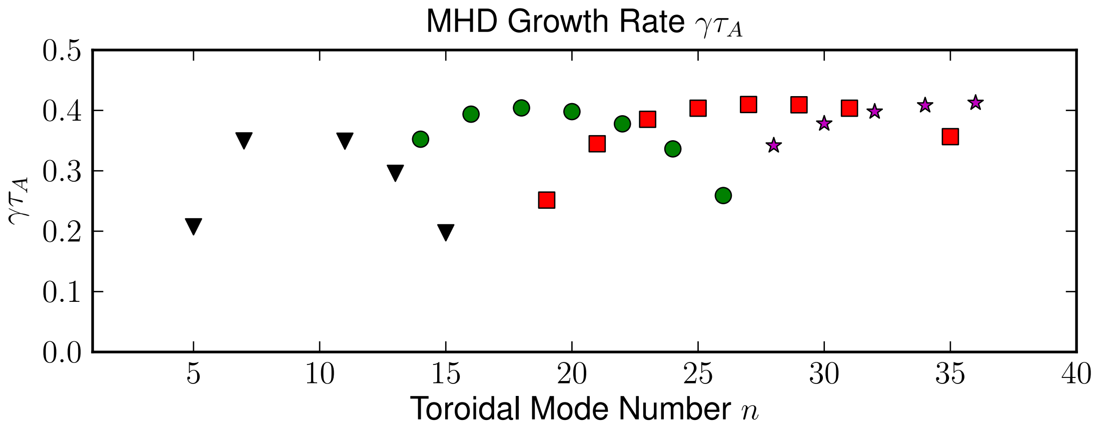

Figure 13: The MHD spectrum is composed of distinct bands of modes.

and an imaginary (growing) frequency. The modes are observed to drift in the electron diamagnetic direction. The drift frequency is greatest for modes located near the magnetic axis, and it decreases with the radius of the mode rational surface. The drift frequencies of the first band of modes, Figure 14A, are small compared to the MHD growth rates. Here extended MHD has a minimal effect on the linear growth rate. The drift frequencies of the second band of modes, Figure 14B, are comparable to the MHD growth rates for modes located near the magnetic axis, and a slight reduction in the growth rate is observed. The drift frequency is small for the modes located near the last closed flux surface, and their growth rates are minimally altered. In the third and fourth bands, Figures 14C-D, the frequencies of the modes located near the magnetic axis exceed their MHD growth rates, and a significant reduction in the growth rate, relative to the MHD growth rate, is observed. A 71% reduction is observed for the $n = 18$ $m = 10$ mode, and a 76% reduction is observed for the $n = 28$ $m = 16$ mode. The real frequencies of modes located near the separatrix are still less than their MHD growth rates, and the growth rates are only slightly reduced. Complete stabilization is not observed for any of the modes.

The growth rates are calculated for a smaller range of mode numbers using two simplified models. The gyroviscous model uses the ion gyroviscous stress in the momentum equation with MHD Ohm's law, and the two-fluid model uses the two-fluid Ohm's law but neglects ion gyroviscosity. The linear growth rates calculated using the two models are shown in Figure 15 for the second band of modes. The

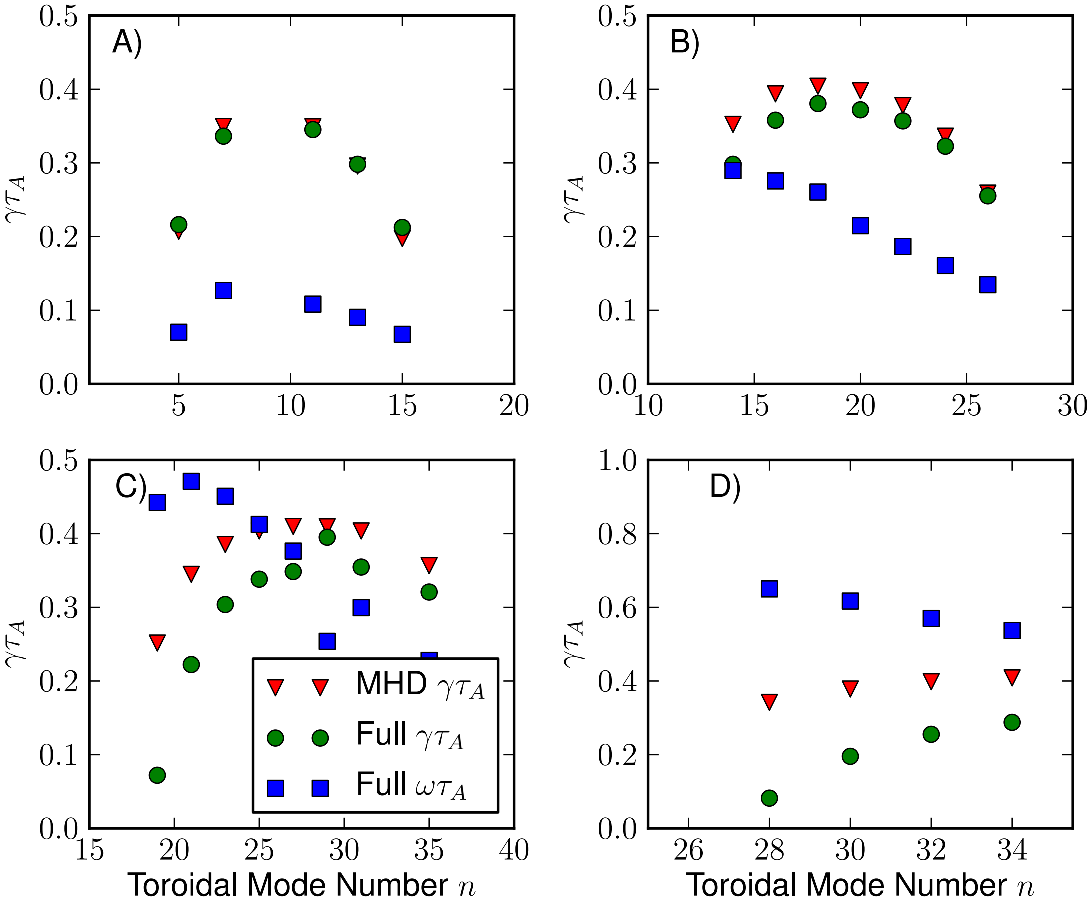

Figure 14: Extended MHD physics reduces the growth rates of the mode for sufficiently large toroidal mode number. Each graph represents a different band of modes shown in Figure 13 A) is the black band, B) green, C) red, and D) purple.

two-fluid model is more stable than MHD near the magnetic axis where the real frequency is largest, but less stable near the separatrix where the real frequency is small. The gyroviscous model is always more stable than the MHD model.

Near the magnetic axis, the most stable model is the full model that includes both effects. Here both the gyroviscous and two-fluid models are more stable than MHD. However, near the separatrix the gyroviscous model is more stable than the full model. Here the two-fluid model is less stable than MHD. The real frequency of the full model, Figure 15B, is always greater than the individual frequencies of the two simplified model.

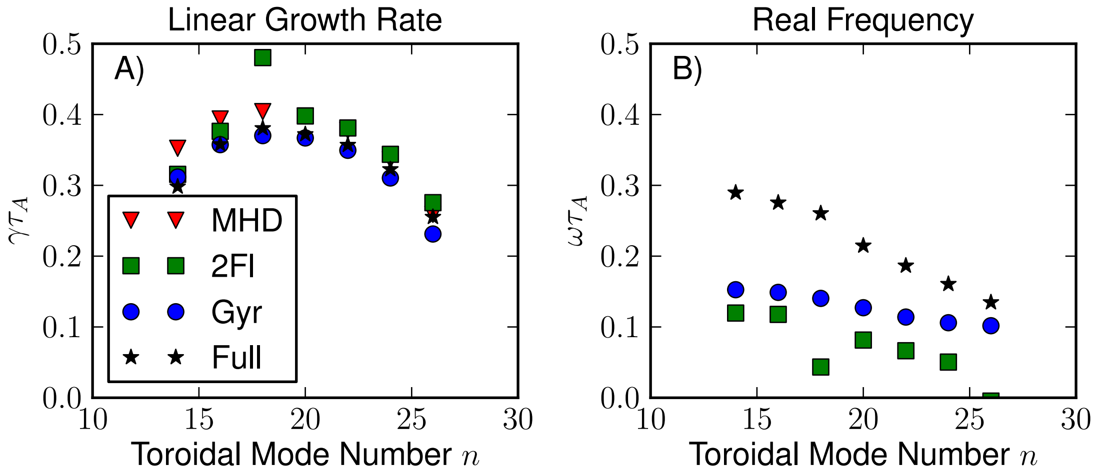

Figure 15: Linear growth rates ($\gamma\tau_A$) for one band of modes using the MHD, gyroviscous, two-fluid, and full extended MHD models.

The calculation of the linear growth rates using the resistive and extended MHD models is repeated using an equilibrium with a non-uniform density profile. This is motivated by the extended MHD g-mode dispersion relation derived by Zhu et al. [36], where the stabilization of the g-mode model is sensitive to the equilibrium density and temperature gradients. In this second series of calculations the equilibrium density profile is calculated such that P/ρ^{γ_s} is constant across the domain, where $\gamma_s = 5/3$ is the ratio of specific heats.

The linear growth rates for the first two bands of modes are shown in Figure 16. Here the growth rates and real frequencies are normalized using the Alfven time calculated with the value of the number density at the magnetic axis. This Alfven time is the same Alfven time used in previous calculations. As before we identify different bands of modes, where the modes with the larger toroidal mode number are resonant farther from the magnetic axis. The MHD growth rates of the modes in the nonuniform density equilibria are greater than the growth rates in the uniform density equilibria. This is understood to be the result of the lower average density and thus reduced inertia. The peak growth rate, for a given band of modes, is shifted outwards towards the separatrix where density is the smallest.

The extended MHD effects have the greatest effect on modes located near the separatrix where

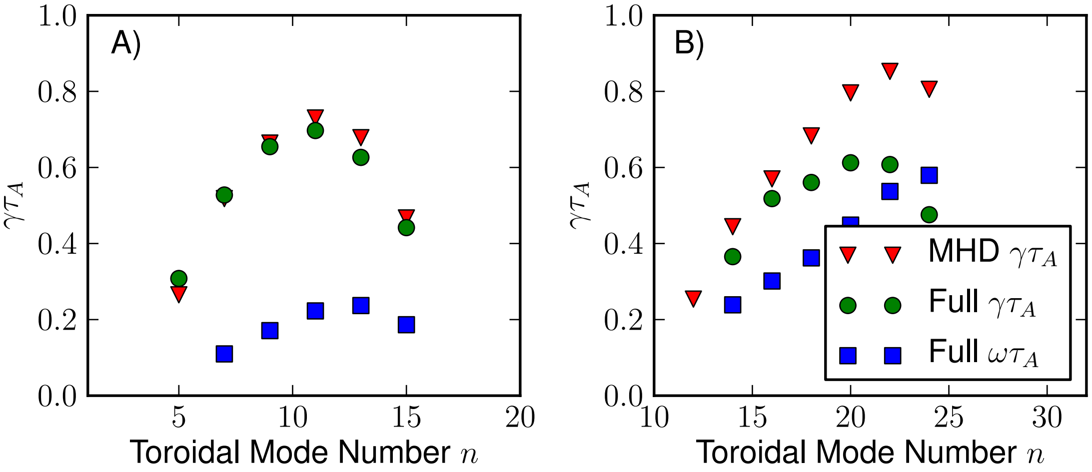

Figure 16: Calculated linear growth rates using the background density calculated assuming $P \propto n^\gamma$ for both the resistive MHD and full MHD models.

the real frequency is largest. The density is smallest near the separatrix, and it makes sense that the extended MHD effects, which scale inversely with the density, are most significant in the low density region. This is in contrast to the uniform density equilibrium where the extended MHD effects have the greatest impact on modes located near the magnetic axis. The net stabilization is comparable between the two different equilibria, and complete stabilization is not observed for any mode in either case.

A third series of calculations is performed to investigate the effects of equilibrium ion flow. These calculations use a uniform density profile, and an ad hoc ion diamagnetic flow is added to the equilibrium. The ion diamagnetic flow is calculated using $\vec{V}_0 = \frac{\vec{B}\times\nabla P_i}{neB^2}$. We assume that the flow has a negligible effect on the force balance and use a Grad-Shafranov solution for static conditions. The flow is then calculated from these quantities.

The growth rates with flow are shown in the Figure 17 for the resistive MHD and the full extended MHD models. The equilibrium flow reduces the growth rates of the resistive MHD modes, and it gives these modes a real frequency. The stabilization due to the diamagnetic flow is greater than the stabilization for extended MHD without flow. This stabilization is slightly reduced when extended MHD is used with flow, due to a cancellation of drifts. Extended MHD introduces drifts that propagates in the electron diamagnetic direction, opposite to the applied ion diamagnetic flow. When both effects are

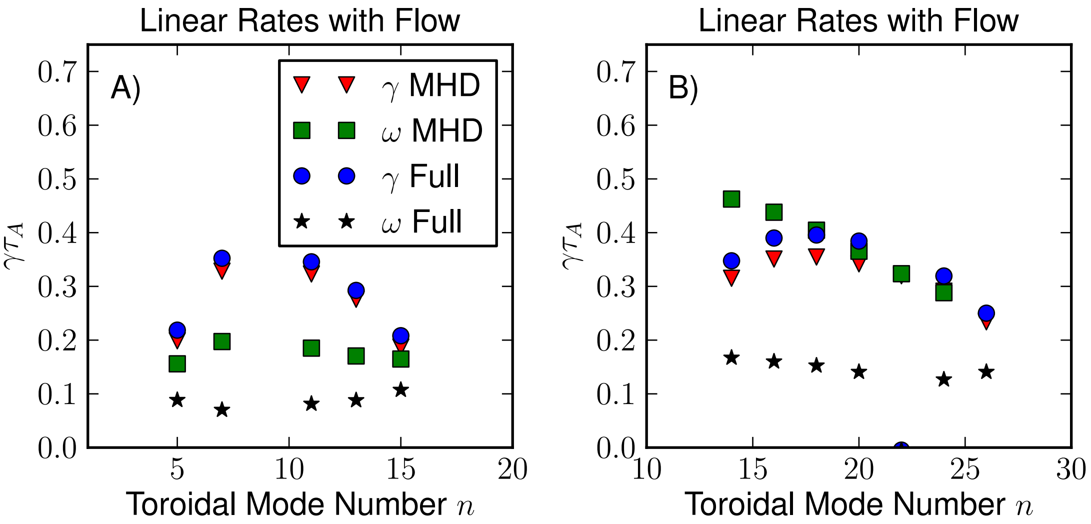

Figure 17: Linear growth rates with an equilibrium ion diamagnetic flow for the resistive MHD and full extended MHD models.

included the resulting drift frequency is reduced and the net stabilization is reduced.

In summary, these decaying spheromak equilibria are susceptible to ideal interchange modes for a wide range of pressures. The extended MHD effects are studied in a high-β equilibrium characteristic of the hottest spheromaks observed in SSPX. Extended MHD has a significant stabilizing effect on the high-n modes. For instance the growth rate of the $n = 28$ mode is reduced by 76%. However, complete stabilization is not observed in any case, and the extended MHD effects have minimal impact on the low-n modes. The low-n modes have the greatest impact on the magnetic field topology in nonlinear conditions. Additionally, the extended MHD model loses is validity for these high-n modes where the small Larmor radius assumption breaks down. We also note that the analysis of the Mercier stability parameter for this high-β case shows that $D_M > 20$ across the entire domain. This is consistent with the large growth rates that are observed and the lack of extended MHD stabilization[30][31].

In the next section we study of a second class decaying spheromak equilibria that more accurately represent SSPX equilibria. The effects of extended MHD are studied for a range of pressures.

4.2 Equilibria Representative of SSPX Discharge 14590

In the previous section all of the extended MHD calculations are performed at pressure that is characteristic of the hottest spheromaks in SSPX. Here we consider the extended MHD effects over a range pressures. The equilibria use a bias poloidal flux that represents the applied flux in gun driven spheromaks. The $F(\psi)$ profile is calculated from equilibrium reconstructions, and the pressure profile is tailored to be interchange stable near the axis and near the edge. As before, these calculations are performed in a cylindrical flux conserver with a rectangular cross-section.

The equilibrium parameters are based off of a reconstruction of SSPX discharge 14590[10]. This discharge was one of a series of optimized discharges with low fluctuations and good core confinement. This discharge reached a peak electron temperature of 350 eV, but the peak temperature varied from 200 eV to 400 eV in similar discharges.

4.2.1 Grad-Shafranov Equilibrium

NIMEQ is used to a construct equilibria representative of SSPX shot 14590. Computations represent the SSPX flux conserver using a toroidally symmetric rectangular cross-section with a height of 0.5 m and radius of 0.5 m. The flux along the bottom of the domain is specified by the function:

$$\psi(R,0) = \begin{cases} \frac{\psi_{gun}}{R_{gun}}\left(2R_{gun}^2 R^2 - R^4\right) & R \leq R_{gun} \\ \frac{\psi_{gun}}{R_{gun}} & R > R_{gun}. \end{cases} \tag{4.1}$$

The flux along the outboard wall is:

$$\psi(0.5,Z) = \begin{cases} \frac{\psi_{gun}}{Z_m^2}\left(Z - Z_m\right) & Z \leq Z_m \\ 0 & Z > Z_m. \end{cases} \tag{4.2}$$

The flux along the top of the flux conserver is $\psi(R,0.5) = 0$. This parameterization of the flux is designed to mock SSPX's gun region across the bottom of the domain. All equilibria use R_{gun} =0.35 m, Z_m =0.1 m, and Ψ_0 =4.093 mWb. The vacuum ψ and the corresponding $\vec{B}_p$ are shown in Figure 18.

Experimental reconstructions of the SSPX equilibria during quiescent phases of the discharge find that the parallel current density is best parameterized as a quadratic polynomial, $\lambda = \lambda_0\left(1 + \alpha\hat{\psi}^2\right)$,

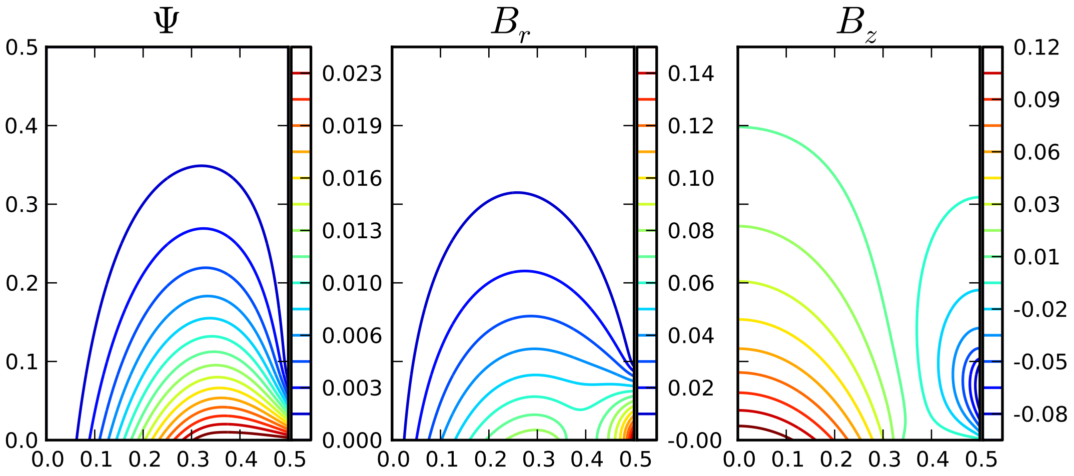

Figure 18: Contours of the vacuum poloidal flux Ψ, radial magnetic field B_r, and vertical magnetic field B_z. The poloidal flux is constant across the gun region spanning $R = 0.35\,\mathrm{m}$ to $R = 0.5\,\mathrm{m}$ along the bottom of the domain.

in the closed flux region [10]. The reconstructions treat λ as a constant in the open flux region, $\lambda = \lambda_e$. Here λ_0 is the value of the parallel current density at the magnetic axis, and λ_e is the value in the edge. The fitting parameter α is positive for driven equilibria, and it is negative for decaying equilibria.

A cubic profile for $F(\psi)$ is used to reproduce this λ parameterization:

$$F(\psi) = \begin{cases} -\lambda_e \psi & \text{open flux} \\ F_0 - \lambda_0 \Delta\psi \left(\frac{\alpha}{3} \left(\hat{\psi}^3 - 1 \right) + \left(\hat{\psi} - 1 \right) \right) & \text{closed flux,} \end{cases} \tag{4.3}$$

where $\Delta\psi = (\psi_s - \psi_0)$ is the difference between flux at the separatrix and the flux at the magnetic axis. Taking the derivative of $F(\psi)$ with respect to ψ yields the quadratic profile $F'(\psi) = -\lambda_0 \left(1 + \alpha \hat{\psi}^2 \right) \approx -\lambda$ in the closed flux region and $F'(\psi) = -\lambda_e$ in the open flux region. The approximation $F'(\psi) = -\lambda$ is exact when $P'(\psi) = 0$. The parameter $F_0 = -\lambda_e \psi_s$ is chosen to enforce continuity of F across the separatrix. The constant α is calculated using $\alpha = \lambda_e/\lambda_0 - 1$. Equilibria are generated using the reported values from an experimental reconstruction: $\lambda_0 = 9.69\,\mathrm{m}^{-1}$, $\lambda_e = 8.86\,\mathrm{m}^{-1}$, $\psi_0 = 115.50\,\mathrm{mWb}$, and $\psi_s = 25.72\,\mathrm{mWb}$ [10].

The pressure profile is modeled using the quartic function:

$$P\left(\psi\right)=\begin{cases}P_e & \hat{\psi}>0.9\\ \Delta P\left(1-4\left(\frac{\hat{\psi}}{0.9}\right)^3+\left(\frac{\hat{\psi}}{0.9}\right)^4\right)+P_0 & \hat{\psi}\leq 0.9,\end{cases} \tag{4.4}$$

where ΔP is the difference between the pressure on axis and the pressure at the wall . This pressure profile is tailored to ensure stability to pressure driven modes near the magnetic axis and near the separatrix. The pressure gradient has a cubic dependence on $\hat{\psi}$ near the magnetic axis, this ensures that the ideal Mercier stability parameter, D_M, asymptotes to zero at the magnetic axis when q' linearly asymptotes to zero at the axis. The pressure is constant on the open field $\hat{\psi} > 1$ and in a small region of closed flux near the separatrix, $1.0 > \hat{\psi} > 0.9$.

Near the separatrix the safety factor has a local minimum, and the shear goes through zero. The shear in this region is too weak to stabilize interchange modes. Prescribing a zero pressure gradient across the region $1.0 > \hat{\psi} > 0.9$ stabilizes local interchange modes where the shear is weak.

The pressure in the open flux region is calculated assuming a temperature of 25 eV and density of $5 \times 10^{19}\,\mathrm{m}^{-3}$. These values are characteristic of the edge of SSPX discharges. A family of equilibria are generated with peak pressures ranging from 800 Pa to 5600 Pa. A uniform density is used and pressure gradients are entirely due to temperature gradients. The corresponding peak temperatures range from 50 eV to 350 eV. Table 5 list a number parameters for these equilibria. All values are calculated using the magnetic axis as a reference point.

The minor radius of the plasma is approximately 0.25 m. The Hall parameter, Λ, which is the ion skin depth, d_i, normalized by this radius, is about 0.13 for all equilibria, independent of the pressure. The normalized ion gyro-radius is order $\sqrt{\beta}$ smaller than the Hall parameter, and its value at the magnetic axis ranges from 0.005 to 0.0142 for the different equilibria.

The tabulated electrical diffusivity, η/μ_0, is the Spitzer diffusivity calculated using the electron temperature on axis. The resistive diffusion time, τ_R, and Lundquist number, S, are calculated using this diffusivity. However, the electrical diffusivity used in linear calculations (presented below) is specified to be a uniform constant independent of the temperature. These tabulated values of η/μ_0, τ_R, and S illustrate the range of physically relevant parameters.

The safety factor, pressure, and Mercier stability parameter are shown for three equilibria in Figure

	3-5-0	3-5-1	3-5-2	3-5-3	3-5-4	3-5-5	3-5-6
P_{axis} (Pa)	5570	4775	3979	3183	2387	1592	796
T_{axis} (eV)	348	298	248	199	149.0	99.3	49.7
B_{axis} (T)	0.536	0.536	0.537	0.537	0.538	0.539	0.539
τ_A (μs)	0.303	0.302	0.302	0.302	0.301	0.301	0.301
η/μ_0 $\left(\mathrm{m}^2/\mathrm{s}\right)$	0.0634	0.0799	0.105	0.147	0.226	0.415	1.17
τ_R (s)	3.94	3.13	2.38	1.70	1.11	0.602	0.213
S	1.30×10^7	1.04×10^7	7.88×10^6	5.65×10^6	3.67×10^6	2.00×10^6	7.09×10^5
β_{axis}	4.88%	4.17%	3.47%	2.77%	2.08%	1.38%	0.69%
d_i (cm)	3.22	3.22	3.22	3.22	3.22	3.22	3.22
ρ_i (cm)	0.355	0.329	0.300	0.268	0.232	0.189	0.134

Table 5: Summary of equilibria properties for a hydrogen plasma using $n = 5 \times 10^{19}\,\mathrm{m}^{-3}$ and $T = T_i = T_e$.

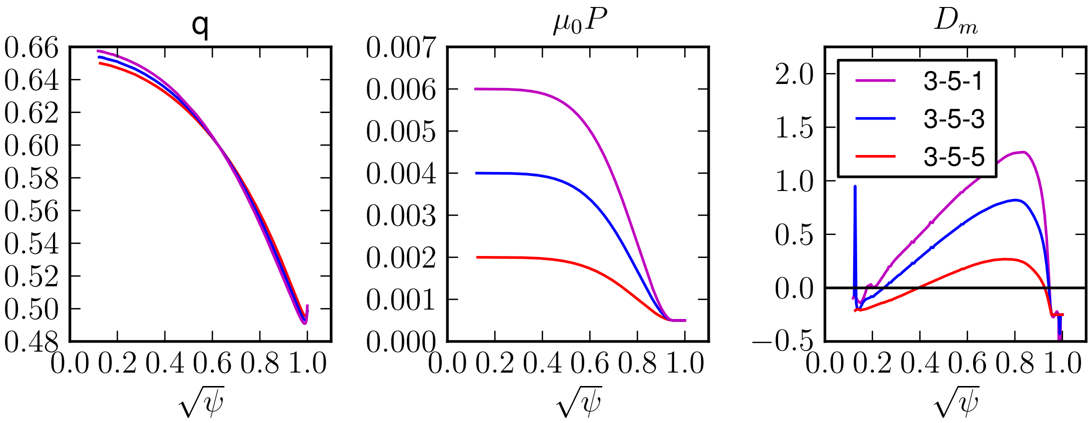

Figure 19: The safety factor, q, pressure profile, $P(\psi)$, and Mercier stability parameter D_M for the 3-5-1 equilibria.

19. Here the magnetic axis is located at $\sqrt{\psi} = 0$, and the separatrix is located at $\sqrt{\psi} = 1$. As before q is strictly below 2/3, and the $n = 3$ $m = 2$ mode is not resonant. However, the minimum value of q drops below 1/2 near the separatrix, and the $n = 2$ $m = 1$ mode is resonant. The minimum value of q

decreases with increasing pressure.

The ideal Mercier stability criteria is violated even at low pressure. The 3-5-5 equilibrium, which has a peak temperature of approximately 100 eV, has a maximum stability parameter of $D_M \approx 0.27$. This Mercier parameter is small enough that the resulting instabilities should have slow growth rates and extended MHD effects are expected to be strongly stabilizing. The 3-5-1 equilibrium has a maximum stability parameter that greatly exceeds the ideal limit, $D_M \approx 1.3$. The resulting instabilities should have large growth rates, and extended MHD is expected to have a weak effect on their growth rates. The 3-5-1 equilibrium has a peak temperature of 300 eV which is still colder than the electron temperatures observed in shot 14590. Contours of the equilibrium poloidal flux, toroidal magnetic field, and pressure are shown in Figure 20 for the 3-5-1 equilibrium.

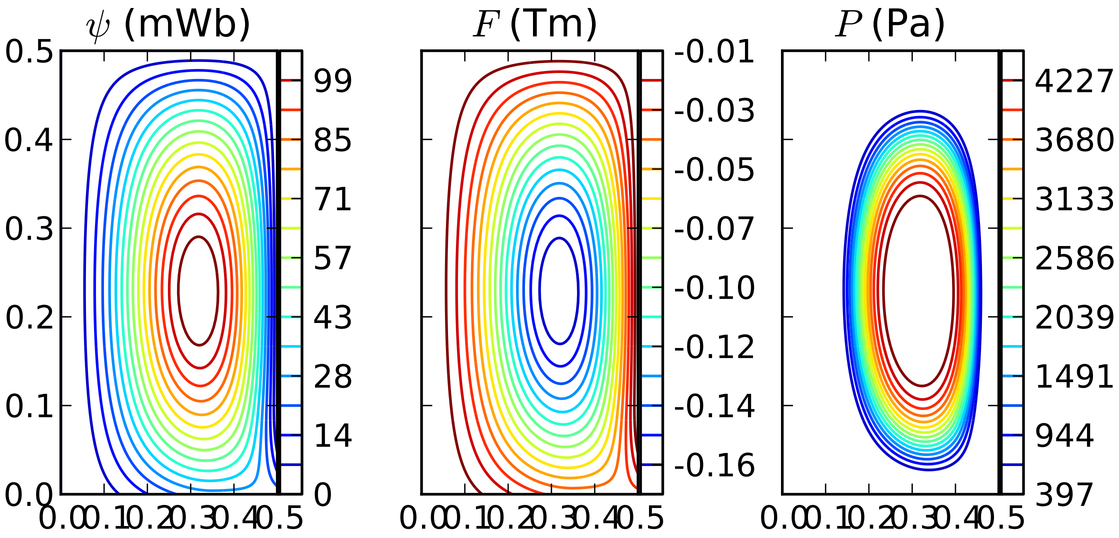

Figure 20: Contours of the equilibrium poloidal flux, ψ, toroidal magnetic field, $F = RB_\phi$ and pressure, P for the 3-5-1 equilibrium.

4.2.2 Resistive MHD Stability Analysis

Linear resistive MHD calculations are performed using a 60x60 bi-quintic mesh with toroidal mode numbers ranging from $n = 1$ to 12. Multiple calculations are performed for each mode number varying S from $S = 5.2 \times 10^4$ to 1.3×10^7, where a uniform resistivity profile is used. These Lundquist numbers correspond to Spitzer resistivities for plasma with electron temperature ranging from 10 eV to 350 eV, and they cover the range of temperatures and resistivities across the profile of the SSPX discharge. The lower S values are characteristic of the resistivity in colder edge, and the high S values are characteristic of the core. The calculations also use a small amount of artificial number density diffusivity, D_n, isotropic viscosity, ν_{iso}, and isotropic thermal diffusivity, χ_{iso} to aid the numerics. These diffusivities are scaled with the electrical diffusivity keeping $\eta/\mu_0 = 10D_n = 10\nu_{iso} = 100\chi_{iso}$.

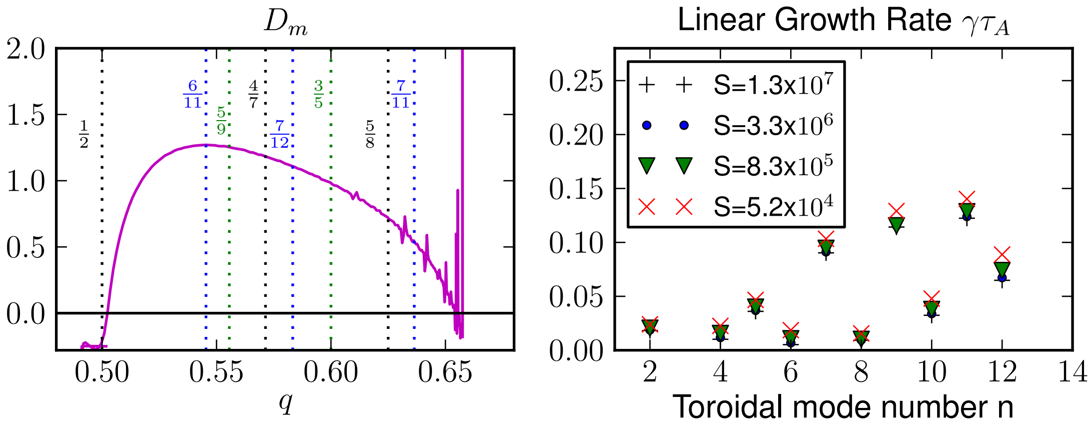

Figure 21: The Mercier stability parameter D_M and the linear growth rate are shown for the 3-5-1 equilibrium. D_M is plotted as a function of the safety factor q, where the magnetic axis is located near $q = 0.66$ and the separatrix is near $q = 0.5$. The growth rate of the dominant mode for each toroidal mode is shown for the range of S.

Linear calculations show that the fastest growing modes for a given equilibrium have the largest D_M. This is illustrated in Figure 21, which shows the Mercier stability parameter and the calculated linear growth rates for the 3-5-1 equilibrium. The stability parameter is plotted as a function of safety factor q. Here the magnetic axis is located on the left near $q = 0.66$, and the separatrix is on the right near $q = 0.5$. The vertical dashed lines indicate the locations of rational surfaces. The growth rates are plotted as a function of the toroidal mode number. Only the dominant mode is shown for each n. The growth rates are plotted for several values of S. At low S the growth rates decrease with increasing S. However, ideal behavior is observed for $S \gtrsim 3 \times 10^6$. Here the growth rates are insensitive to S.

The fastest growing mode is the $n = 11$ $m = 6$ mode which has an ideal growth rate of $\gamma\tau_A = 0.12$.

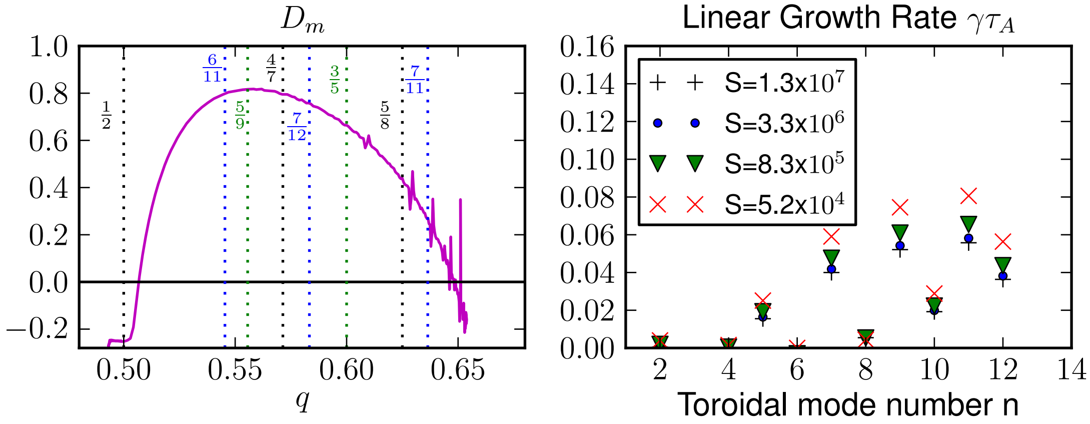

Figure 22: The Mercier stability parameter D_M and the linear growth rate are shown for the 3-5-3 equilibrium. D_M is plotted as a function of the safety factor q, where the magnetic axis is located near $q = 0.66$ and the separatrix is near $q = 0.5$.

This mode is resonant on the $q \approx 0.54$ surface, which is located near the maximum in D_M. The next fastest growing modes are the $n = 9$ $m = 5$, the $n = 7$ $m = 4$, and the $n = 12$ $m = 7$ modes. Each of these modes are resonant on surfaces with a progressively smaller stability parameters. The $n = 2$, $n = 4$, and $n = 6$ modes are all located in the region where the pressure gradient is zero by design. Here $D_M = -0.25$, and these weakly growing modes are not classical interchange modes. These modes are also located near the minimum of q. Here there are two $q = 1/2$ surfaces close to each other. The non-resonant $n = 3$ mode is stable.

Similar behavior is observed for the 3-5-3 and 3-5-5 equilibria. The stability parameters and growth rates for these two equilibria are shown in Figures 22 and 23. The growth rate scales with the pressure. The growth rate of the most unstable mode is $\gamma\tau_A \approx 12\%$ for 3-5-1 equilibrium at $S = 1.3 \times 10^6$. This equilibrium has the largest pressure. The growth rate of the most unstable modes for the 3-3-3 and the 3-5-5 equilibria are $\gamma\tau_A \approx 5\%$ and $\gamma\tau_A \approx 2\%$ respectively.

The growth rates of the modes resonant on the $q = 1/2$ surfaces decrease with decreasing peak pressure. However, these modes are located where the pressure gradient is zero. In the 3-5-3 equilibria, the $n = 6$ mode is only detectable at the highest resistivity, and in the 3-5-5 equilibria the n= 2, $n = 4$

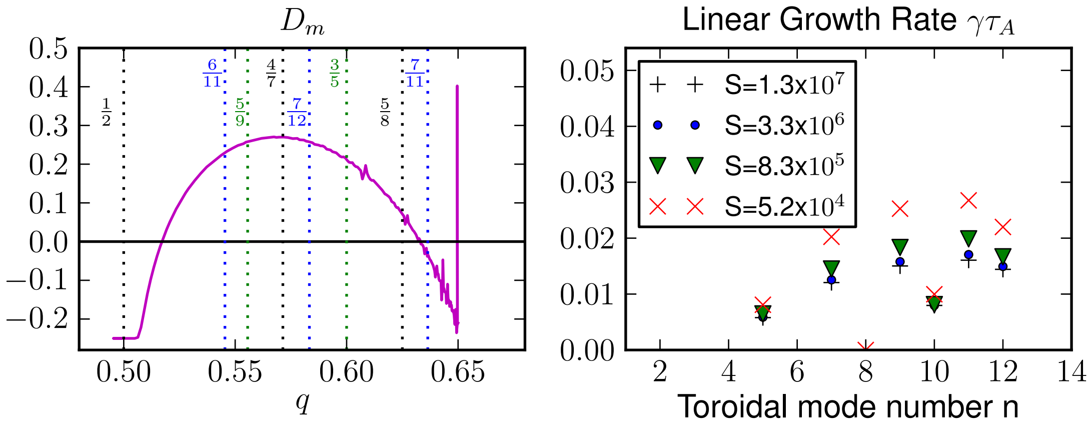

Figure 23: The Mercier stability parameter D_M and the linear growth rate are shown for the 3-5-5 equilibrium. D_M is plotted as a function of the safety factor q, where the magnetic axis is located near $q = 0.66$ and the separatrix is near $q = 0.5$.

and $n = 6$ modes all appear to be stable. The changes in the growth rate are likely due to changes in the q profile. In the 3-5-5 equilibria the $q = 1/2$ surfaces are barely resonant, and the distance between the two $q = 1/2$ surfaces is small. The distance between the two $q = 1/2$ surfaces increases as the minimum safety factor decreases.

Figure 24 illustrates the general trend that the linear growth rate increases with D_M, here the growth rate is shown as a function of the linear stability parameter for the three equilibria. However, this trend is not exact. Consider the modes with $D_M \approx 0.7$. In the high pressure equilibrium, 3-5-1, this mode is the $n = 8$ $m = 5$ mode. It is resonant near the magnetic axis where the pressure gradient is relatively weak. It has a normalized growth rate of $\gamma\tau_A \approx 0.01$. In the medium pressure equilibrium, 3-5-3, the $n = 5$ $m = 3$ and $n = 10$ $m = 6$ modes are resonant on surfaces with $D_M \approx 0.67$. They are located farther from the magnetic axis than the $n = 8$ $m = 5$ mode, and their growth rates are around $\gamma\tau_A \approx 0.02$. Even though they have similar D_M values as the $n = 8$ mode observed in the 3-5-1 equilibrium, their growth rates are twice as large. These difference show that D_M alone is not enough to characterize the growth rate of a mode. This is reasonable, since low-n modes have large scale structure and D_M is only a localized measure of stability.

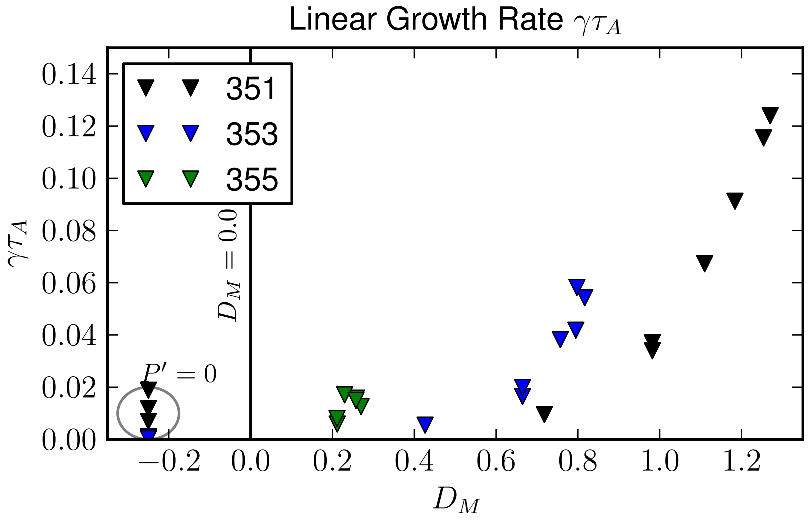

Figure 24: Linear growth rates plotted as a function of the stability parameter D_M for the 3-5-1, 3-5-3, and 3-5-5 equilibria at S=3.3×10^6.

4.2.3 Extended MHD stability Analysis

The linear stability analysis is repeated using the full extended model the includes both the two-fluid Ohm's law and ion gyroviscosity. The calculated rates for the high pressure equilibrium, 3-5-1, are shown in Figure 25 for the resistive MHD model and the full model. Here the extended MHD effects are destabilizing, they increase the linear growth. The inclusion of the extended MHD effects increases the growth rates of the $n = 11$ $m = 7$ mode, the most unstable mode, from its MHD value of $\gamma\tau_A = 0.12$ to $\gamma\tau_A = 0.16$, a 33% increase. The extended MHD effects increase the $n = 8$ $m = 5$ growth increase from $\gamma\tau_A = .009$ to $\gamma\tau_A = .063$, a 600% increase!

Similar changes in the growth rate are observed for the 3-5-3 and 3-5-5 equilibria. The growth rates for these two equilibria are shown if Figures 26 and 27. These results are unexpected. The low pressure equilibrium, 3-5-5, has a maximum stability of $D_M \approx 0.25$. Inferring from previous work on extended MHD effects on local interchange [30][31], we expect that extended MHD should have a strong stabilizing effect on these modes.

The magnitude of the real frequencies for these three equilibria are shown in Figures 25-27. In the

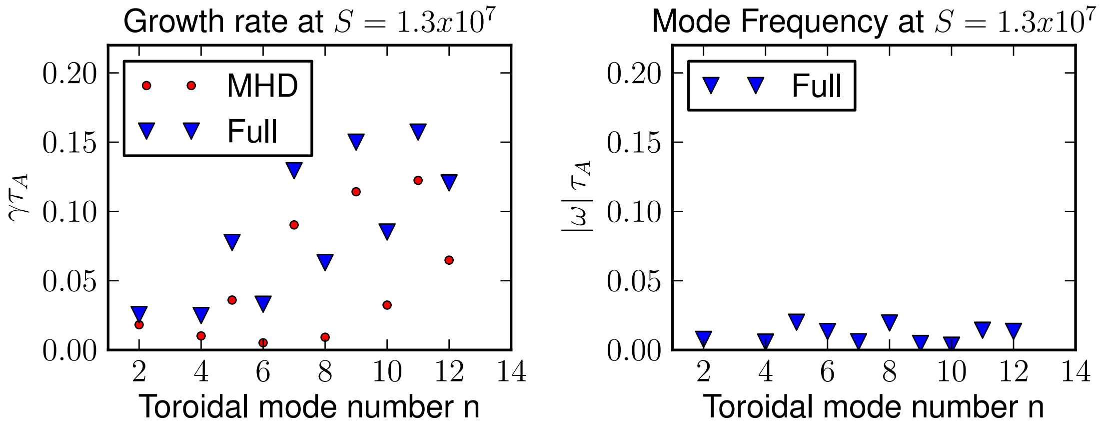

Figure 25: Linear growth rates are real frequencies for the 3-5-1 equilibria calculated using the resistive MHD and the full extended MHD models.

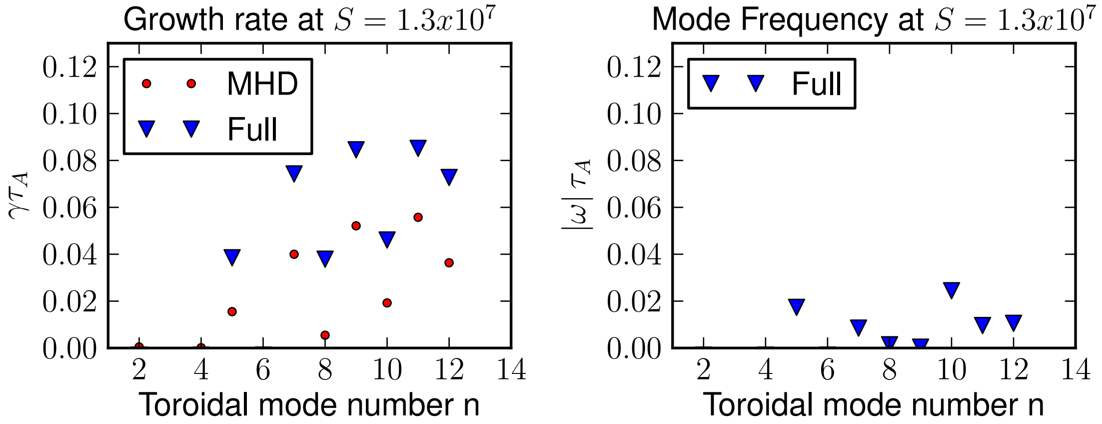

Figure 26: Linear growth rates are real frequencies for the 3-5-3 equilibria calculated using the resistive MHD and the full extended MHD models.

high pressure equilibrium, the real frequencies are small compared to the MHD growth rates for the fastest growing modes. For the medium pressure equilibrium, 3-5-3, the real frequencies are comparable to the MHD growth rate, and for the low pressure equilibrium, 3-5-5, the real frequencies exceed the MHD growth rate. Analysis of the gravitational interchange mode suggests that significant stabilization occurs when the real frequencies of the mode are comparable in magnitude to its MHD growth rate[13].

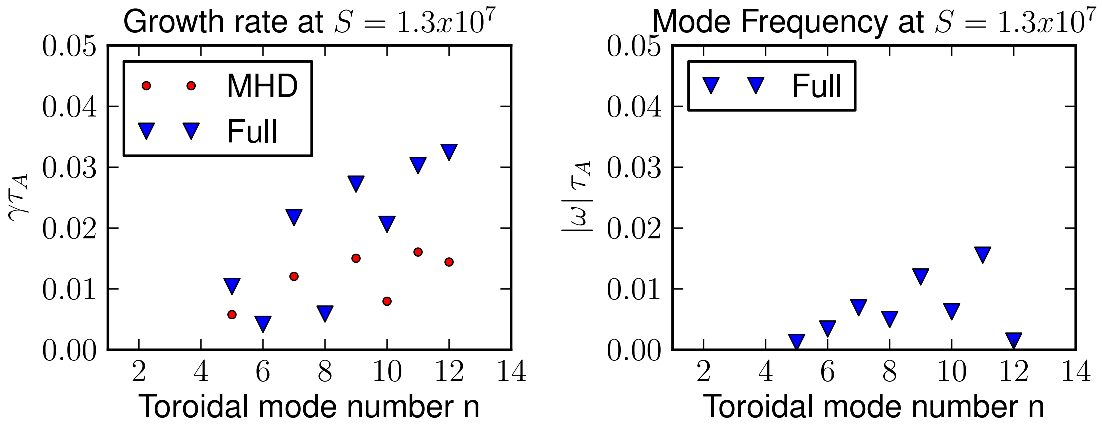

Figure 27: Linear growth rates are real frequencies for the 3-5-5 equilibria calculated using the resistive MHD and the full extended MHD models.

This is not observed.

In contrast, growth rates calculated with the gyroviscous model are smaller than the resistive MHD growth rates. Gyroviscosity has the greatest effect on the slowest growing modes, and it reduces their growth rates by as much as 50%, for the high pressure equilibrium. The stabilization is weaker for the faster growing modes. The growth rates of the fastest growing modes are only reduced by $\sim 5\%$.

The results with the gyroviscous model suggest that the increased growth rates observed in the full extended model are due to physical effects modeled by the two-fluid Ohm's law. For these equilibria, the linear calculations using the two-fluid model that includes the two-fluid Ohm's law but neglects gyroviscosity are dominated by a numerical instability. We are unable to determine if the enhanced growth rate is primarily due to two-fluid physics or an interaction between the two-fluid effects and gyroviscosity.

4.2.4 Discussion of 14590 Model Equilibria

The resistive MHD analysis of the 14590 model equilibria yields results that are similar to those of the first model equilibria. Here we took special care to construct realistic equilibria that represent SSPX discharges. The vacuum poloidal flux profile is representative of the bias flux applied around the gun region. The current profile is prescribed to match that of those reported for equilibrium reconstructions. Similar data is not available for the pressure profile, but we proscribed a pressure profile that has good stability properties near the magnetic axis and near the edge.

Analysis of the Mercier stability criteria show that these equilibria violate the ideal Mercier stability criteria even at low pressure. At experimentally relevant pressures the Mercier stability criteria is order unity, and rapidly growing interchange modes are expected. This is in agreement with linear resistive MHD calculations which yield modes that grow as fast as $\gamma\tau_A = 0.12$. For a given equilibrium, the fastest growing modes are typically resonant on the surface with the largest D_M.

Extended MHD calculations yield an unexpected result. Here the linear growth rates are increased when the full extended MHD model is used. This result is observed for all of the low-n modes. Calculations using gyroviscosity with an MHD Ohm's law are more stable than MHD. This implies that the increased growth rate is due to the two-fluid Ohm's law. This result is explored in more detail in the next section using screw pinch equilibria.

4.3 Straight Spheromak Model

Cylindrical screw pinch equilibria are used to model spheromak equilibria. We refer to these screw pinch equilibria as "straight spheromaks." These equilibria are a generalization of those used by Jardin, Delucia, and Glasser (JDG) [78][79][80], where the pressure is calculated by specifying a uniform Suydam parameter across the domain. The resulting pressure gradient is given by the formula $\mu_0 p' = -\alpha r \frac{B_z^2}{8}\left(\frac{q'}{q}\right)^2$, where $\alpha = 1$ corresponds to marginal ideal stability, $D_s = 0.25$. The equilibria use a quadratic safety factor profile, $q = q_0\left(1 - q_2\frac{r^2}{a^2}\right)$, that allows for an arbitrary minor radius, a, and a non-zero safety factor at the boundary, $r = a$. The parameter q_2 controls the change in the safety factor across the domain. The safety factor at the boundary is related to q_2 by $q_2 = 1 - \frac{q(a)}{q_0}$. The finite safety factor at the boundary is useful for modeling CHI spheromaks which have non-zero toroidal field at their separatrices due to currents on the open field. We do not model the plasma in the open field region in these straight spheromaks.

The prescription of the pressure profile is a useful control for studying interchange modes. Varying α allows us to study interchange modes that are resistively unstable, weakly ideal unstable, and strongly ideal unstable. In addition the numerical mesh is aligned with the circular flux surfaces, and we mesh pack around the mode rational surface. This allows us to efficiently resolve interchange modes on smaller meshes, greatly reducing the computational cost. Jardin showed that these straight spheromak equilibria exhibit stability properties similar to spheromak equilibria in toroidal geometry for linear modes with $n \neq 1$[78].

The equilibrium fields are calculated using

$$
\begin{aligned}
B_r &= J_r = 0 && (4.5)\\
B_\theta &= \frac{xB_0}{q_0}\exp\left(-\int_0^x g\left(x'\right)dx'\right) && (4.6)\\
B_z &= \frac{q_0 B_\theta}{x}\left(1 - q_2 x^2 \epsilon^{-2}\right) && (4.7)\\
J_\theta &= \frac{B_\theta q_0}{\mu_0 x R}\left(2q_2 x\epsilon^{-2} + g\left(x\right)\left(1 - q_2 x^2\epsilon^{-2}\right)\right) && (4.8)\\
J_z &= \frac{B_\theta}{\mu_0 x R}\left(2 - xg\left(x\right)\right) && (4.9)\\
\mu_0 p &= \mu_0 p_0 - \alpha\int_0^x x\frac{B_z^2}{8}\left(\frac{-2q_2 x\epsilon^{-2}}{1 - q_2 x^2\epsilon^{-2}}\right)^2 dx, && (4.10)
\end{aligned}
$$

where $B_0 = B_z\left(0\right)$, $p_0 = p\left(0\right)$, $x = r/R$, $R = L/2\pi$ is the effective major radius, L is the periodic length of the cylinder, and $\epsilon = a/R$. We define the function $g\left(x\right) = K\frac{2x + Ax^3}{B + x^2 + Cx^4}$, with coefficients $A = \frac{q_0^2 q_2^2\epsilon^{-4}(2-\alpha/2)}{\left(1 - q_2\epsilon^{-2}q_0^2\right)}$, $B = \frac{q_0^2}{\left(1 - 2q_2\epsilon^{-2}q_0^2\right)}$, $C = \frac{q_0^2 q_2^2\epsilon^{-4}}{\left(1 - 2q_2\epsilon^{-2}q_0^2\right)}$, and $K = \frac{\left(1 - q_2\epsilon^{-2}q_0^2\right)}{\left(1 - 2q_2\epsilon^{-2}q_0^2\right)}$. Gaussian quadrature is used to numerically evaluate the integrals.

The equilibrium density and temperature are calculated from the pressure. We consider the two cases of uniform density and uniform temperature. In the case of uniform density, pressure gradients are due entirely to temperature gradients. In the case of uniform temperature, the pressure gradients are due to density gradients. A few calculations include an equilibrium ion diamagnetic flow. The flow is calculated using $\vec{V}_0 = \frac{\vec{B}_0 \times \nabla p_{i0}}{neB_0^2}$. We assume that the flow is sufficiently slow such that is has a negligible effect on the force balance.

4.3.1 Benchmarking

Jardin, Delucia, and Glasser (JDG) extensively studied the stability of these straight spheromak equilibria using ideal and resistive MHD [78][79]. In the second paper they also present a series of calculations that studies the effect of the two-fluid Ohm's law on a resistive interchange mode. We use their result to benchmark NIMROD two-fluid spheromak computations.

In their calculation JDG study the two-fluid stabilization of $n = 2$ $m = 1$ resistive interchange. Their calculation uses an isothermal equilibrium with $q_0 R/a = 0.8$, $\alpha = 0.7$, $na/R = 2$, and $S = 10^5$. Their calculations use a two-fluid Ohm's law based on the ion momentum equation

$$E + \vec{v} \times \vec{B} = \eta \vec{J} + \frac{m_i}{e} \frac{D\vec{v}}{Dt} + \frac{1}{ne} \nabla p_i, \tag{4.11}$$

where $\frac{D\vec{v}}{Dt} = \frac{\partial \vec{v}}{\partial t} + \vec{v} \cdot \nabla \vec{v}$ is the material derivative. In their calculations, JDG assume cold ions. They neglect the ion pressure term in their Ohm's law, and they ignore ion gyroviscosity.

The growth rates calculated by JDG are shown in Figure 10 in [79]. In the MHD limit, $\Lambda = 0$, the mode has a growth rate of $\gamma \tau_A \approx 5.5 \times 10^{-3}$. The growth rate monotonically decreases with increasing Λ, and at $\Lambda = 0.14$ the growth rate is reduced to $\gamma \tau_A \approx 0.5 \times 10^{-3}$. Complete stabilization occurs around $\Lambda = 0.15$. The real frequency of the mode increases from $\omega \tau_A = 0$, in the MHD limit, to $\omega \tau_A \approx 16 \times 10^{-3}$ at $\Lambda = 0.14$. We note that JDG don't quote numerical values for the growth rate, and we estimate their calculated growth rates and frequencies from Figure 10 in [79]. The values are only approximately correct as the estimation introduces considerable error.

We perform a similar calculation with NIMROD using a cylinder with minor radius a =1 m and periodic length of L =2 π m (this corresponds to a major radius of R =1 m). The safety factor decreases from $q_0 = 0.8$ at the magnetic axis to $q\,(a) = 0$ at the wall, and the magnetic field on axis is B_0 =1 T. A deuterium plasma is used with a density of n_0 =2.38×10^{20} m^{-3}. The electrical diffusivity is set to $\eta/\mu_0 = 10\,\mathrm{m}^2/\mathrm{s}$ yielding $S = 10^5$. A small viscosity $\nu_{iso} = 10^{-2}\,\mathrm{m}^2/\mathrm{s}$, thermal diffusivity, $\chi = 10^{-3}\,\mathrm{m}^2/\mathrm{s}$, and number density hyper-diffusivity, $D_h = 10^{-5}\,\mathrm{m}^4/\mathrm{s}$, are used to provide numerical stability. Unlike JDG our computations have a small nonzero density at the edge, $n(a) = 0.09 n_0$. This ensures that all waves have a finite velocity in the domain. We also use hot ions with $T_e = T_i$.

The results of our linear calculations are shown in Figure 28. These calculations use the two-fluid Ohm's but neglect gyroviscosity. The relative strength of the two-fluid terms in Ohm's law are scaled by adjusting the electron charge. The MHD limit corresponds to $\Lambda = 0$. Here the linear growth rate is $\gamma \tau_A = 5.66 \times 10^{-3}$. This growth rate decreases with increasing Λ. At $\Lambda = 0.135$ the growth rate is reduced to $\gamma \tau_A = 1.14 \times 10^{-3}$. The real frequency increases from $\omega \tau_A = 0$ at $\Lambda = 0$ to $\omega \tau_A = 1.35 \times 10^{-2}$

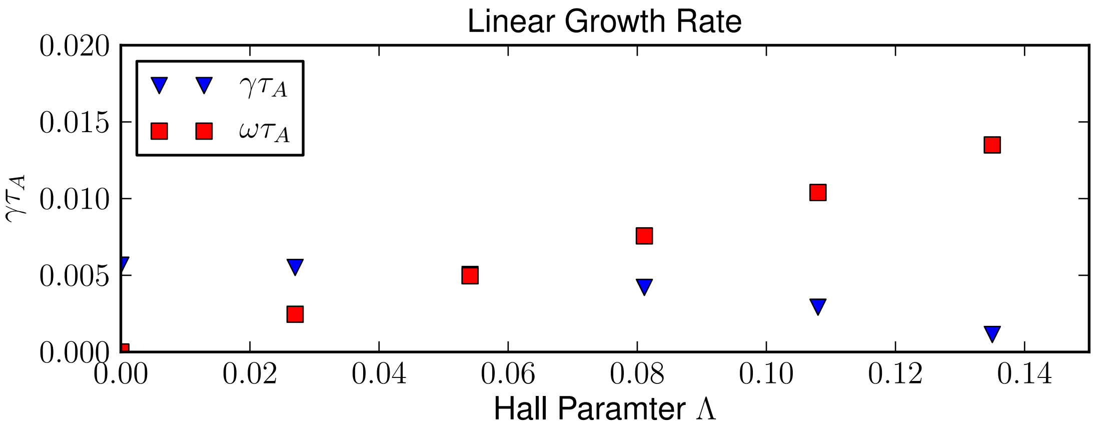

Figure 28: The linear growth rates and real frequency of the $m = 1$ $n = 2$ interchange mode for $D_s = 0.175$.

at $\Lambda = 0.135$. However a numerical instability dominates the calculations for $\Lambda > 0.135$ and we do not directly observe stability. However if the trend in Figure 28 continues, we expect to observe complete stabilization around $\Lambda \approx 0.15$.

Our ability to do a direct quantitative comparison with JDG is limited since we are estimating their growth rates from a figure. The fact that we are using warm ions also has an effect on the two-fluid calculations. Despite these difference we see reasonable agreement. In the MHD limit our linear growth rate, $\gamma\tau_A = 5.66 \times 10^{-3}$, is comparable to that of JDG $\gamma\tau_A \approx 5.5 \times 10^{-3}$. We also expect complete stabilization near the same approximate $\Lambda \approx 0.15$. There is some disagreement in the growth rate at $\Lambda \approx 0.14$. At $\lambda = 0.135$ we calculate a rate of $\gamma\tau_A = 1.14 \times 10^{-3}$ which is larger than the JDG rate of $\gamma\tau_A = 0.5 \times 10^{-3}$ at $\Lambda = 0.14$. Some of the difference is due to the fact that we're calculating the growth rate at two different values of Λ, and here the growth rate is a strong function of Λ. The finite ion temperature may also account for some of the difference. Calculations in a later section show that reducing the ion pressure fraction reduces the growth rate. Nevertheless, the comparison between the JDK results and the NIMROD calculations provides support for the two-fluid NIMROD spheromak computations, over a numerically limited range of parameters.

4.3.2 SSPX Relevant Cylindrical Equilibria

To model SSPX equilibria in cylindrical geometry we set radius $a = 0.25\,\mathrm{m}$ and periodic length $L = 2\,\mathrm{m}$. This length corresponds to an approximate major radius of $0.32\,\mathrm{m}$. The minor radius is chosen be half the height of the SSPX flux conserver. The major radius is based off of NIMEQ generated equilibria that use SSPX relevant parameters. In these equilibria the magnetic axis is usually located around $0.3\,\mathrm{m}$. This is a little more than half the radius of the SSPX flux conserver.

The safety factor on the magnetic axis is specified to be $q_0 = 0.66$ and at the boundary it is $q\left(a\right) = 0.52$. These values are chosen such that the $q = 1/2$ and $q = 2/3$ surfaces are not in the domain. The two lowest order resonant surfaces in the domain are the $q = 3/5$ and $q = 4/7$ surfaces. The magnetic field at the magnetic axis is $B_0 = 0.5\,\mathrm{T}$.

A family of equilibria are generated with α ranging from $\alpha = 0.8$ to 8.0. These correspond to cases with Suydam parameters ranging from $D_s = 0.2$ to 2.0. The case $D_s = 0.2$ is ideal interchange stable but resistive interchange unstable. It is slightly below the ideal marginal stability point of $D_s = 0.25$. Cases with $D_s > 0.25$ are all ideal interchange unstable. The case $D_s = 0.5$ is the least ideal unstable case that we consider. It is twice the marginal limit. $D_s = 2.0$, is the most unstable case considered, it is eight times the marginal limit. The pressure at the edge is set to $p\left(a\right) \approx 400\,\mathrm{Pa}$ in all the equilibria. This pressure corresponds to a density of $n = 5 \times 10^{19}\,\mathrm{m}^{-3}$ and electron and ion temperatures of $T_e = T_i = 25\,\mathrm{eV}$. These values are representative of plasma conditions in the open flux region of SSPX.

The safety factor q and parallel current λ are shown in Figure 29. The parallel current only depends on the safety factor and the physical dimensions of the cylinder. The safety factor and parallel current are both independent of pressure gradient, and neither profiles changes as α is varied. In these equilibria, the λ profile decreases radially outwards from the magnetic axis and is representative of decaying spheromaks. However the values of λ are smaller than typical experimental values, and the λ gradients are a little larger than observed in the experiment. For comparison, the λ in the straight spheromak equilibria varies from approximately $9.5\,\mathrm{m}^{-1}$ to $4.7\,\mathrm{m}^{-1}$, whereas typical λ values in SSPX range from approximately $12\,\mathrm{m}^{-1}$ to $8.5\,\mathrm{m}^{-1}$[10].

The equilibrium magnetic field, current density, pressure, and temperature are shown in Figure 30. The temperature is calculated for the case of uniform density with $n = 5 \times 10^{19}\,\mathrm{m}^{-3}$ and assumes

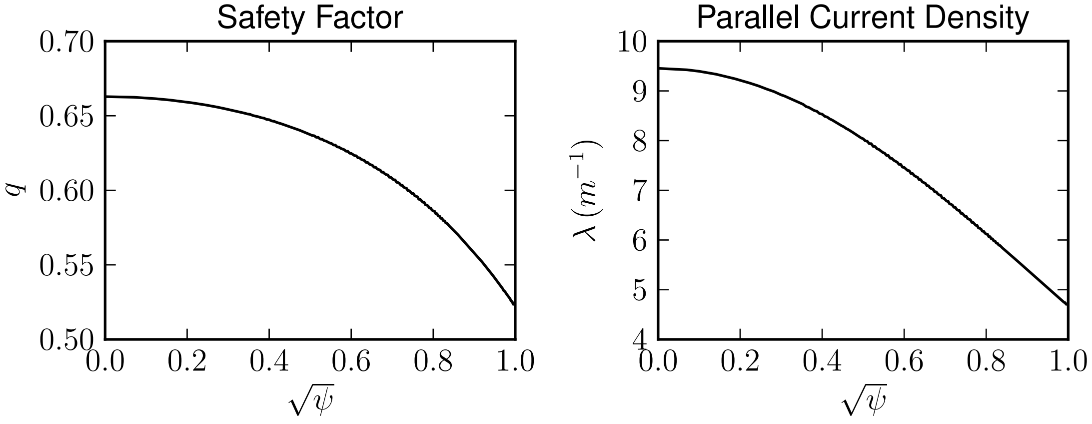

Figure 29: Safety factor (q) and parallel current (λ) profiles for straight spheromak equilibria.

equal electron and ion temperatures, $T_e = T_i$. There is a minor change in the equilibrium magnetic fields and currents as the Suydam parameter is increased from $D_s = 0.2$ to 2.0. The pressure on axis increases from 700 Pa to 3400 Pa, and the temperature on axis increases from 45 eV to 210 eV. These peak temperatures are colder than observed in SSPX, even in cases where D_s greatly exceeds the marginal stability condition. However, the cylindrical approximation neglects toroidal effects which are stabilizing. These effects allow for a larger pressure gradient for a given stability parameter D. Thus we expect the cylindrical model to under-predict the pressure (and thus the temperature) for a given D.

4.3.3 Linear Resistive MHD Calculations

The straight spheromak equilibria are used to study linear interchange modes using various extended MHD models. We start by studying interchange modes using resistive MHD and then incrementally incorporate gyroviscous, two-fluid, and two-temperate effects into our model. The resistive MHD calculations act as a control which we compare with the extended MHD models.

The linear calculations use hydrogen plasma with $m_i \approx 1.67 \times 10^{-27}$ kg and $Z = 1$. The Alfven velocity for $n = 5 \times 10^{19}\,\mathrm{m}^{-3}$ is $V_A = 1.54 \times 10^{6}$ m/s. This corresponds to an Alfven time of $\tau_A = 1.62 \times 10^{-7}$ s, where the minor radius, $a = 0.25$ m, is used as the characteristic length scale. We vary

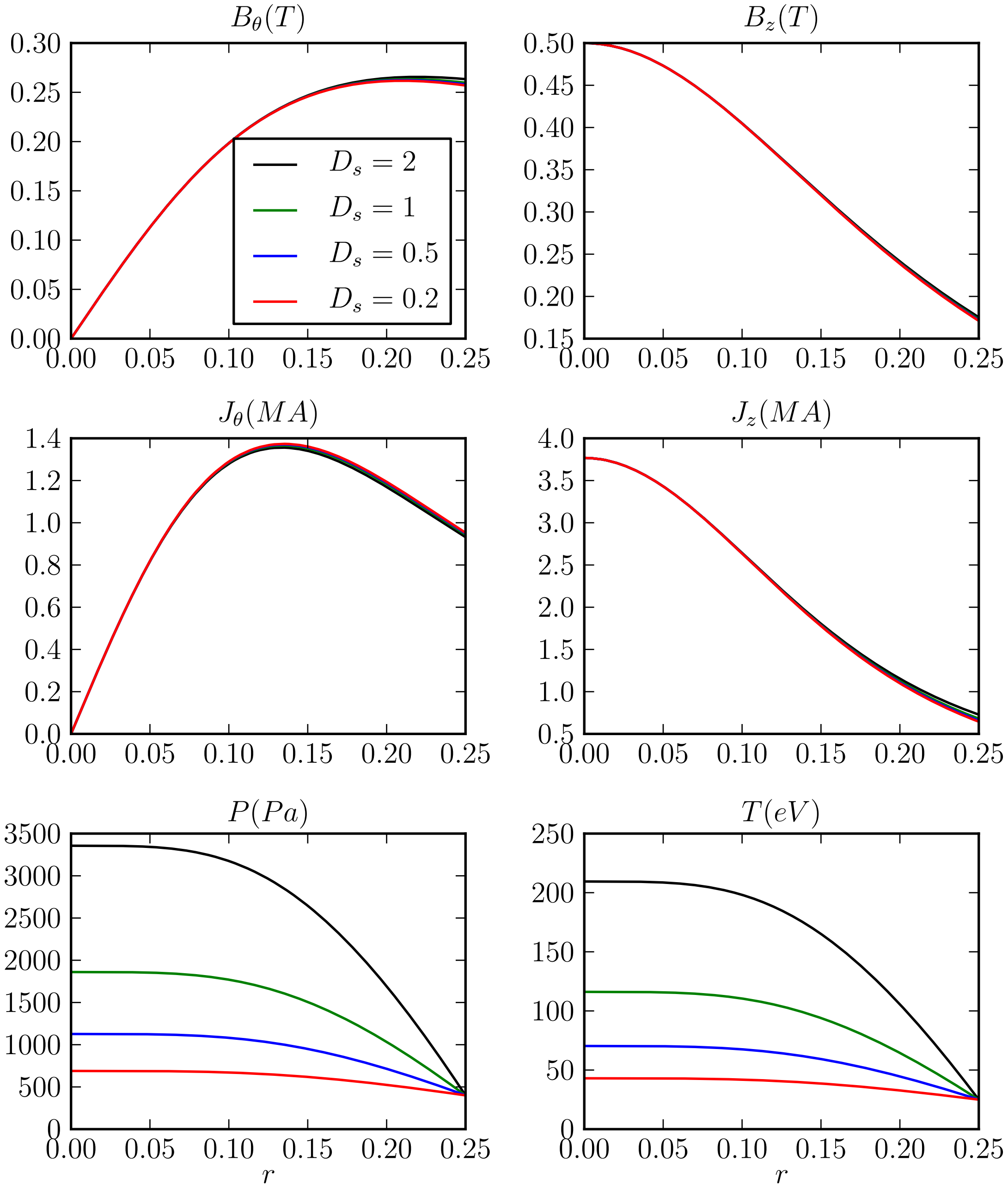

Figure 30: Equilibrium magnetic field, current, pressure, and temperature for the straight spheromak. The temperature is calculated assuming uniform number density of $5 \times 10^{19}\,\mathrm{m}^{-3}$ and $T = T_i = T_e$.

the electrical diffusivity from $\eta/\mu_0 = 4.0\,\mathrm{m}^2/\mathrm{s}$ to $0.625\,\mathrm{m}^2/\mathrm{s}$. These diffusivities correspond to Lundquist numbers ranging from $S = 9.64 \times 10^4$ to 6.17×10^6. The Lundquist number in SSPX discharges typically varies from 10^5 to 5×10^6[6]. The ion skin depth is $d_i = 3.22\,\mathrm{cm}$ which corresponds to a Hall parameter $\Lambda = d_i/a = (\tau_a \Omega_i)^{-1} = 0.13$. The ion sound gyro-radius, $\rho_s = C_s/\Omega_i$, ranges from 1.8 mm at $T_e = 45\,\mathrm{eV}$ to 3.8 mm at $T_e = 210\,\mathrm{eV}$. In normalized units these correspond to $\rho_s/a = 0.0071$ and 0.015 respectively.

A characteristic ion diamagnetic frequency is calculated using $\omega_{*i} = \frac{m}{r_s}\frac{\Delta p_i}{aneB_0}$, where Δp_i is the change in the ion pressure from the magnetic axis to the wall, and r_s is the radius of the rational surface. The normalized ion diamagnetic frequency, $\omega_{*i}\tau_A$, for an $m = 3$ $n = 5$ mode resonant on the $q = 0.6$ surface with an density of $n = 5 \times 10^{19}\,\mathrm{m}^{-3}$ varies from 4.3×10^{-3} for $D_s = 2.0$ to 4.3×10^{-4} for $D_s = 0.2$.

The linear calculations use bi-quintic elements with 40 elements in the radial and 20 elements in poloidal direction. The elements are packed radially around the mode rational surface. The default time step is $\Delta t = 10^{-8}\,\mathrm{s}$, however many calculations require a smaller step for numerical stability. Sensitivity studies show that these parameters yield linear growth rates accurate to 1%. These calculations use small amounts of viscosity, particle diffusion and hyper-diffusion, thermal conduction, and magnetic divergence diffusion to provide numerical stability. All calculations use a number density hyper diffusivity of $4 \times 10^{-6}\,\mathrm{m}^4/\mathrm{s}$. The magnetic divergence diffusivity varies from $10^4\,\mathrm{m}^2/\mathrm{s}$ to $10^6\,\mathrm{m}^2/\mathrm{s}$. The thermal diffusivity χ_{iso}, number density diffusivity D_n, and viscosity ν_{iso} are varied with the electrical diffusivity such that $\eta/\mu_0 = 10\nu_{iso}$, $\eta/\mu_0 = 10D_n$, and $\eta/\mu_0 = 100\chi_{iso}$.

Figure 31 shows the resistive MHD linear growth rates for the $n = 5$ $m = 3$ mode. These calculations use the uniform density $n = 5 \times 10^{19}\,\mathrm{m}^{-3}$. Figure 31A shows the linear growth rates as a function of the Suydam parameter, D_S, for $S = 6.17 \times 10^6$. The solid vertical line indicates the marginal ideal stability condition, $D_s = 0.25$. Near the marginal point the growth rates are small, $\gamma\tau_A = 0.016\%$ for $D_s = 0.5$, and the growth rate increases with increasing D_s. This is in agreement with theory, which predicts exponentially small growth rates near the marginal point [30][31]. Figure 31B shows the linear growth rate as a function of the resistivity. Resistive interchange scaling of $\gamma\tau_A \sim S^{-1/3}$ is observed for $D_s = 0.2$[32]. The cases with $D_s > 0.25$ behave ideally in that their growth rates don't scale with the resistivity. For example, the growth rate of the $D_s = 0.5$ case only changes by 2% as S is increased from 9.6×10^4 to $S = 6.2 \times 10^6$. This change is comparable to the accuracy of our numerical mesh. The observed change in the growth rate is even smaller for larger D_S.

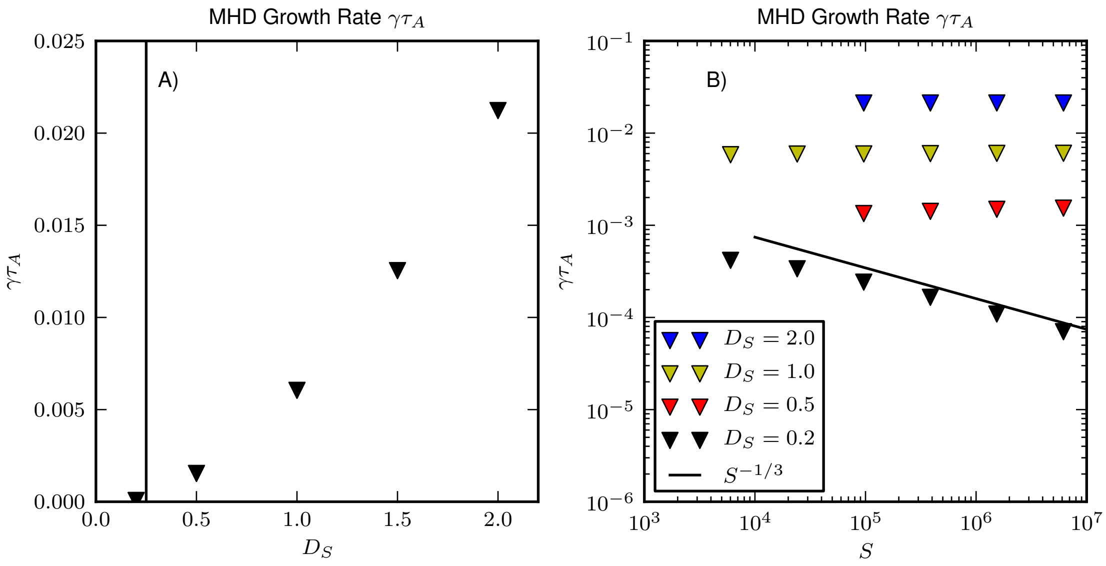

Figure 31: Resistive MHD growth rates for uniform density equilibrium with $n = 5 \times 10^{19}\,\mathrm{m}^{-3}$. The growth rates are plotted as a function of the Suydam parameter D_s in A. The vertical line indicates the ideal marginal stability point $D_S = 0.25$. The growth rates are plotted as a function of Lundquist number in B. The case $D_s = 0.2$ exhibits resistive interchange scaling.

The resistive MHD calculations are repeated for two other equilibria. The first uses a uniform equilibrium number density with $n = 10^{20}\,\mathrm{m}^{-3}$. This equilibrium is shown in anticipation of extended MHD calculations, where the magnitude of the gyroviscous stress and the Hall term both scale with density. The second equilibrium uses a uniform equilibrium temperature profile with $T_e = 25\,\mathrm{eV}$. The MHD growth rates for the uniform $n = 10^{20}\,\mathrm{m}^{-3}$ equilibria are shown in Figure 32. The normalized growth rates and Lundquist numbers are calculated using $\tau_A = 2.29 \times 10^7\,\mathrm{s}$, which is calculated using $n = 10^{20}\,\mathrm{m}^{-3}$. We only calculate the growth rates at $S = 6.82 \times 10^4$ and 4.36×10^6 for $D_S \geq 1.0$. The growth rates are identical at the two values of S in these cases, and the calculations at intermediate S are skipped to save computation time. The growth rate for $D_s = 0.5$ changes by 4% as S is varied, and the growth rate of resistive mode $D_s = 0.2$ scales as $S^{-1/3}$.

The normalized growth rate for ideal interchange modes should be insensitive to the density. In comparing the growth rates calculated using the uniform density equilibria with $n = 5 \times 10^{19}\,\mathrm{m}^{-3}$ and $n = 10^{20}\,\mathrm{m}^{-3}$, we see that is indeed the case. The growth rate for $D_s = 2.0$ is $\gamma\tau_A = 2.11\%$ when the density is $n = 5 \times 10^{19}\,\mathrm{m}^{-3}$ and $\gamma\tau_A = 2.12\%$ when $n = 10^{20}\,\mathrm{m}^{-3}$. The difference is about 0.5%.

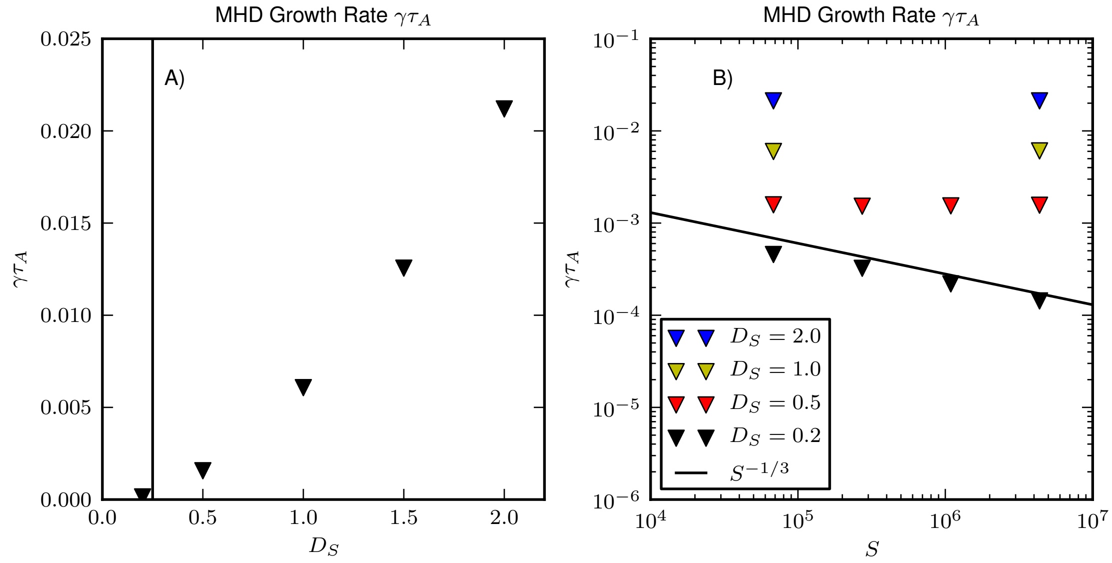

Figure 32: Resistive MHD growth rates for uniform density equilibrium with $n = 10^{20}\,\mathrm{m}^{-3}$. The growth rates are plotted as a function of the Suydam parameter D_s in A. The vertical line indicates the ideal marginal stability point $D_S = 0.25$. The growth rates are plotted as a function of Lundquist number in B. The case $D_s = 0.2$ exhibits resistive interchange scaling.

The MHD growth rates for the isothermal equilibria with $T_i = T_e = 25\,\mathrm{eV}$ are shown in Figure 33. The edge density in these equilibrium is fixed at $n = 5 \times 10^{19}\,\mathrm{m}^{-3}$, and the density on axis increases with increasing D_s. The normalized growth rate and Lundquist number are calculated using the edge density which gives $\tau_A = 1.62 \times 10^{-7}\,\mathrm{s}$. The linear growth rates for the isothermal equilibria exhibits the same qualitative behavior as the uniform density cases. The normalized growth rates are smaller than the uniform density cases. This is expected because we normalized the growth rates by edge density which is less than the density at the mode rational surface.

Figure 34 shows the linear mode structure of $\tilde{b}$ and $\tilde{v}$ for the ideal modes. The mode structures are calculated using the $n = 5 \times 10^{19}\,\mathrm{m}^{-3}$ uniform density equilibrium at $S = 1.5 \times 10^{6}$. These plots show the real components of $\tilde{b}_r$, $\tilde{v}_\perp$, and $\tilde{v}_\parallel$, and the imaginary components of $\tilde{b}_\perp$, $\tilde{b}_\parallel$, and $\tilde{v}_r$. The

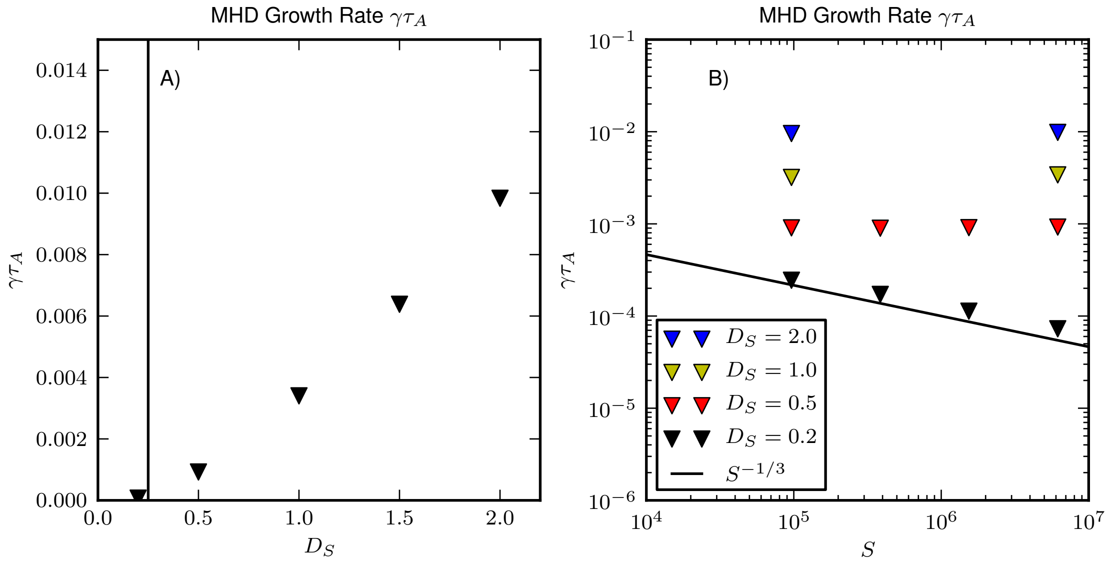

Figure 33: Resistive MHD growth rates for isothermal equilibria with $T_e = T_i = 25\,\mathrm{eV}$. The normalized growth rates $\gamma\tau_A$ and Lundquist number S are normalized using an Alfven time calculated using the edge density $n = 5 \times 10^{19}\,\mathrm{m}^{-3}$.

perpendicular direction is defined as $\hat{e}_\perp = \hat{b} \times \hat{e}_r$. The modes are plotted along the radial cord where $\tilde{b}_r$ is purely real. Along this cord $\tilde{b}_r$, $\tilde{v}_\perp$, and $\tilde{v}_\parallel$ are purely real, and they are completely out of phase with $\tilde{b}_\perp$, $\tilde{b}_\parallel$, and $\tilde{v}_r$.

The top row shows $D_s = 0.5$, the middle row shows $D_s = 1.0$, and the bottom row shows $D_s = 2.0$. The vertical axis in each figure is scaled such that largest component of $\tilde{b}$ or $\tilde{v}$ has an maximum amplitude of ±1. Therefore the units of the vertical axis are arbitrary, but the relative heights of the radial, perpendicular, and parallel components are not. The horizontal axis extends from $r/a = 0.5$ to $r/a = 1.0$.

Both $\tilde{b}_r$ and $\tilde{b}_\perp$ are concentrated outside of the rational surface, $r > r_s$, and they are of similar magnitude. The parallel magnetic field, $b_\parallel$, is also concentrated outside of the rational surface, but its amplitude is much smaller than the other two components. At the rational surface (indicated by the solid vertical line), $\tilde{b}_r$ is approximately 0, while $\tilde{b}_\perp$ is finite. Similarly $\tilde{v}_\parallel$ and $\tilde{v}_\perp$ are of comparable magnitude while v_r is small. The perpendicular flow, $\tilde{v}_\perp$, peaks just outside the rational surface, and the parallel flow $\tilde{v}_\parallel$, which is approximately zero at the rational surface, peaks far outside of the rational

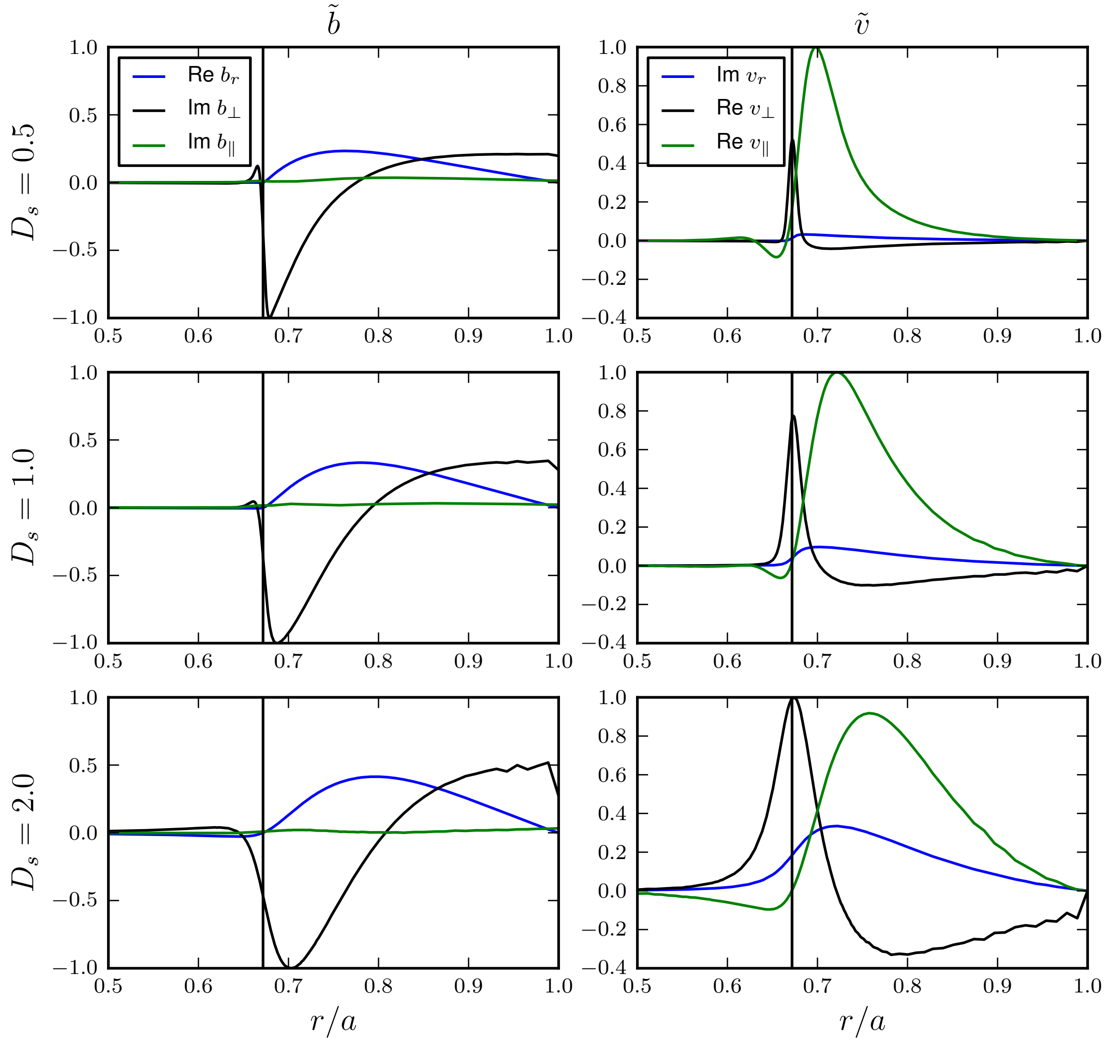

Figure 34: The perturbed $\tilde{b}$ and $\tilde{v}$ for $D_s = 0.5$, 1.0, and 2.0 calculated using resistive MHD with $S = 1.5 \times 10^6$. The amplitudes are arbitrary. Solid vertical line indicate the rational surface.

surface. All threes components of both $\tilde{b}$ and $\tilde{v}$ are small inside of $r/a = 0.5$.

The width of the modes increases with increasing D_s. The relative amplitude of the different components of $\tilde{b}$ and $\tilde{v}$ also changes with D_s. However increasing D_s does not change the shape of the modes.

Some of the plots in Figure 34 exhibit small noise, particularly for $r/a \gtrsim 0.8$. The noise is due to the fact that the initial value calculations haven't completely converged on the linear mode structure. The noise will disappear if the calculations are advance further in time. However, in all these cases, the initial value calculations are carried out until the growth rate converges to an tolerance that is smaller than 0.1% (this error is smaller than the accuracy of our numerical representation).

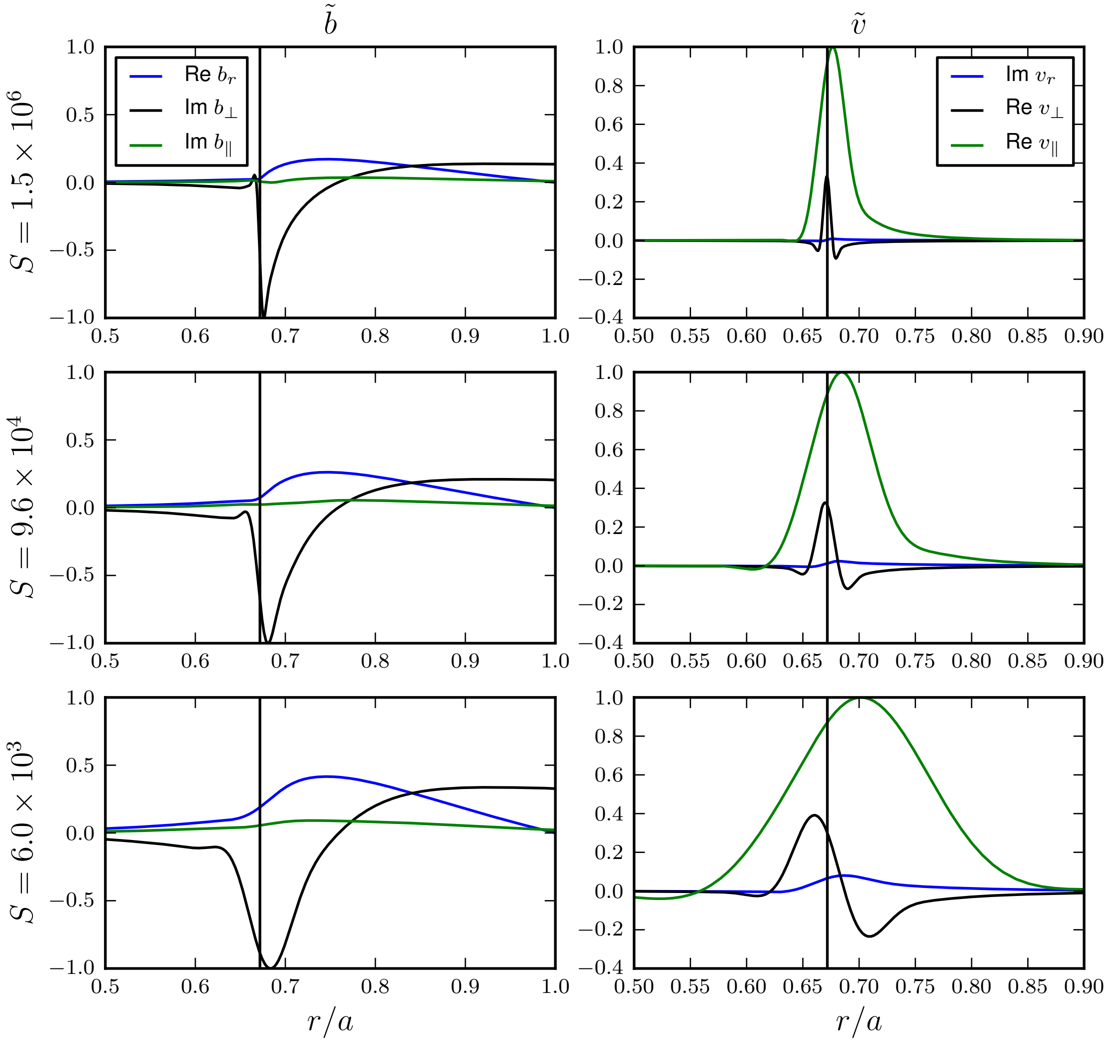

Figure 35: The perturbed $\tilde{b}$ and $\tilde{v}$ for $D_s = 0.2$ calculated using resistive MHD with $S = 6.0 \times 10^3$, 9.6×10^4, and 1.5×10^6.

The mode structure of the resistive interchange mode, $D_s = 0.2$, is shown in Figure 35 for $S = 6.0 \times 10^3$, 9.6×10^4, and 1.5×10^6. The modes are plotted along the radial cord where $\tilde{b}_r$ is purely real. The plots show the real components of $\tilde{b}_r$, $\tilde{v}_\perp$, and $\tilde{v}_\|$, and the imaginary components of $\tilde{b}_\perp$, $\tilde{b}_\|$, and $\tilde{v}_r$ (all the other components of $\tilde{b}$ and $\tilde{v}$ are zero along this cord).

The global mode structure of the resistive modes is similar to that of the ideal unstable modes. The components $\tilde{b}_r$ and $\tilde{b}_\perp$ are concentrated outside of the rational surface, and $\tilde{b}_\|$ is small. The parallel flow, $\tilde{v}_\|$, is large and peaked outside of the rational surface and $\tilde{v}_r$ is small. However there are some subtle differences. At the rational surface $\tilde{b}_r$ is finite for the resistive modes, but zero for the ideal modes. The perpendicular flow, $\tilde{v}_\perp$, peaks inside the rational surface for the resistive modes, while is peaks outside of the rational surface for the ideal modes.

Decreasing the Lundquist number S, increasing the resistivity, broadens the profiles of the resistive modes. At high S, $\tilde{v}_\perp$ and $\tilde{v}_\|$ are highly localized to the rational surface. Similarly $\tilde{b}_\perp$ is strongly peaked near the rational surface. All three of these profiles broaden significantly as S is decreased.

In summary the resistive MHD calculations agree with what we expect from theory and previous work. All three equilibria exhibit the same qualitative behavior. The linear growth rates increase with increasing D_S. Near the marginal point, $D_S = 0.25$, the growth rates are small. The growth rates of the ideal unstable modes, $D_s > 0.25$, do not depend of the resistivity. The ideal stable, $D_s = 0.2$, exhibits resistive interchange scaling, $\gamma\tau_A \sim S^{-1/3}$. We note that Ebrahimi et al. studied the transition from resistive to ideal stability in a cylindrical equilibrium with shear[94]. The equilibrium is relevant to a reversed field pinch and focused on an $m = 1$ instability. Figures 31A-B correspond to Figures 2 and 4 in their work. There is good agreement between our work and theirs. However, their growth rates are larger than ours, and their calculated growth rates show some dependence on the resistivity for $D_s \lesssim 1.0$.

4.3.4 Linear Calculations with Gyroviscosity

The linear calculations of the previous section are repeated including gyroviscosity in the momentum equation. The gyroviscosity is calculated self-consistently from the equilibrium. The calculations use the same physical and numerical parameters as the resistive MHD calculations. Figure 36 shows the linear growth rates and real frequencies for the $n = 5 \times 10^{19}\,\mathrm{m}^{-3}$ uniform density equilibrium. The gyroviscous growth rates are compared to the resistive MHD growth rates in Figure 36A. Gyroviscosity has a minimal effect on the growth rate of strongly ideal unstable modes $D_s \geq 1.0$. For $D_s = 2.0$, gyroviscosity reduces the growth rate by 0.6%, and for $D_s = 1.0$ gyroviscosity reduces the growth rate by 1.0%. These differences are comparable to the accuracy of our numerical representation. For the weakly ideal unstable case, $D_s = 0.5$, gyroviscosity reduces the growth rate by 25% to 35%. For this case the growth rate is weekly dependent on S. It changes by 7% as S is varied, but no clear trend is observed.

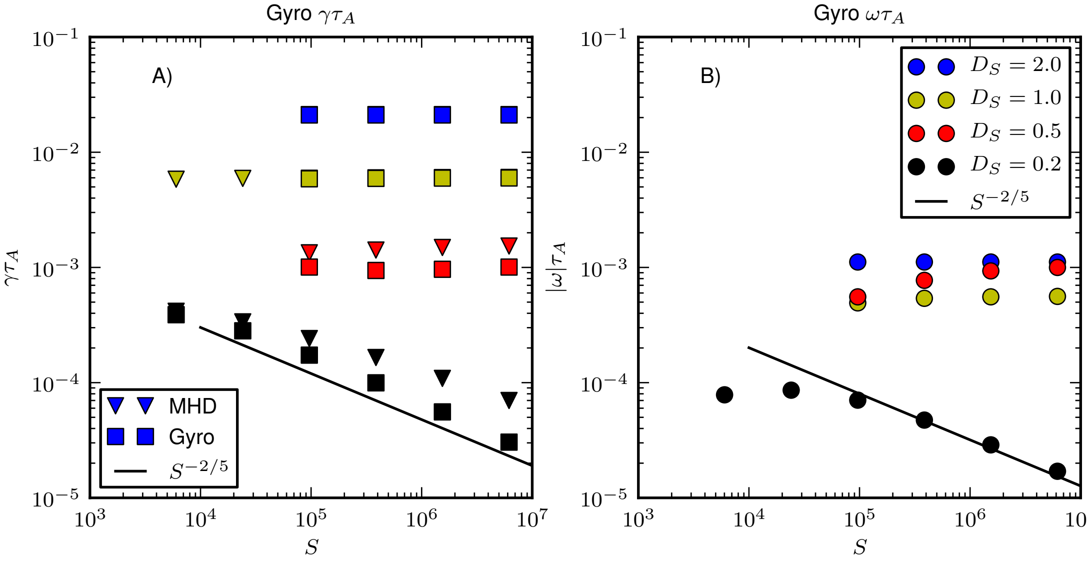

Figure 36: Gyroviscous growth rates and real frequencies for the uniform density equilibrium with $n = 5 \times 10^{19}\,\mathrm{m}^{-3}$. The growth rates calculated using resistive MHD (triangles) and gyroviscosity (squares) are shown in A). The magnitude of the real frequency for the gyroviscous calculations are shown in B).

The growth rate of the resistive mode, $D_s = 0.2$, scales as $\gamma\tau_A = S^{-2/5}$. This scaling is stronger than the resistive MHD scaling, $S^{-1/3}$, but not as strong as S^{-1} predicted for the limit $\omega_* \gg \gamma$ [31]. Gyroviscosity has the greatest stabilizing effect at large S, since the gyroviscous model scaling has a stronger dependence on S than the resistive MHD scaling. The growth rate is reduced by 7% at $S = 6.2 \times 10^3$ while the growth rate is reduced by 57% at $S = 6.2 \times 10^6$.

Gyroviscosity also imparts a real frequency on to the modes. The magnitude of these frequencies are shown in Figure 36B. The magnitude of real frequency is small compared to the growth rate for $D_s = 1.0$ and 2.0, while the growth rate is comparable in magnitude to the frequency for $D_s = 0.2$ and 0.5 . The real frequency exhibits no dependence on S for $D_s = 2.0$. It increases with S for $D_s = 0.5$ and 1.0. For $D_s = 1.0$ the real frequency increases by 14% as S increases from 9.6×10^4 to 6.2×10^6. For $D_s = 0.5$ the real frequency increases by 80% over the same range in S. For $D_s = 0.2$ the real frequency decreases with increasing S. At high S the real frequency scales as $S^{-2/5}$.

The growth rates and real frequencies for the $n = 10^{20}\,\mathrm{m}^{-3}$ equilibrium are shown in Figure 37, and the rates for the isothermal equilibrium in Figure 38. The effect of gyroviscosity in these two equilibria is similar to that in the $n = 5 \times 10^{19}\,\mathrm{m}^{-3}$ equilibrium with one exception. The real frequency changes non-monotonically for $D_s = 0.5$ in $n = 10^{20}\,\mathrm{m}^{-3}$ equilibrium. Here the real frequency has a maximum around $S = 10^6$. The net stabilizing effect with $n = 10^{20}\,\mathrm{m}^{-3}$ is always less than the stabilizing effect for $n = 5 \times 10^{19}\,\mathrm{m}^{-3}$. This is understood by noting that the normalized diamagnetic drift frequency scales as $1/\sqrt{n}$ while the normalized MHD growth rate, $\gamma_{mhd}\tau_A$, is independent of n. The ratio of the drift frequency to the growth rate is a measure of the relative strength of gyroviscosity to the MHD drive, and it decreases with increasing n.

Gyroviscosity alters the phase of the mode. Figure 39 shows the mode structure for $D_s = 1.0$ and Figure 40 shows the mode structure for $D_s = 0.2$. The plots show both the real (solid lines) and imaginary (dashed lines) components of $\tilde{b}$ and $\tilde{v}$ along the radial cord where Re b_r is maximal. Along this cord, $\tilde{b}_r$ is mostly real. Consider the ideal unstable case, $D_s = 1.0$. Here the real components of b_r, $v_\perp$, and $v_\parallel$ and the imaginary components of $b_\perp$ and v_r resemble the MHD mode structure. However, now the real components of $b_\perp$ and v_r and the imaginary components of $v_\perp$ and $v_\parallel$ are nonzero, indicating a phase shift.

The real components of $b_\perp$ and v_r and the imaginary components of $v_\perp$ and $v_\parallel$ are also nonzero for the resistive interchange case, $D_s = 0.2$. At $S = 6.0 \times 10^3$, the gyroviscous stabilization is weak, and the real components of b_r, $v_\perp$, and $v_\parallel$ and the imaginary components of $b_\perp$ and v_r resemble the MHD mode structure. At $S = 1.5 \times 10^6$, where the gyroviscous stabilization is significant, the imaginary component of $v_\parallel$ is depressed at the rational surface. Here the real component of $v_\parallel$ is the largest velocity component and resembles the imaginary component $v_\parallel$ in MHD calculations.

Figure 41 shows how the growth rates depends on the strength of the gyroviscosity. Note that the

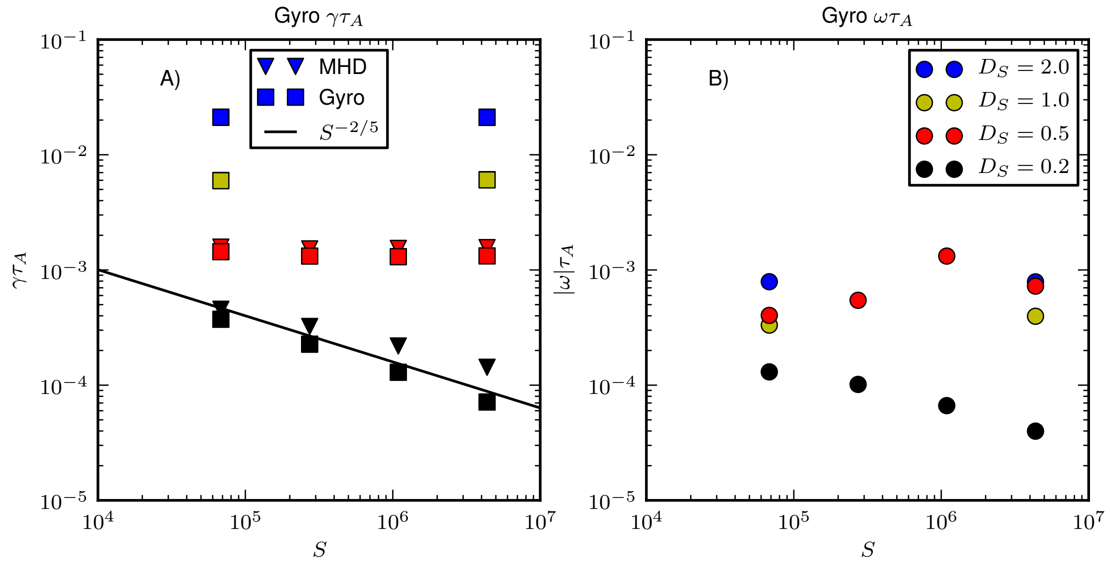

Figure 37: Gyroviscous growth rates and real frequencies for the uniform density equilibrium with $n = 10^{20}\,\mathrm{m}^{-3}$. The growth rates calculated using resistive MHD (triangles) and gyroviscosity (squares) are shown in A). The magnitude of the real frequency for the gyroviscous calculations are shown in B).

vertical and horizontal axis in Figures 41A-D use different scales. In these calculations the strength of the gyroviscosity is artificially amplified. Numerically this is done by changing an input parameter in the code, but physically this is equivalent to changing the electron charge. The Hall parameter, $\Lambda = d_i/a$, is used to indicate the strength of the gyroviscosity to make a direct comparison to calculations that use the full extended MHD model (presented in the next section). The growth rates in Figure 41 are calculated for the $n = 5 \times 10^{19}\,\mathrm{m}^{-3}$ equilibrium with $S = 9.6 \times 10^{4}$. The vertical line indicates the case from the previous calculations, where the gyroviscosity is not amplified. The MHD limit without gyroviscosity corresponds to $\Lambda = 0.0$.

Similar behavior is observed for all D_s as the strength of the gyroviscosity is varied. The growth rate decreases monotonically with increasing Λ. The behavior of the growth rate and the real frequency as a function of Λ changes with increasing Λ. At small Λ the graph of $\gamma\tau$ curve downwards, its second derivative is negative. Here each incremental increase in Λ has a greater stabilizing effect than the previous increase in Λ. At small Λ the real frequency increase linearly with Λ.

At an intermediate value of Λ the growth rate goes through an inflection point where the curvature

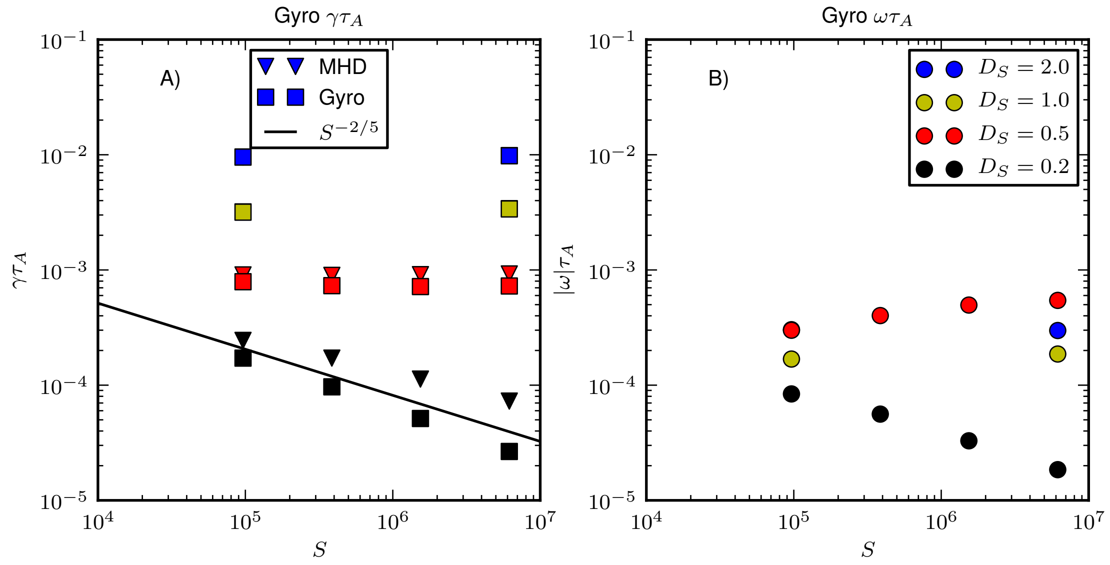

Figure 38: Gyroviscous growth rates and real frequencies for the isothermal equilibrium. The growth rates calculated using resistive MHD (triangles) and gyroviscosity (squares) are shown in A). The magnitude of the real frequency for the gyroviscous calculations are shown in B).

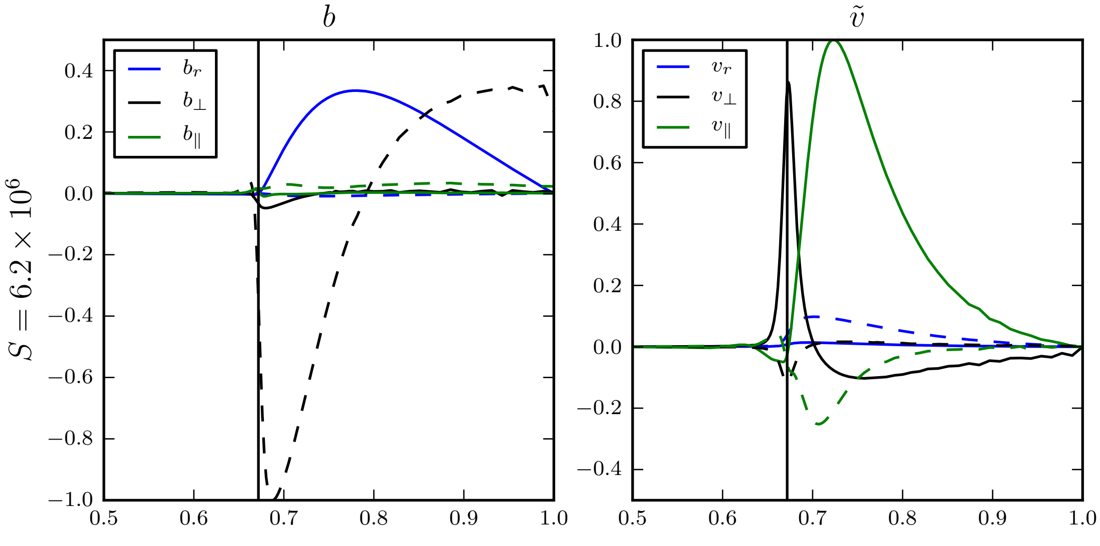

Figure 39: The gyroviscous mode structure is shown for $D_s = 1.0$. The solid (dashed) lines represent the real (imaginary) components of $\tilde{b}$ and $\tilde{v}$.

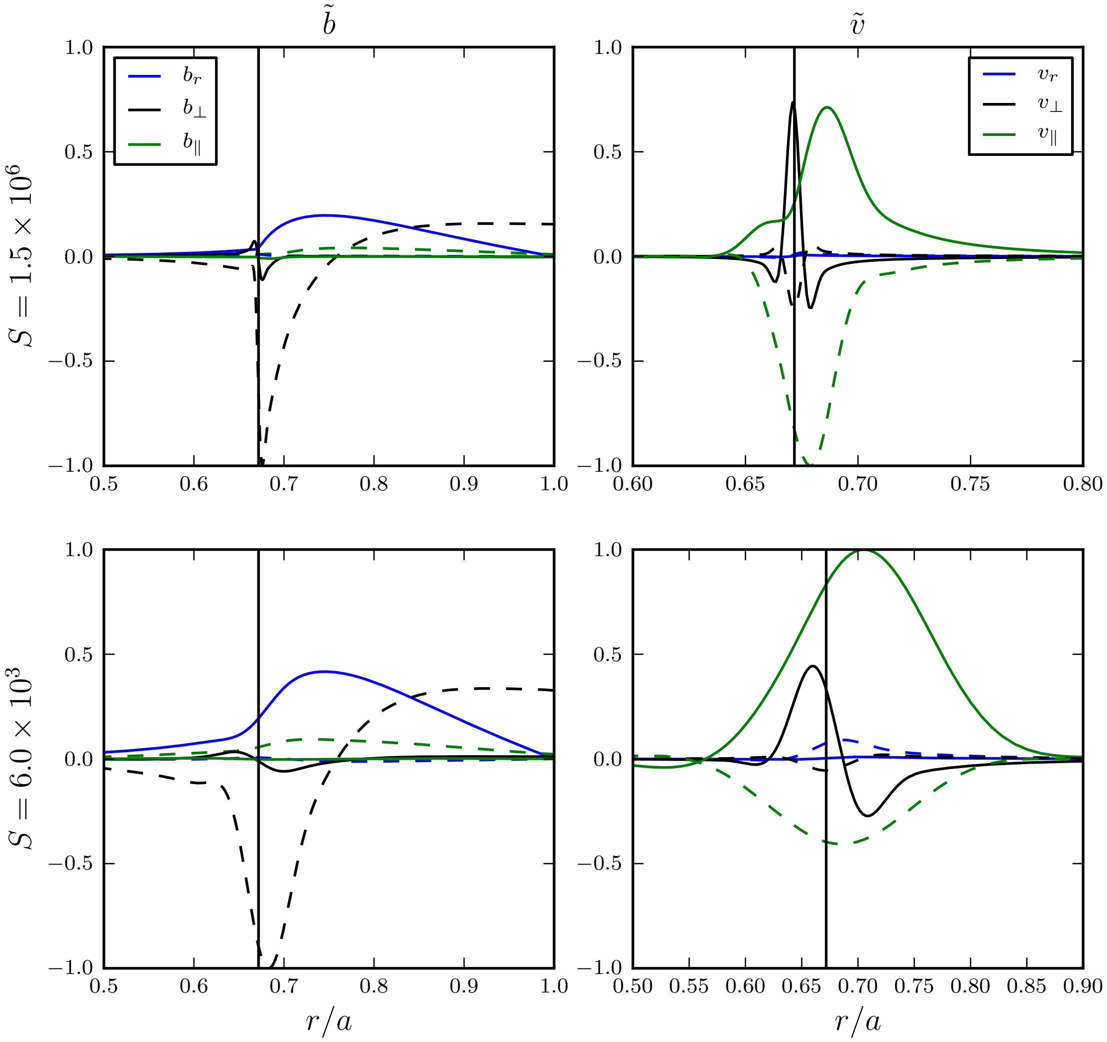

Figure 40: The gyroviscous mode structure is shown for $D_s = 0.2$ at two different values of S. The solid (dashed) lines represent the real (imaginary) components of $\tilde{b}$ and $\tilde{v}$.

of the growth rate changes sign, after which the graph curves upwards. Here each incremental increase in Λ has a smaller effect on the growth rate than the previous increase. The real frequency of the mode peaks near the inflection point, and after that the frequency decreases with increasing Λ.

The gyroviscosity has a significant effect on the modes with $D_s = 0.2$ and 0.5 at realistic values of Λ,

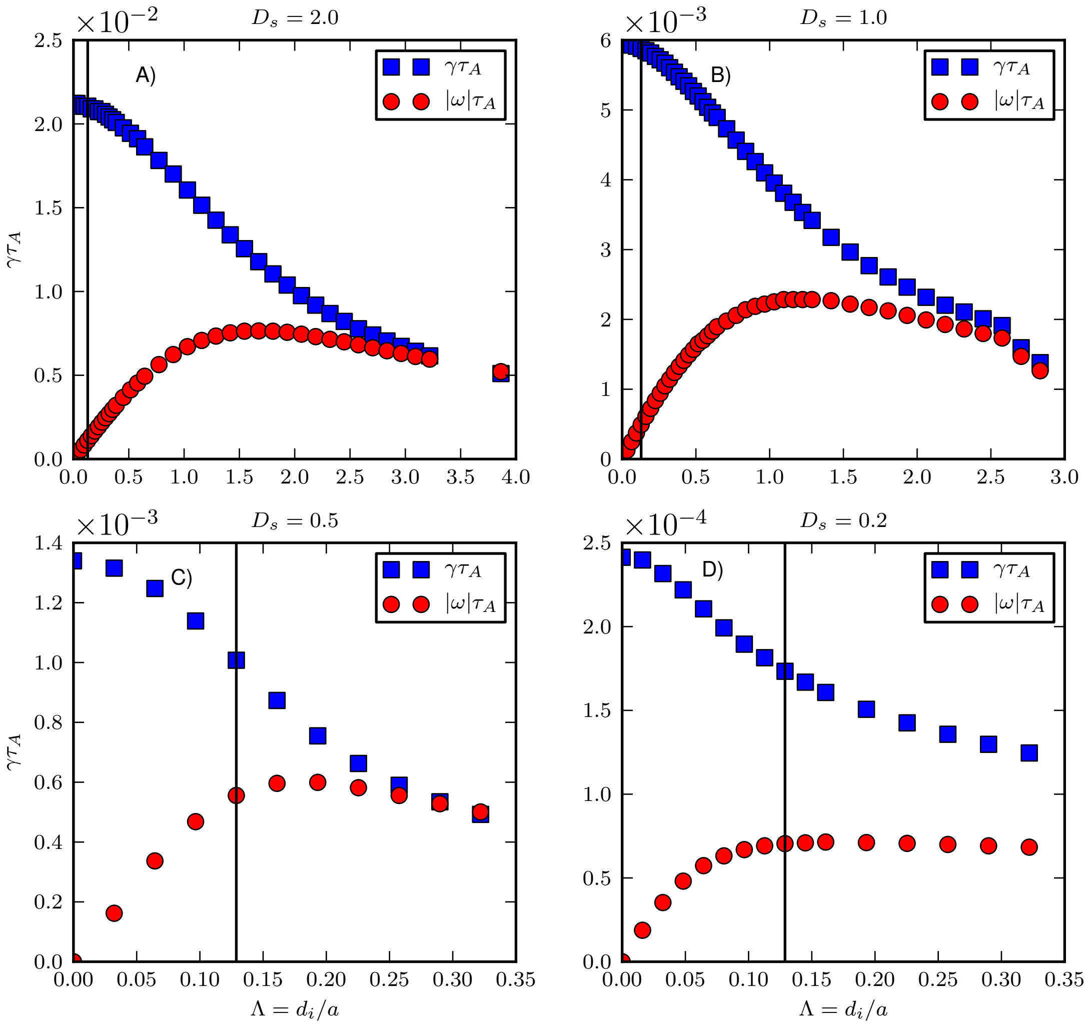

Figure 41: The growth rate and real frequency, calculated using the gyroviscous model, as a function of the Hall parameter Λ for A) $D_s = 2.0$, B) $D_s = 1.0$, C) $D_s = 0.5$, and D) $D_s = 0.2$. Calculations are for the $n = 5 \times 10^{19}\,\mathrm{m}^{-3}$ equilibrium and use $S = 9.6 \times 10^4$. The vertical line $\Lambda = 0.12$ indicates the physical Hall parameter for these equilibria.

where the gyroviscous model is physically valid. However, unrealistically large gyroviscosity is needed to significantly reduce the growth rate for $D_s = 1.0$ and $D_S = 2.0$. At these large values of Λ the small

Larmor radius assumption breaks down and kinetic effects not included in our model are important. The $D_s = 1.0$ case has an additional regime at very high Λ where the curvature of γ goes negative a second time, and the growth rate rapidly decreases with Λ. This regime only occurs at values of large Λ where kinetic effects are important.

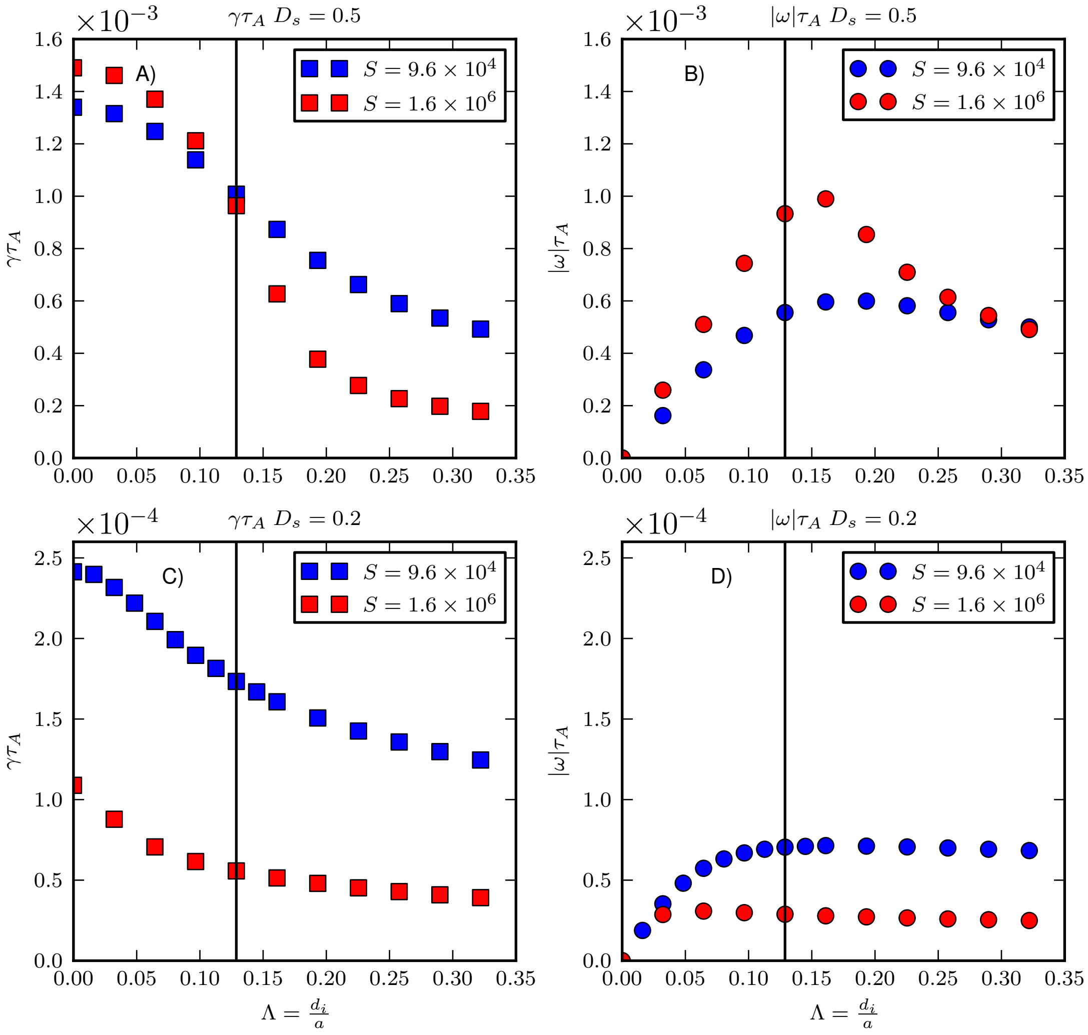

Figure 42: The growth rate and real frequency, calculated using the gyroviscous model, as a function of the Hall parameter Λ for two different values of S. Calculations use the $n = 5 \times 10^{19}\,\mathrm{m}^{-3}$ equilibria, and the vertical line at $\Lambda = 0.12$ indicates the physical Hall parameter.

The calculation of the growth rate as a function of Λ is repeated at $S = 1.6 \times 10^6$ for $D_s = 0.2$ and $D_s = 0.5$. Figure 42 compares the calculated growth rates and real frequencies at $S = 9.6 \times 10^4$ and 1.6×10^6. For the $D_s = 0.5$ equilibrium the higher S case has a slighter larger growth rate than the low S case at small Λ. However, at large Λ the gyroviscosity has a greater effect on the growth at high S than low S. At large Λ there is significant difference in the growth rate, with the high S case being more stable. The real frequency also exhibits a stronger dependence on Λ at higher S. The maximum frequency is greater at high S. This is consistent with Figures 36-37 where the real frequency increases with S for $D_s = 0.5$.

The case with physical gyroviscosity, $\Lambda = 0.12$, resides in this transition region where the $D_s = 0.5$ growth rate is most sensitive to Λ. At smaller values of Λ the growth rate only exhibits a weak dependence on S, while at large values of Λ there is a clear dependence on S.

Figure 43 shows the $D_s = 0.5$ mode structure at $\Lambda = 0.064$ and $\Lambda = 0.257$ for $S = 1.6 \times 10^6$. The most significant changes are in $\tilde{v}_{\|}$ and $\tilde{v}_{\perp}$. At small Λ the magnitude of real components of $\tilde{v}_{\|}$ and $\tilde{v}_{\perp}$ are greater than the magnitude of the imaginary components. At large Λ the real and imaginary components of $\tilde{v}_{\perp}$ have a similar magnitude, and the imaginary component of $\tilde{v}_{\|}$ is larger than the real component. The structure of the real component of $\tilde{v}_{\|}$ changes significantly near the rational surface. At small Λ the real component is positive and increases monotonically across the surface. At large Λ the real component of $\tilde{v}_{\|}$ is negative and has even symmetry about the rational surface. There is little change in the perturbed magnetic field, $\tilde{b}$, as Λ is increased.

In summary the gyroviscous model is always more stable than the MHD model and increasing the strength of the gyroviscous stress reduces the growth rate. Gyroviscosity has the greatest effect on the resistive mode at high S. Here the growth rate and real frequency scales as $\gamma\tau_A \sim S^{-2/5}$. The gyroviscosity also has a significant effect for $D_s = 0.5$ reducing the growth rate by as much as 35%. Gyroviscosity has little effect on the $D_S = 1.0$ and $D_S = 2.0$ cases.

4.3.5 Single Temperature Extended MHD Calculations

The linear calculations are repeated using the full extended MHD model that includes the two-fluid Ohm's law and ion gyroviscosity in the momentum equation. The two-fluid Ohm's law includes the

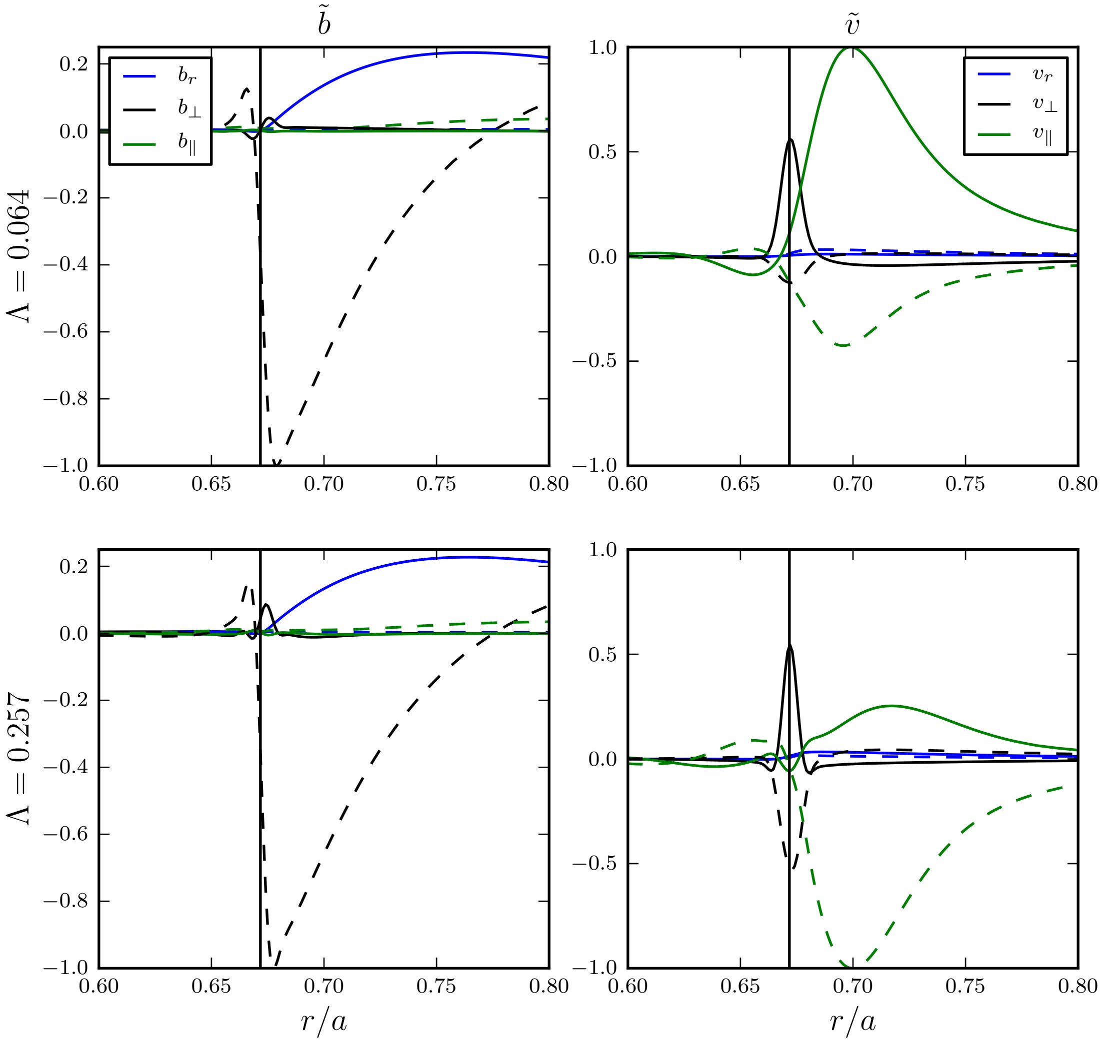

Figure 43: Gyroviscous mode structure for $D = 0.5$ at $S = 1.6 \times 10^6$. The solid (dashed) lines represent the real (imaginary) components of $\tilde{b}$ and $\tilde{v}$.

Hall term, electron pressure, and the $\frac{\partial}{\partial t}\vec{J}$ part of the electron inertia term, where the electron inertia is calculated using the physical value for electron mass. These calculations use a single temperature advance, and unless otherwise stated the electron and ions temperatures are equal.

An intermediate model worth considering includes the two-fluid Ohm's law but neglects gyroviscosity. This model would allow for the direct study of two-fluid effects on the interchange mode. However, calculations that use the two-fluid Ohm's law are computationally difficult. These calculations are hindered by unphysical numerical modes. Gyroviscosity helps stabilizes the numerical modes. The model that uses the two-fluid Ohm's law with gyroviscosity is significantly more robust than the two-fluid model that neglects gyroviscosity. This model with gyroviscosity is more consistent than the model without. For these reasons we forgo studying the intermediate two-fluid model that neglects gyroviscosity. Even with gyroviscosity the linear calculations with the two-fluid Ohm's law are challenging. The most difficult calculations involve modes with small physical growth rates and large Λ. In some cases extremely small time steps, $\gamma \Delta t < 10^{-6}$, are required to avoid numerical instabilities.

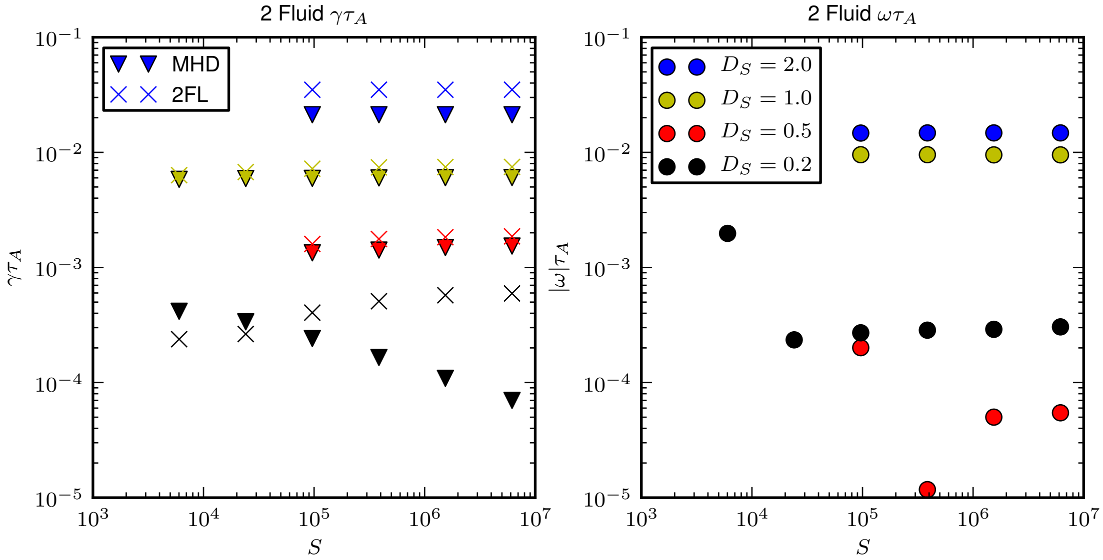

Figure 44: The growth rate A) and real frequency B) as a function of S using the full extended MHD single temperature model with the uniform $n = 5 \times 10^{19}\,\mathrm{m}^{-3}$ equilibria. The extended MHD growth rates (x) are compared with the MHD growth rates (circles).

The linearly calculated growth rates for the uniform $n = 5 \times 10^{19}\,\mathrm{m}^{-3}$ equilibria are shown in Figure 44. Unlike results from the gyroviscous model, the extended MHD growth rates are greater than the MHD growth for all D_s with $S \gtrsim 10^5$. The growth rate is increased by 65% for $D_s = 2.0$, the growth rate is increased by approximately $20 - 25\%$ for $D_s = 0.5$ and $D_S = 1.0$. The greatest difference is for

$D_s = 0.2$ at high S. At $S = 6.2 \times 10^6$ the extended MHD growth rate is 7 to 8 times larger than the resistive MHD growth rate. The extended MHD growth rate for $D_s = 0.2$ increases with decreasing resistivity. The growth rate increases from $\gamma\tau_A = 4.0 \times 10^{-4}$ at $S = 9.6 \times 10^4$ to $\gamma\tau_A = 5.9 \times 10^{-4}$ at $S = 6.2 \times 10^6$, an increase of 48%.

The real frequency of the modes is nearly constant for $D_s = 0.2$, 1.0, and 2.0, and the magnitude of the frequency for these modes increases with D_s. However, the magnitude of the frequency for $D_s = 0.5$ is smaller than that for the $D_s = 0.2$ case, and the frequency dramatically decreases between $S = 9.6 \times 10^4$ and $S = 3.9 \times 10^5$. This large change in the frequency is indicative of a transition to a new instability. A similar change in frequency is observed for $D_s = 0.2$ at small S.

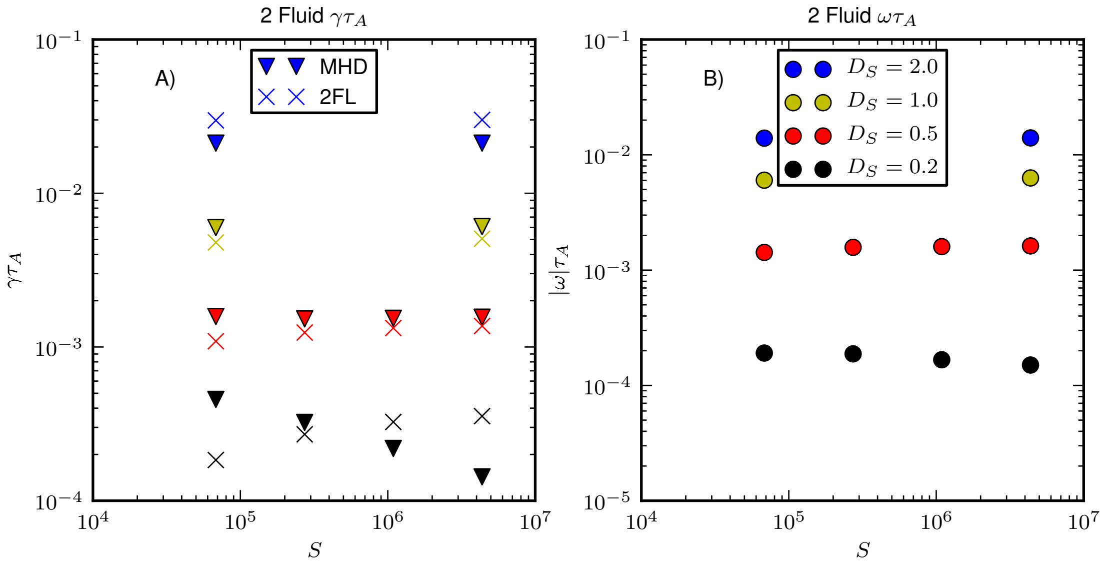

Figure 45: The growth rate A) and real frequency B) as a function of S using the extended MHD single temperature model with the uniform $n = 10^{20}\,\mathrm{m}^{-3}$ equilibria. The extended MHD growth rates (x) are compared with the MHD growth rates (circles).

The growth rates and frequencies for the $n = 10^{20}\,\mathrm{m}^{-3}$ equilibrium are shown in Figure 45, and the growth rates for the isothermal equilibrium are shown in Figure 46. In both of these equilibria the extended MHD model has a mixed effect. In some cases the extended MHD growth rates are greater than the MHD growth rates, while in other cases the extended MHD growth rates are smaller than the MHD growth rates. The magnitude of the real frequencies increase monotonically with D_S for the uniform $n = 10^{20}\,\mathrm{m}^{-3}$ equilibrium, and there are no jumps in the real frequency as S is increased. The magnitude of the frequency for $D_s = 0.5$ is still less than the frequency for $D_s = 0.2$ for the isothermal equilibrium, and again there are no jumps in frequency as S is varied. The real frequencies for all D_s are of the same magnitude for the isothermal equilibria, where these frequencies vary by several orders of magnitude for both the uniform $n = 5 \times 10^{19}\,\mathrm{m}^{-3}$ and uniform $n = 10^{20}\,\mathrm{m}^{-3}$ equilibria.

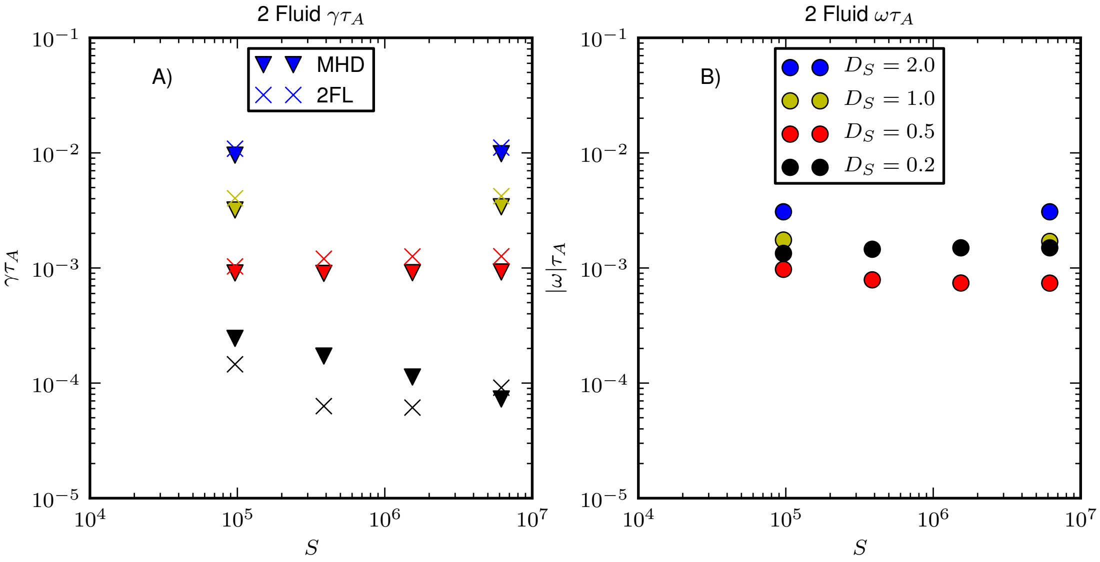

Figure 46: The growth rate A) and real frequency B) as a function of S using the full extended MHD single temperature model for the isothermal equilibria. The extended MHD growth rates (x) are compared with the MHD growth rates (circles).

To understand this behavior we look at the dependence of the extended MHD growth rate on Λ for the uniform density equilibria with $n = 5 \times 10^{19}\,\mathrm{m}^{-3}$. Figure 47 shows the growth rate as $S = 9.6 \times 10^4$. Here there are two (or more) instabilities that dominate at different Λ. The extended MHD effects are stabilizing at small Λ for all the cases with $D_s \leq 1.0$. Here the growth rate decreases with increasing Λ.

There is a transition to a second instability at finite Λ. The growth rate of this second instability increases with Λ. This transition occurs at $\Lambda \approx 0.6$ for $D_s = 0.2$, $\Lambda \approx 0.3$ for $D_s = 0.5$, and $\Lambda \approx 0.6$ for $D_s = 1.0$. There is a noticeable jump in the real frequency around this transition for $D_s = 0.2$ and $D_s = 0.5$. The real frequency of for $D_s = 0.5$ jumps a third time between $\Lambda = 0.10$ and $\Lambda = 0.12$ possibly indicating a third mode. However, the growth rate changes smoothly between these two values.

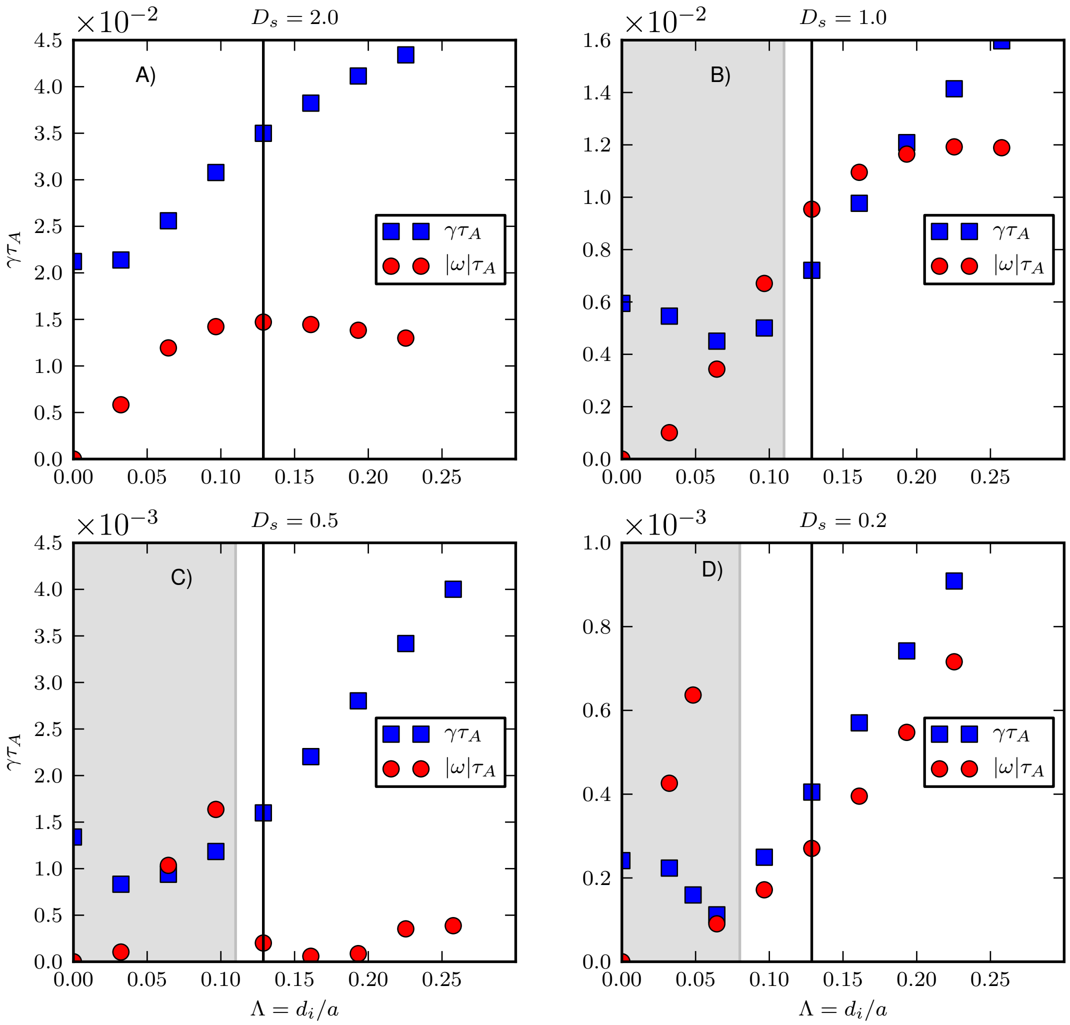

Figure 47: The extended MHD growth rates and real frequencies are shown as a function of Λ for the uniform density equilibria with $n = 5 \times 10^{19}\,\mathrm{m}^{-3}$ at $S = 9.6 \times 10^4$.

There is a small range of Λ where the extended MHD effects are stabilizing. The approximate range is indicated by the shaded region in Figure 47. At $n = 5 \times 10^{19}\,\mathrm{m}^{-3}$, the physically relevant Hall parameter is $\Lambda = 0.12$ (indicate by the black vertical lines). This value of Λ lies outside the region where extended MHD is stabilizing. Here the second instability is the dominant mode. However, at

$n = 10^{20}\,\mathrm{m}^{-3}$ the physically relevant hall parameter is $\Lambda = 0.6$, and it lies within the region where extended MHD is stabilizing for $D_s \leq 1.0$. This is consistent with the observation that extended MHD is sometimes stabilizing in the higher density equilibrium.

The growth rates exhibit a similar dependence on Λ at $S = 1.5 \times 10^6$. The growth rates and the real frequencies for $D_s = 1.0$ and $D_s = 2.0$ do not change between $S = 9.6. \times 10^4$ and $S = 1.5 \times 10^6$. While the growth rate and real frequency of the second mode increases with S for $D_S = 0.2$ and $D_s = 0.5$.

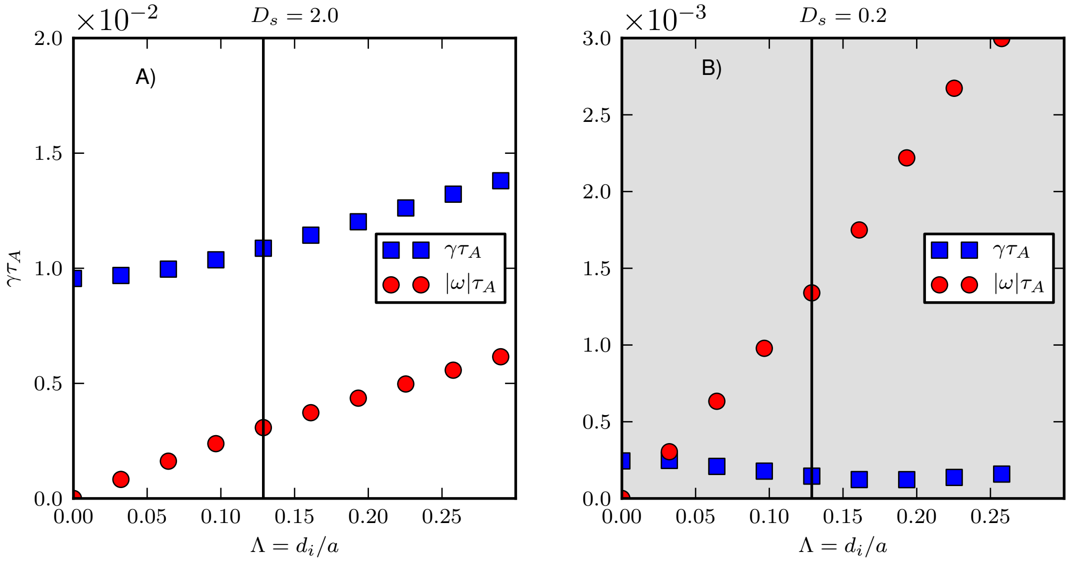

Figure 48: The full extended MHD growth rates and real frequencies are shown as a function of Λ for the isothermal equilibria at $S = 9.6 \times 10^4$.

This transition to a second instability is not clearly observed in the isothermal equilibrium. The growth rates for this equilibrium are shown for the $D_s = 0.2$ and $D_s = 2.0$ in Figure 48 at $S = 9.6 \times 10^4$. For $D_s = 2.0$ the growth rate and real frequency increases with Λ for all Λ. Similar behavior is observed for $D_s = 0.5$ and $D_s = 1.0$. For $D_s = 0.2$ the extended MHD effects reduce the growth rate at small Λ. The growth rate has a minimum value around $\Lambda = 0.19$ and slowly increase with Λ beyond this point. The extended MHD effects are stabilizing for $D_s = 0.2$ when $\Lambda \leq 0.25$. A numerical mode arises at $\Lambda > 0.25$ that prevents us from exploring this regime.

Figure 49 shows the mode structure for the $n = 5 \times 10^{19}\,\mathrm{m}^{-3}$ uniform density equilibrium with $D_s = 1.0$ at $S = 9.6 \times 10^4$ at two different values of Λ. As with the gyroviscous case, the mode structure is plotted along the cord where the real component of b_r has its maximum amplitude. The solid (dashed) lines are the real (imaginary) components of b and v.

The first value of the Hall parameter, $\Lambda = 0.032$, occurs before the transition to the second mode, and here the extended MHD effects are stabilizing. Extended MHD has huge impact on the mode structure even at this small value of Λ. The three component of $\tilde{b}$ have similar amplitudes and structure. They are small inside of the rational surface, and they peak just outside of the ration surface. The real component of $\tilde{b}_{||}$ is negative, while the real components of $\tilde{b}_r$ and $\tilde{b}_\perp$ are positive. Similarly the imaginary components also of $\tilde{b}$ all have similar shape and amplitude. However, now $\tilde{b}_\perp$ and $\tilde{b}_{||}$ have the same sign, while $\tilde{b}_r$ has the opposite sign.

Figure 50 shows the mode structure for the $n = 5 \times 10^{19}\,\mathrm{m}^{-3}$ uniform density equilibrium with $D_s = 0.2$ at $S = 9.6 \times 10^4$. $\Lambda = 0.048$ is before the transition to the second mode, and here the extended MHD effects are stabilizing. The components of $\tilde{b}$ resemble the resistive MHD mode structure. The biggest difference is that $\tilde{b}_\perp$ has a significant real component, which has odd symmetry about the rational surface. The real components of $\tilde{v}_\perp$ and $\tilde{v}_{||}$ also resemble the MHD mode structure. The imaginary components are finite and have an oscillatory structure.

The larger value of the Hall parameter, $\Lambda = 0.161$, represents conditions where the second mode is unstable. Here the extended MHD growth rate is larger than the resistive MHD growth rate. There is a subtle change in shape of $\tilde{b}$. Here the real component of $\tilde{b}_r$ is zero at the rational surface. Similarly $\tilde{b}_\perp$ is now finite at the rational surface. The oscillatory nature of $\tilde{v}_{||}$ is more pronounced, and now the oscillations have their maximum amplitude inside of the rational surface.

The existence of this second instability counteracts the extended MHD stabilization of the interchange mode. However, JDG did not observe a second instability in their two-fluid calculations [79]. As previously mentioned, they assumed cold ions and the total pressure in their calculations is entirely due to the electrons. Motivated by the difference between the two results, we perform a second series of calculation where the electron temperature is 3 times the ion temperature. The total pressure in these equilibria is a fixed constant independent of the ratio of the two temperatures. The results are shown in Figure 51 for $D_s = 1.0$ and $D_s = 2.0$. There is little change in the growth rate for $\Lambda \lesssim 0.05$, where the interchange mode is the dominant mode. However at larger values of Λ, where the second instability dominates, the case with the colder ions has smaller growth rates. This trend is consistent

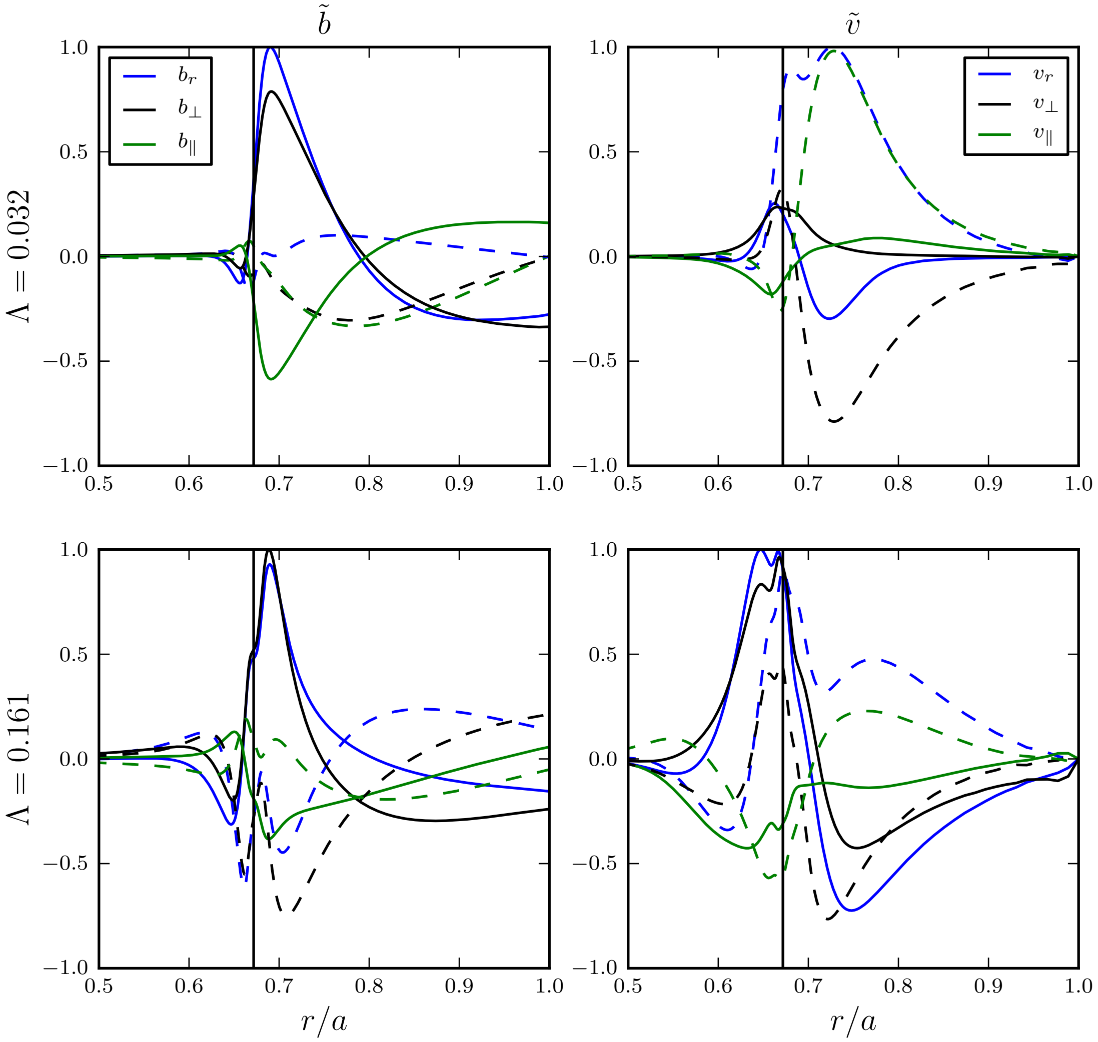

Figure 49: The full extended MHD mode structure is shown for $D_s = 1.0$ for Λ values of the primary mode (0.012) and of the second mode (0.161). The solid (dashed) lines represent the real (imaginary) components of $\tilde{b}$ and $\tilde{v}$. Calculations use the uniform density $n = 5 \times 10^{19}\,\mathrm{m}^{-3}$ equilibrium at $S = 9.6 \times 10^4$.

with the differences between our results and those of JDG. We also note that our analysis of the g-mode, discussed in Section 4.4, shows a second instability that is only present with finite ion temperature.

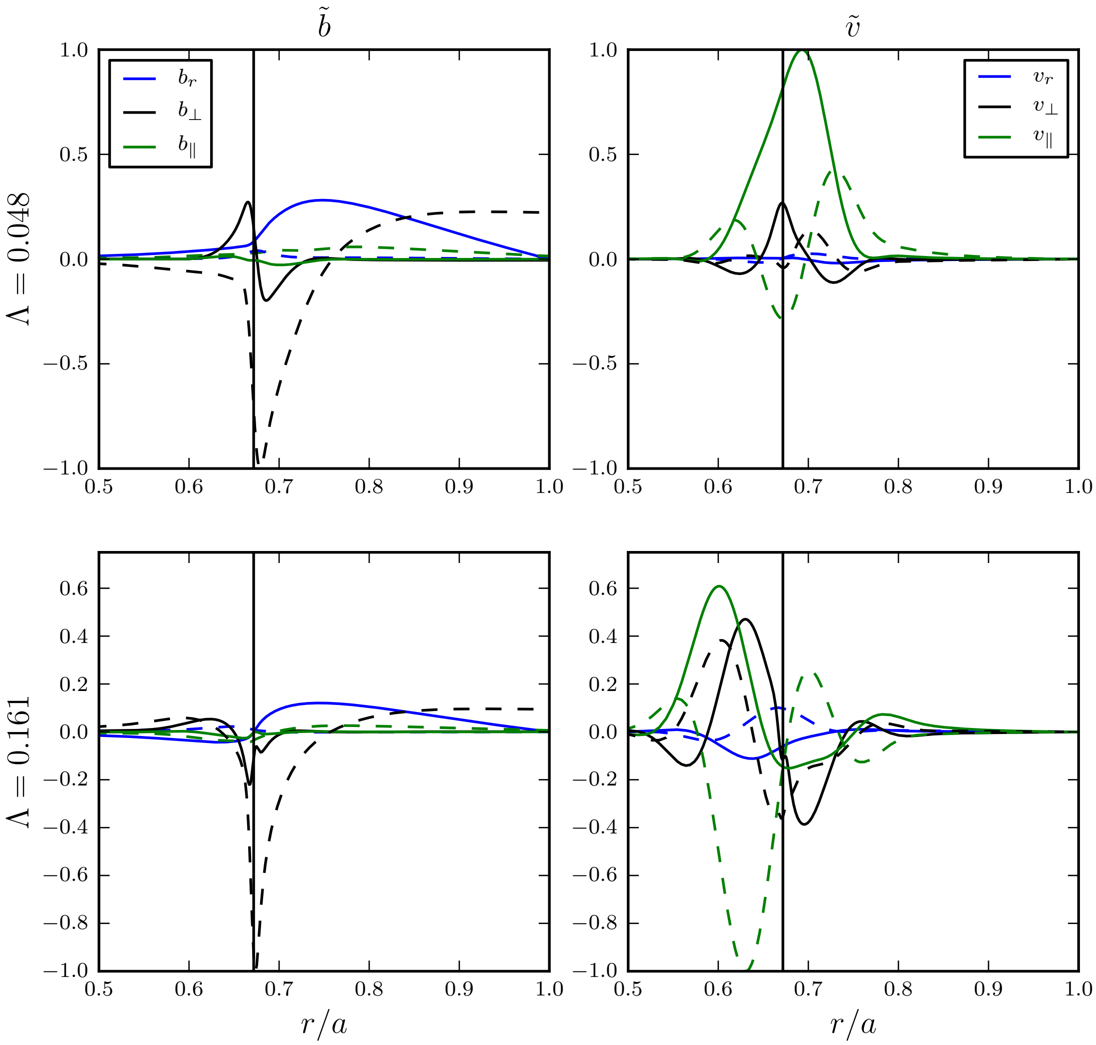

Figure 50: The full extended MHD mode structure is shown for $D_s = 0.2$. The solid (dashed) lines represent the real (imaginary) components of $\tilde{b}$ and $\tilde{v}$. Calculations use the $n = 5 \times 10^{19}\,\mathrm{m}^{-3}$ uniform density equilibrium at $S = 9.6 \times 10^4$.

4.3.6 Linear Extended MHD Two-Temperature Calculations

The final model that we considered includes both gyroviscosity and the two-fluid Ohm's law. In addition, this model also allows for separate electron and ion temperature advances and includes the

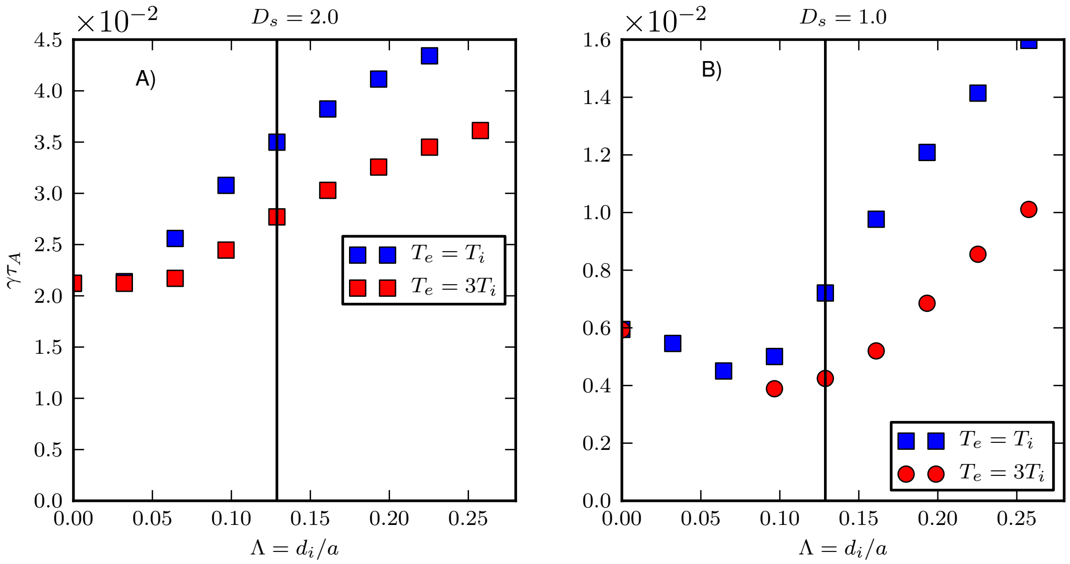

Figure 51: Increasing the ratio of T_e/T_i decreases the linear growth rate at large Λ. The linear growth rates are shown for two values of T_e/T_i. These calculation use the single temperature extended MHD model with a uniform density of $n = 5 \times 10^{19}\,\mathrm{m}^{-3}$ at $S = 9.6 \times 10^4$.

diamagnetic heat flux $\vec{q}_*$. The equilibrium ion and electron temperatures are assumed to be equal. The equilibrium also includes an applied ion-diamagnetic flow. The flow is not included in the force balance when calculating the equilibrium $\vec{B}$, $\vec{J}$, and p. The equilibria are still in approximate force balance if flows are sufficiently slow.

The two-temperature model is the most difficult model computationally, and it requires increased particle and thermal diffusivity. In these calculations we only consider the $S = 9.6 \times 10^4$ case, and use $7\eta/\mu_0 = D_n = \chi_{iso}$. The isotropic viscosity is still small compared to the electrical diffusivity $\eta/\mu_0 = 10\nu_{iso}$.

The linear growth rates are calculated as a function of Λ by increasing the electron charge. The equilibrium ion flow is scaled consistently with the electron charge. The linear growth rates and their real frequencies are shown in Figures 52-53. Figures 52A-B show the growth rate and real frequency for $D_s = 2.0$, and Figures 52C-D show the growth rate and real frequency for $D_s = 1.0$. Similarly, Figures 53A-B show the growth rate and real frequency for $D_s = 0.5$, and Figures 53C-D show the growth rate and real frequency for $D_s = 0.2$. The shaded region roughly indicates the range of Λ where the

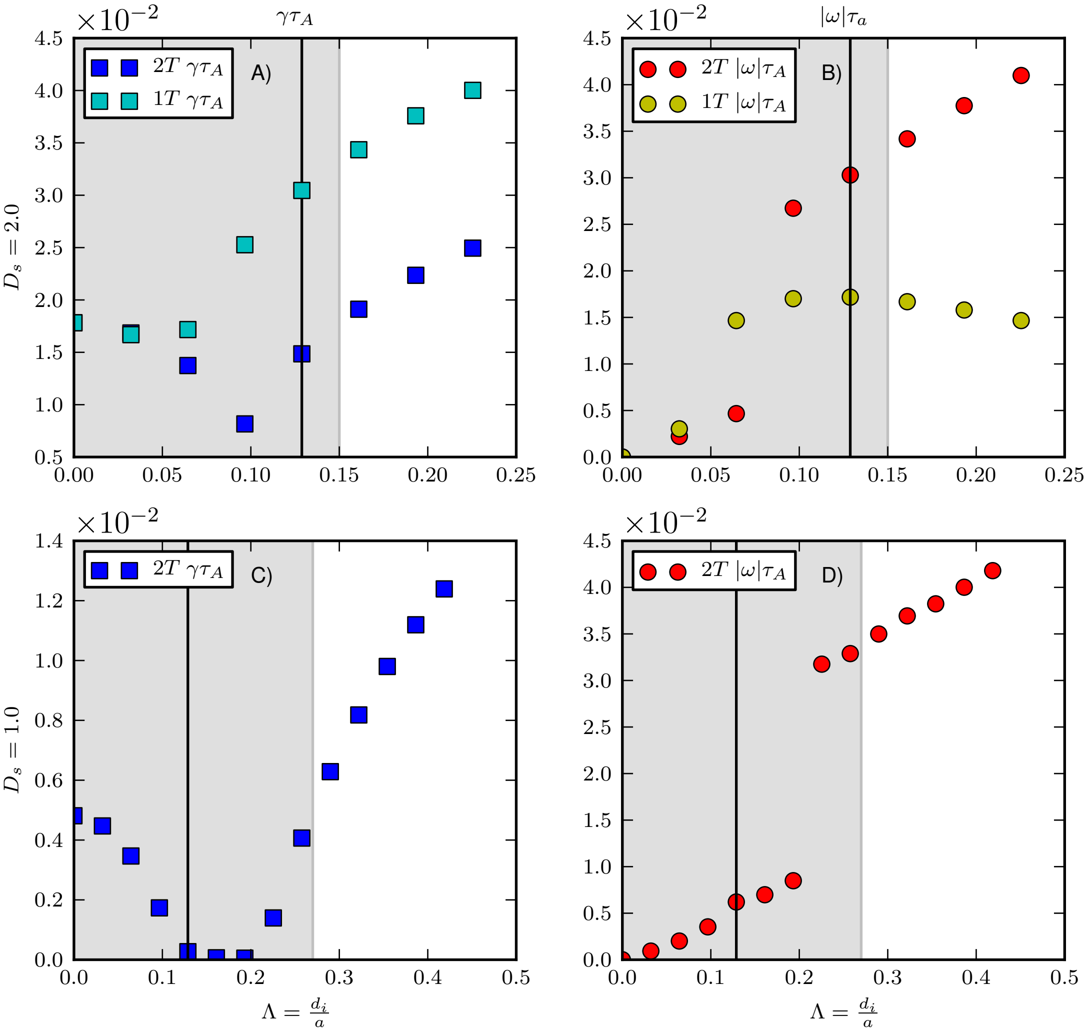

Figure 52: The linear growth rates and real frequencies calculated using the full extended MHD model with separate electron and ion temperature advances are shown for $D_s = 2.0$ (A-B) and $D_s = 1.0$ (C-D). Also shown in A-B are the linear growth rates calculated using the single temperature full extended MHD model.

extended MHD two-temperature growth rate is smaller than the resistive MHD growth rate. The solid vertical line indicates the physical Λ for $n = 5 \times 10^{19}\,\mathrm{m}^{-3}$.

The enhanced particle and thermal diffusivities have a noticeable stabilizing effect on the MHD

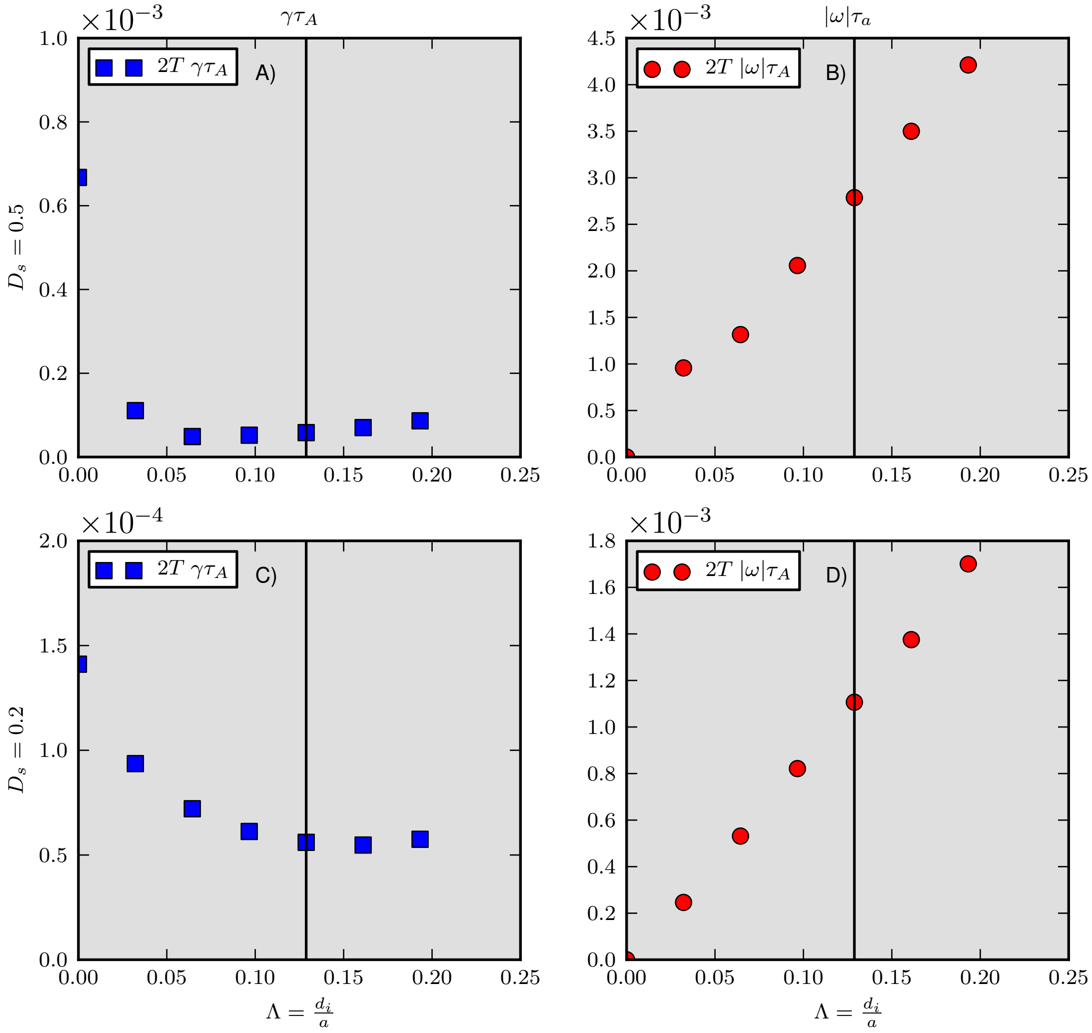

Figure 53: The linear growth rates and real frequencies calculated using the full extended MHD model with separate electron and ion temperature advances are shown for $D_s = 0.5$ (A-B) and $D_s = 0.2$ (C-D)

growth rate ($\Lambda = 0$). At $D_s = 2.0$ these effects decrease the MHD growth rate by 16%. At $D_s = 0.2$ they decrease MHD growth rate by 42%. One series of extended MHD single-temperature calculations is rerun at $D_S = 2.0$ with the two-temperature dissipation parameters. This allows for direct comparison of the two models. The results of this single temperature calculation are also shown in 52A-B.

Consider the $D_s = 1.0$ case which is shown Figure 52C-D. This case clearly shows that there are two separate instabilities. The interchange mode exists at small Λ and its growth rate is reduced with increasing Λ. The real frequency of the mode increases roughly linearly with Λ. At $\Lambda = 0.12$ the interchange mode is almost completely stabilized. The growth rate has been reduced by 94%. Between $\Lambda = 0.12$ and $\Lambda = 0.20$ the growth rate remains small and decreases with Λ, but the real frequency continues to increases linearly with Λ. In this region the growth rate is comparable to the growth rate of the resistive interchange mode. At $\Lambda = 0.12$ the growth rate is $\gamma\tau_A = 2.7 \times 10^{-4}$. Around $\Lambda = 0.20$ a second mode goes unstable. The transition to the second mode is clearly indicated by the jump in the real frequency. The growth rate and real frequency of the second mode increases with Λ. The growth rate surpasses that of the MHD interchange mode around $\Lambda = 0.27$

Similar behavior is observed for $D_s = 2.0$; however, the second instability goes unstable and becomes the dominant mode before the interchange mode is mostly stabilized. A jump in the real frequency is observed between $\Lambda = 0.06$ and $\Lambda = 0.09$, where the growth rate is minimal. The growth rate at $\lambda = 0.9$ is 46% of the MHD growth rate. The transition to the second mode occurs at higher Λ for the two-temperature calculations than is does for the single temperature calculation. The two-temperature calculation is significantly more stable than the single temperature calculation for $\Lambda > 0.5$.

The extended MHD two-temperature model reduces the growth rate for $D_s = 0.5$, Figure 53A-B, and $D_s = 0.2$, Figure 53C-D, for $\Lambda < 0.20$. The second instability is not observed in these two cases. This model has a dramatic effect on the $D_s = 0.5$ mode even at small Λ. Here the growth rate is reduced to levels comparable to that of resistive interchange mode. At $\Lambda = 0.03$ the growth rate is reduced to $\gamma\tau_A = 10^{-4}$.

4.3.7 Discussion of Straight Spheromak Results

The analysis of the straight spheromak equilibria show that different extended MHD models yield significantly different results, quantitatively and qualitatively. The gyroviscous model is always stabilizing, but only has a significant effect for $D_s \lesssim 0.5$. A second instability is present in the single temperature extended MHD model that includes gyroviscosity and the two-fluid Ohm's law. This second instability is unstable at experimentally relevant Λ and has a growth rate that is comparable to the resistive MHD growth rate. This second instability is the dominant mode at SSPX relevant values of Λ, and its growth rate is often greater than the MHD interchange growth rate. The instability is also present in the two-temperature extended MHD model. The growth rate of the second instability is reduced in the two-temperature model, and the onset of the second instability is delayed to higher Λ. As a result, there is a range of SSPX relevant parameters where there is significant stabilization. In particular, there is significant stabilization at physical values of Λ for $D_s \lesssim 1.0$. This is 4 times the Suydam stability point.

There have been a few other studies of extended MHD effects on resistive interchange modes that use this or similar equilibria. JDG used this family of equilibria to study $m = 1$ interchange modes for $D_s = 0.175$ [79]. They found complete stabilization of these modes for $\Lambda \gtrsim 0.2$, and they don't encounter a second instability. However, they use a single-temperature two-fluid model that assumes cold ions. We find that the growth rate of the second mode decreases with decreasing ion pressure (at fixed total pressure), but taking the cold ion limit is not tractable in our computations. Hammet and Tang also studied resistive interchange modes in these equilibria using a gyrokinetic ballooning model [81]. They order drift waves out of the system in their analysis. In the next section we analyze the gravitational interchange mode and find a second instability due to the interaction between the ion drift wave and the stabilized g-mode. If the instability in the straight spheromak is due to a similar interaction, then the absence of ion drift waves in both JDG and Hammet and Tang explains why neither study observe the second instability.

4.4 Analysis of the Extended MHD g-mode

The g-mode is often used as a model to study the interchange mode by introducing a fictitious gravitational force to represent magnetic curvature. An introduction to the g-mode is presented in Section 2.3.2. Our aim is to use the g-mode to illustrate the variety of linear modes that arises in various extended MHD models. We expect a similar range of properties for the pressure driven interchange mode.

The analysis uses the local dispersion relation derived by Zhu et al. for the g-mode in a slab[36].

Zhu considers the static equilibrium described by

$$\vec{V} = 0 \tag{4.12}$$

$$\vec{B} = B\hat{e}_z \tag{4.13}$$

$$\frac{d}{dx}\left(p + \frac{B^2}{2\mu_0}\right) = \rho g \tag{4.14}$$

$$neE_x = \frac{d}{dx}p_i - \rho g, \tag{4.15}$$

where gravity points in the x direction and is balanced by gradients in the pressure and magnetic field. Equilibrium quantities only vary in the x direction.

The dispersion relation is derived using the extended MHD model implemented in NIMROD (Equations 2.87-2.92). The model includes gyroviscosity and uses a two-fluid Ohm's law that includes the Hall term and electron pressure but neglects electron inertia. The model also assumes an adiabatic equation of state neglecting the diamagnetic heat flux q_*. Perturbed quantities vary as $\tilde{f} = \tilde{f}(x)\, e^{ik_y y - i\omega t}$. The model uses the ordering $k_y L \sim \epsilon^{-1}$, $k_y r_i \sim 1$, and $\tilde{v}_y \sim \epsilon \tilde{v}_x$ where $\epsilon \ll 1$ is a small parameter, L is the equilibrium gradient scale length, and $r_i^2 = P_i/\left(\rho\Omega^2\right)$ is the ion Larmor radius squared. Formally extended MHD is only physically valid for $k_y r_i \ll 1$, but the ordering $k_y r_i \sim 1$ permits the study of the extended MHD model at all values of $k_y r_i$.

Zhu's dispersion relation for the g-mode is

$$A\omega^3 + \omega_*\omega^2 + \omega\Gamma_{FLR}^2 + D = 0 \tag{4.16}$$

$$A = 1 + \gamma_s\beta + \delta^2\frac{\tau k_y^2 r_i^2}{4}\beta \tag{4.17}$$

$$\omega_* = \delta\left[\left(1+\gamma_s\beta\right)\left(1+\beta\right)\omega_{pi} + \left(2+\gamma_s\beta\right)\tau\beta\omega_g\right] + \lambda\left[\omega_g + \omega_{pi} - \gamma_s\omega_{ni} - \delta^2\frac{k_y^2 r_i^2}{4}\omega_{ni}\right] \tag{4.18}$$

$$\Gamma_{FLR}^2 = \Gamma_M^2\left(1+\gamma_s\beta\right) + \frac{g^2}{V_a^2} + \delta\lambda\Gamma_1^2 \tag{4.19}$$

$$\Gamma_M^2 = -\frac{\rho'}{\rho}g \tag{4.20}$$

$$\Gamma_1^2 = \left(1+\beta\right)\left(\omega_{pi}+\omega_g\right)\omega_{pi} - \left(\left(1+\gamma_s\beta\tau\right)\omega_g + \left(1+\beta\right)\gamma_s\omega_{pi}\right)\omega_{ni} + \left(\omega_g+\omega_{pi}\right)\tau\beta\omega_g \tag{4.21}$$

$$D = \lambda\Gamma_M^2\left(\omega_{pi} - \gamma_s\omega_{ni}\right), \tag{4.22}$$

where $\omega_g = -k_y g/\Omega$ is the gravitational drift frequency, $\omega_{pi} = k_y P_i'/\left(\Omega\rho\right)$ is the total ion diamagnetic frequency, $\omega_{ni} = k_y P_i\rho'/\left(\Omega\rho^2\right)$ is the ion diamagnetic frequency due to density gradients, γ_s is the ratio of specific heats, $V_a^2 = B^2/(\mu_0\rho)$ is the Alfven velocity squared, $\tau = p_i/p$ is the ion pressure fraction, and $\beta = \mu_0 P/B^2$. The markers λ and δ indicate contributions due to the two-fluid Ohm's law and gyroviscosity respectively. In the $0-\beta$ MHD limit the dispersion relation is $\omega^2 = -\Gamma_M^2$, and instability occurs if $\rho' g$ is negative.

Equations 4.16-4.22 are made dimensionless by normalizing the frequency by the $0-\beta$ MHD growth rate: $X = \omega/\Gamma_M$. We are interested in the unstable case and assume that Γ_M is real. We also normalize the gravitational drift frequency by the MHD growth rate: $G = \omega_g/\Gamma_M$. The diamagnetic drift frequencies are normalized by the gravitational drift frequency: $P = \omega_{pi}/\omega_g$ and $N = \omega_{ni}/\omega_g$. Finally we introduce the scale factors $R^2 = k_y^2 r_i^2/G^2$ and $S = g^2/\left(V_a^2\Gamma_M^2\right)$. The resulting dispersion relation is

$$(A_0 + A_2) X^3 + (X_{*1} + X_{*3}) X^2 + \left(\Gamma_0^2 + \Gamma_2^2\right) X + D_1 = 0 \tag{4.23}$$

$$A_0 = 1 + \gamma_s\beta \tag{4.24}$$

$$A_2 = \delta^2 \frac{\tau G^2 R^2}{4}\beta \tag{4.25}$$

$$X_{*1} = G\left(\delta\left[(1+\gamma_s\beta)(1+\beta)P + (2+\gamma_s\beta)\tau\beta\right] + \lambda\left[1 + P - \gamma_s N\right]\right) \tag{4.26}$$

$$X_{*3} = -\delta^2\lambda G^3 \frac{R^2}{4} N \tag{4.27}$$

$$\Gamma_0^2 = 1 + \gamma_s\beta + S \tag{4.28}$$

$$\Gamma_2^2 = \delta\lambda G^2\left[(1+\beta)(P+1)P - ((1+\gamma_s\beta\tau) + (1+\beta)\gamma_s P)N + (1+P)\tau\beta\right] \tag{4.29}$$

$$D_1 = \lambda G\left(P - \gamma_s N\right). \tag{4.30}$$

In this normalization R, N, P, and S are properties of the equilibrium only. The relative strength of two-fluid and gyroviscous terms are contained in G. Increasing G corresponds to increasing k_y/Ω, hence $k_y r_i$, for a fixed equilibrium. The subscripts of the coefficients A_i, X_{*i}, Γ_i^2, and D_i indicate how the coefficients scale with G. For example A_2 scales as G^2.

The parameters R and S are related to N by the equations $R = \sqrt{N}$ and $S = \tau\beta/N$. The limit of physically validity $\left(k_y^2 r_i^2 \ll 1\right)$ expressed in dimensionless variables is $G^2R^2 \ll 1$. The dependence on the density gradient in R and S is due to the fact that Γ_M depends on the density gradient.

The normalized gravitational drift frequency G is negative when g points in the positive x direction.

Equation 4.23 is symmetric under the transformation $G \to -G$ and $X \to -X$. Physically, this represents the change of coordinates such that $\vec{g}$, which is antiparallel to $\nabla \rho$, points in the negative x direction.

The normalized ion diamagnetic frequency $N = -\rho' / (\rho g)$ is positive for the unstable g-mode. Positive N implies that the gravitational drift propagates in the ion (density) diamagnetic direction, and waves with frequencies proportional to positive (negative) G propagate in the ion (electron) diamagnetic direction. The magnitudes of P and N are determined by MHD force balance $\partial_X \left(p + B^2/2\mu_0\right) = \rho g$ and the ion pressure fraction τ.

The full extended MHD model is difficult to analyze, and two partial models are often considered. The first simplified model includes gyroviscosity but neglects the two-fluid Ohm's law. The second model includes the two-fluid Ohm's law but neglects gyroviscosity. We refer to these two simplified models as the gyroviscous and two-fluid models respectively. We refer to the extended MHD model that includes both effects self-consistently as the full model. Due to their frequent use, it is important to understand how these two simplified models behave and how their behavior departs for the full extended MHD model. These simplified models are also useful in validating numerical models since they test different terms in the physical model.

Zhu et al. thoroughly analyzes the gyroviscous model[36], and we discuss this case for completeness. They only briefly comment on the two-fluid and full models, noting that there are cases where stabilization may fail when D/ω is finite.

Equation 4.23 is a cubic polynomial with real coefficients. It always has at least one real root. The system is stable if there are three real roots. Otherwise the system is unstable, and two roots are complex conjugates. One of the complex conjugates is a growing unstable mode, and the other is a damped stable mode. The growing and damped modes have the same real frequency and propagate in the same direction.

A perturbative expansion is used to evaluate the roots in the small $|G|$ limit. The method of dominant balance is used in the large $|G|$ limit, where the scaling $X \sim O\left(G^n\right)$ is assumed. The exponent n is chosen such the highest order terms in Equation 4.23 balance. The resulting balance is used to calculate the asymptotic behavior of X. The roots of Equation 4.23 are also calculated numerically for arbitrary G.

4.4.1 Small G Perturbation Theory

The roots to Equation 4.23 in the small $|G|$ limit are found using a perturbative expansion. We introduce the small parameter $\epsilon \sim O(G)$. The complex frequency X and Equation 4.23 are expanded into terms of order ϵ^n. This expansion produces a hierarchy of equations. The three lowest order equations are:

$$\epsilon^0 : A_0 X_0^3 + \Gamma_0^2 X_0 = 0 \tag{4.31}$$

$$\epsilon^1 : X_1 = -\frac{D_1 + X_{*1} X_0^2}{3X_0^2 A_0 + \Gamma_0^2} \tag{4.32}$$

$$\epsilon^2 : X_2 = \frac{-X_0}{3X_0^2 A_0 + \Gamma_0^2}\left(3X_1^2 A_0 + 2X_{*1}X_1 + \Gamma_2^2\right). \tag{4.33}$$

Equation 4.31 has three solutions $X_0 = 0$ and $X_0 = \pm i\sqrt{\Gamma_0^2/A_0}$. Inserting $X_0 = 0$ into Equations 4.32-4.33 produces the solution

$$X = -D_1/\Gamma_0^2 + O\left(\epsilon^3\right) \tag{4.34}$$

Equation 4.34 describes a stable ion drift wave. Its direction of propagation is determined by the sign of D_1.

The two roots $X_0 = \pm i\sqrt{\Gamma_0^2/A_0}$ correspond to the unstable g-mode and its corresponding damped complex conjugate. Inserting X_0 into Equations 4.32-4.33 produces the solution

$$X = Y_1 \pm i\sqrt{\frac{\Gamma_0^2}{A_0}}\left(1 + \frac{1}{2\Gamma_0^2}\left(3Y_1^2 A_0 + 2X_{*1}Y_1 + \Gamma_2^2\right)\right) + O\left(\epsilon^3\right) \tag{4.35}$$

$$Y_1 = \frac{A_0 D_1 - X_{*1}\Gamma_0^2}{2\Gamma_0^2 A_0}. \tag{4.36}$$

Equation 4.35-4.36 describes the extended MHD modifications to the g-mode at small $|G|$. There are two effects. First, extended MHD imparts a finite real frequency of order G^1. Second, extended MHD modifies the growth rate of the mode. This modification to the growth rate is order G^2. The sign of $3Y_1^2 A_0 + 2X_{*1}Y_1 + \Gamma_2^2$ determines if Extended MHD increases or decreases the growth rate at small $|G|$. The term Γ_2^2 appears in the lowest order correction to the growth rate. This term is second order in G and is normally neglected in derivations that assumes a small ordering for the extended MHD effects. However, the lowest order correction to the growth rate is at second order, and including Γ_2^2 is necessary for consistency. Similarly the term D_1 appears in the lowest order corrections to both the real frequency and the growth rate. This term is linear in G, yet it is absent in derivations of the g-mode that predate Zhu et al. Equations 4.34 and 4.35 are analyzed in more detail in the following sections.

4.4.2 Gyroviscous g-mode Analysis

The dispersion relation for the gyroviscous model is found by setting $\delta = 1$ and $\lambda = 0$ in Equations 4.23- 4.30. The dispersion relation in this case is

$$\left(A_0 + A_2\right) X^3 + X_{*1} X^2 + X\Gamma_0^2 = 0 \tag{4.37}$$

$$A_0 = 1 + \gamma_s \beta \tag{4.38}$$

$$A_2 = \frac{\tau G^2 R^2}{4}\beta \tag{4.39}$$

$$X_{*g} = G\left[\left(1 + \gamma_s\beta\right)\left(1 + \beta\right)P + \left(2 + \gamma_s\beta\right)\tau\beta\right] \tag{4.40}$$

$$\Gamma_0^2 = 1 + \gamma_s\beta + S. \tag{4.41}$$

There are three solutions to the cubic dispersion relation. The first solution is the zero frequency mode $X = 0$. The other two solutions are found using the quadratic equation

$$X = \frac{1}{2A}\left(-X_{*g} \pm \sqrt{X_{*g}^2 - 4A\Gamma_0^2}\right), \tag{4.42}$$

where $A = A_0 + A_2$. The two roots will be real (indicating stability) if $X_*^2 - 4A\Gamma_0^2 > 0$, and they will be complex (indicating instability) if $X_*^2 - 4A\Gamma_0^2 < 0$. The stability requirement that $X_*^2 - 4A\Gamma^2 > 0$ can be expressed as

$$G^2\left[\frac{\left[\left(1 + \gamma_s\beta\right)\left(1 + \beta\right)P + \left(2 + \gamma_s\beta\right)\tau\beta\right]^2}{1 + \gamma\beta + S} - \tau R^2\beta\right] \geq 4\left(1 + \gamma\beta\right). \tag{4.43}$$

The inequality is never satisfied for real G if the term in brackets is negative, and complete gyroviscous stabilization does not occur. This equation is analogous to Equation 22 in [36], whose authors note that in the limit that $\beta = 0$ the bracketed term is positive. In this limit complete gyroviscous stabilization always occurs at significantly large G.

The bracketed term in Equation 4.43 is also positive for $P \geq N > 0$. The condition $P \geq N$ corresponds to the situation where density gradients and temperature gradients are both directed opposite gravity.

We begin the proof by defining the functions $U\left(P,N\right)=\left(aP+b\right)^2-cN-d$ and $V\left(P\right)=\left(aP+b\right)^2-cP-d$ where $a=\left(1+\gamma_s\beta\right)\left(1+\beta\right)$, $b=\left(2+\gamma_s\beta\right)\tau\beta$, $c=\tau\beta\left(1+\gamma_s\beta\right)$, and $d=\tau^2\beta^2$. The function U is the bracketed term in Equation 4.43 multiplied by $\left(1+\gamma_s\beta+\frac{\tau\beta}{N}\right)$. (Recall that physically $S=\frac{\tau\beta}{N}$ and $R^2=N$). Positive U implies that the bracketed term is positive. The function V is the limiting cases of U where $P=N$.

The difference between the two functions is $U\left(P,N\right)-V\left(P\right)=-d\left(N-P\right)$. By assumption $P\geq N$ and $U\left(P,N\right)-V\left(P\right)\geq 0$. Therefore if V is positive for positive P, then U is positive for $P\geq N>0$. V is a quadratic in P and it has a global minimum at

$$P_{min}=\frac{c}{2a}-b=\frac{\tau\beta}{2}\frac{1-2\left(2+\gamma\beta\right)\left(1+\gamma\beta\right)\left(1+\beta\right)}{2\left(1+\gamma\beta\right)\left(1+\beta\right)^2}\leq 0. \tag{4.44}$$

It is sufficient to evaluates $V\left(P=0\right)$ since P_{min} is negative:

$$V\left(0\right)=b^2-d=\tau^2\beta^2\left(3+4\gamma_s\beta+\gamma_s^2\beta^2\right)\geq 0. \tag{4.45}$$

The proof is complete.

X scales as G^{-1} in the limit that $|G|\gg 1$, Equation 4.42. Therefore, even in cases where complete stabilization is not possible, the asymptotic growth rate still goes to zero with G^{-1}.

In the limit of $|G|\ll 1$, the perturbative expansion (Equation 4.35) yields

$$X\approx\frac{-X_{*g}}{2\left(1+\gamma_s\beta\right)}\pm i\sqrt{\frac{1+\gamma_s\beta+S}{1+\gamma_s\beta}}\left(1-\frac{X_{*g}^2}{8\left(1+\gamma_s\beta\right)\left(1+\gamma_s\beta+S\right)}\right)+O\left(G^3\right). \tag{4.46}$$

At small G, the gyroviscous g-mode has a real frequency, and the mode propagates in a direction determined by the sign of X_*. X_* is positive for positive P, and the mode propagate in the electron diamagnetic direction. The second term in parenthesis in Equation 4.46 is positive definite, indicating that gyroviscosity is stabilizing at small $|G|$.

Figure 54 shows the numerically calculated frequencies for equilibrium parameters where complete stabilization is possible. There are three modes: the unstable branch of the g-mode (green), the stable branch (blue), and the trivial zero frequency mode (red). Initially the two branches of the g-mode have the same real frequency. The frequency is negative indicating that they propagate in the electron diamagnetic direction. Increasing G decreases the growth rate of the unstable branch, and complete

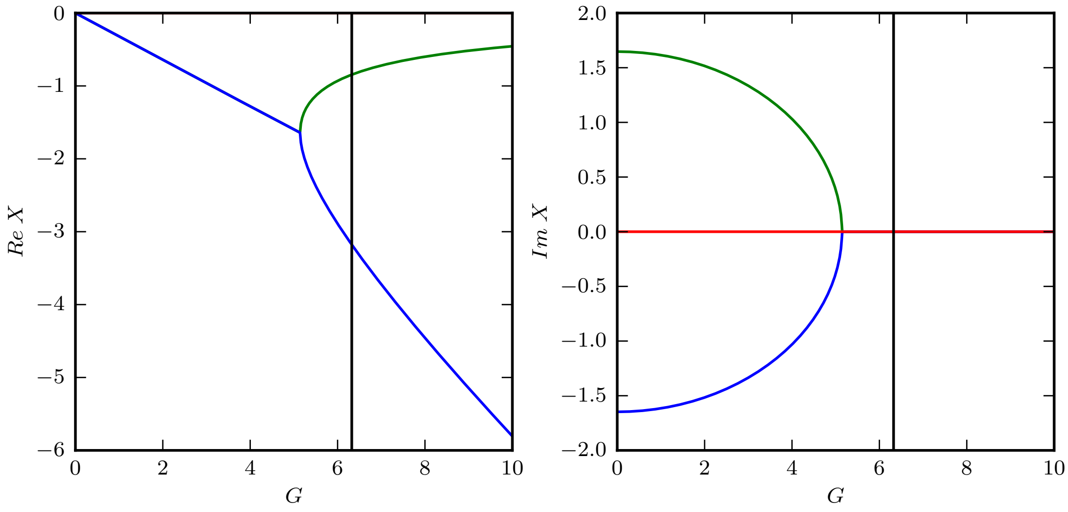

Figure 54: Linear growth rates characteristic of the gyroviscous g-mode with complete stabilization. Initially both the unstable branch (green) and the stable branch (blue) have the same real frequency. After stabilization, the two modes have different real frequencies. Both branches eventually asymptote to zero at large G(not shown).

stabilization is observed around $G \approx 5$. At the point of complete stabilization, the real frequencies of the two branches of the g-mode split. At sufficiently large G, beyond the range of the plot, both real frequencies asymptote to zero. However, at large G the model is not physically valid.

Figure 55 shows the numerically calculated frequencies for a case where complete stabilization fails. Here the growth rate of the unstable branch continually decreases with increasing G and asymptotes to zero as G^{-1}. The real frequency of both branches of the g-mode are the same for all G. The frequency is again negative indicating that the mode propagates in the electron direction. Initially its magnitude increases with G, but it peaks at an intermediate value, and then it asymptotes to zero at the rate G^{-1}.

4.4.3 Two-Fluid g-mode Analysis

The dispersion relation for the two-fluid model is found by setting $\delta = 0$ and $\lambda = 1$ in Equations 4.16-4.22. The resulting dispersion relation is

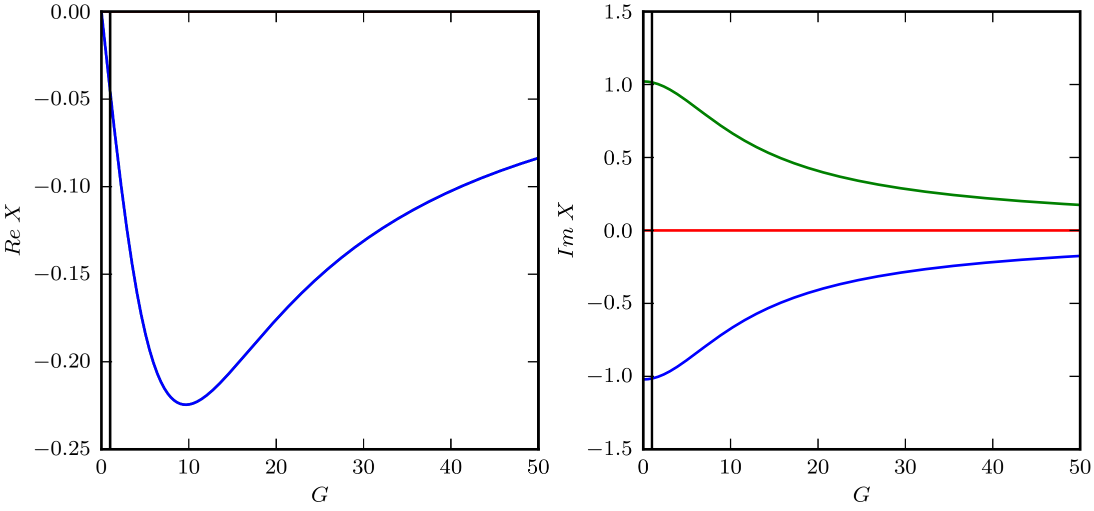

Figure 55: Linear growth rates characteristic of the gyroviscous g-mode in the absences of complete stability. Both branches of the g-mode have the same real frequency for all G. The real and imaginary frequencies asymptote to zero at large G.

$$AX^3 + X_* X^2 + X\Gamma^2 + D = 0 \tag{4.47}$$

$$A = 1 + \gamma_s \beta \tag{4.48}$$

$$X_* = G\left(1 + P - \gamma_s N\right) \tag{4.49}$$

$$\Gamma^2 = 1 + \gamma_s \beta + S \tag{4.50}$$

$$D = G\left(P - \gamma_s N\right). \tag{4.51}$$

We consider the limit where $\beta = 0$ (which also implies that $S = 0$), but allow for finite P and N. None of the terms containing β depend on G, and setting $\beta = 0$ does not change the qualitative behavior of the model. It effectively re-scales the coefficients in Equation 4.47. Additionally, β is small for most systems of interest, and neglecting it has a small quantitative effect. The model two-fluid g-mode dispersion relation that we analyze is

$$X^3 + X_* X^2 + X + D = 0 \tag{4.52}$$

$$X_* = G\left(1 + H\right) \tag{4.53}$$

$$D = GH. \tag{4.54}$$

Equation 4.52 only depends on the two parameters G and $H = P - \gamma_s N$. The parameter H is a normalized modified ion diamagnetic drift frequency. It is purely a function of equilibrium quantities.

4.4.4 The Small G Limit

Equations 4.34-4.36 are used to calculate to the solutions to the two-fluid dispersion relation in the limit $|G| \ll 1$. In this model $\Gamma_0^2 = A_0 = 1$, $\Gamma_2^2 = 0$, $D_1 = GH$, and $X_{*1} = G\left(1 + H\right)$. Inserting these relations into Equation 4.34 produces the stable drift wave $X = -GH$ or equivalently $\omega = -\omega_{pi} + \gamma_s \omega_{ni}$. The drift wave propagates in the electron diamagnetic direction when $\omega_{pi} > \gamma_s \omega_{ni}$ and in the ion direction when $\omega_{pi} < \gamma_s \omega_{ni}$.

Evaluating Equations 4.35-4.36 for the two-fluid model produces $X = -G/2 \pm i\left[1 - G^2\left(1 + 4H\right)/8\right]$. The + solution is the unstable g-mode, and the − solution is the corresponding damped mode. Two-fluid effects stabilize the mode at small $|G|$ when $H > -1/4$ and destabilize the mode when $H < -1/4$. A higher-order perturbative expansion is required to evaluate the case $H = 1/4$. Both branches of the g-mode propagate in the electron diamagnetic direction.

4.4.5 Stability Analysis Based on the Critical Points

The critical points $x_a \leq x_b$ of the polynomial $Q\left(X\right) = X^3 + X_* X^2 + X + D$, satisfy the condition $Q'\left(x_a\right) = Q'\left(x_b\right) = 0$. A necessary condition for stability is that x_a and x_b must both be real with $Q\left(x_a\right) \geq 0$ and $Q\left(x_b\right) \leq 0$. The direction of the inequalities results from the fact that the leading order coefficient, A, is positive. If $x_a = x_b$ then stability requires $Q\left(x_a\right) = Q\left(x_b\right) = 0$.

This stability criteria follows from the mean value theorem and the requirement that $Q\left(X\right)$ have three real roots. The proof is easily observed graphically. Figure 56 illustrates the different types of behavior. Figure 56A shows the case where there are no critical points. Here the slope of $Q\left(X\right)$ is always positive, and there will only be one real root. This case is unstable. Figure 56B shows the case where there are two critical points. The green line indicates the stable case with $Q\left(x_a\right) > 0$ and $Q\left(x_b\right) < 0$. It has three real roots. The red line has $Q\left(x_b\right) > 0$ and the blue line has $Q\left(x_b\right) < 0$. Both of these lines have only one real root and they are unstable.

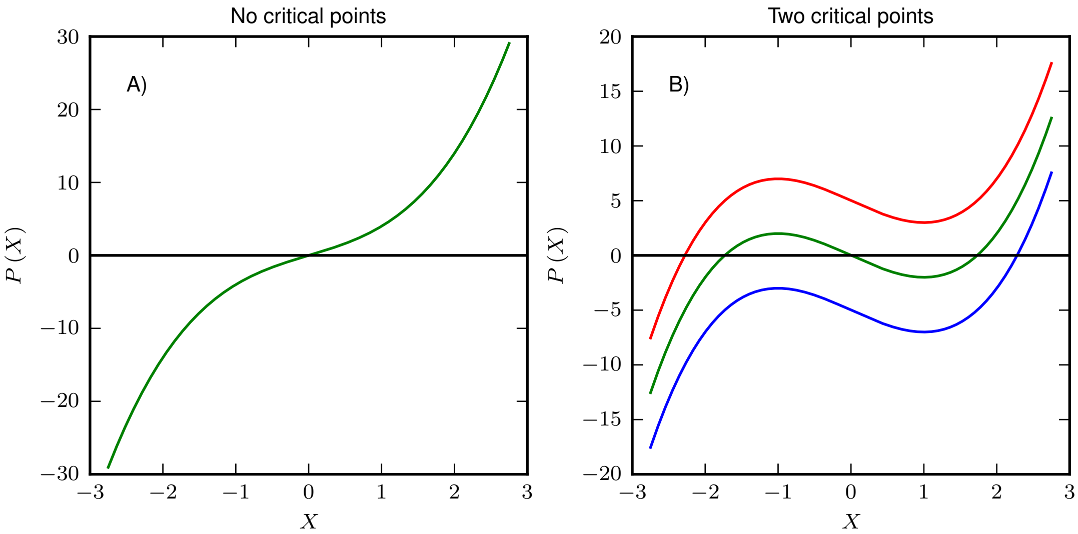

Figure 56: Stability corresponds to the case where the polynomial $Q\left(X\right)$ has three real roots. Figure A) illustrates the case where there are no critical points. Here there is only one real root. Figure B) illustrates the case where there are 2 critical points. The critical point occur at $x_a = -1$ and $x_b = 1$. The green line has $Q\left(x_a\right) > 0$ and $Q\left(x_b\right) < 0$ as required for stability. It has three real roots. The red line has $Q\left(x_b\right) > 0$ and the blue line has $Q\left(x_a\right) < 0$. Both of these lines have one real root.

The critical points of $Q\left(X\right)$ are

$$x_{a,b} = \frac{-G\left(1+H\right)}{3} \pm \frac{1}{3}\sqrt{G^2\left(1+H\right)^2 - 3}. \tag{4.55}$$

Stability requires that the two critical points given in Equation 4.55 are real. It follows that a necessary (but not sufficient) condition for stability is

$$G^2\left(1+H\right)^2 \geq 3. \tag{4.56}$$

Equation 4.56 shows that conditions with $H = -1$ and $G = 0$ are in the unstable regime.

4.4.6 The Large G Limit

The preceding discussion is used to the analyze the stability in the limit that $|G| \gg 1$ for $H \neq -1$ ($H = -1$ is unstable). In this limit the critical points are $x_{a,b} \approx (0, -2G(1+H)/3)$. The sign of $G(1+H)$ determines which critical point is associated with x_a and which point is associated with x_b. The corresponding values of Q are $Q(0) \approx GH$ and $Q(-2G(1+H)/3) \approx 4G^3(1+H)^3/27$.

Consider the critical point at $X = -2G(1+H)/3$. If $G(1+H) > 0$ then this critical point is the first critical point (x_a) and stability requires that $Q(-2G(1+H)/3) \approx 4G^3(1+H)^3/27 \geq 0$. This condition is satisfied by assumption. If $G(1+H) < 0$ then this point is the second critical point and stability requires that $Q(-2G(1+H)/3) \approx 4G^3(1+H)^3/27 \leq 0$. This condition is also satisfied, and $Q(-2G(1+H)/3)$ always has the correct sign for stability. Thus, the stability of system is determined by the sign of $Q(0)$.

Now consider the point $X = 0$ for the two cases $H > -1$ and $H < -1$. If $H > -1$ then $G(1+H)$ is positive for $G > 0$ and negative for $G < 0$. For $G > 0$ the critical point at $X = 0$ is the second critical point and stability requires that $Q(0) = GH \leq 0$. This is true for $H \leq 0$. If $G < 0$ then $X = 0$ is the first critical point and stability requires that $Q(0) = GH \geq 0$. This is true for $H \leq 0$. Therefore $-1 < H \leq 0$ is stable but $H > 0$ is unstable.

If $H < -1$ then $G(1+H)$ is positive for $G < 0$ and negative for $G > 0$. For $G < 0$ the critical point at $X = 0$ is the second critical point and stability requires the $GH \leq 0$. However both G and H are negative and the inequality is never satisfied. Similarly for $G > 0$ the critical point at $X = 0$ is the first critical point and stability requires the $GH \geq 0$. This inequality is never satisfied since G is positive and H is negative. Therefore $H < -1$ is unstable. This analysis is summarized in Table 6.

Equation 4.52 is also analyzed in the limit $|G| \gg 1$ by assuming that X scales as G^1 and G^0 for $H \neq -1$. In limit that X scales as G^1 the first two terms of Equation 4.52 both scale as G^3 while the last two terms scale as G. For $|G| \gg 1$ the first two terms dominate, and balancing these terms yields an ion drift wave $X = -G(1+H)$. This wave propagates in electron diamagnetic direction for $H > -1$ and the ion diamagnetic direction for $H < -1$.

Similarly, in the limit that X scales as G^0 the second and fourth terms in Equation 4.52 are both linear in G while the first and third terms have no G dependence. Balancing the second and fourth

	$(G>0,H>-1)$	$(G<0,H>-1)$	$(G>0,H<-1)$	$(G<0,H<-1)$
$G(1+H)$	positive	negative	negative	positive
$-\frac{2}{3}G(1+H)$	negative	positive	positive	negative
x_a	$-\frac{2}{3}G(1+H)$	0	0	$-\frac{2}{3}G(1+H)$
x_b	0	$-\frac{2}{3}G(1+H)$	$-\frac{2}{3}G(1+H)$	0
$Q(x_a)$	$\frac{4}{27}G^3(1+H)^3$	GH	GH	$\frac{4}{27}G^3(1+H)^3$
$Q(x_b)$	GH	$\frac{4}{27}G^3(1+H)^3$	$\frac{4}{27}G^3(1+H)^3$	GH
$Q(x_a)\geq 0$	True	True for $H\leq 0$	False	True
$Q(x_b)\leq 0$	True for $H\leq 0$	True	True	False
Stable	Stable if $H\leq 0$	Stable if $H\leq 0$	Unstable	Unstable

Table 6: Logic determining the stability in the limit that $G^2 \gg 1$. The system will be stable if and only if $Q(x_a)\geq 0$ and $Q(x_b)\leq 0$. The resulting condition for stability is $-1<H\leq 0$.

terms yields the two solutions $X=\pm\sqrt{\frac{-H}{1+H}}$. In agreement with the critical point analysis, $H\leq -1$ and $H>0$ are unstable. The asymptotic growth rate at large $|G|$ is $\sqrt{\frac{H}{1+H}}$. This growth rate is independent of k_y/Ω and is of order unity implying that the growth rate scales with the MHD growth rate.

In the case $H=-1$ the asymptotic behavior is found by assuming that X scales as $G^{1/3}$. Here the cubic term and the constant term balance. The three modes are $X=G^{1/3}$ and $X=G^{1/3}\left(-1/2\pm i\sqrt{3}/2\right)$. Here, ultraviolet catastrophe occurs in that the growth rate of unstable branch asymptotes to infinity.

4.4.7 Numerical Solutions of the Two-Fluid Model

The roots of the polynomial $Q(X)$ are calculated numerically in order to analyze the stability for arbitrary G and H. The real and complex roots are plotted as a function of G for fixed H. Increasing $|G|$ corresponds to increasing the Hall parameter for a fixed equilibrium.

The roots of Equation 4.52 are shown in Figure 57 for the case where $H=0$. This case is analogous to the Roberts-Taylor dispersion relation $\omega^2+\omega_*\omega+\Gamma^2=0$[13], but it includes a zero frequency drift wave, this is blue line in Figure 57. The unstable g-mode and the corresponding stable branch are in red and green respectively. Complete stabilization of the unstable branch is observed for $|G|\geq 2$. These two modes have a real frequency of $-G/2$ for $|G| < 2$. Their real frequencies split at $|G| = 2$. For large G one frequency tends towards 0 and the other tends towards $-G$.

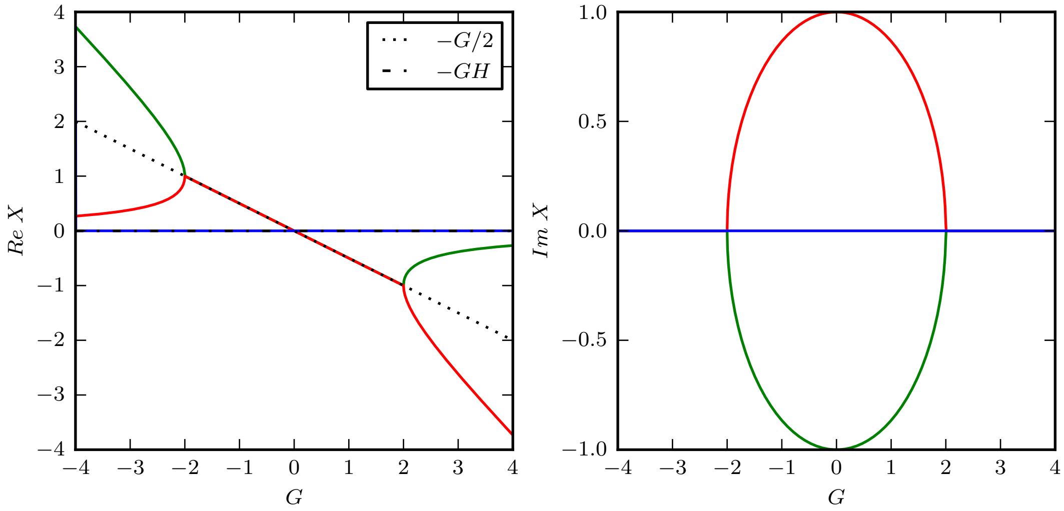

Figure 57: The real and imaginary frequencies of the three modes are shown for H=0. The red line is the unstable g-mode, blue is the drift wave, and green is the stable branch. Complete stabilization occurs at $G^2 = 4$.

Similar behavior is observed for $-1/4 < H < 0$. Figure 58 shows the case for $H = -1/8$. Here the two-fluid effects stabilize the unstable g-mode for all G. The red and green lines correspond to the unstable and stable branches of the g-mode and the blue line is the drift wave. The drift wave has a finite frequency since $H \neq 0$. The drift wave and the two branches of the g-mode always propagate in opposite directions for $H < 0$. The critical G at which complete stabilization is observed increases with H. Complete stabilization occurs at $|G| \approx 2.57$ for the case shown in Figure 58.

In the region $-1 < H < -1/4$, the analysis predicts that the two-fluid effects increase the growth rate of the unstable mode at small $|G|$, but complete stabilization is expected at large $|G|$. Figure 59 shows the case for $H = -1/2$. The growth rate of the unstable g-mode increases for small $|G|$ and peaks around $|G| \approx 2.3$ with a maximum growth rate of $Im\,(X) \approx 1.1$. The growth rate decreases for $|G| > 2.3$, and complete stabilization occurs at $|G| \approx 6.67$. The maximum growth rate and critical G required for complete stabilization increase with decreasing H. At $H = -1$ complete stabilization

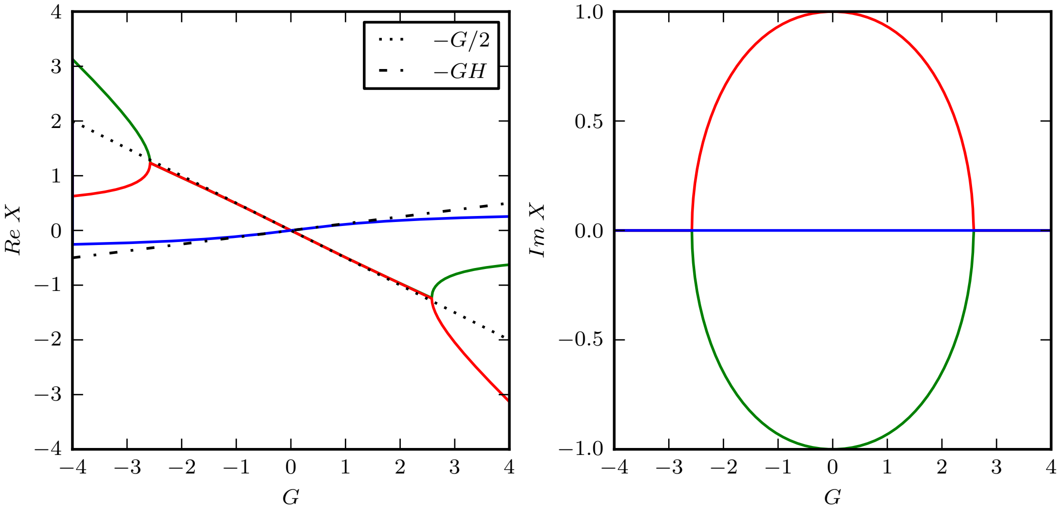

Figure 58: The complex frequencies of the three modes are shown for $H = -1/8$. This case is representative of all cases with $-1/4 < H < 0$. Complete stabilization is observed for $|G| \gtrsim 2.57$. The ion drift wave has a finite real frequency. The g-mode and the ion drift wave propagates in opposite directions.

is lost, and for $H \leq -1$ the two fluid effects are destabilizing for all G. Figure 60 shows the case for $H = -3/2$ and is representative of all cases for $H < -1$. The maximum growth rate decreases as H is decreased below negative one. In the limit $G \to \pm\infty$ the asymptotic growth rate is $\sqrt{\frac{H}{H+1}}$.

Now consider the cases where $H > 0$. Figure 61 shows the case for $H = .04$. Here the two-fluid effects are stabilizing for small $|G|$ and complete stabilization occurs at $|G| \approx 1.85$. However as $|G|$ is increased, a second mode goes unstable at $|G| \approx 2.55$. Figure 62 shows an enhanced view of the region $0 < G < 4$. For $H > 0$ the drift wave and the two branches of the g-mode drift in the same direction. At $G \approx 2.55$ the drift wave intercepts the low frequency branch of the stabilized g-mode. Here the second instability goes unstable. Like the g-mode, this second instability has a corresponding damped mode.

As H increases, the critical G for complete stabilization decreases and so does the critical G for the onset of the second instability. The width of the region of stability also decreases. At $H = 1/8$ these two points coincide and complete stability only occurs at $|G| = \frac{8}{9}\sqrt{3}$. The case is shown in Figure 63. This point satisfies the stability criterion in Equation 4.56 exactly. It also corresponds to the point

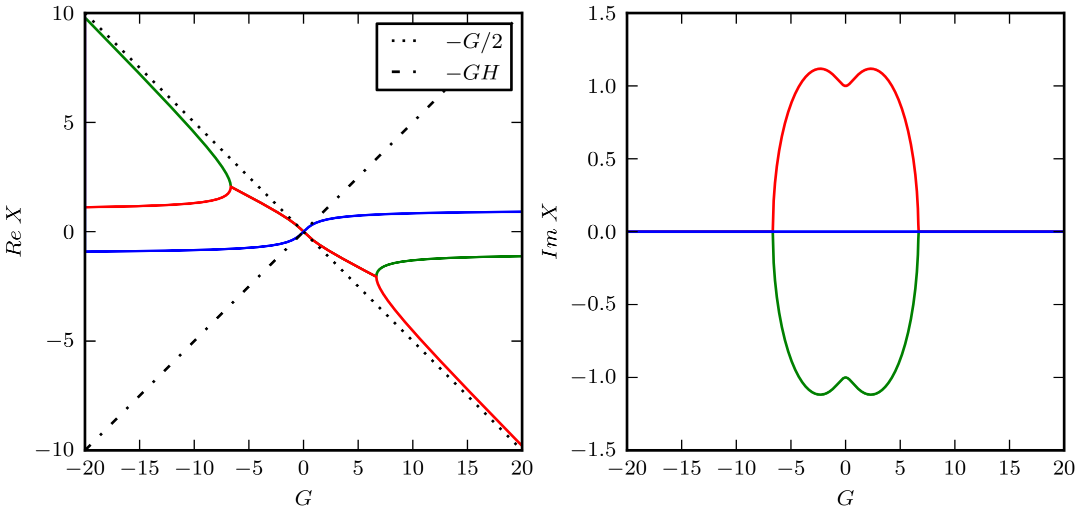

Figure 59: The complex frequencies of the three modes are shown for $H = -1/2$. This case is representative of all cases with $-1 < H < -1/4$. The two-fluid effects increase the linear growth rate for small $|G|$. The two-fluid effects decrease the growth rate at sufficiently large $|G|$, and complete stabilization is observed.

where the drift wave intersects the g-mode at the point where the g-mode is completely stabilized. Here both branches of the g-mode and drift wave all have the same frequency.

For $H > 1/8$ there is no region of stability. A representative case is shown in Figure 64 for $H = .15$. For all positive H the asymptotic growth rate as $G \to \pm\infty$ is $\sqrt{\frac{H}{H+1}}$. This asymptotic growth rate approaches 1 as H is increased from 0. For positive H the maximum growth is always less than 1.

4.4.8 Discussion of Two-Fluid g-mode Results

The two-fluid modifications of the g-mode are more complicated than the dynamics represented by the Roberts Taylor dispersion relation $\omega^2 + \omega_* \omega + \Gamma^2_{MHD}$ [13]. The stabilization properties of Equation 4.52 strongly depend on the parameter H which only depends on the equilibrium ion pressure, density, and gravity. A dependences on temperature is implicit in the relation between pressure and density. The stability properties are summarized as follows. The g-mode is unstable for $H \leq -1$, and two-fluid effects enhance the growth rate of the unstable mode for all G. For $-1/4 > H > -1$, two-fluid

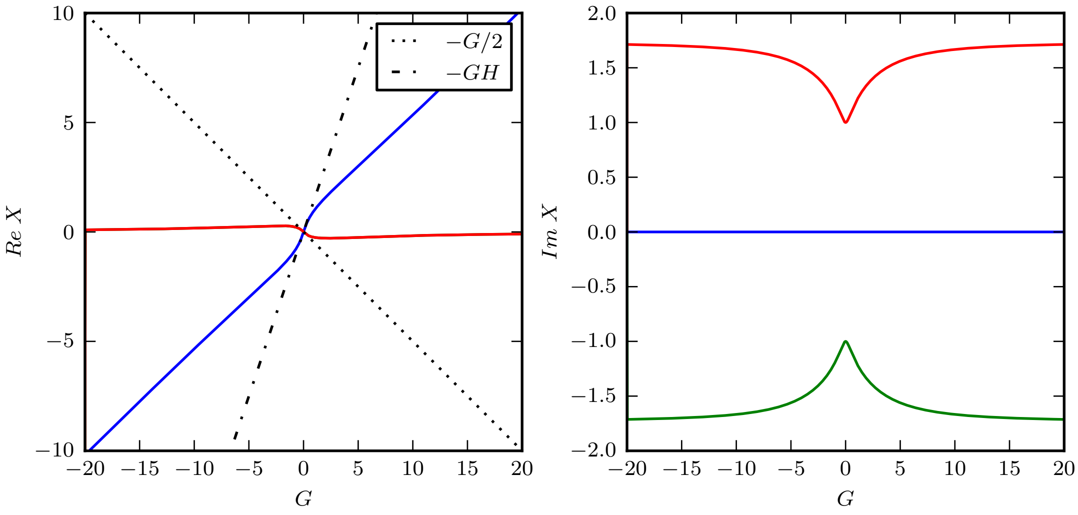

Figure 60: The complex frequencies of the three modes are shown for $H = -3/2$. This case is representative of all cases with $H < -1$. There is no stabilization of the g-mode and the two-fluid effects increase the growth rate of the unstable mode for all G. For the case shown, the growth rate asymptotes to $\sqrt{3}$ as $|G| \to \infty$.

effects enhance the growth rate at small $|G|$, but are stabilizing at large $|G|$. Complete stabilization is observed for sufficiently large $|G|$. Two-fluid effects are stabilizing for all G for $0 \geq H \geq 1/4$ and complete stabilization always occurs at a sufficiently large $|G|$. For $1/8 \geq H > 0$ the two-fluid effects are stabilizing for small $|G|$ and complete stabilization occurs for a range of G. However a second mode goes unstable at large enough $|G|$. For $H > 1/8$ the two-fluid effects are stabilizing for small G but complete stabilization never occurs.

A key result is the appearance of a second instability when $H > 0$. For $1/8 > H > 0$ this second instability forms when the drift wave interacts with the low frequency branch of the stabilized g-mode. The two waves merge in a growing mode and a damped mode.

In terms of physical quantities the parameter H is

$$H = \frac{-p_i\left(\frac{T'}{T} - (\gamma_s - 1)\frac{n'}{n}\right)}{\rho g} = \frac{-p_i \frac{n'}{n}\left(\eta_i - (\gamma_s - 1)\right)}{\rho g} \tag{4.57}$$

where $\eta_i = \frac{nT'}{n'T}$. The second expression relates H to the ion temperature gradient (ITG) stability

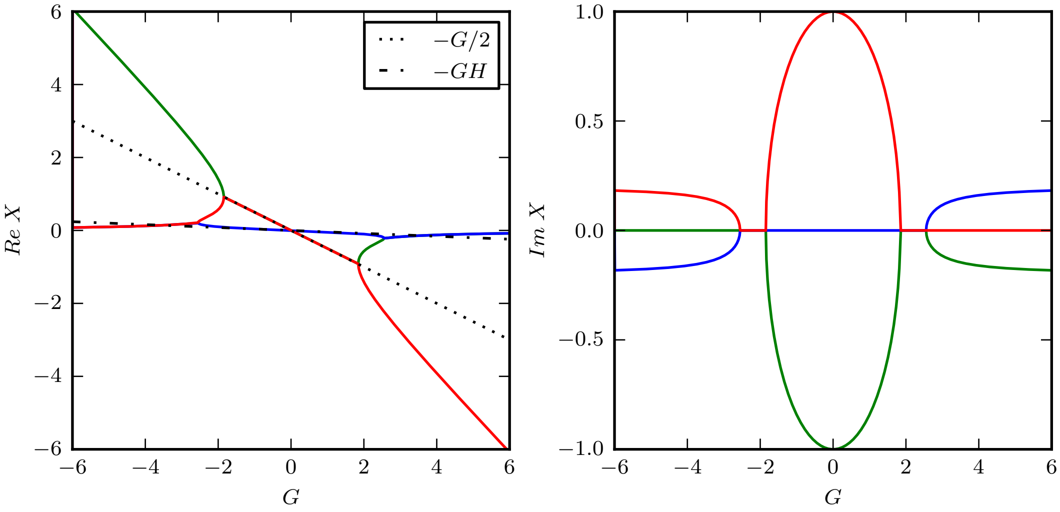

Figure 61: The complex frequencies of the three modes are shown for $H = 0.04$. Complete stabilization of the g-mode occurs at $|G| \approx 1.85$. A second mode is destabilized at $|G| \approx 2.55$. The second mode goes unstable when the drift wave intercepts the low frequency branch of the stabilized g-mode. This new mode is unstable for all $|G| \gtrsim 2.55$ and has an asymptotic growth rate of 0.196.

parameter η_i. The condition $H > 0$ corresponds to $\eta_i > 2/3$ for $\gamma_s = 5/3$ (the unstable g-mode requires $\frac{n'}{n}$ and g have opposite signs). The criteria that a secondary mode is unstable ($\eta_i > 2/3$) is the same criteria for ITG instability.

Despite having the same stability criteria, the are a number of differences between the second instability and ITG mode. The second mode is driven unstable by an interaction between the stable drift wave and the low frequency branch of the g-mode. The ITG is a parallel sound wave that is driven unstable by an interaction with ion drifts [15]. The growth rate of the second mode scales with the growth rate of the MHD g-mode, while the growth rate of the ITG scales with the sound wave frequency. The ITG requires $k_\parallel \neq 0$ but the model (Equation 4.52) assumes $k_\parallel = 0$. Similarly, the ITG is stable in fluid models that neglect gyroviscosity, which we have done. These differences suggest that this new mode is not an ITG.

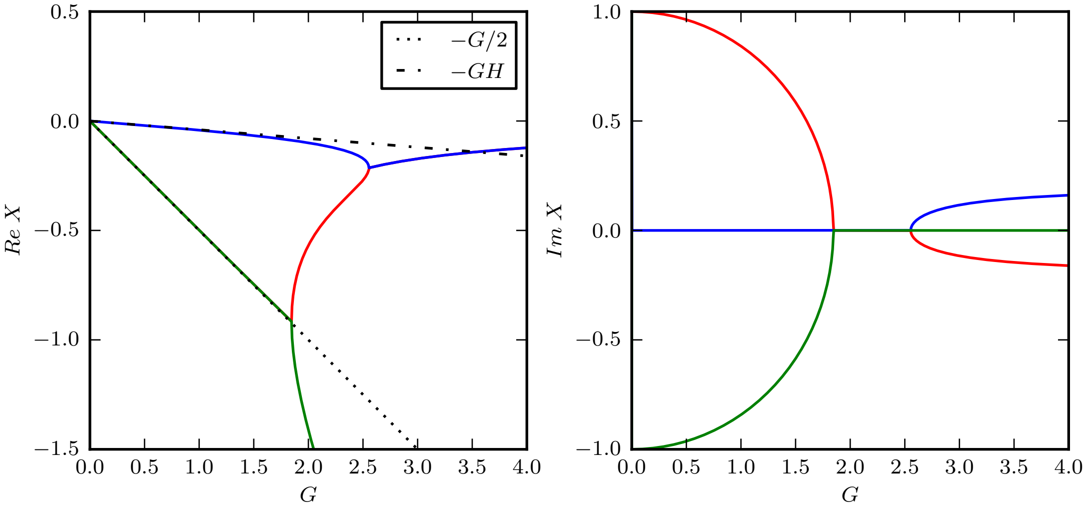

Figure 62: The frequencies of the three modes are shown again for $H = 0.04$. Here the graph focuses on the region where the g-mode is stabilized and the second mode is destabilized.

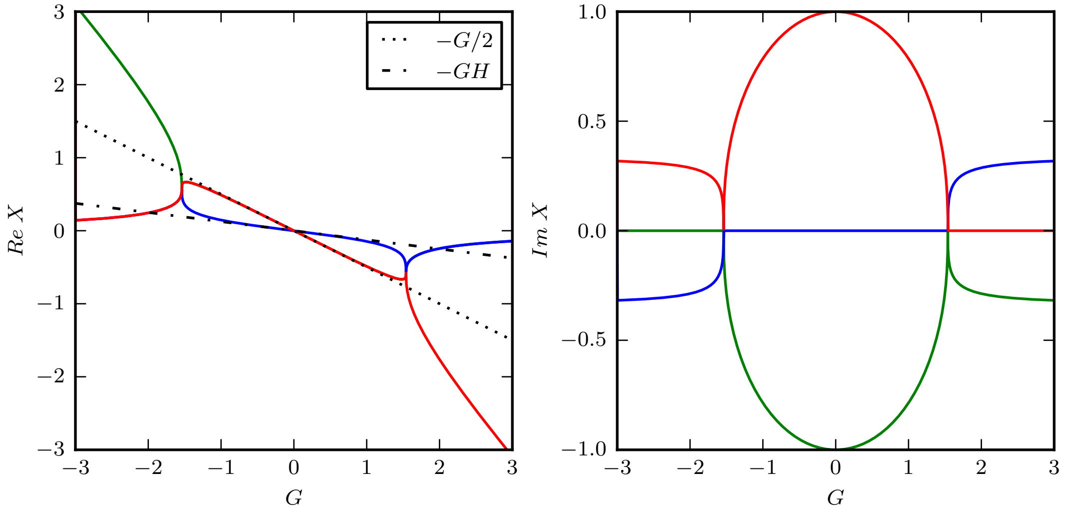

Figure 63: The complex frequencies of the three modes are shown for $H = 1/8$. The ion-drift wave (blue) intersects both branches of the g-mode (red and green) at the point $|G| = \frac{8}{9}\sqrt{3}$. Here the MHD g-mode is completely stabilized and the second mode simultaneously goes unstable.

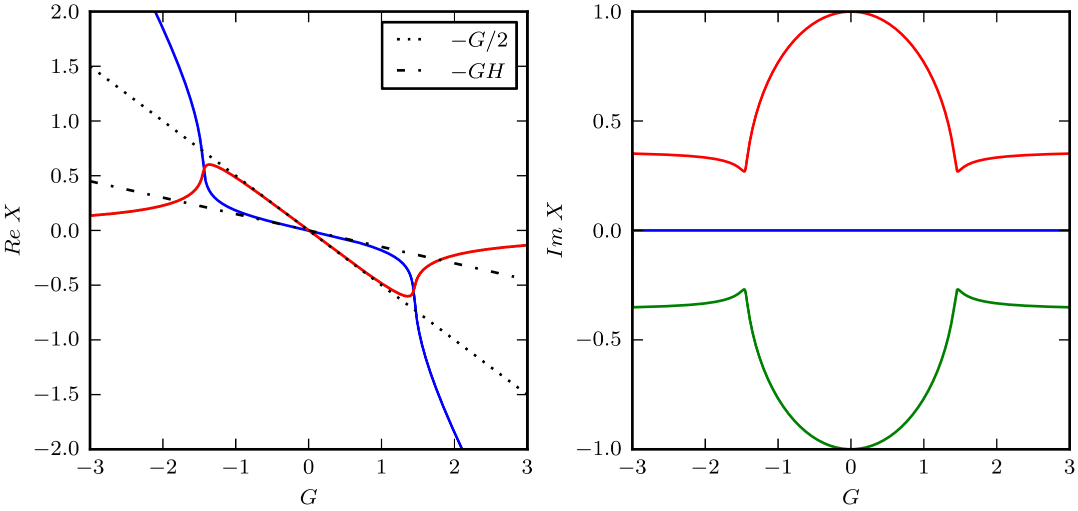

Figure 64: The complex frequencies of the three modes are shown for $H = 0.15$. This case is representative of all cases with $H > 1/8$. Here the real frequency of the drift wave (blue) intersects the real frequency of g-mode before the g-mode is stabilized. There is no region of complete stability.

4.4.9 Analysis of the Full Extended MHD g-mode

We now analyze the full g-mode dispersion relation that includes both gyroviscosity and the two-fluid Ohm's law (Equations 4.23-4.30). The analysis first considers the limit $|G| \ll 1$ and then considers various large $|G|$ limits. Finally, the solutions to Equation 4.23 are evaluated numerically.

Equations 4.34-4.36 describe the solution in the limit $|G| \ll 1$. Equation 4.34 produces the stable drift wave $X = -G_1/\Gamma_0^2$. As is the case for the two-fluid model, the direction of propagation is determined by the sign of $P - \gamma_s N$. The wave propagates in the electron direction if $P > \gamma_s N$ and in the ion direction if $P < \gamma_s N$. Equations 4.35-4.36 describe the g-mode and the corresponding damped mode.

Now consider the limit of large $|G|$ and finite R. The model isn't physically valid in this limit as it violates $k_y r_i \ll 1$. However, this limit occurs in small scale dynamics of numerical codes that use the extended MHD model. The dispersion relation in this limit is

$$A_2 X^3 + X_{*3} X^2 + \Gamma_2^2 X + D_1 = 0. \tag{4.58}$$

The three roots of the equation can be found using the orderings $X \sim G^1$ and $X \sim G^{-1}$. In the limit $X \sim G^1$ the first two terms dominate and the approximate solution is

$$X \approx -\frac{X_*3}{A_2} + O\left(G^0\right) = \frac{GN}{\tau\beta} + O\left(G^0\right). \tag{4.59}$$

In the limit $X \sim G^{-1}$ the quadratic, linear, and constant terms dominate. The resulting solutions are

$$X \approx -\frac{\Gamma_2^2}{2X_{*3}}\left(1 \mp \sqrt{1 - \frac{4D_1X_{*3}}{\Gamma_2^4}}\right) + O\left(G^{-2}\right). \tag{4.60}$$

The first mode is a drift wave that propagates in the ion direction. The second two modes limit to zero frequency modes as $G \to \infty$. They are stable if $1 > 4D_1X_{*3}/\Gamma_2^4$. A sufficient condition for stability is $0 > 4D_1X_{*3} = G^4R^2N\left(P - \gamma_sN\right)$ or more simply $\gamma_sN > P$. The condition $\gamma_sN > P$ is equivalent to $\eta_i < 2/3$ for $\gamma_s = 5/3$. The ratio $4D_1X_{*3}/L_2^4$ is often small for realistic parameters, and there are many cases that are stable but violate the criteria $\gamma_sN > P$, so $\gamma_sN > P$ does not represent a necessary condition for stability in any sense.

The above results are only valid if A_2, X_{*3}, Γ_2^2, and D_1 are all nonzero. The qualitative behavior of the model can change if any of these terms are zero. An interesting case to consider is $X_{*3} = 0$ and $\Gamma_2^2 = 0$. The terms X_{*3} and Γ_2^2 represent the coupling between the two-fluid effects and gyroviscosity. They only appear when both effects are included in the model self-consistently. Neglecting these two terms is representative of simple models that "add" two-fluid effects and gyroviscosity, but don't account for the coupling.

When $X_{*3} = 0$ and $\Gamma_2^2 = 0$ the dispersion relation is

$$A_2X^3 + X_{*1}X^2 + \Gamma_0^2X + D_1 = 0. \tag{4.61}$$

The roots of the equation are found by using the ordering $X \sim G^{-1/3}$. In this limit the first and the last term balance, and to lowest order, the roots are

$$X = \left(\frac{-D_1}{A_2}\right)^{-1/3} \tag{4.62}$$

and

$$X = \left(\frac{-D_1}{A_2}\right)^{-1/3}\left(\frac{-1}{2} \pm \frac{\sqrt{3}}{2}i\right). \tag{4.63}$$

The first mode is a stable wave, the other two solutions are an unstable mode and the corresponding stable mode. The growth rate of the unstable mode scales $G^{-1/3}$, and all three modes approach zero frequency as G approaches ∞.

The coupling between the two-fluid effects and gyroviscosity has a significant stabilizing effect at large $|G|$. In this limit the g-mode can be stable with coupling, but it is always unstable without the coupling.

4.4.10 Numerical Calculations of the Full Model

The roots of the full of the full extended MHD dispersion relation are calculated numerically to study the stability at intermediate G. We start by considering an equilibrium with $\beta = 1\%$, $\gamma_s = 5/3$, and $\tau_i = 1/2$. Figure 65 shows the maximum growth rate for $N = 10$ as a function of P and G. The color contours indicate the normalized growth rate, and white regions are stable. The horizontal line at $P = 10$ marks the point where $P = N$. Here the equilibrium temperature gradient is zero. Below this line the temperature gradient opposes the density gradient, and above this line the two gradients point in the same direction. The vertical line at $G \approx 0.032$ marks the spot where $k_y r_i = 1/10$. The maximum value of G shown corresponds to $k_y r_i = 1/2$.

Stabilization of the g-mode does not occur for $k_y r_i < 1/2$ when $P \lesssim N$. It may occur at larger values of G, but here the extended MHD model is not valid. However, when $P > N$ there is a large region of stability at finite G. Often, when P is small, complete stability isn't achieved until the validity of the extended MHD model is questionable; however, at sufficiently large P stability occurs where extended MHD is valid. At sufficiently large P, there are three instabilities separated by two regions of stability.

The three roots of the dispersion relation are shown for $P = 100$ in Figures 66 and 67. Figure 66 focuses on the region around the g-mode and the second instability. The three modes are the unstable g-mode (red), its damped counterpart (blue) and an ion drift wave (green). All three modes propagate in the electron diamagnetic direction, and initially both branches of the g-mode have the same real frequency. At the point of stabilization the two branches of the g-mode become real waves with distinct

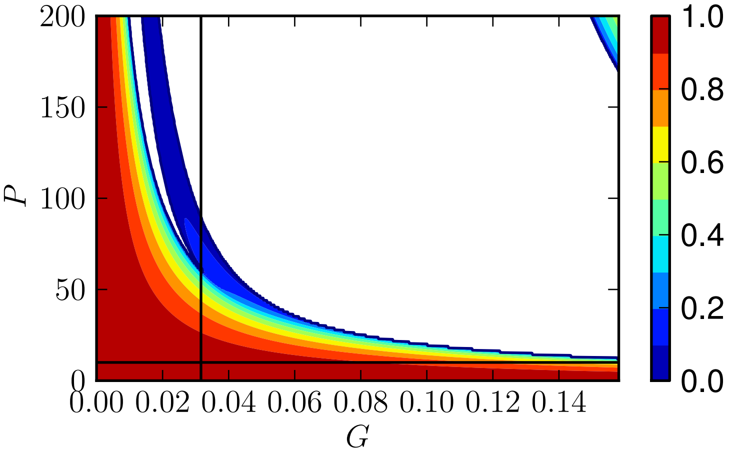

Figure 65: Linear growth rate for the full model with $N = 10$ $\beta = 1.0\%$. Regions of stability are white. The vertical line at $G \approx 0.032$ marks $k_y r_i = 1/10$ and the horizontal line marks $P = N$. The domain of G corresponds to $0 \le k_y r_i \le 0.5$.

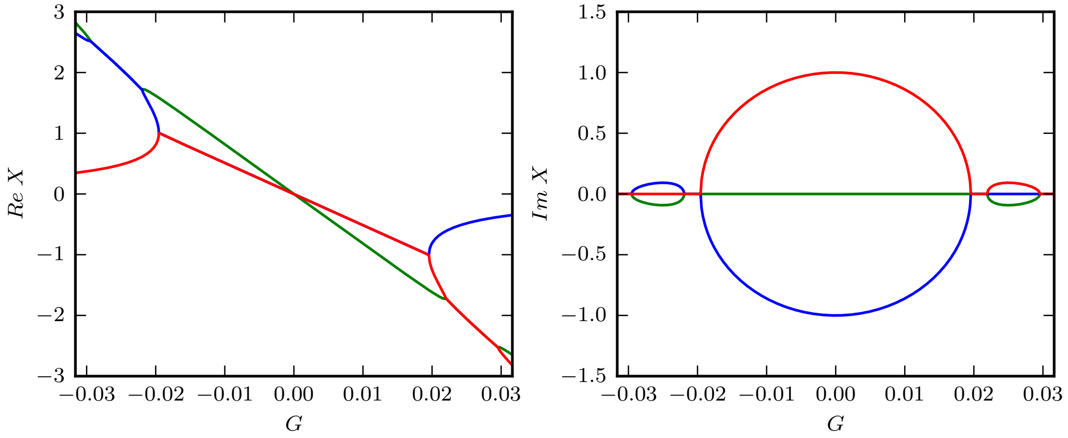

Figure 66: Linear spectrum for the full model with $N = 10$, $P = 100$, and $\beta = 1.0\%$. Similar to the two-fluid model, there is a secondary instability that is driven unstable when the ion-drift wave interacts with the high frequency branch of the stabilized g-mode.

real frequencies. Then the ion drift wave intersects the high frequency branch, and this interaction creates a new instability. This new instability has a growth rate that is less than the MHD growth rate, it is stabilized at a large value of G, and after stabilization its two branches become real waves with distinct frequencies. Figure 67 shows that these two real waves recombine at an even larger value of G to produce a third instability. This third instability has a growth rate that is larger than the original MHD growth rate, but it exists in a region where extended MHD is not valid. The third instability has a maximum growth rate that is approximately 260 times larger than the MHD growth rate. It is eventually stabilized around $G = 4.0$ (not shown).

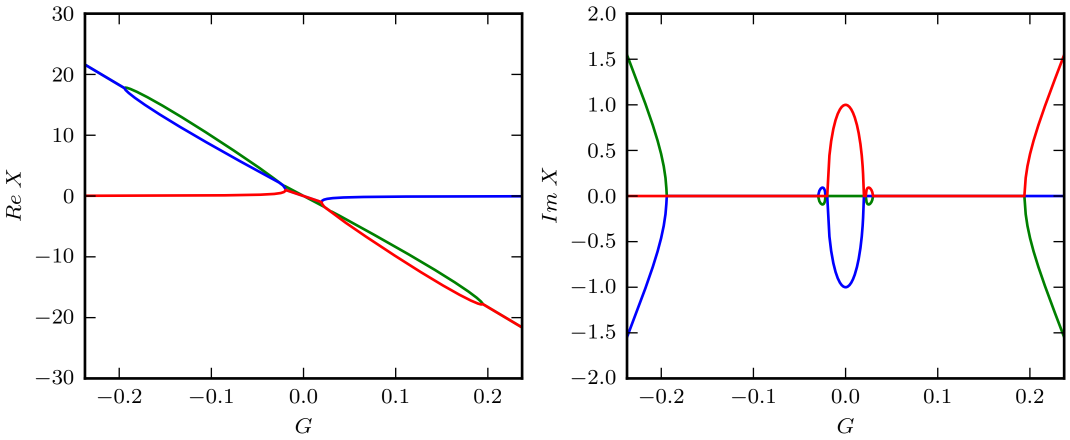

Figure 67: The linear spectrum calculated using the full model using the same parameters as Figure 66. The domain is expanded to show the onset of the third instability. This mode is destabilized when the two stabilized branches on the second instability recombine.

Between $P = 50$ and $P = 60$, the g-mode and second instability merge. Here there is no region of stability separating the two modes. However, the interaction of the drift wave with the g-mode still has an effect on the stability. As illustrated in Figure 68, there is a noticeable bulge in the growth rate that extends the region of instability.

Results shown in Figure 65 are representative of the dynamics for a wide range of N and β. In general when $P \gg N$ there are at least three distinct instabilities. The first mode is the MHD g-mode, the second mode is driven by the interaction between the high frequency branch of stabilized g-mode and the ion drift wave, and the third instability is a recombination two branches of the previously stabilized mode. As P decreases there is a critical point where the g-mode and the second mode merge, and they are no longer distinguishable. This critical point increases with both N and β.

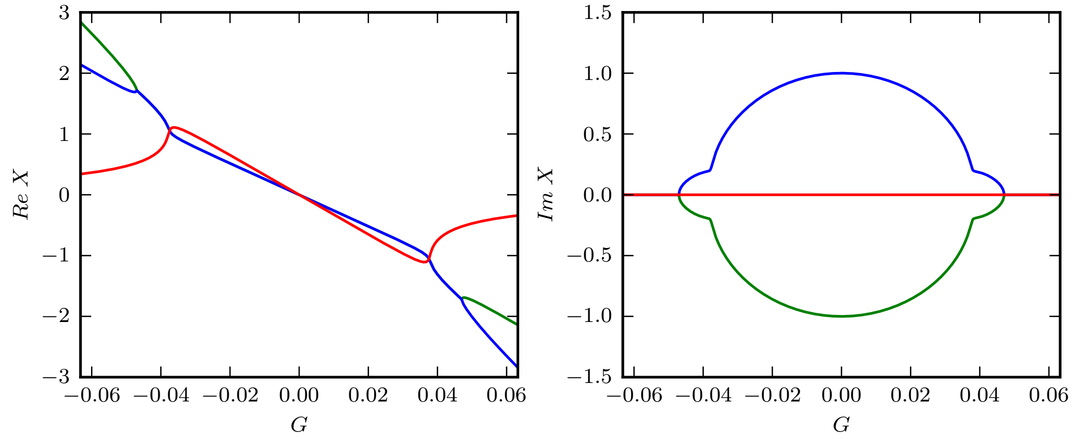

Figure 68: The linear spectrum calculated using the full model with $N = 10$, $P = 50$, and $\beta = 1.0\%$. Here there is no region of stability between the g-mode and the second mode. However, the second mode delays the onset of stability.

The second mode is similar to the mode observed in the two-fluid model in that they are both driven unstable by an interaction between the ion drift wave and one of the branches of the g-mode. However, there are some qualitative differences between the two modes. In the two-fluid model the mode is destabilized when the ion drift wave interacts with the low frequency branch of the stabilized g-mode. At small positive H the g-mode and this second mode are distinct modes, while at larger vales of H these two modes merge into one. Note that $H = P - \gamma_s N$, and increasing H corresponds to increasing P for fixed N. In the full model the second mode is driven unstable by an interaction between the ion drift wave and the high frequency branch of the stabilized g-mode. At small values of P, the g-mode and the second mode are indistinguishable, but at sufficient large values of P the two modes become distinct. In the two-fluid model, this second mode is unstable at $G = \infty$, while in the full model the mode is stabilized at finite G.

The third instability is a concern for numerical codes, such as NIMROD, that use the extended MHD model. While this mode usually exists in a regime where extended MHD is not physically valid, it exists in the model. It may arise is computations that require highly resolved meshes. It has a maximum growth rate that greatly exceeds the MHD growth rate, and it can easily dominate simulations when present. While not universal, this mode is unstable for a wide range of P, N, and β.

Finally there are cases at high β that contain a fourth instability. This fourth instability exists at values of G that are greater than the third regime of the instability, and the extended MHD model is not valid. The growth rate of this fourth mode is less than the maximum growth rate of the third mode. Numerical strategies that address the third mode should be adequate to address this fourth instability.

4.4.11 Conclusion of g-mode Analysis

The analysis of the g-mode produces a cautionary tale. We've analyzed the g-mode dispersion relation using three different extended MHD models. The first two models are incomplete representations of the third model which includes gyroviscosity and two-fluid effects. This third model is also incomplete in that it neglects the diamagnetic heat flux.

The first observation is that all three models have qualitatively different stability properties. The gyroviscous model is always more stable than MHD, and increasing G always decreases the growth rate. There is only one instability in this model, the g-mode, but there are situations where complete stabilization fails. The stability of the two-fluid model is determined by a balance between drifts due to equilibrium ion density and ion temperature gradients. This is characterized by the ITG stability parameter η_i. A secondary instability exists when $\eta_i > 2/3$. This instability is driven unstable due to an interaction between the ion drift wave and the low frequency branch of the stabilized g-mode. Near $\eta_i = 2/3$ there is a region of stability separating the g-mode and the second instability. However, at sufficiently large η_i the two modes merge, and the region of stability disappears. This second mode grows at a rate comparable to the MHD g-mode, and it is unstable at infinite G. A similar mode is observed in the full model, but there are qualitative differences. In the full model, this instability is driven unstable by an interaction between the ion drift wave and the high frequency branch of the stabilized g-mode. Initially, when this mode appears there is no region of stability separating it from the g-mode. However, at sufficiently large η_i, the two modes are distinct and separated by a region of stability. This second instability is stabilized at finite G.

The second observation is that the full extended MHD model contains unphysical modes with large growth rates. These modes exist at large $k_y r_i$, where the small Larmor radius assumption isn't valid.

These instabilities have growth rates that are much greater than the MHD growth rate of the g-mode, and they are present in codes, like NIMROD, that use the extended MHD model.

The dynamics of all three models is due to ion drifts. The quantities N, P, and R all have factors of τ implicit in their definitions. (Note that the τ dependence in $S = \tau\beta/N$ is artificial). In the cold ion limit the g-mode dispersion relation greatly simplifies:

$$(1+\gamma_s\beta)\,\omega^2 + \omega_g\omega + \Gamma_M^2\,(1+\gamma_s\beta) + \frac{g^2}{V_a^2} = 0. \tag{4.64}$$

This is the cold ion limit of the Roberts-Taylor dispersion relation corrected for finite compressibility. Here complete stabilization alway occurs when ω_g is significantly large.

While the different models have limited physical relevance, they are still useful tools for benchmarking extended MHD codes. The two-fluid and gyroviscous model dispersion relations can be used to independently test the implementation of the two-fluid Ohm's law and gyroviscosity. While the full model is a test of both terms and their mutual interaction.

Finally we close by noting the similarities and differences between the frequencies for g-mode and the numerically calculated frequencies for the pressure driven interchange in a screw pinch (Section 4.3). The growth rate and frequencies calculated using the gyroviscous model are similar for both models. For example, compare Figures 41 and 55. In both cases the gyroviscous model is always stabilizing, and increasing the Hall parameter decreases the growth rate. In both cases similar variations in the real frequency are observed.

When using the full extended MHD model, a second instability is present in both the straight spheromak and g-mode equilibria. However, the growth rate of the second mode exceeds the MHD growth rate in the straight spheromak while the growth rate is always less than the MHD growth rate in the g-mode equilibria. Both equilibria exhibit cases where there is a clear separation between the two modes, and both equilibria exhibit cases that smoothly transition from one mode to the other. In the straight spheromak model, decreasing the ion temperature at fixed pressure decreases the growth rate of the second mode. In the g-mode equilibria, decreasing the ion temperature delays the onset of the second mode and decreases its growth rate. In the g-mode the second instability is due to an interaction between a ion drift wave and the g-mode. It is not clear that the second instability in the straight spheromak model is due to a similar interaction.

4.5 Mercier Limited Equilibrium

We now return to our analysis of pressure driven interchange modes in spheromak equilibria. The Mercier criteria is often used to study pressure limits in spheromak equilibria. As discussed in Section 2.4.5, many studies determine the maximum stable pressure by assuming $D_M = 0$ across the entire domain. The pressure gradient on each flux surface is calculated from the definition of D_M. The pressure that results is assumed to be the maximum achievable pressure. However, the growth rates of linear modes near marginal stability, $D_M = 0$, are exponentially small, and non-ideal effects have a significant impact. In cases where the non-ideal effects are stabilizing, the assumption that $D_M = 0$ yields a conservative estimate for the pressure. In this section, we relax this condition by assuming that D_M is a finite uniform constant. This is used to calculate the D_M value necessary to explain the temperature observed in SSPX.

Equilibria are constructed for conditions relevant to SSPX shot 14590 using a parameterization similar to the parameterization used in Section 4.2. Equilibria are constructed in the same cylindrical flux conserver which has a height of 0.5 m and a radius of 0.5 m. The boundary flux is prescribed using Equations 4.1 and 4.2, and the $F(\psi)$ profile is prescribed using Equation 4.3. These are the boundary-flux and $F(\psi)$ profiles used in the linear stability study presented in Section 4.2. However, we now prescribe $P(\psi)$ such that D_M is nearly uniform across the domain.

The pressure gradient in the closed flux region is prescribed to be a ratio of two polynomials

$$P' = \frac{\hat{\psi}\left(1-\hat{\psi}\right)\left(\sum_{n=0}^{3} A_n \hat{\psi}^n\right)}{1+B\hat{\psi}}, \tag{4.65}$$

and the pressure gradient is assumed to be zero in the open flux region. The coefficients A_n and B are calculated to yield the desired D_M (discussed below). The resulting pressure in the closed flux region is

$$\begin{aligned} P = \frac{1}{\Delta\psi}\Big(A_0 G_1\left(\hat{\psi},B\right) + \left(A_1 - A_0\right) G_2\left(\hat{\psi},B\right) + \left(A_2 - A_1\right) G_3\left(\hat{\psi},B\right) + \\ \left(A_3 - A_2\right) G_4\left(\hat{\psi},B\right) - A_3 G_5\left(\hat{\psi},B\right)\Big) + P_0, \end{aligned} \tag{4.66}$$

where P_0 is the value of the pressure in the open flux, $\Delta\psi$ is the difference between the poloidal flux on axis and the last closed flux surface, and

$$G_n\left(x,a\right) = \int_1^x dx \frac{x^n}{1+ax} = \frac{\left(-1^n\right)}{a^{n+1}} \ln\left(\frac{1+ax}{1+a}\right) + \sum_{m=1}^{n} \frac{\left(-1\right)^{m-1}\left(x^{n+1-m}-1\right)}{a^m\left(n+1-m\right)}. \tag{4.67}$$

An iterative processes is used to calculate the coefficients A_n and B that yield $D_M = \alpha$ across the domain. First, we note that the definition of the Mercier criteria, Equation 2.59, can be expressed as a quadratic function of the pressure gradient

$$\begin{aligned} &P'^2\left(\frac{\mu_0}{4\pi^2}\right)\left(\left\langle\frac{1}{B^2\left(RB_p\right)^2}\right\rangle\left\langle\frac{B^2}{\left(RB_p\right)^2}\right\rangle - \left\langle\frac{1}{\left(RB_p\right)^2}\right\rangle^2\right) + \\ &P'\left(\frac{-V''}{4\pi^2}\left\langle\frac{B^2}{\left(RB_p\right)^2}\right\rangle + \frac{Fq'}{2\pi}\left\langle\frac{1}{\left(RB_p\right)^2}\right\rangle\right) - \frac{q'^2}{V'}\left(\alpha+\frac{1}{4}\right) = 0. \end{aligned} \tag{4.68}$$

This equation is solved to find the pressure gradient on each flux surface that yields the desired value of D_M. This equation has two solutions; however, one of the solutions is large and negative. The other solution is the physically relevant solution.

An initial equilibrium is calculated to seed the iteration. The equilibrium is analyzed using the Mercier utility discussed in Section 3.3. The utility outputs the flux surface averages needed to evaluate Equation 4.68. This equation is then solved for P' on a number of flux surfaces. This result is fit to the pressure gradient prescribed by Equation 4.65, giving a guess for the coefficients A_n and B. They are then used to construct a new equilibrium, and the process is repeated until convergence is achieved.

Figure 69 shows the calculated stability parameter for three cases D_M = 0.2, 0.5, and 0.75. The procedure produces a nearly flat D_M profile for $0.25 < \sqrt{\psi} < 0.95$ that closely matches the desired value. Here the difference between the calculated D_M and the desired D_M is less than 5%. The Mercier utility has difficulty near the magnetic axis, $\sqrt{\psi} < 0.25$, and the calculated values of D_M are not reliable. The peak in D_M near the separatrix, $\sqrt{\psi} = 1$, is due to a minimum in q. Here the Mercier criteria diverges in the presence of a finite pressure gradient. While not perfect this procedure does a reasonable job of creating equilibria with nearly uniform D_M.

A family of equilibria are generated with D_M ranging from 0 to 1.5, and their peak temperature is calculated assuming a uniform density $n = 5 \times 10^{19}\,\mathrm{m}^{-3}$, equal electron and ion temperatures, and an edge temperature of 25 eV. The resulting peak electron temperatures are plotted as a function of D_M in Figure 70. A D_M value of approximately 1.25 is needed in order to reach the experimentally

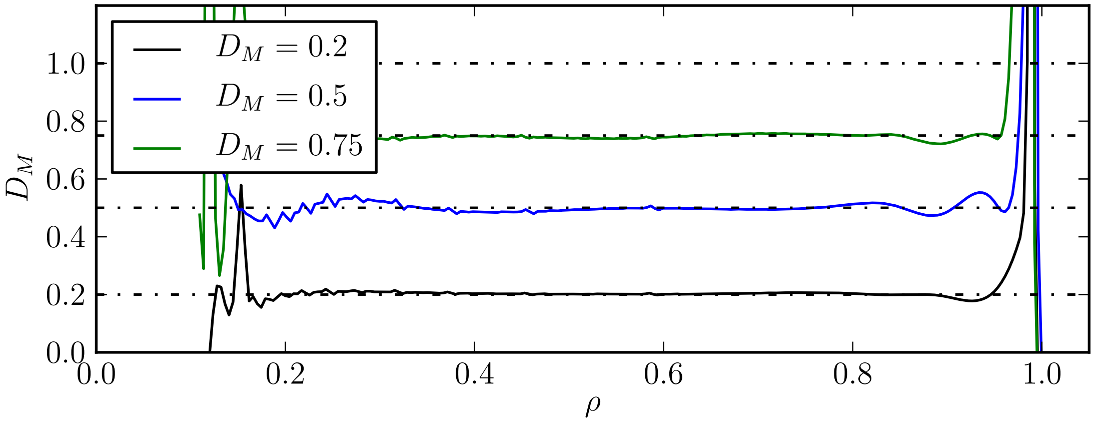

Figure 69: Calculated stability profiles for constant D_M equilibria. The dotted lines represent the desired value of D_M profile, and the solid lines represent the D_M profiles that result after several iterations.

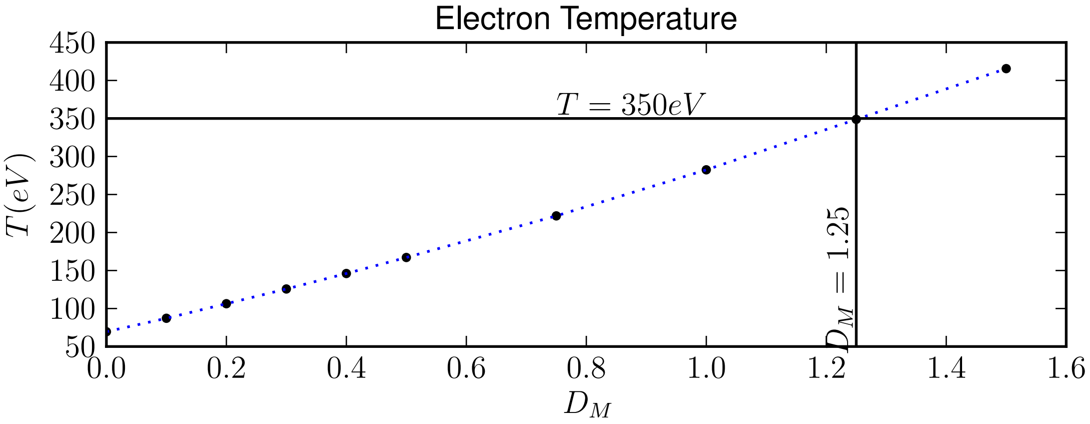

Figure 70: Electron temperatures as a function of the D_M. The electron temperature is calculated assuming a uniform density of $n = 5 \times 10^{19}\,\mathrm{m}^{-3}$ and $T_i = T_e$.

observed temperature of 350 eV.

This value of D_M greatly exceeds marginal stability, and rapidly growing ideal interchange modes are expected. We consider the results from the straight spheromak model, Section 4.3, to asses the effect of extended MHD. The analysis using the separate temperature extended MHD model shows significant stabilization for $D_s \leq 1.0$. If the result holds in toroidal geometry, then significant stabilization is expected for $D_M \leq 0.75$. This is smaller than the minimum value of D_M needed to explain the 350 eV temperatures observed in experiments.

4.6 Summary and Discussion

This chapter explores the linear stability of interchange modes using extended MHD in three different geometries. The simplest geometry is the g-mode in a slab, which uses a fictitious gravity to represent the magnetic curvature. The second geometry is a linear periodic cylindrical screw pinch designed to represent spheromak equilibria. The final geometry models decaying spheromak equilibria representative of SSPX discharges using an axisymmetric rectangular cross-section to represent the SSPX flux conserver.

The analysis of the local dispersion relation for the g-mode shows that the two-fluid Ohm's law introduces an ion drift wave that interacts with the MHD g-mode to produce a second instability. This mode is not present in the model that uses the MHD Ohm's law and includes ion gyroviscosity in the momentum equation. This gyroviscous model is always more stable than the resistive MHD model.

Similar results are observed in our linear calculations in both straight spheromak equilibria and decaying spheromak equilibria. The gyroviscous model is always more stable than the resistive MHD model. The growth rate calculated using the gyroviscous model always decreases with increasing Hall parameter.

In some cases the growth rates calculated using the two-fluid Ohm's law, with and without ion gyroviscosity in the momentum equation, are smaller than those calculated using resistive MHD, while in other cases the two-fluid growth rates are larger. Analysis using the straight spheromak shows a second instability that grows at a rate comparable to the MHD growth rate. In many of our single temperature calculations, this second instability is the fastest growing mode at the experimentally relevant Hall parameter. However, the onset of the mode is at larger Hall parameter values when the electron and ion temperatures are evolved separately and the diamagnetic heat flux is included in the model. Significant stabilization occurs for $D_s \leq 1$ in the straight spheromak when separate temperature evolution is modeled.

Several authors study the stabilization of interchange modes using the straight spheromak equilibria. Jardin, Delucia, and Glasser study the stability using a model that includes the two-fluid Ohm's law but assume cold ions[79]. Hammet and Tang use a gyrokinetic model but they order draft waves out of the system [81]. Neither of these studies observe the second instability. However, ion drift waves are absent in both models. Our analysis of the g-mode shows that the second instability arises due to an interaction between an ion drift wave and the g-mode. If a similar interaction is responsible for the second instability in the cylindrical and toroidal cases, then the absence of ion drift waves explains why neither of the previous studies observe the second mode.

In the most complete model, extended MHD effects have a strong stabilization influence for $D_s \leq 1.0$. If a similar result holds in toroidal geometry, then the stabilization should be significant for $D_M \leq 0.75$. However, using equilibria with uniform constant D_M across the domain, we estimate that $D_M \approx 1.25$ is needed to explain the temperatures observed in SSPX discharge 14590.

Chapter 5

Nonlinear Simulations

The previous chapter studied the linear stability of interchange modes using extended MHD. The primary conclusion of the linear analysis is that the hottest spheromaks in SSPX are linearly interchange unstable in extended MHD. However, nonlinear analysis is needed to determine the net effect of these modes. In this chapter we present three different series of nonlinear simulations of spheromaks relevant to SSPX.

The first series of simulations models the formation and controlled decay of SSPX using multiple extended MHD models. These simulations are based off of the simulations of early SSPX discharges performed by Sovinec et al. [5], and they are performed in a shaped geometry representative of the SSPX flux conserver. These simulations use temperature-dependent transport coefficients and self-consistently model the thermal transport with the magnetic field evolution. However, the magnetic field is noisy near the curved surfaces of the flux conserver in the simulations that use the two-fluid Ohm's law. The noise stimulates NIMROD's diffusive magnetic divergence control, enhancing the decay of the poloidal flux. This leads to artificially weak spheromaks.

To avoid the issues with curved surfaces, other simulations approximate the SSPX flux conserver as having a rectangular cross-section. Additionally, in this work we are primarily interested in the nonlinear dynamics of the controlled decay phases. So simulations that only model the decay phase are initialized with spheromak equilibria generated in NIMEQ. This allows us to forgo simulating the computationally expensive formation phase. A peaked current forms as the spheromak heats in simulations initialized with cold spheromak equilibria. The temperature-dependent resistivity leads to a nonuniform decay of the plasma currents. The resulting current gradients drive tearing modes which move inwards. Thermal confinement is lost when the tearing modes reach the magnetic axis.

A third series of simulations is initialized with hot spheromaks that freely decay. Two dimensional and three dimensional simulations are performed of the decaying spheromaks. This allows us to separate the interchange dynamics from the thermal transport. There is little difference between the 2-D and 3-D simulations initialized with a 200 eV equilibrium. This initial equilibrium is ideal interchange unstable, but the interchange dynamics has a minimal effect on the nonlinear evolution. However, 3-D simulations initialized with a 300 eV equilibrium undergo an instability which limits the peak temperature.

5.1 Full Discharge Simulations of Early SSPX Discharge

Extended MHD simulations are performed approximating the early SSPX discharge series 4620-4662. This series of discharges has been previously modeled in NIMROD using resistive MHD[70]. The resistive MHD simulations reproduce the current and magnetic field evolution of the experiment, but underpredict the peak electron temperature. The temperature in the simulation is limited to approximately 80 eV where the experiment measured electron temperatures as hot as 120 eV. We note that these early experiments were far from optimized.

The simulations are performed in a 24×48 bi-cubic finite element mesh representative of the poloidal cross-section of the SSPX flux conserver and includes part of the SSPX gun region. The toroidal direction is represented by 6 Fourier modes ($n = 0 - 5$). Current injection is modeled by applying a toroidal magnetic field along the bottom boundary of the gun. Heat is removed along the bottom row of elements in the gun when current is actively being driven. This prevents an artificial hot boundary layer from short-circuiting the gun.

The formation is modeled using single-temperature resistive MHD. Here the gun current is linearly ramped up from 0 kA to 400 kA at $t = 0.08$ ms. The gun current is then maintained at 400 kA until the end of the formation pulse at 0.12 ms. Following the formation phase, the gun current is turned off, and the spheromak freely decays until 0.5 ms. At 0.5 ms a second 200 kA current pulse is applied to sustain the plasma edge current. The current is maintained until the end of the simulation at 2 ms.

Four different models are used in simulating the free and controlled decay phases that follow the formation. The four models are single-temperature resistive MHD, separate-temperature resistive MHD, single-temperature extended MHD, and separate-temperature extended MHD. The extended MHD models include ion gyroviscosity in the momentum equation and use the two-fluid Ohm's law. All models use temperature-dependent resistivity and thermal conduction. The single-temperature models evolve a single-temperature equation assuming that $T_e = T_i$. The parallel thermal conductivity is taken to be the electron parallel thermal conductivity, and the perpendicular thermal conductivity is taken to be the ion perpendicular thermal conductivity. The separate-temperature models evolve the electron and ion temperatures separately. They use the respective parallel and perpendicular conductivities. The nonlinear form of the diamagnetic heat flux is not implemented in NIMROD and is not used. Ohmic heating is used, and the separate-temperature simulations model a collisional electron-ion equilibration.

The transport coefficients are calculated using the high magnetization limit of the Braginskii model for hydrogen plasma with $n = 5 \times 10^{19}\,\mathrm{m}^{-3}$ and $Z = 1$. The electron thermal diffusivities are $\chi_{\parallel e} = 387 T_e^{5/2}$ m^2/s and $\chi_{\perp e} = 0.039 T_e^{1/2}/B^2$ m^2/s for T_e in eV and B in T. The ion thermal diffusivities are $\chi_{\parallel i} = 15.6 T_i^{5/2}$ m^2/s and $\chi_{\perp i} = 0.5 T_i^{1/2}/B^2$ m^2/s. A uniform electron-ion collisional thermal equilibration rate of $\nu_{ei} = 4.1 \times 10^4\,\mathrm{s}^{-1}$ is used. This value corresponds to a 15 eV plasma and overestimates the collisional equilibration. Isotropic viscosity of 2000 m^2/s and artificial particle diffusivity and hyper-diffusivity of 200 m^2/s and 10 m^4/s are used to aid the numerics.

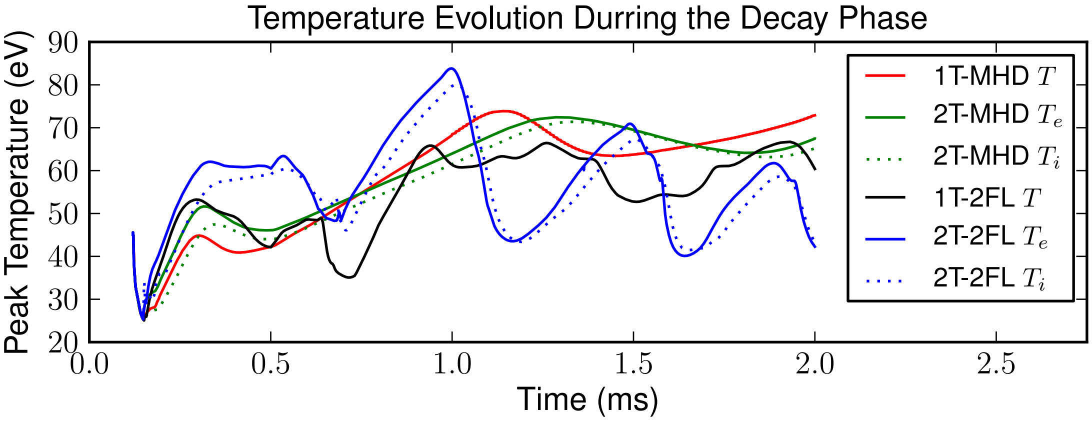

Figure 71: The simulated temperature evolution of SSPX discharges 4620-4662. The temperature evolution over the decay phase is calculated using four different extended MHD models.

Figure 71 shows the temperature evolution for each of the models during the free decay and controlled decay phases of the simulation. The plotted temperatures are the maximum temperatures in a reference poloidal cross-section. The single-temperature resistive MHD simulations reach a peak temperature of 74 eV in agreement with earlier work[5]. The separate-temperature resistive MHD simulation behaves qualitatively similar to the single-temperature simulation, and the electrons and ions both reach a peak temperature of 72 eV.

The single-temperature extended MHD simulation predicts less energy confinement than the resistive MHD simulations. Shortly after the application of the 200 kA pulse, a large $n = 3$ mode rapidly cools the spheromak to 35 eV. Following this crash, the spheromak reheats, but a series of instabilities limits the temperature to 66 eV. Following the crash the magnetic energies of all the non-symmetric modes increase in time.

The separate-temperature extended MHD simulation reaches a peak electron temperature of 84 eV and peak ion temperature of 80 eV. However, this model predicts lower temperatures than the resistive MHD models during most of the controlled decay phase. Like the single-temperature extended MHD simulation, the separate-temperature simulation undergoes a large $n = 3$ crash shortly after the application of the second pulse. Upon recovery the simulation undergoes a series of large cyclical $n = 3$ and $n = 4$ sawtooth events.

There are several shortcomings with these simulations that we improve upon in other simulations (presented below). The current and magnetic field in the extended MHD simulations are noisy in the curved regions of the SSPX flux conserver. This noise creates magnetic divergence errors which are diffused out of the system by NIMROD's divergence cleaner. This leads to an artificially enhanced rate of poloidal flux loss, resulting in significantly weaker spheromaks. For example, the flux in single-temperature resistive MHD simulation decays from 58 mWb at 0.12 ms to 37 mWb at 0.5 ms, and the flux in the separate-temperature MHD simulation decays to 38 mWb. The flux in the single- and separate- temperature extended MHD simulations decay to 29 mWb and 32 mWb, respectively. The resulting spheromaks have weaker magnetic fields and are less stable. To avoid the errors associated with the curved regions, other simulations approximate the SSPX flux conserver using a rectangular cross-section.

A second problem is that these simulations use insufficient toroidal resolution to resolve the instabilities that arise. The resistive MHD simulations are also performed using increased toroidal resolution ($n = 0 - 10$), and these cases behavior qualitatively similar to the lower resolution cases. The increased resolution simulations reach slightly hotter temperature with a peak $T \approx 83\,\mathrm{eV}$. All the simulations presented below use increased toroidal resolution.

The formation and early decay phases are the most computationally expensive phases of the simulation. Here the non-symmetric components of the magnetic field are large, and the field lines are stochastic. In this study, we are primarily interested in the stability of high temperature spheromaks, late in the decay phase when the non-symmetric components are small and flux surfaces exist. In simulations presented below, we circumvent the computationally expensive formation and early decay phases by initializing the simulations with spheromak equilibria generated in NIMEQ.

Finally, the isotropic viscosity used in these simulations is too large, and prohibits the study of nonlinear interchange dynamics. Calculations show that viscosities on the order of $1000\,\mathrm{m}^2/\mathrm{s}$ reduce the linear growth rate of ideal interchange modes by an order of magnitude (or more). The simulations described in the following sections use smaller viscosities.

5.2 Decaying Simulations Initialized with Cold Spheromaks

A second series of nonlinear simulations is performed modeling the decay of spheromak equilibria. These simulations use a cylinder of radius 0.5 m and height of 0.6 m. Here the poloidal cross-section of the SSPX flux conserver is approximated with a rectangular mesh. The elongated height is characteristic of the SSPX experiments in the last phase of operation, where the height of the flux conserver was increased to improve the current amplification during the formation[7].

The simulations are initialized with NIMEQ-generated spheromak equilibria that are allowed to decay over the course of the simulated evolution. These spheromaks are initially cold with a peak temperature of 50 eV. The decay is modeled using single-temperature resistive MHD, where the temperature-dependent transport coefficients are calculated for hydrogen plasma. The resulting transport model is the same as the single-temperature model used in the previous nonlinear simulation (Section 5.1). A 40x48 bi-cubic mesh is used to represent the poloidal cross-section. The toroidal direction is represented by 11 Fourier modes ($n = 0 - 10$).

The evolution of the peak temperature is shown in Figure 72. The figure shows the evolution of simulations that use the resistive MHD Ohm's law with and without ion gyroviscosity in the momentum

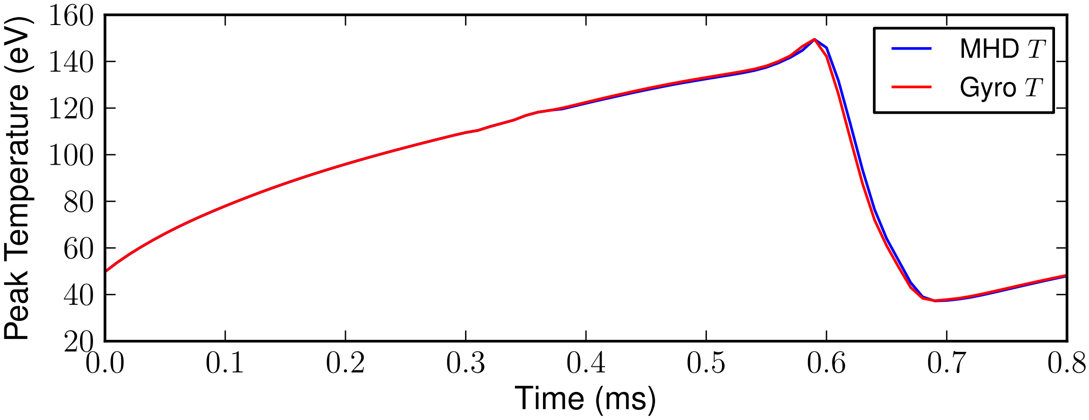

Figure 72: The temperature evolution of the spheromaks initialized with cold equilibrium.

equation. There is little difference between the two simulations. Initially the spheromak heats ohmically. Around 0.6 ms thermal confinement is lost, the temperature crashes, and afterwards the spheromak remains cold. The evolution of the temperature across the mid-plane is shown in Figure 73 for the resistive MHD simulation that neglects ion gyroviscosity. At 0.2 ms there is hot 80 to 100 eV core plasma surrounded by cold 15 eV edge plasma. The width of the hot core region shrinks as time progresses until it disappears around 0.6 ms. This corresponds to the temperature crash in Figure 72.

The colder edge plasma is approximately 20 to 30 times more resistive than the hotter core plasma. This causes the edge currents to decay more rapidly than the core currents. The resulting current gradients drive tearing modes in the edge. The magnetic field in the edge becomes stochastic. Poincare plots are shown in Figure 74 illustrating the degradation of the magnetic field. The stochastic field enhances the thermal transport. The core plasma shrinks as the region of stochastic field grows. The current gradients move inwards with the shrinking core, which is followed by the stochastic field. The process continues until the stochastic region reaches the magnetic axis around 0.6 ms. Here thermal confinement is lost, and the magnetic field is stochastic everywhere. This dynamic is not observed in simulations that use a spatially uniform resistivity.

These simulations start with a safety factor that is greater than 2/3 across the domain. However, near the separatrix q is only slightly greater than 2/3. As the currents decay the 2/3 surface becomes

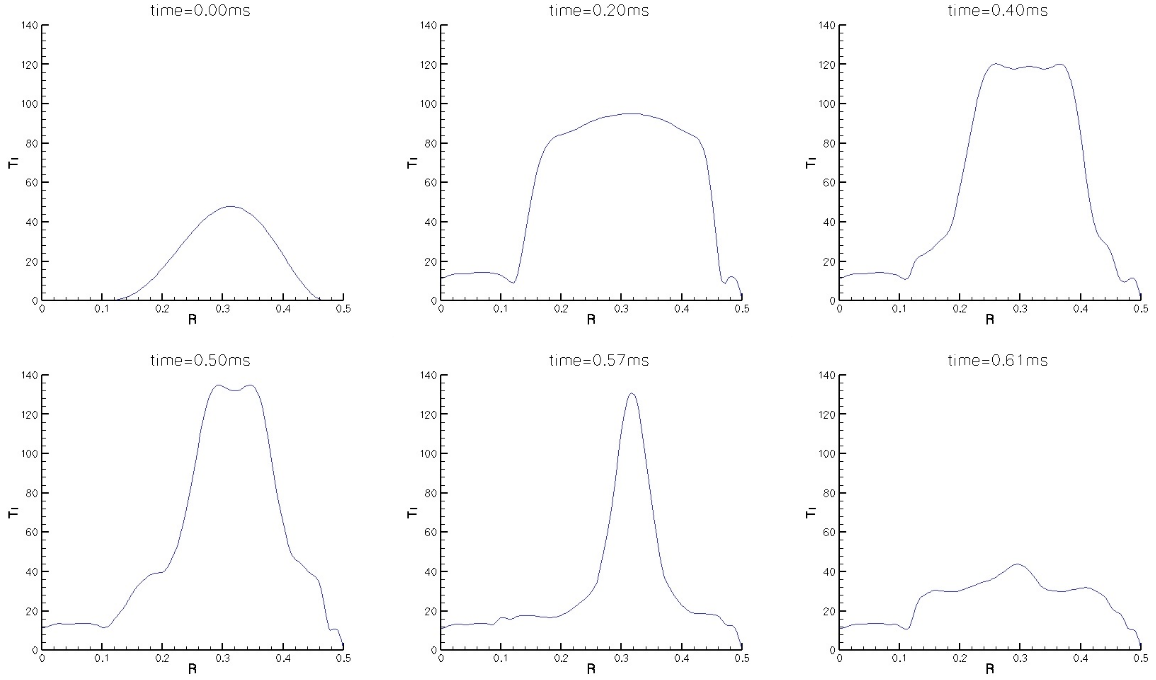

Figure 73: The temperature in eV across the mid-plane. Initially the spheromak heats an hot core region is thermally insulated from the colder edge. The width of the core region shrinks as the simulation progresses, and completely disappears at 0.61 ms.

resonant in the edge. Here the temperature and current gradients are large, and there is a strong drive for tearing modes. The resulting $m = 2$ $n = 3$ mode is the mode that degrades thermal confinement.

These simulations suffer from an unrealistic initial condition. The simulations are initialized with a cold spheromak that is intended to represent the conditions at the beginning of the decay phase. This initial spheromak has small 3-D perturbations, and it starts with good flux surfaces. These flux surfaces lead to confinement that is better than realistic conditions, and the spheromak rapidly heats. In the experiment there are large 3-D perturbations at the beginning of the decay. These perturbations result from the remnants of the formation currents that amplify the flux. The field is mostly stochastic at the beginning of the decay due to these perturbations. The stochastic field limits the temperature gradients and thereby limits the current gradients which drive tearing. In the experiment, the spheromak heats as the remnant formation currents decay allowing flux surfaces to form. The difference between the simulations and experiments suggest that some level of fluctuation early in the decay phase are essential

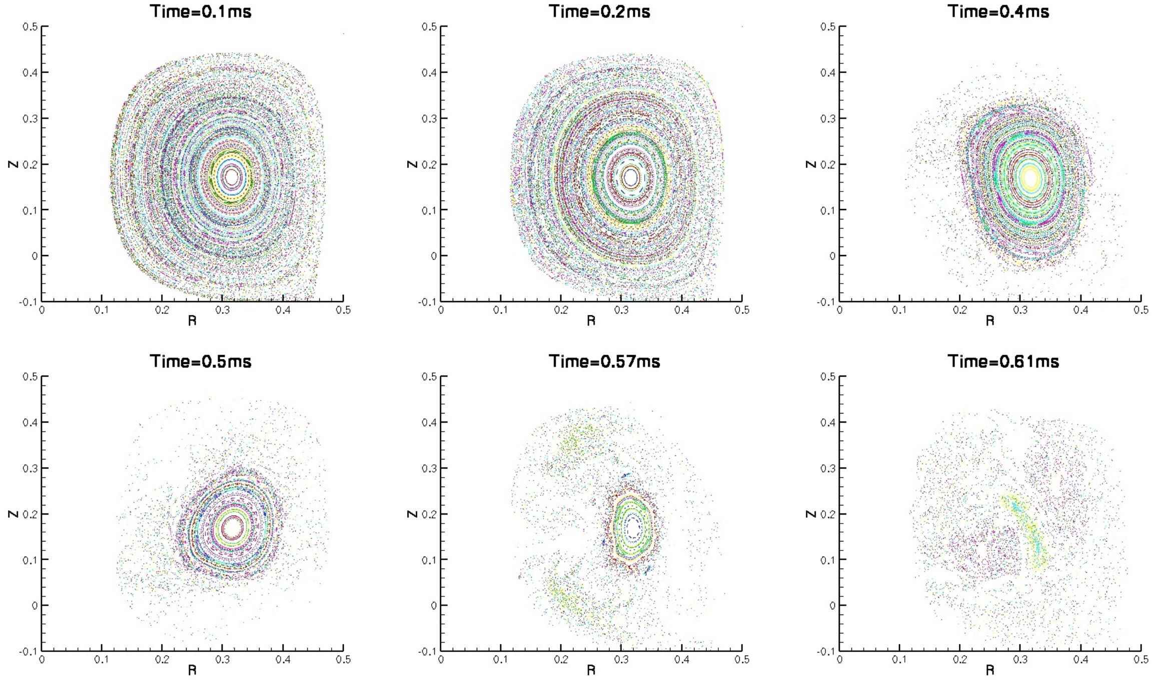

Figure 74: Poincare plots showing the degradation of the magnetic field. Initially the magnetic field is characterized by good flux surfaces. Instabilities stochasticize the magnetic field in the edge, and the region of stochastic field progresses inwards as the simulation progresses.

to discharges that develop into high performance spheromaks later.

5.3 Decaying Simulations Initialized with Hot Spheromaks

A final series of nonlinear simulations is initialized with the equilibria described in Section 4.2. These equilibria are generated using parameters based on SSPX discharge 14590 [10], and they are allowed to freely decay. We present results for simulations initialized with the 3-5-1 and 3-5-3 equilibria. The 3-5-1 equilibrium has an initial temperature of 300 eV and the 3-5-3 equilibrium has an initial temperature of 200 eV. The linear analysis shows that both of these equilibria are unstable to multiple low-n ideal interchange modes that have growth rates on the order of $\gamma\tau_A \approx 10\%$. The initial applied perturbations are small, and the spheromak plasma heats, at least initially, like the cases in the previous section. However, here q is below $2/3$ and the $m = 2$ $n = 3$ mode is not resonant.

Resistive MHD simulations are performed using temperature-dependent resistivity and thermal conductivities. The transport coefficients are calculated using the high magnetization limit of the Braginskii model for hydrogen plasma with an effective charge of $Z = 1$. A single-temperature advance is used assuming $T_i = T_e$ with anisotropic thermal conduction. The parallel electron conductivity is used in the parallel direction, and the perpendicular ion conductivity is used in perpendicular direction. Ohmic heating is included, allowing the spheromaks to heat as they decay. An isotropic viscosity of $10\,\mathrm{m}^2/\mathrm{s}$ is used.

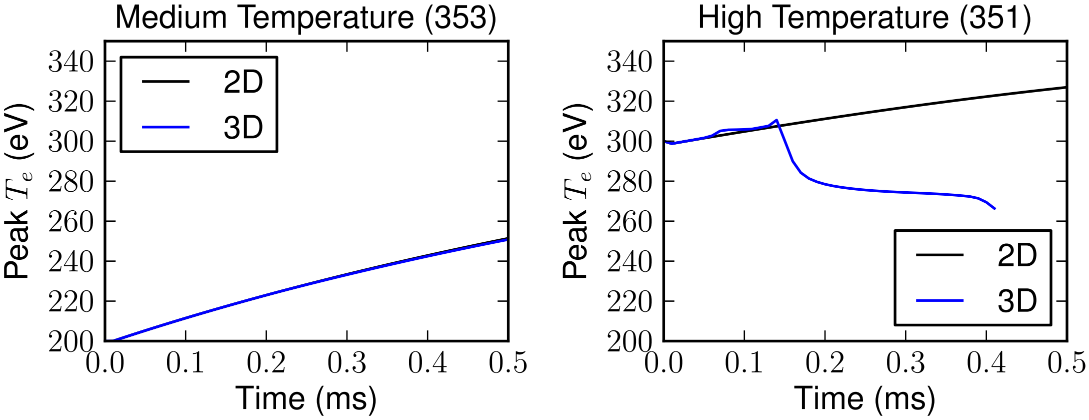

Figure 75: Evolution of the peak electron temperature during the free decay of the medium and high temperature spheromaks. The electron temperatures are shown for both the 2D (black) and 3D (blue) simulations.

Both axisymmetric and fully 3-D nonlinear simulations are performed. The axisymmetric simulations use only the $n = 0$ Fourier harmonics and model the evolution of the spheromak due to collisional transport. The 3-D simulations keep 22 Fourier components with $n = 0 - 21$. Convergence is confirmed using a simulation of the 3-5-3 equilibrium with 43 Fourier components ($n = 0 - 42$), and only a small difference is observed between the two simulations. The 3-D simulations capture the interchange dynamics in addition to the collisional transport. Comparing the 2-D and 3-D simulations allows us to separate the interchange dynamics from the collisional transport.

The temperature evolution is shown for the two equilibria is Figure 75. The maximum temperature in a reference poloidal cross-section is shown for both the 2-D and 3-D simulations. For the first 0.5 ms there is little difference between in the peak temperatures of 2-D and 3-D simulations initialized with 3-5-3 equilibrium. Here the interchange dynamics plays little role in the thermal evolution. However, the temperature evolution of the 2-D and 3-D simulations initialized with the hotter 3-5-1 equilibrium are noticeably different. The 2-D simulation continuously heats, while an instability limits the temperature in the 3-D simulation. The instability occurs after 0.15 ms, limiting the temperature to 280 eV. A second instability arises 0.41 ms into the simulation that leads to a complete loss of confinement.

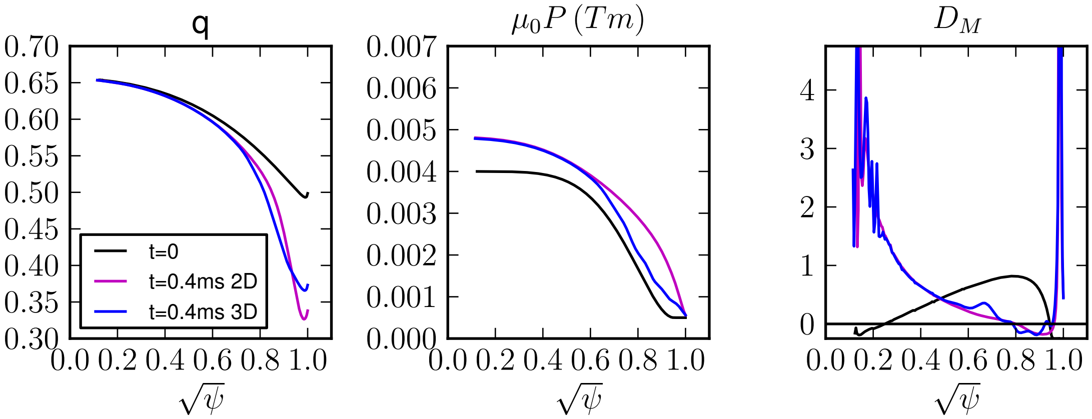

Figure 76: Safety factor, pressure, and Mercier stability parameter profiles for the simulation initialized with the 200 eV spheromak (353). The profiles are shown at the beginning of the simulation (black) at 0.4 ms into the decay for the 2D (purple) and 3D (blue) simulations.

The safety factor, pressure and Mercier stability parameter are shown for the 3-5-3 case at the beginning of the simulation and 0.4 ms into the simulation in Figure 76. The safety factor is greatly reduced in the edge near the separatrix . This is due to decay of the edge currents, and is characteristic of gun-formed spheromaks that are allowed to freely decay. Shortly after 0.5 ms this simulation crashes due to a mode resonant in the edge. The pressure profiles of 2-D and 3-D simulations are nearly identical in the core, but there are noticeable differences in the edge. Here, the pressure of the 3-D simulation is reduced compared to the 2-D simulation, due to MHD activity in the edge. The Mercier profile is strongly peaked near the magnetic axis and greatly exceeds the marginal stability point. However, there is good agreement between the 2-D and 3-D simulations implying that the interchange dynamics has a minor role in the evolution. The Mercier parameter is small in edge, where there are noticeable difference in the pressure between the two simulations. The stability criterion is not satisfied over $\sqrt{\psi} \lesssim 0.8$.

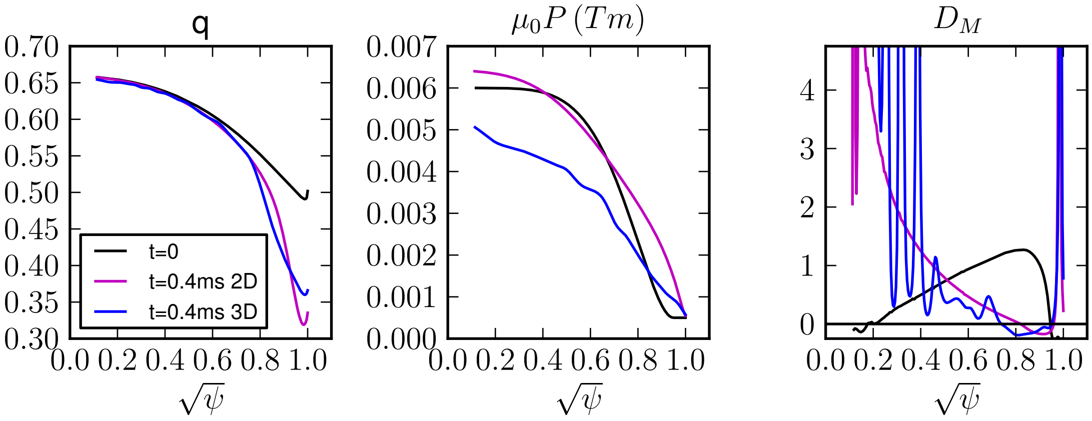

Figure 77: Safety factor, pressure, and Mercier stability parameter profiles for the simulation initialized with the 300 eV spheromak (351). The profiles are shown at the beginning of the simulation (black) at 0.4 ms into the decay for the 2D (purple) and 3D (blue) simulations.

The safety factor, pressure, and Mercier stability parameter are shown for the 3-5-1 case at the beginning of the simulation and 0.4 ms into the simulation in Figure 77. This is shortly before the onset of the second instability that destroys confinement. Again, the safety factor is greatly reduced near the edge due to the decay of edge currents. The 3-D pressure is smaller than the 2-D pressure throughout the domain. The Mercier parameter is peaked at the magnetic axis and greatly exceeds the stability criterion. The profile is highly oscillatory for the 3-D simulation. The troughs in D_M occur near low order rational surfaces where the pressure gradient is reduced due to mode activity, and the peaks occur between rational surfaces. Note that the Mercier utility only uses symmetric fields, and the reported D_M is an approximation for the 3-D simulation.

The Mercier stability profile that results from the 2-D simulations is shown as a function of the safety factor in Figure 78. The separatrix is located on the left near the smaller values of q, and the magnetic axis is located on the right near the large values of q. The rational surfaces with $n \leq 12$

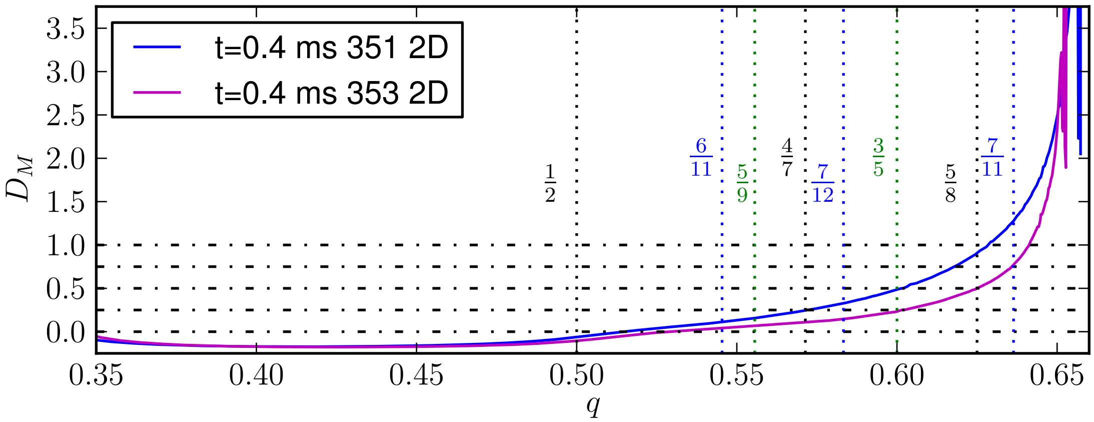

Figure 78: Mercier stability parameter profile 0.4 ms into the decay for 2D simulations initialized with the 200 eV (purple) and 300 eV (blue) spheromak equilibria. The separatrix is located on the left near $q = 0.35$ and the magnetic axis is on the right near $q = 0.65$. The location of several low-order rational surfaces are indicated.

located between $q = 1/2$ and $q = 2/3$ are indicated. As previously stated the collisional transport leads to a D_M profile that is strongly peaked near the magnetic axis. However, there are a limited number of low-order rational surfaces in this region.

Most of the low-order rational surfaces reside in a region where the D_M parameter is smaller. In the simulation initialized with the 200 eV spheromak (3-5-3) most of the low-order rational surfaces have $D_M < 0.25$. Here the linear analysis predicts slowly growing modes. The stability parameter is $D_M \approx 0.5$ at the 5/8 surface, and it is $D_M \approx 0.75$ at the 7/11 surface. The linear analysis predicts that modes resonant here should have significant growth rates, yet they don't appear to significantly affect the evolution. The linear analysis in Section 4.2 calculates growth rates that are on the order of $10^5\,\mathrm{s}^{-1}$ for $D_M \gtrsim 0.5$. A 0.5 ms simulation is about 50 e-folding times, more than enough time for such an instability to grow out of the noise.

In the hotter simulation (3-5-1), the stability parameter is between $0.25 < D_M < 1.00$ for many of the low-order rational surfaces. The large values of D_M are consistent with the instability in the 3-D simulations that limits the temperature. However, it is not obvious that there is a critical value of D_M for which the instability affects confinement.

The simulation of the colder 200 eV spheromak is limited by the decay of the currents on the open field. The above simulations evolve the free decay of the spheromak where no sustainment pulse is applied. Attempts to apply a control pulse in the simulations have not extended the decay. If the applied currents are too weak, they unrealistically short out across the gun and never encircle the spheromak. If the currents are too strong they drive instabilities that severely degrade confinement.

5.4 Conclusions of Nonlinear Simulations

Several series of nonlinear simulations have been performed. The first series of simulations models the full discharge of an early series of SSPX discharges. These simulations use multiple extended MHD models. However, poor confinement is observed when the two-fluid Ohm's law is used. These simulations are noisy near curved surfaces of the SSPX discharge. The noise leads to an artificially increased rate of poloidal flux loss and results in weaker spheromaks. To avoid this issue, other simulations use a rectangular mesh to approximate the poloidal cross-section of the SSPX flux conserver. The simplified-geometry simulations are also initialized using spheromak equilibria generated in NIMEQ. This allows us to skip the computationally expensive formation.

Simulations initialized with cold equilibria, representative of temperatures at the beginning of the free decay, are limited by tearing modes. Rapid heating of the core plasma leads to spatially non-uniform resistivity. This leads to non-uniform decay of the current density, and the resulting current gradients drive tearing modes. In the experiment remnants of the formation currents degrade flux surfaces, limit the temperature gradients, and reduce the tearing drive. Differences between these simulations and the experiment suggest that some fluctuations early in the decay phase allow the spheromak to reach high temperatures later.

A final series of simulations is initialized with hot spheromaks and are allowed to freely decay. Simulations initialized with a 300 eV equilibrium undergo an instability which cools the spheromak, limiting its temperature to 280 eV. Simulations initialized with a 200 eV spheromak continuously heat for 0.5 ms and reach a peak temperature around 250 eV. The duration of the colder simulations are limited by the decay of the currents on the open field. Here no control pulse is applied, and q drops below 1/2. Modes resonant on this surface grow and eventually disrupt the plasma.

During the decay of the hot spheromaks, the collisional transport leads to a pressure profile where D_M is strongly peaked in the core, and D_M is smaller throughout the domain. These equilibria have low shear in the core, and there are a limited number of rational surfaces in the region where D_M is large. The profile violates the ideal stability criterion only slightly at most of the low-order resonant surfaces. Our linear analysis suggests that the resulting modes should grow slowly, and extended MHD may have a significant stabilizing effect in these conditions.

Chapter 6

Conclusions

One of the outstanding issues in spheromak research is to identify the mechanism(s) that limit the pressure in spheromaks. In this work we help to address this issue by studying the effects of extended MHD on interchange stability in high temperature spheromaks. The work is motivated by a difference between the measured electron temperatures in SSPX and the temperatures calculated in resistive MHD simulations. The simulations are more susceptible to instabilities which cool the plasma. The temperatures in the resistive MHD simulations are limited by pressure driven instabilities. Our original hypotheses was that extended MHD effects, not present in the prior simulations, introduce drifts that stabilize these instabilities, thereby allowing the spheromak to reach hotter temperatures. However, the main conclusion is that linear extended MHD stabilization does not significantly enhance the stability of modes resonant on low-order rational surfaces at experimental conditions.

The linear analyses of SSPX-relevant equilibria show that they are ideal interchange unstable. This is in agreement with evaluation of the Mercier stability criteria, which finds that these equilibria violate the ideal marginal stability condition. Extended MHD significantly reduces the growth rates of the high-n modes. However, experimentally the low-n modes have the greatest impact on the confinement, and extended MHD has a mixed effect on the low-n modes. In some cases extended MHD effects are weakly stabilizing, while in other cases they are destabilizing.

A cylindrical screw pinch model is used to better understand the extended MHD results on the low-n modes. A second instability is present in extended MHD calculations that include the two-fluid Ohm's law. This mode appears at finite Hall parameter, and it grows at a rate comparable to the MHD interchange. The diamagnetic heat flux, which is often neglected in analysis, has a significant stabilizing effect. It delays the onset of the second mode. When the diamagnetic heat flux is neglected, the second instability dominates at SSPX-relevant Hall parameters, and its growth rate often exceeds the MHD growth rate. However, extended MHD is strongly stabilizing for $D_s \leq 1$ when the diamagnetic heat flux is included in the calculation. One way to relate cases used for linear analysis with SSPX is to consider the D_M-value needed to achieve the peak experimental temperature of $T_e = 350\,\text{eV}$ with a uniform D_M profile. This requires $D_M \approx 1.25$. This value approaches the $D_M \approx 0.75$ condition, where strong stabilization is observed, but it is not in the strongly stabilized regime. (Recall that D_M in toroidal equilibria corresponds to $D_s + 0.25$ in screw pinch equilibria).

To understand the nature of the second instability we analyze the extended MHD dispersion relation for the local gravitational interchange mode derived by Zhu et al. [36]. The two-fluid Ohm's law introduces an ion drift wave. This drift wave can interact with the g-mode to produce a second instability, similar to the instability observed in the spheromak calculations. In both the g-mode analysis and the spheromak analysis, this instability is absent in calculations that include ion gyroviscosity in the momentum equation but use the resistive MHD Ohm's law. However, in the g-mode analysis, the growth rate of this second mode is always smaller than the MHD growth rate.

We've performed a number of nonlinear simulations to assess the nonlinear impact of the interchange modes on the spheromak evolution. We performed full discharge simulations of early SSPX discharges using multiple extended models. The extended models suffered from an artificial enhancement of poloidal flux loss due to numerical noise in the curved regions of the mesh. Other simulations approximate the cross-section of the SSPX flux conserver with a rectangular mesh to avoid this error. These later simulations are also initialized with NIMEQ-generated equilibria and skip the computationally expensive formation phase.

Simulations initialized with cold equilibria, representative of temperatures at the beginning of the free decay, are limited by tearing modes. Rapid heating of the core plasma leads to a spatially non-uniform resistivity. This leads to non-uniform decay of the current density, and the resulting current gradients drive tearing modes. In the experiment remnants of the formation currents degrade flux surfaces, and limit temperature gradients that form early on. Ultimately this reduces the tearing drive. Differences between these simulations and the experiment suggest that some fluctuations early in the decay phase allow the spheromak to reach high temperatures later.

A final series of simulations is initialized with hot spheromaks and are allowed to freely decay. Simulations initialized with a 300 eV equilibrium undergo an instability which cools the spheromak, limiting it to 280 eV. Simulations initialized with a 200 eV equilibrium continuously heat for 0.5 ms and reach a temperature around 250 eV. The duration of the colder simulations are limited by the decay of the currents on the open field. No sustainment pulse in applied, and q drops below 1/2. Modes resonant on this surface grow and eventually disrupt the plasma.

The resistive decay of the hot spheromaks show that the collisional transport leads to a pressure profile where D_M is strongly peaked in the core. Throughout most of the domain, D_M is small and most of the low-order resonant surfaces only weakly violate the ideal stability parameter. The resulting linear modes should grow slowly, and extended MHD may have a significant stabilizing effect.

The results of the linear calculation are consistent with the results of nonlinear simulations. The linear analysis shows that decaying spheromak equilibria are ideal interchange unstable. Linear growth rates on the order of $\gamma\tau_A = 10\%$ are observed at conditions relevant to high-temperature spheromaks. Both current driven tearing modes and pressure driven interchange modes are observed in nonlinear simulations. These modes grow to large amplitude and limit the peak temperature in the simulations. Linear calculations show that extended MHD effects do not significantly alter the stability properties of the highest temperature discharges. Extended MHD does not improve the performance of the nonlinear simulations. In some cases there is little difference between the resistive and extended MHD simulations, while in other cases there are significant differences in the simulated decay. However, the spheromak undergoes large destructive instabilities when either model is used. Linear calculations show that the diamagnetic heat flux has an important stabilizing effect. The nonlinear simulations do not include this heat flux, and more work is needed to understand its effect on the nonlinear evolution.

Considering both our linear and nonlinear results, we are unable to account for the differences between experiment and simulations using fluid-based extended MHD models. There are several other possible explanations that may explain the difference. As discussed in Section 2.4.3, Ji et al. [61] consider the effect of kinetic modifications to the parallel heat flux at low-collisionality. The collisional heat flux used in NIMROD overestimates the parallel heat flux in low-collisionality regimes. Ji et al. consider the effect of the kinetic modifications to the heat flux on the temperature in SSPX using an integral closure derived by taking moments of the drift kinetic equation. The authors evolve a high resolution simulation of an early SSPX discharge using resistive MHD with the collisional closure. Late in the simulation the authors apply the kinetic closure. The temperature is evolved to equilibration, keeping all the other fields fixed it time. With the kinetic closure the temperature is 6% hotter than the collisional closure. This temperature still falls short of the experimental measurement. These experiments were limited to 120 eV, and the difference between the two closures is expected to be more pronounced at hotter temperatures.

It would also be worth reexamining the formation phase of SSPX discharges using extended MHD. Comparisons between NIMROD and SSPX show that simulations correctly calculate the saturated flux over a wide range of parameters [95]. These simulations maintain the formation pulse until the flux saturates. However, in many of the full discharge simulations, where the simulated formation pulse approximates the experimental formation pulse, the magnetic field in the simulations is weaker than the magnetic field in the experiment. For example in [5] the magnetic energy in the simulation is about 80% of the magnetic energy of the experiment. It may be that while resistive MHD is correctly predicting the saturated flux, it is not correctly reproducing the temporal dynamics. Extended MHD effects can increase the rate of magnetic reconnection, and could possibly lead to an enhanced rate of flux amplification. Experimentally the peak temperature/pressure is bounded by $\beta_e \sim 5\%$[8]. Given a limiting β, the temperature then scales quadratically with the magnetic field: $T_e \approx \beta_e B^2$. A modest difference in the magnetic field would lead to greater temperature difference. Using this scaling, a 10% increase in the magnetic field would lead to a 20% increase in the temperature.

The extended MHD linear stability properties of low-n modes are not sufficiently different than resistive MHD to alter the dominant modes observed in the resistive MHD simulations. In addition new modes are present in calculations. While NIMEQ facilitates nonlinear simulations of the decay phase and some cases show confinement despite low-level MHD activity, robust evolution in the conditions of SSPX is not obtained.

Another major result of this work in the development of the NIMEQ code[11]. NIMEQ is a general purpose Grad-Shafranov equilibrium solver. Special consideration is given to the geometric axis at $R = 0$ to ensure regularity for compact configurations. NIMEQ allows users to specify different prescriptions for $F(\psi)$ and $P(\psi)$ in the open and closed flux regions. This allows us to model current on the open field. NIMEQ is developed within the NIMROD framework, eliminating interpolation errors that would otherwise arise when importing an externally generated equilibrium into NIMROD. The accuracy of the calculated equilibria converges spectrally for sufficiently smooth equilibria. This allows for the generation of accurate equilibria on relatively small meshes.

Appendix A

Calculations Involving the Coulomb Wave Function

The FRC equilibria, Equations 3.6-3.8, used to the benchmark NIMEQ are described by 0-th order Coulomb wave functions. A number of numerical routines were developed to perform the comparison between numerical and analytic solutions. Routines are needed to calculate $F_0(\eta, \rho)$ and $F_0'(\eta, \rho)$, where the prime denotes a derivative in ρ. The zeros of F_0 are needed in order to satisfy the radial boundary condition. This is done by choosing a value of ρ and finding the smallest positive η such that $F_0(\eta, \rho) = 0$. The values of ρ that are zeros of F_0' for given η are needed to locate the radial location of the magnetic axis and calculate the poloidal flux on the axis.

The Coulomb wave function $F_L(\eta, \rho)$ is the regular solution to the differential equation

$$\frac{d^2 F_L}{d\rho^2} + \left[1 - \frac{2\eta}{\rho} - \frac{L(L+1)}{\rho^2}\right] F_L = 0. \tag{A.1}$$

It has the expansion

$$F_L(\eta, \rho) = C_L(\eta)\, \rho^{L+1} \Phi_L(\eta, \rho), \tag{A.2}$$

where Φ_L is the power series

$$\Phi_L(\eta, \rho) = \sum_{n=L+1}^{\infty} A_n^L(\eta)\, \rho^{n-L-1}, \tag{A.3}$$

with $A_{L+1}^L = 1$, $(L+1) A_{L+2}^L = \eta$, and $(n+L)(n-L-1) A_n^L = 2\eta A_{n-1}^L - A_{n-2}^L$ for $n > L+2$. The normalization $C_L(\eta)$ is calculated using the recursion relation

$$C_L = \frac{\sqrt{L^2+\eta^2}}{L(2L+1)} C_{L-1}, \tag{A.4}$$

where $C_0^2 = \frac{2\pi\eta}{e^{2\pi\eta}-1}$[96]. The derivative of the Coulomb wave function has the expansion

$$\frac{dF_L(\eta,\rho)}{d\rho} = C_L(\eta)\,\rho^L \Phi_L^*(\eta,\rho), \tag{A.5}$$

where

$$\Phi_L^*(\eta,\rho) = \sum_{n=L+1}^{\infty} nA_n^L(\eta)\,\rho^{n-L-1}. \tag{A.6}$$

Routines to calculate $F_0(\eta,\rho)$ and $F_0'(\eta,\rho)$ are added to NIMEQ. The terms $\Phi_0(\eta,\rho)$ and $\Phi_0^*(\eta,\rho)$ are calculated recursively using Equations A.3 and A.6. Convergence is tested, after each term is added to the series, using the inequalities:

$$A_N^0\rho^{N-1} < \epsilon\left(\sum_{n=1}^{N} nA_n^0\rho^{n-1}\right) \tag{A.7}$$

for F_0 and

$$NA_N^0\rho^{N-1} < \epsilon\left(\sum_{n=1}^{N} nA_n^0\rho^{n-1}\right) \tag{A.8}$$

for F_0', where $\epsilon = 10^{-20}$ is the desired tolerance. F_0 is calculated from the converged Φ_0 using $F_0 = C_0\rho\Phi_0$, and F_0' is calculated from the converged Φ_0^* using $F_0' = C_0\Phi_0^*$. The accuracy is tested by comparing the calculated values for F_0 with data tabulated in [96] for several values of ρ and η. Table 7 shows that the numerical calculations reproduce the tabulated values of F_0 to six decimal places. There is uncertainty in the last digit of the tabulated data.

η	ρ	Calculated F_0	Tabulated F_0
2	1.2	0.4298468	0.4298470
1	2.8	1.0169066	1.0169066
3	3.6	0.1598555	0.1598556

Table 7: Comparison of numerically calculated values of the Coulomb wave function, F_0, with tabulated values of F_0.

A separate code is written to calculate the roots of the Coulomb wave function for fixed ρ_0. $C_0(\eta)$ is positive for positive η, and values of η that are zeros of $F_0(\eta,\rho_0)$ are also zeros of $\Phi_0(\eta,\rho_0)$. Newton iterations are used to find the zeros of $\Phi_0(\eta,\rho_0) = 0$:

$$\eta^{i+i} = \eta^i - \left.\frac{\phi_0}{\frac{\partial\Phi_0}{\partial\eta}}\right|_{\eta^i,\rho_0}, \tag{A.9}$$

where η^i is the value of η at the i-th iteration. Convergence is tested by checking to see that magnitudes of both F_0 and Φ_0 are less than a specified tolerance. In practice, the tightest tolerance achievable is found to be around 10^{-14} using double precision floating point arithmetic. The resulting value of η is found to be accurate to 1 part in 10^{10}. The η derivative is derived from Equation A.3:

$$\frac{\partial \Phi_0}{\partial \eta} = \sum_{n=1}^{\infty} \frac{\partial A_n^0}{\partial \eta} \rho^{n-1}, \tag{A.10}$$

where $\frac{\partial A_1^0}{\partial \eta} = 0$, $\frac{\partial A_2^0}{\partial \eta} = 1$, and $n\,(n-1)\,\frac{\partial A_n^0}{\partial \eta} = 2A_{n-1}^0 + 2\eta \frac{\partial A_{n-1}^0}{\partial \eta} - \frac{\partial A_{n-2}^0}{\partial \eta}$ for $n > 2$.

Finally, the vales of ρ that are zeros of $F_0'\left(\eta_0, \rho\right)$ for a specified η_0 are needed to locate the position of the magnetic axis and determine the value of the magnetic flux at the axis. $C_0\left(\eta\right)$ does not depend on ρ, and zeros of Φ_0^* are zeros of F_0'. Newton iterations are used to find the zeros of Φ_0^*:

$$\rho^{i+i} = \rho^i - \left. \frac{\Phi_0^*}{\frac{\partial \Phi_0^*}{\partial \rho}} \right|_{\eta_0, \rho^i}, \tag{A.11}$$

where now ρ is being iterated upon at constant η_0. The derivate in the denominator on the right side of the equation is now with respect to ρ, and it is found from Equation A.6:

$$\frac{\partial \Phi_0^*}{\partial \rho} = \sum_{n=2}^{\infty} n\,(n-1)\,A_n^0\left(\eta\right)\rho^{n-2}. \tag{A.12}$$

Convergence is tested by checking that both Φ_0^* and F_0' are less than the desired tolerance of 10^{-14}.

Appendix B

Extension of the Suydam and Mercier Criteria

The characteristic safety factor profile of a CHI spheromak has a local minimum just inside the separatrix. Here the magnetic shear, which is proportional to q', is zero. The Mercier stability parameter scales as $1/q'^2$, and it diverges where $q' = 0$. A characteristic safety factor profile and the corresponding Mercier stability parameter profile for a CHI spheromak are shown in Figure 79. In this appendix we consider the validity of the Suydam and Mercier stability parameters near surfaces where $q' = 0$. These criteria are derived using a local analysis that involves expanding q around a rational surface. The linear term, $q'x$, is assumed to be the dominate term, and higher order terms are neglected (x is the distance from rational surface). However, near the surface where $q' = 0$ the linear term is small, and higher order terms may be significant.

We modify the analysis of the Suydam and Mercier criteria in regions near the $q' = 0$ surface. When we expand q about a rational surface we assume that the linear term is negligible and the quadratic term dominates. This assumption is valid in regions where $|q''x| \gg |q'|$. The quadratic term introduces shear away from the rational surface. In doing this calculation we are curious if this shear, absent in the standard analysis, provides an extra degree of stabilization. However, the analysis shows that both the standard Suydam and Mercier criteria correctly predict ideal stability in this region.

The extension of the Suydam parameter, which applies to screw pinch equilibria, follows the derivation of the Suydam parameter presented in Chapter 9 of Freidberg's Ideal MHD textbook [97]. The

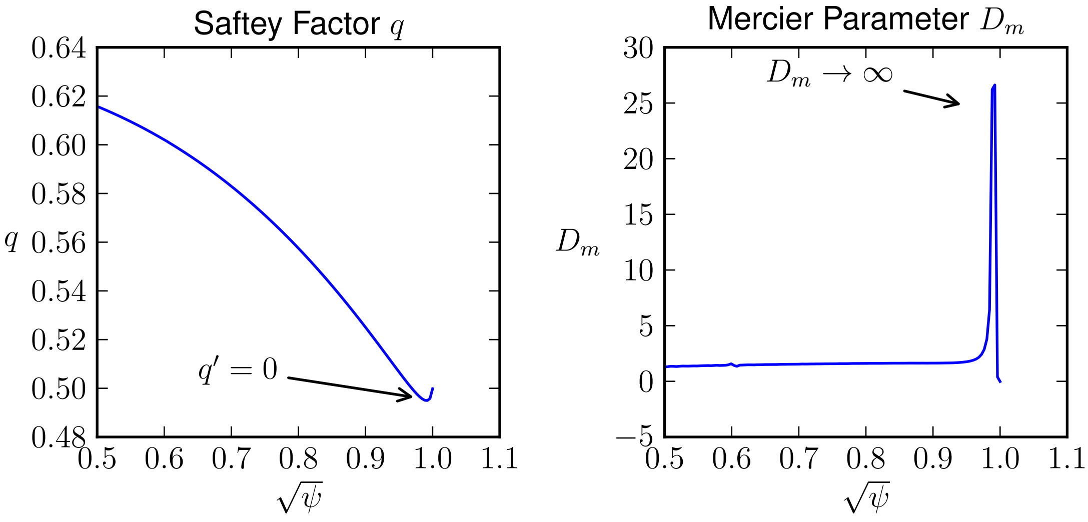
Saftey Factor q

Mercier Parameter D_m

Figure 79: The safety factor and Mercier stability parameter for a typical CHI spheromak equilibrium. The safety factor has a minimum inside of the separatrix, and the Mercier stability parameter diverges at this minimum.

derivation starts from Newcomb's equation:

$$\delta W = \frac{2\pi^2 R}{\mu_0}\int dr\left(f\xi'^2 + g\xi^2\right) \tag{B.1}$$

$$f = \frac{rF^2}{k^2 + \frac{m^2}{r^2}} = \frac{rF^2}{k_0^2} \tag{B.2}$$

$$g = 2\frac{k^2}{k_0^2}\mu_0 p' + \frac{k_0^2 r^2 - 1}{k_0^2 r^2} rF^2 + \frac{2k^2}{rk_0^4}\left(kB_z - \frac{mB_\theta}{r}\right)F \tag{B.3}$$

where the radial displacement, ξ, is assumed to vary as $\xi\left(\vec{r}\right) = \xi\left(r\right)e^{(im\theta + ikz)}$, $k_0 = k^2 + \frac{m^2}{r^2}$, and $F = \vec{K}\cdot\vec{B}_0 = \frac{m}{r}B_\theta + kB_z$. The equilibrium is ideal MHD stable if $\delta W \geq 0$ for all possible displacements.

The mode is assumed to be localized around a rational surface r_s where $q\left(r_s\right) = \frac{m}{n}$. Physical quantities are expanded around the rational surface, and lowest order terms in $x = r - r_s$ are kept. If $p' \neq 0$ then to lowest order $g \approx 2\frac{k^2}{k_0^2}\mu_0 p'\Big|_{rs}$. In the standard derivation of the Suydam parameter $f \approx \frac{r_s F'^2}{k_0^2}\Big|_{rs} x^2$ to lowest order, where $F' = kB_z\frac{q'}{q}$. In region near the $q' = 0$ surface, the lowest order nonzero term in f is $f \approx \frac{r_s F''^2}{k_0^2}\Big|_{rs} x^4$ where $F'' = kB_z\frac{q''}{q}$.

The local δW equation for $q' \neq 0$ is

$$\frac{\delta W}{2\pi^2}\frac{\mu_0}{R} = \frac{r_s k_z^2 B_z^2}{k_0^2}\frac{q'^2}{q^2}\int_{-\Delta}^{\Delta} dx\left(x^2\xi'^2 - D_s\xi^2\right) \tag{B.4}$$

where $D_s = -\frac{2\mu_0 p'}{rB_z^2}\frac{q^2}{q'^2}\Big|_{rs}$ is the Suydam parameter, and the integral is evaluated up to a small distance, Δ, from the rational surface. The corresponding δW equation for $q' = 0$ but $q'' \neq 0$ is

$$\frac{\delta W}{2\pi^2}\frac{\mu_0}{R} = \frac{r_s k_z^2 B_z^2}{k_0^2}\frac{q''^2}{q^2}\int_{-\Delta}^{\Delta} dx\left(x^4\xi'^2 - D_{II}\xi^2\right) \tag{B.5}$$

where $D_{II} = -\frac{8\mu_0 p'}{rB_z^2}\frac{q^2}{q''^2}\Big|_{rs}$ is a stability parameter analogous to D_S. In both cases stability depends on the sign of an integral of the form $I = \int dx\left(x^n\xi'^2 - D\xi^2\right)$. If there exists a displacement such that the integral I is negative, then instability will result.

The integral is evaluated using integration by parts

$$\int_a^b dx\left(x^n\xi'^2 - D\xi^2\right) = -\int_a^b dx\xi\left(\frac{d}{dx}\left(x^n\frac{d\xi}{dx}\right) + D\xi\right) + x^n\xi\frac{d\xi}{dx}\Big|_a^b. \tag{B.6}$$

The leads to the identification of the Euler-Lagrange equation

$$\frac{d}{dx}\left(x^n\frac{d\xi}{dx}\right) + D\xi = 0. \tag{B.7}$$

The Euler-Lagrange equation for $q' \neq 0$ has $n = 2$ and $D = D_s$. The general solution of this equation is

$$\xi = |x|^{-1/2}\left(c_1\sin\alpha + c_2\cos\alpha\right), \tag{B.8}$$

where $\alpha = \frac{1}{2}\sqrt{4D_s - 1}\ln|x|$. This solution is singular at the rational surface, $x = 0$, and the solution is oscillatory if $D_s > \frac{1}{4}$. The "wave length" of oscillation decreases with decreasing x.

The Euler-Lagrange equation for $q' = 0$ and $q'' \neq 0$ is given by $n = 4$ and $D = D_{II}$. The general solution is

$$\xi = |x|^{-3/2}\left(c_1 J_{-3/2}\left(\frac{\sqrt{D_{II}}}{x}\right) + c_2 Y_{-3/2}\left(\frac{\sqrt{D_{II}}}{x}\right)\right) \tag{B.9}$$

where J_i and Y_i are Bessel functions of the first and second kind. The order of the Bessel functions are half of an odd integer, and the Bessel function are expressible as a series of sines and cosines

$$J_{-3/2}(z) = \sqrt{\frac{2\pi}{z}}\left(\frac{\cos z}{z} + \sin z\right) \tag{B.10}$$

$$Y_{-3/2}(z) = -\sqrt{\frac{2\pi}{z}}\left(\frac{\sin z}{z} - \cos z\right). \tag{B.11}$$

The solution is singular at the rational surface, and it is oscillatory for $D_{II} > 0$. The "wave length" of these oscillations decreases with decreasing x.

The oscillatory nature of the solutions allows for the construction of an unstable trial function. A sketch of the trail function is shown in Figure 80 for $q' = 0$. The radial displacement has even symmetry around the rational surface, and we treat $x > 0$. The domain is divided into three regions: $0 < x < x_1$, $x_1 < x < x_2$, and $x_2 < x$.

In the region $0 < x < x_1$, the radial displacement is a constant $\xi = \xi_0$ and its contribution to the integral I is $-D\xi_0^2 x_1$. In the second region, $x_1 < x < x_2$, the radial displacement satisfies the Euler-Lagrange equation and therefore has zero contribution to I. In the third region $x_2 < x$ the displacement is zero, and it does not contribute to I.

The interfaces between the different regions can also contribute to the integral I through the term $x^n \xi \frac{d\xi}{dx}\Big|_a^b$ in Equation B.6. If the Euler-Lagrange solution is oscillatory, then there always exists a point x_1 where $\xi\left(x_1\right) \neq 0$ but $\frac{d\xi(x_1)}{dx} = 0$. If the solution is oscillatory, then there also exists a point x_2 where $\xi\left(x_2\right) = 0$. In these cases the interface terms have zero contribution to the integral I.

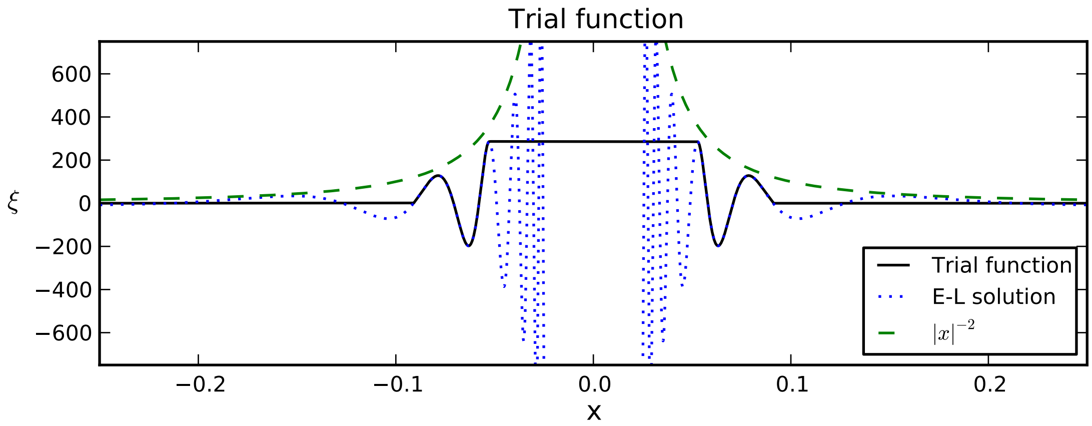

Figure 80: A unstable trial function (solid black line) for $q' = 0$. The solution to the Euler-Lagrange equation (dotted blue line) is bounded by the function $|x|^{-2}$ (dashed green line). The Euler-Lagrange solution is not shown near the rational surface for clarity.

Taking into account the symmetry about the rational surface, the total contribution to the integral

I is $-2D\xi_0^2 x_1$, and δW is negative if $D > 0$. The two condition for instability are 1) the solution to the Euler-Lagrange equation is oscillatory and 2) the corresponding stability parameter D is positive.

In the traditional Suydam analysis, $q' \neq 0$, the solution is oscillatory for $D_s > \frac{1}{4}$. In the extension to surfaces near the $q' = 0$ surface the solution is oscillatory if $D_{II} > 0$. In both cases $D > 0$ if the solution is oscillatory. Therefore instability results if oscillatory.

The Suydam criteria for instability, $D_s = \frac{-2\mu_0 p'}{r_s B_z^2} \frac{q^2}{q'^2} > \frac{1}{4}$, can be expressed in terms of a critical pressure gradient $\mu_0 p' < \frac{-q'^2}{q^2} \frac{r_s B_z^2}{8}$. In the absences of sheer, $q' = 0$, instability is predicted for $\mu_0 p' < 0$.

In our accounting for finite q'', the corresponding criteria for instability near the $q' = 0$ surface is $D_{II} = \frac{-8\mu_0 p'}{r_s B_z^2} \frac{q^2}{q''^2} > 0$, or equivalently $\mu_0 p' < 0$. This result agrees with the Suydam prediction, and accounting for q'' does not change the stability boundary.

The two theories produce different results for the mode structure. The radial displacement of the Suydam mode decreases as $|x|^{-1/2}$ while the displacement for the mode with $q' = 0$ decreases as $|x|^{-2}$. While beyond the scope of this analysis, this increased localization may be important when calculating the growth rate and suggests that non-ideal effects may have a greater significance near the $q' = 0$ surface.

The above analysis applies to regions where $|q'| \ll |q''|\, x_2$, where x_2 is effectively the width of the trial function. The Euler-Lagrange solution has the property that the wave length of oscillation decreases with decreasing distance from the rational surface. This property always allows for the construction of a sufficiently narrow trial function such that $|q'| \gg |g''|\, x_2$ except at surfaces where $q' = 0$ exactly. Therefore Suydam analysis is valid everywhere except at the $q' = 0$ surface.

The analysis is easily extended to higher order cases where $q' = 0$, $q'' = 0$, $\cdots$, $q^{(m-1)} = 0$, but $q^{(m)} \neq 0$. The Euler-Lagrange equation for these cases is $\frac{d}{dx}\left(x^{2m}\frac{d\xi}{dx}\right) + D\xi = 0$, where $D \sim \frac{-\mu_0 p'}{r B_z^2} q^2 \left(q^{(m)}\right)^{-2}\Big|_{r_s}$. The Euler-Lagrange equation has the general solution

$$\xi = |x|^{-m+1/2}\left(c_1 J_{-\frac{2m-1}{2m-2}}\left(\frac{\sqrt{D}}{(1-m)\,|x|^{m-1}}\right) + c_2 Y_{-\frac{2m-1}{2m-2}}\left(\frac{\sqrt{D}}{(1-m)\,|x|^{m-1}}\right)\right). \tag{B.12}$$

The Bessel functions are oscillatory for $D > 0$, indicating instability. The instability condition $D > 0$ is equivalent to the condition $\mu_0 p' < 0$, in agreement with the Suydam prediction. Accounting for higher order corrections to the shear does not change the local stability boundary.

The extension of the Mercier criteria to the $q' = 0$ surface follows the derivation presented Mercier's paper [27]. The only difference in the derivation is in going from Equation 20 to Equation 22 in his paper. This is where Mercier introduces the local approximation. Mercier uses a linear approximation for the safety factor $q = (\psi - \psi_0)\, q'(\psi_0)$. At the $q' = 0$ surface, the linear term is zero and the quadratic term is the dominant term. This leads to the approximation $q = \frac{1}{2}(\psi - \psi_0)^2\, q''(\psi_0)$. Similarly the shear near the rational surface is approximately $q'(\psi) = (\psi - \psi_0)\, q''(\psi_0)$. (In his paper Mercier uses the quantity $\nu = n\,(m - nq)$).

This approximation results in the δW equation

$$\begin{aligned}\delta W_F = \frac{\pi}{2}\int d\psi d\chi \Bigg(& \frac{B_p^2\rho^2}{B^2}\left[\frac{r^2}{J}\left[\frac{JF'}{r^2} - (\psi-\psi_0)\, q'' - \frac{1}{2}(\psi-\psi_0)^2 q''\frac{\rho'}{\rho}\right]^2\right.\\ & \left.+\frac{2jF}{rB_p^2}\left[\frac{JF'}{r^2} - (\psi-\psi_0)\, q'' - \frac{1}{2}(\psi-\psi_0)^2 q''\frac{\rho'}{\rho}\right] + \frac{Jj^2F^2}{r^4B_p^4}\right] - 2JK\rho^2\Bigg)\end{aligned} \tag{B.13}$$

where $\rho(\psi)$ is the radial displacement, J is the Jacobian, $j = \mu_0 J_t$ is the toroidal current,

$$K = -\frac{FF'}{R^2}\frac{\partial\,(B_pJ/R)}{\partial\psi} - \mu_0 p'\frac{\partial\,(B_pJ)}{\partial\psi}, \tag{B.14}$$

and all physical quantities are evaluated at the rational surface. Mercier uses an orthogonal coordinate system (ψ, θ, χ) where θ is the toroidal angle, and χ is a poloidal angel. Equation B.13 is analogous to Equation 23 in [27]:

$$\begin{aligned}\delta W_F = \frac{\pi}{2}\int d\psi d\chi \Bigg(& \frac{B_p^2\rho^2}{B^2}\left[\frac{r^2}{J}\left[\frac{JF'}{r^2} - q' - (\psi-\psi_0)\, q'\frac{\rho'}{\rho}\right]^2\right.\\ & \left.+\frac{2jF}{rB_p^2}\left[\frac{JF'}{r^2} - q' - (\psi-\psi_0)\, q'\frac{\rho'}{\rho}\right] + \frac{Jj^2F^2}{r^4B_p^4}\right] - 2JK\rho^2\Bigg).\end{aligned} \tag{B.15}$$

The terms in Equations B.13 and B.15 that are proportional to $\rho\rho'$ are integrated by parts converting them into terms proportional ρ^2. Following this integration by parts, the energy equation is written in the compact form $\delta W = C^2R$. For the case $q' = 0$

$$R_{II} = \int d\psi \left[\, x^4 \rho'^2 - \left(A_{II} + B_{II} x\right) \rho^2 \right] \tag{B.16}$$

$$C_{II}^2 = q''^2 \frac{\pi}{8} \oint d\chi \frac{r^2}{J} \frac{B_p^2}{B^2} \tag{B.17}$$

$$A_{II} = -\oint \left[\frac{B_p^2 J}{r^2 C_{II}^2 B^2} \left(F' + \frac{jF}{rB_p^2} \right)^2 - \frac{2JK}{C_{II}^2} \right] d\chi \tag{B.18}$$

$$B_{II} = \oint \left[q'' \frac{B_p^2}{B^2 C_{II}^2} \left(F' + \frac{jF}{rB_p^2} \right) \right] d\chi \tag{B.19}$$

where $x = \psi - \psi_0$.

The corresponding equation in Mercier's derivation, $q' \neq 0$ is $\delta W = C^2 R$ where

$$R_M = \int d\psi \left[\, x^2 \rho'^2 - A \rho^2 \right] \tag{B.20}$$

$$C_M^2 = q'^2 \frac{\pi}{2} \oint d\chi \frac{r^2}{J} \frac{B_p^2}{B^2} \tag{B.21}$$

$$A_M = -\oint \left[\frac{B_p^2 r^2}{J C^2 B^2} \left(\left(F' + \frac{jF}{rB_p^2} \right) \frac{J}{r^2} - \frac{q'}{2} \right)^2 - \frac{2JK}{C^2} \right] d\chi + \frac{1}{4} \tag{B.22}$$

As is the case for screw pinch equilibria, stability depends on the sign of the integral R. The integral for the case with shear, $q' \neq 0$, has the same form as the screw pinch case, and instability results if $A_M > \frac{1}{4}$. The integral for $q' = 0$ is similar to the screw pinch case, except there is a new term that is linear is x.

To treat this new case we need to find the solution to the Euler-Lagrange equation $x^4 \rho'' + 4x^3 \rho' + \left(B_{II} x + A_{II}\right) \rho = 0$. The solution has an irregular singularity at $x = 0$. This is due to the quartic nature of the leading order term. To remove this singularity the solution assumed to have the form $\rho = e^{\frac{L}{x}} Y$. Inserting this form into the Euler-Lagrange equation gives the new equation

$$x^2 Y'' + \left(4x - 2L\right) Y' + \frac{1}{X} \left(B_{II} - 2L\right) Y = 0 \tag{B.23}$$

where $L = \pm\sqrt{-A_{II}}$. For $L = +\sqrt{-A_{II}}$ Equation B.23 has the solution

$$Y = x^m \sum_{n=0}^{\infty} a_n x^n \tag{B.24}$$

$$m = \frac{B_{II}}{2L} - 1 \tag{B.25}$$

$$a_1 = \frac{m^2 + 3m}{2L} a_0 \tag{B.26}$$

$$a_2 = \frac{m^2 + 5m + 4}{4L} a_1 \tag{B.27}$$

$$a_{n+1} = \frac{m^2 + 3m + 2mn + n^2 + 3n}{2L\,(n+1)} a_n. \tag{B.28}$$

The exponential part of the solution, $e^{\frac{\sqrt{-A_{II}}}{x}}$, is the important term. If $A_{II} > 0$, then this term will be oscillatory near the rational surface. The wavelength of the oscillations decreases with decreasing x. This oscillatory nature allows for the construction of an unstable trail function. The trail function is created similar to the cylindrical case. We note that the linear term, $B_{II} x \rho^2$ is an odd function and has zero net contribution to the integral.

The Mercier parameter, A_M, diverges at the surface where $q' = 0$; however, the product $C_M^2 A_M$ does not. For positive C^2 the Mercier criteria becomes $C_M^2 A_M > \frac{C_M^2}{4}$. Evaluating this inequality at the $q' = 0$ surface produces

$$-\oint \left[\frac{B_p^2 J}{r^2 B^2} \left(F' + \frac{jF}{r B_p^2} \right)^2 - 2JK \right] d\chi > 0. \tag{B.29}$$

Similarly, the stability criteria derived for the $q' = 0$ surface can be expressed as $C_{II}^2 A_{II} > 0$. This gives the instability criteria

$$-\oint \left[\frac{B_p^2 J}{r^2 B^2} \left(F' + \frac{jF}{r B_p^2} \right)^2 - 2JK \right] d\chi > 0. \tag{B.30}$$

The two inequalities are identical showing that the Mercier criteria correctly predicts the stability of the $q' = 0$ surface.

Bibliography

[1] P. Wieser, editor. *Research Needs for Magnetic Fusion Energy Sciences*, 2009.

[2] F. J. Wysocki, J. C. Fernández, I. Henins, T. R. Jarboe, and G. J. Marklin. Evidence for a pressure-driven instability in the CTX spheromak. *Physical Review Letters*, 61(21):2457–2460, Nov 1988.

[3] C. R. Sovinec, A. H. Glasser, T. A. Gianakon, D. C. Barnes, R. A. Nebel, S. E. Kruger, D. D. Schnack, S. J. Plimpton, A. Tarditi, and M. S. Chu. Nonlinear magnetohydrodynamics simulation using high-order finite elements. *Journal of Computational Physics*, 195(1):355 – 386, 2004.

[4] E. B. Hooper, L. D. Pearlstein, and R. H. Bulmer. MHD equilibria in a spheromak sustained by coaxial helicity injection. *Nuclear Fusion*, 39(7):863–871, 1999.

[5] C. R. Sovinec, B. I. Cohen, G. A. Cone, E. B. Hooper, and H. S. McLean. Numerical investigation of transients in the SSPX spheromak. *Physical Review Letters*, 94(3):035003, Jan 2005.

[6] E. B. Hooper, B. I. Cohen, H. S. McLean, R. D. Wood, C. A. Romero-Talamas, and C. R. Sovinec. NIMROD resistive magnetohydrodynamic simulations of spheromak physics. *Physics of Plasmas*, 15(3):032502, 2008.

[7] R. D. Wood, D. N. Hill, H. S. McLean, E. B. Hooper, B. F. Hudson, J. M. Moller, and C. A. Romero-Talamas. Improved magnetic field generation efficiency and higher temperature spheromak plasmas. *Nuclear Fusion*, 49(2):025001 (4pp), 2009.

[8] R. D. Wood, D. N. Hill, E. B. Hooper, S. Woodruff, H. S. McLean, and B. W. Stallard. Improved operation of the SSPX spheromak. *Nuclear Fusion*, 45(12):1582–1588, 2005.

[9] C. R. Sovinec, J. M. Finn, and D. del Castillo-Negrete. Formation and sustainment of electrostatically driven spheromaks in the resistive magnetohydrodynamic model. *Physics of Plasmas (1994-present)*, 8(2):475–490, 2001.

[10] H. S. McLean, R. D. Wood, B. I. Cohen, E. B. Hooper, D. N. Hill, J. M. Moller, C. Romero-Talamas, and S. Woodruff. Transport and fluctuations in high temperature spheromak plasmas. *Physics of Plasmas*, 13(5):056105, 2006.

[11] E. C. Howell and C. R. Sovinec. Solving the Grad-Shafranov equation with spectral elements. *Computer Physics Communications*, 185(5):1415 – 1421, 2014.

[12] S. I. Braginskii. Transport processes in a plasma. *Reviews of Plasma Physics*, 1:205–311, 1965.

[13] K. V. Roberts and J. B. Taylor. Magnetohydrodynamic equations for finite Larmor radius. *Physical Review Letters*, 8(5):197–198, Mar 1962.

[14] D. Biskamp, E. Schwarz, and J. F. Drake. Two-fluid theory of collisionless magnetic reconnection. *Physics of Plasmas (1994-present)*, 4(4):1002–1009, 1997.

[15] D. D. Schnack, J. Cheng, D. C. Barnes, and S. E. Parker. Comparison of kinetic and extended magnetohydrodynamics computational models for the linear ion temperature gradient instability in slab geometry. *Physics of Plasmas (1994-present)*, 20(6):–, 2013.

[16] H. Grad and H. Rubin. Hydromagnetic equilibria and force-free fields. In *Proceedings of the Second United Nations Conference on the Peaceful Uses of Atomic Energy*, volume 31, page 190. United Nations, 1958.

[17] V. D. Shafranov. On magnetohydrondynamical equilibrium configurations. *Soviet Physics JETP-USSR*, 6(3):545–554, 1958.

[18] L. S. Solovev. Theory of hydromagnetic stability of toroidal plasma configuartions. *Soviet Physics JETP-USSR*, 26(2):400, 1968.

[19] S. B. Zheng, A. J. Wootton, and Emilia R. Solano. Analytical tokamak equilibrium for shaped plasmas. *Physics of Plasmas*, 3(3):1176–1178, 1996.

[20] A. J. Cerfon and J. P. Freidberg. “One size fits all” analytic solutions to the Grad-Shafranov equation. *Physics of Plasmas*, 17(3):032502, 2010.

[21] M. N. Rosenbluth and M. N. Bussac. MHD stability of spheromak. *Nuclear Fusion*, 19(4):489, 1979.

[22] J. M. Finn, W. M. Manheimer, and E. Ott. Spheromak tilting instability in cylindrical geometry. *Physics of Fluids*, 24(7):1336–1341, 1981.

[23] P. B. Parks and M. J. Schaffer. Analytical equilibrium and interchange stability of single- and double-axis field-reversed configurations inside a cylindrical cavity. *Physics of Plasmas*, 10(5):1411–1423, 2003.

[24] H. L. Berk, J. H. Hammer, and H. Weitzner. Analytic field-reversed equilibria. *Physics of Fluids*, 24(9):1758–1759, 1981.

[25] Bernstein I. B., Frieman E. A., Kruskal M. D., and Kulsrud R. M. An energy principle for hydromagnetic stability problems. *Proceedings of the Royal Society of London A*, 244:17, 1958.

[26] B. R. Suydam. Stability of a linear pinch. *Proccedings of the Second United Nations International Conference on the Peaceful uses of Atomic Energy*, 31:157, 1958.

[27] C. Mercier. Stability criterion of a hydromagnetic toroidal system with scalar pressure. *Nuclear Fusion*, pages 801–808, 1962.

[28] J. M. Greene. A brief review of magnetic wells. *Comments Plasma Phys. Controlled Fusion*, 17(6):389–402, 1997.

[29] H. Grad. Magnetofluid-dynamic spectrum and low shear stability. *Proceedings of the National Academy of Sciences*, 70(12):3277–3281, 1973.

[30] T. E. Stringer. Effect of finite Larmor radius on the interchange instability in a cylindrical plasma. *Nuclear Fusion*, 15(1):125, 1975.

[31] S. Gupta, J. D. Callen, and C. C. Hegna. Violating Suydam criterion produces feeble instabilities. *Physics of Plasmas*, 9(8):3395–3401, 2002.

[32] B. Coppi, J. M. Greene, and J. L. Johnson. Resistive instabilities in a diffuse linear pinch. *Nuclear Fusion*, 6(2):101, 1966.

[33] A. H. Glasser, J. M. Greene, and J. L. Johnson. Resistive instabilities in general toroidal plasma configurations. *Physics of Fluids (1958-1988)*, 18(7):875–888, 1975.

[34] D. D. Schnack, D. C. Barnes, D. P. Brennan, C. C. Hegna, E. Held, C. C. Kim, S. E. Kruger, A. Y. Pankin, and C. R. Sovinec. Computational modeling of fully ionized magnetized plasmas using the fluid approximation. *Physics of Plasmas*, 13(5):058103, 2006.

[35] M. N. Rosenbluth, N. A. Krall, and N. Rostoker. Finite Larmor radius stabilzaition of weakly unstable confined plasmas. *Nucl. Fusion Suppl.*, 1:143, 1962.

[36] P. Zhu, D. D. Schnack, F. Ebrahimi, E. G. Zweibel, M. Suzuki, C. C. Hegna, and C. R. Sovinec. Absence of complete Finite-larmor-radius stabilization in extended mhd. *Physical Review Letters*, 101(8):085005, Aug 2008.

[37] N. M. Ferraro and S. C. Jardin. Finite element implementation of Braginskii's gyroviscous stress with application to the gravitational instability. *Physics of Plasmas*, 13(9):092101, 2006.

[38] J. J. Ramos. General expression of the gyroviscous force. *Physics of Plasmas (1994-present)*, 12(11):–, 2005.

[39] J. D. Huba. Finite Larmor radius magnetohydrodynamics of the Rayleigh-Taylor instability. *Physics of Plasmas*, 3(7):2523–2532, 1996.

[40] J. M. Finn, W. M. Manheimer, and T. M. Antonsen. Drift-resistive interchange and tearing modes in cylindrical geometry. *Physics of Fluids (1958-1988)*, 26(4):962–973, 1983.

[41] R. J. Hastie, J. J. Ramos, and F. Porcelli. Drift ballooning instabilities in tokamak edge plasmas. *Physics of Plasmas*, 10(11):4405–4412, 2003.

[42] E. S. Benilov and O. A. Power. A drift model of interchange instability. *Physics of Plasmas (1994-present)*, 14(8):1–7, 2007.

[43] W. E. Quinn and Compact Toroid Staff. Compact toroid experiments: Spheromaks and field-reversed configurations. *Nuclear Instruments and Methods in Physics Research*, 207(1-2):121 – 127, 1983.

[44] C. W. Barnes, J. C. Fernández, I. Henins, H. W. Hoida, T. R. Jarboe, S. O. Knox, G. J. Marklin, and K. F. McKenna. Experimental determination of the conservation of magnetic helicity from the balance between source and spheromak. *Physics of Fluids*, 29(10):3415–3432, 1986.

[45] F. J. Wysocki, J. C. Fernández, I. Henins, T. R. Jarboe, and G. J. Marklin. Improved energy confinement in spheromaks with reduced field errors. *Physical Review Letters*, 65(1):40–43, Jul 1990.

[46] T. R. Jarboe, F. J. Wysocki, J. C. Fernández, I. Henins, and G. J. Marklin. Progress with energy confinement time in the CTX spheromak. *Physics of Fluids B: Plasma Physics*, 2(6):1342–1346, 1990.

[47] R. M. Mayo, D. J. Hurlburt, and J. C. Fernández. Ion temperature profile deconvolution and corrections to confinement parameters in spheromaks. *Physics of Fluids B: Plasma Physics*, 5(11):4002–4010, 1993.

[48] M. G. Rusbridge, S. J. Gee, P. K. Browning, G. Cunningham, R. C. Duck, A. al-Karkhy, R. Martin, and J. W. Bradley. The design and operation of the SPHEX spheromak. *Plasma Physics and Controlled Fusion*, 39(5):683–714, 1997.

[49] D. M. Willett, P. K. Browning, S. Woodruff, and K. J. Gibson. The internal magnetic structure and current drive in the SPHEX spheromak. *Plasma Physics and Controlled Fusion*, 41(5):595–612, 1999.

[50] P. K. Browning, G. Cunningham, S. J. Gee, K. J. Gibson, A. al-Karkhy, D. A. Kitson, R. Martin, and M. G. Rusbridge. Power flow in a gun-injected spheromak plasma. *Physical Review Letters*, 68(11):1718–1721, Mar 1992.

[51] R. Martin, S. J. Gee, P. K. Browning, and M. G. Rusbridge. The direct determination of the current density and mu profiles of a spheromak. *Plasma Physics and Controlled Fusion*, 35(2):269–279, 1993.

[52] A. al-Karkhy, P. K. Browning, G. Cunningham, S. J. Gee, and M. G. Rusbridge. Observations

of the magnetohydrodynamic dynamo effect in a spheromak plasma. *Physical Review Letters*, 70(12):1814–1817, Mar 1993.

[53] R. C. Duck, P. K. Browning, G. Cunningham, S. J. Gee, A. al-Karkhy, R. Martin, and M. G. Rusbridge. Structure of the n = 1 mode responsible for relaxation and current drive during sustainment of the SPHEX spheromak. *Plasma Physics and Controlled Fusion*, 39(5):715–736, 1997.

[54] D. Brennan, P. K. Browning, R. A. M. Van der Linden, A. W. Hood, and S. Woodruff. Stability studies and the origin of the n = 1 mode in the SPHEX spheromak experiment. *Physics of Plasmas*, 6(11):4248–4259, 1999.

[55] S. Woodruff and M. Nagata. Instantaneous current and field structure of a gun-driven spheromak for two gun polarities. *Plasma Physics and Controlled Fusion*, 44(12):2539–2553, 2002.

[56] D. D. Ryutov, R. H. Cohen, and D. N. Hill. A phenomenological model of the current filamentation instability driven by cathode processes in the livermore spheromak. *Plasma Physics Reports*, 29(7):605, 2003.

[57] Z. Wang, G. A. Wurden, Cris W. Barnes, C. J. Buchenauer, H. S. McLean, D. N. Hill, E. B. Hooper, R. D. Wood, and S. Woodruff. Density and h[sub alpha] diagnostics and results for the sustained spheromak physics experiment. *Papers from the thirteenth topical conference on high temperature plasma diagnostics*, 72(1):1059–1062, 2001.

[58] S. Woodruff, E. B. Hooper, L. D. Pearlstein, R. Bulmer, D. N. Hill, C. T. Holcomb, H. S. McLean, J. Moller, B. W. Stallard, and R. D. Wood. Observation of a pressure limit in a gun-driven spheromak. *Physics of Plasmas*, 13(4):044506, 2006.

[59] M. M. Marchiano, E. G. Cook, R. W. Geer, R. O. Kemptner, H. S. McLean, N. N. Martovetsky, J. M. Moller, K. L. Morris, B. W. Stallard, J. A. Watson, and R. D. Wood. Bank upgrade for SSPX at LLNL. *Pulsed Power Conference, 2005 IEEE*, pages 688 –691, june 2005.

[60] E. B. Hooper, C. A. Romero-Talamás, L. L. LoDestro, R. D. Wood, and H. S. McLean. Aspect-ratio effects in the driven, flux-core spheromak. *Physics of Plasmas*, 16(5):052506, 2009.

[61] J. Ji, E. D. Held, and C. R. Sovinec. Moment approach to deriving parallel heat flow for general collisionality. *Physics of Plasmas (1994-present)*, 16(2):–, 2009.

[62] H. C. Lui, C. K. Chu, and A. Aydemir. Two-dimensional simulation of the formation of the princeton spheromak. *Physics of Fluids*, 24(4):673–678, 1981.

[63] S. C. Jardin and W. Park. Two-dimensional modeling of the formation of spheromak configurations. *Physics of Fluids*, 24(4):679–688, 1981.

[64] T. Sato, A. M. M. Todd, and H. Okuda. Numerical simulation of slow spheromak formation: Flux control by formation speed. *Physics of Fluids*, 26(3):775–779, 1983.

[65] A. G. Sgro and D. Winske. Simulation of the formation of the PS-1 spheromak. *Physics of Fluids*, 24(6):1156–1163, 1981.

[66] P. N. Guzdar, J. M. Finn, K. W. Whang, and A. Bondeson. The role of magnetic reconnection and differential rotation in spheromak formation. *Physics of Fluids*, 28(10):3154–3166, 1985.

[67] T. Sato, Y. Oda, S. Otsuka, K. Katayama, and M. Katsurai. Numerical simulation of axisymmetric spheromak merging. *Physics of Fluids*, 26(12):3602–3611, 1983.

[68] T. Sato and T. Hayashi. Three-dimensional simulation of spheromak creation and tilting disruption. *Physical Review Letters*, 50(1):38–40, Jan 1983.

[69] T. Hayashi and T. Sato. Simulation studies on line-tying stabilization of spheromak tilting instability. *Physics of Fluids*, 27(4):778–780, 1984.

[70] Takaya H. and T. Sato. Spheromak global instabilities and stabilization by nearby conductors. *Physics of Fluids*, 28(12):3654–3666, 1985.

[71] Y. Oda. 3D MHD simulation study on pressure-driven instability of spheromak in a flux conserver. *Journal of the Physical Society of Japan*, 54(3):958–966, 1985.

[72] K. Katayama and M. Katsurai. Three-dimensional numerical simulations of the relaxation process in spheromak plasmas. *Physics of Fluids*, 29(6):1939–1947, 1986.

[73] A. G. Sgro, A. A. Mirin, and G. Marklin. The evolution of a decaying spheromak. *Physics of Fluids*, 30(10):3219–3236, 1987.

[74] R. Horiuchi, T. Sato, and M. Uchida. Simulation study of stepwise relaxation in a spheromak plasma. *Physics of Fluids B: Plasma Physics*, 4(3):672–682, 1992.

[75] E. M. Freire and R. A. Clemente. Critical beta for analytical spheromak equilibria. *Plasma Physics and Controlled Fusion*, 27(4):389, 1985.

[76] R. M. Mayo and G. J. Marklin. Numerical calculation of Mercier beta limits in spheromaks. *Physics of Fluids (1958-1988)*, 31(6):1812–1815, 1988.

[77] P. Gautier, R. Gruber, and F. Troyon. Numerical study of the ideal-mhd stability limits in oblate spheromaks. *Nuclear Fusion*, 21(11):1399, 1981.

[78] S.C. Jardin. Ideal magnetohydrodynamic stability of the spheromak configuration. *Nuclear Fusion*, 22:629–42, 1982.

[79] J. DeLucia, S. C. Jardin, and A. H. Glasser. Resistive stability of the cylindrical spheromak. *Physics of Fluids*, 27(6):1470–1482, 1984.

[80] J. DeLucia and S. C. Jardin. Nonlinear evolution of the resistive interchange mode in the cylindrical spheromak. *Physics of Fluids*, 27(7):1773–1784, 1984.

[81] G.W. Hammett and W.M. Tang. Kinetic and resistive effects on interchange instabilities for a cylindrical model spheromak. *Nuclear Fusion*, 23(11):1503, 1983.

[82] U. Shumlak and T. R. Jarboe. Stable high beta spheromak equilibria using concave flux conservers. *Physics of Plasmas (1994-present)*, 7(7):2959–2963, 2000.

[83] C. R. Sovinec and J. R. King. Analysis of a mixed semi-implicit/implicit algorithm for low-frequency two-fluid plasma modeling. *Journal of Computational Physics*, 229(229):5803 – 5819, 2010.

[84] J. P. Boyd. *Chebyshev and Fourier Spectral Methods.* Dover Publications, Inc., 2nd edition, 2000.

[85] C. R. Sovinec, T. A. Gianakon, E. D. Held, S. E. Kruger, D. D. Schnack, and NIMROD Team. NIMROD: A computational laboratory for studying nonlinear fusion magnetohydrodynamics. *Physics of Plasmas*, 10(5):1727–1732, 2003.

[86] J. Wesson. *Tokamaks*. Oxford Science Publications, 3rd edition, 2004.

[87] P. M. Bellan. *Spheromaks*. Imperial College Press, 2000. and references therein.

[88] L. C. Steinhauer. Review of field-reversed configurations. *Physics of Plasmas*, 18(7):070501, 2011.

[89] G. Strang and G. J. Fix. *An Analysis of the Finite Element Method*. Prentice-Hall, 1973.

[90] J. P. Boyd. The asymptotic Chebyshev coefficients for functions with logarithmic endpoint singularities: mappings and singular basis functions. *Applied Mathematics and Computation*, 29(1):49 – 67, 1989.

[91] A. C. Hindmarsh. LSODE and LSODI, two new initial value ordinary differential equation solvers. *SIGNUM Newsl.*, 15(4):10–11, December 1980.

[92] B. J. Burke, S. E. Kruger, C. C. Hegna, P. Zhu, P. B. Snyder, C. R. Sovinec, and E. C. Howell. Edge localized linear ideal magnetohydrodynamic instability studies in an extended-magnetohydrodynamic code. *Physics of Plasmas*, 17(3):032103, 2010.

[93] R. A. Bayliss, C. R. Sovinec, and A. J. Redd. Zero-beta modeling of coaxial helicity injection in the HIT-II spherical torus. *Physics of Plasmas*, 18(9):094502, 2011.

[94] F. Ebrahimi, S. C. Prager, and C. R. Sovinec. Resistive-ideal transition of pressure-driven instabilities in current-carrying plasmas beyond the suydam criterion. *Physics of Plasmas (1994-present)*, 9(6):2470–2473, 2002.

[95] E. B. Hooper, D. N. Hill, H. S. McLean, C. A. Romero-Talamas, and R. D. Wood. Achieving high flux amplification in a gun-driven, flux-core spheromak. *Nuclear Fusion*, 47(8):1064–1070, 2007.

[96] National Bureau of Standards United States. *Tabels of Coulomb Wave Functions*. U.S. Government Printing Office, 1952.

[97] J. P. Freidberg. *Ideal Magnetohydrodynamics*. Plenum Press, 1987.